

**Universidade Federal de Minas Gerais**

**Escola de Engenharia**

**Programa de Pós-Graduação em Engenharia Elétrica**

**RIDE-THROUGH FAULT CAPABILITY IMPROVEMENT  
THROUGH NOVEL CONTROL STRATEGIES APPLIED FOR  
DOUBLY-FED INDUCTION WIND GENERATORS**

Victor Flores Mendes

Tese de Doutorado submetida à Banca Examinadora designada pelo Colegiado do Programa de Pós-Graduação em Engenharia Elétrica da Escola de Engenharia da Universidade Federal de Minas Gerais, como requisito para obtenção do Título de Doutor em Engenharia Elétrica.

Orientador: Prof. Selênio Rocha Silva

Belo Horizonte - MG

Maio de 2013



Programa de Pós-Graduação em Engenharia Elétrica - PPGEE  
Escola de Engenharia - EE  
Universidade Federal de Minas Gerais - UFMG

---

---

## **Ride-Through Fault Capability Improvement Through Novel Control Strategies Applied for Doubly-Fed Induction Wind Generators**

---

**Victor Flores Mendes**

Tese submetida à banca examinadora designada pelo Colegiado do Programa de Pós-Graduação em Engenharia Elétrica da Universidade Federal de Minas Gerais, como parte dos requisitos necessários para à obtenção do título de Doutor em Engenharia Elétrica.

**Orientador :** Prof. Dr. Selênio Rocha Silva  
**Co-orientador :** Prof. Dr. Ing. Wilfried Hofmann

Belo Horizonte, Maio de 2013.





TESE DE DOUTORADO Nº 159

**RIDE-THROUGH FAULT CAPABILITY IMPROVEMENT THROUGH NOVEL  
CONTROL STRATEGIES APPLIED FOR DOUBLY-FED INDUCTION WIND  
GENERATORS**

**Victor Flores Mendes**

DATA DA DEFESA: 17/05/2013



**"Ride-through Fault Capability Improvement Through Novel  
Control Strategies Applied for Doubly-fed Induction Wind  
Generators"**

**Victor Flores Mendes**

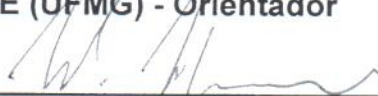
Tese de Doutorado submetida à Banca Examinadora designada pelo Colegiado do Programa de Pós-Graduação em Engenharia Elétrica da Escola de Engenharia da Universidade Federal de Minas Gerais, como requisito para obtenção do grau de Doutor em Engenharia Elétrica.

Aprovada em 17 de maio de 2013.

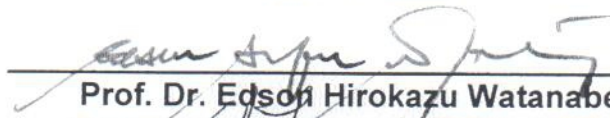
Por:



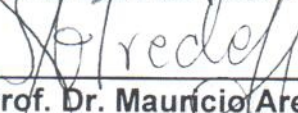
**Prof. Dr. Selênio Rocha Silva**  
DEE (UFMG) - Orientador



**Prof. Dr. Wilfried Hofmann**  
Elektrotechnisches Institute (Technische Universitt Dresden)  
Co-Orientador



**Prof. Dr. Edson Hirokazu Watanabe**  
Engenharia Elétrica (COPPE - UFRJ)



**Prof. Dr. Mauricio Aredes**  
Engenharia Elétrica (COPPE-UFRJ)



**Prof. Dr. Sidelmo Magalhães Silva**  
DEE (UFMG)



**Prof. Dr. Seleme Isaac Seleme Júnior**  
DELT (UFMG)



*Dedicated to my wife,  
my daughter and fa-  
mily.*

*“Learn from yesterday, live for today, hope for tomorrow. The important thing is not to stop questioning.”*

Albert Einstein

---

---

# Acknowledgment

---

I would like to thank:

God in first place;

my wife, Marina, who is always supporting me and without her everything would be harder;

my little princess, Eduarda whose smile is my greatest motivation;

my parents, Edilson and Silvana, the reasons I am here;

my brothers, Vinicius and Peu, for being so close even being far;

my mother in law and father in law, Eduardo e Vera, who always have been like parents for me;

my grandfathers and grandmothers, here or somewhere else;

my Professor and friend Selênio, my master and professional example.

Professor Wilfried Hofmann for the opportunity to develop part of my research at TU-Dresden and the incentive in my work;

the co-workers in the laboratory here in Brazil and in Germany: Clodualdo, João, Fred, Guilherme, Pedrinho, Tameirão, Tomás, Caio, Silas, Heverton, Balduino, Bastian, Sebastian, ... Everyone helped a lot for the realization of this thesis;

the friends and family;

the professors and colleagues of UFMG, UNIFEI and TU Dresden.





---

---

# Table of Contents

---

<b>Resumo</b>	<b>xiv</b>
<b>Abstract</b>	<b>xvi</b>
<b>Table List</b>	<b>xvii</b>
<b>Figure List</b>	<b>xxxiii</b>
<b>Symbol List</b>	<b>xxxvii</b>
<b>Abbreviation List</b>	<b>xl</b>
<b>1 Introduction</b>	<b>1</b>
1.1 Brief History of Wind Energy . . . . .	1
1.2 Overview of Wind Energy Nowadays . . . . .	2
1.3 Technologies of Wind Energy Conversion Systems . . . . .	3
1.4 Voltage Sags . . . . .	6
1.5 Motivation and Objectives . . . . .	8
1.6 Methodology . . . . .	10
1.7 State of Art . . . . .	11
1.8 Contributions . . . . .	15
1.9 Text Organization . . . . .	17

<b>2</b>	<b>Doubly-Fed Wind Energy Conversion System</b>	<b>19</b>
2.1	Introduction . . . . .	19
2.2	The DFIG Technology . . . . .	19
2.2.1	Wound rotor induction generator . . . . .	21
2.2.2	LCL Filter . . . . .	23
2.2.3	Converters . . . . .	24
2.3	Classical Control Strategy . . . . .	24
2.3.1	GSC control . . . . .	24
2.3.2	Phase-Locked Loop (PLL) . . . . .	25
2.3.3	RSC control . . . . .	26
2.4	The Simulation Model . . . . .	28
2.5	The Test Benches . . . . .	30
2.5.1	Sag generator using impedances (ISG) . . . . .	33
2.5.2	Industrial Power Corruptor (IPC) . . . . .	36
2.6	Final Considerations . . . . .	36
<b>3</b>	<b>DFIG Behavior During Balanced Voltage Sags</b>	<b>37</b>
3.1	Introduction . . . . .	37
3.2	Mathematical Modeling . . . . .	37
3.2.1	Time domain model . . . . .	38
3.2.2	Laplace domain model . . . . .	39
3.2.3	Open rotor circuit analysis in time domain . . . . .	42
3.2.4	Open rotor circuit analysis in Laplace domain . . . . .	50
3.2.5	Complete analysis in Laplace domain . . . . .	51
3.3	Experimental Results . . . . .	59
3.3.1	Test 1: Synchronous Speed . . . . .	59
3.3.2	Test 2: Synchronous Speed, Modifying the Control Gains	66
3.3.3	Test 3: Slip = +0.15 . . . . .	67
3.3.4	Test 4: Slip = -0.15 . . . . .	69

3.3.5	Test 5: Slip = -0.15 - Control Saturation . . . . .	71
3.3.6	Rotor currents excursion . . . . .	72
3.4	Simulation Results . . . . .	73
3.5	Final Considerations . . . . .	75
<b>4</b>	<b>DFIG Behavior During Unbalanced Voltage Sags</b>	<b>77</b>
4.1	Introduction . . . . .	77
4.2	Mathematical Modeling . . . . .	77
4.2.1	Time domain model . . . . .	78
4.2.2	Open rotor circuit analysis in time domain . . . . .	79
4.2.3	Laplace domain model . . . . .	86
4.2.4	Open rotor circuit analysis in Laplace domain . . . . .	88
4.2.5	Complete analysis in Laplace domain . . . . .	89
4.3	Experimental Results . . . . .	95
4.3.1	Test 1: Slip = -0.15, maximum natural component ( $\theta_0 = 0^0$ ) . . . . .	95
4.3.2	Test 2: Slip = +0.3, no natural component ( $\theta_0 = 90^0$ ) .	101
4.3.3	Test 3: synchronous speed - maximum natural compo- nent ( $\theta_0 = 0^0$ ) . . . . .	103
4.3.4	Rotor voltage and current excursion . . . . .	104
4.4	Simulation Results . . . . .	106
4.5	Final Considerations . . . . .	108
<b>5</b>	<b>Ride-Through Strategies - Symmetrical Voltage Sags Case</b>	<b>109</b>
5.1	Introduction . . . . .	109
5.2	Magnetizing Current Control (MCC) . . . . .	109
5.2.1	Influence of magnetizing current on stator flux linkage	111
5.2.2	Influence of MCC on the rotor currents . . . . .	116
5.2.3	Influence of the MCC on the rotor voltages . . . . .	118

5.2.4	Influence of the MCC gain on the rotor currents and voltages . . . . .	121
5.2.5	Experimental results . . . . .	124
5.2.6	Application issues . . . . .	130
5.3	Final Considerations . . . . .	131
<b>6</b>	<b>Ride-Through Strategies - Asymmetrical Voltage Sags Case</b>	<b>133</b>
6.1	Introduction . . . . .	133
6.2	Compensation of Torque and Reactive Power Pulsations (CTRP)	134
6.3	Dual PI Controllers (DPIC) . . . . .	140
6.3.1	The DPIC strategy . . . . .	141
6.3.2	Mathematical modeling during the voltage sags . . . . .	144
6.3.3	Calculation of the rotor current references . . . . .	145
6.3.4	Calculation of the grid current references . . . . .	150
6.3.5	Simulation results . . . . .	152
6.3.6	Converter limitation analysis . . . . .	158
6.3.7	Experimental results . . . . .	163
6.3.8	Considerations about the DPIC strategy . . . . .	167
6.4	PI Plus Resonant Controllers(PIRC) . . . . .	168
6.4.1	The PIRC strategy . . . . .	169
6.4.2	Mathematical modeling during voltage sags . . . . .	170
6.4.3	Simulation results . . . . .	174
6.4.4	Considerations about the PIRC . . . . .	178
6.5	Enhanced PIR Control (EPIRC) . . . . .	178
6.5.1	The EPIRC strategy . . . . .	178
6.5.2	Simulation results . . . . .	179
6.5.3	Experimental results . . . . .	179
6.6	Resonant Control Plus Magnetizing Current Control (RMCC)	183
6.6.1	The RMCC strategy . . . . .	183

6.6.2	Simulation results . . . . .	184
6.6.3	Experimental results . . . . .	185
6.7	Final Considerations . . . . .	187
<b>7</b>	<b>Conclusions and Future Work</b>	<b>189</b>
7.1	Conclusions . . . . .	189
7.2	Future Works . . . . .	191
	<b>References</b>	<b>195</b>
<b>A</b>	<b>Controllers Tuning and Orientation</b>	<b>205</b>
A.1	Clark and Park Transforms . . . . .	205
A.2	Modulus Optimum and Symmetrical Optimum . . . . .	207
A.3	Control Mathematical Modeling and Gains Tuning . . . . .	209
A.3.1	GSC control . . . . .	209
A.3.2	RSC control . . . . .	214
A.4	Controller Discretization . . . . .	220
<b>B</b>	<b>TUD Test Bench Parameters</b>	<b>222</b>
<b>C</b>	<b>UFMG Test Bench Parameters</b>	<b>224</b>
<b>D</b>	<b>Simulation Model Parameters</b>	<b>226</b>



---

# Resumo

---

Devido ao aumento da capacidade de potência instalada em parques eólicos pelo mundo, os códigos de rede mais modernos contemplam requisitos específicos para conexão de usinas eólicas às redes elétricas. Dentre esses requisitos está a suportabilidade dos equipamentos aos afundamentos momentâneos de tensão, que indica os limites para desconexão das turbinas eólicas durante estes distúrbios. Além de operar continuamente durante os afundamentos de tensão, alguns códigos de rede requerem ainda o fornecimento de potência reativa para auxiliar na estabilização da rede.

Neste contexto, esse trabalho analisa o comportamento dos aerogeradores de indução duplamente excitados (DFIG - “doubly-fed induction generator”) durante afundamentos de tensão equilibrados e desequilibrados. Primeiramente a análise é realizada através de equacionamentos matemáticos no domínio do tempo e de Laplace que explicam o comportamento das principais variáveis envolvidas no processo bem como a influência do ajuste do controle clássico em tais variáveis. Posteriormente resultados experimentais são utilizados para provar o desenvolvimento matemático e evidenciar o comportamento do gerador e conversores. Tais resultados foram obtidos em duas bancadas de testes: uma de 4kW e outra de 25kW projetada e construída durante este trabalho. Resultados simulados em um modelo representativo de uma turbina de 2MW são também analisados para extrapolar os resultados obtidos nas bancadas de pequeno porte.

Os resultados obtidos para o controle clássico demonstram as fragilidades do sistema. A partir de tais resultados novas estratégias de controle a fim de melhorar a suportabilidade dessa tecnologia são propostas. O controle da corrente de magnetização do gerador é utilizado durante afundamentos equilibrados e para o caso desequilibrado este controle é utilizado em conjunto com controladores ressonantes. Tais estratégias são avaliadas através de simulação e testes experimentais demonstrando-se a melhoria da suportabilidade durante os afundamentos momentâneos de tensão.

As principais contribuições desse trabalho são a modelagem matemática no domínio de Laplace, que permite avaliar o efeito dos controladores no comportamento do sistema durante os afundamentos de tensão, e o desenvolvimento de novas estratégias de controle para a melhoria da suportabilidade da tecnologia DFIG. Ademais, o desenvolvimento de uma bancada de 25kW é uma importante contribuição, pois apresentam-se resultados em potência maior que os usualmente relatados na literatura, além de permitir outros estudos relacionados a esse tema.

Palavras-chaves: Gerador de Indução Duplamente Excitado, Suportabilidade a Afundamentos de Tensão, Afundamentos Momentâneos de Tensão, Sistemas de Conversão de Energia Eólica.



---

---

# Abstract

---

Due to the continuing growth of the installed power capacity of wind farms worldwide, the modern grid codes define specific requirements to the connection of wind turbines to the grid. One of these requirements is the ride-through fault capability, that is, the equipment capability of continuing operating during voltage sags. The grid codes require that, for some levels and duration of voltage sags, the equipment must not be disconnected from the grid and also supplies reactive power in order to contribute to network voltage stabilization.

In this context, the present work analyzes the behavior of the doubly-fed induction generator technology (DFIG) during balanced and unbalanced voltage sags. First, the analysis is developed based on a mathematical modeling in time and Laplace domains that explains the behavior of the main variables and highlight the effect of the classical control tuning on such variables. Then, the mathematical approach is proved through experimental results which evidence the behavior of the generator and converters. Such results were obtained in two test benches with rated power of 4kW and a 25kW which was projected and mounted during this work. Furthermore, simulation results of a representative model of a 2MW turbine are analyzed in order to extrapolate the conclusions made for the small scale test benches.

The results of the classical control show the system weak points. Based on these results novel control strategies are proposed to improve the DFIG ride-through fault capability. The control of the generator magnetizing current is used during symmetrical voltage sags whereas for the asymmetrical case this strategy is combined with resonant controllers. The strategies are evaluated using simulation and experimental results that demonstrate the improvement of the system ride-through fault capability.

The main contributions of this work are the mathematical modeling in the Laplace domain, which permits to evaluate the control effects on the system behavior during the voltage sags, and the proposal of novel control strategies to improve the system ride-through fault capability. Furthermore, the development of a 25kW test bench is a important contribution because results with higher power than the usually presented in the literature are presented and it will permit other studies related to this theme.

Keywords: Doubly-fed Induction Generator (DFIG), Low Voltage Ride-Through Capability (LVRT), Voltage Sags and Wind Conversion Systems.

---

---

# Table List

---

6.1	Percentage of unbalance and of oscillations for different simulated voltage sags ( $\theta_0 = 90^0$ ) . . . . .	153
B.1	Parameters of the generator of the TUD test bench. . . . .	222
B.2	Voltage sag parameters of the TUD test bench. . . . .	222
B.3	Controller gains of the TUD test bench. . . . .	223
B.4	Other parameters of the TUD test bench. . . . .	223
C.1	Parameters of the generator of the UFMG test bench. . . . .	224
C.2	Controller gains of the UFMG test bench. . . . .	225
C.3	Other parameters of the UFMG test bench. . . . .	225
D.1	Parameters of the generator used in the simulation model. . . . .	226
D.2	Controller gains of the simulation. . . . .	226
D.3	Other parameters of the simulation model. . . . .	227



---

---

# Figure List

---

1.1	Total world installed capacity of WECS (Global Wind Energy Council, 2013). . . . .	3
1.2	Technologies of wind energy conversion systems (Blaabjerg et al., 2006). (a) - Generator with direct connection to the grid; (b) - Generator with gearbox and full scale converter; (c) - Gearless generator with full-scale converter; (d) - Doubly-fed generator with partial converter power. . . . .	5
1.3	Active power flow in the DFIG technology as generator (Rabelo, 2009). (a) - Sub-synchronous speed operation; (b) - Super-synchronous speed operation. . . . .	6
1.4	Ride-through fault capability curve required in the Brazilian grid code (ONS, 2009a). . . . .	8
1.5	Ride-through fault capability curve required by EON-Germany grid code (E.ON, 2006). . . . .	9
1.6	The principle of voltage support in the event of grid fault required by EON-Germany grid code (E.ON, 2006). . . . .	9
2.1	DFIG drive topology (Blaabjerg et al., 2006). . . . .	20
2.2	LCL filter schematic circuit. . . . .	23
2.3	Block diagram representation of the GSC control structure. . . . .	25
2.4	PLL topology - PSOGI (Rodriguez et al., 2006). . . . .	26

2.5	Block diagram representation of the RSC control structure. . . . .	27
2.6	Simulation model implemented in Simulink. . . . .	29
2.7	Diagram of the test benches that emulate DFIG systems. . . . .	31
2.8	Picture of the TU Dresden test bench - 4kW system. . . . .	32
2.9	Picture of the UFMG test bench - 25kW system. . . . .	32
2.10	Schematic diagram of the ISG voltage sag generator. . . . .	33
2.11	Tolerance of voltage drop (IEC, 2008). . . . .	34
2.12	Experimental results of the stator voltage for three-phase voltage sags: (a) - TUD test bench: 85%; (b) - UFMG test bench 50%. . . . .	34
2.13	Experimental results of the stator voltage for phase-phase voltage sags: (a) - TUD test bench: 90%; (b) - UFMG test bench 50%. . . . .	35
3.1	Complex plane representation of the stator flux linkage during a 50% three-phase voltage sag. . . . .	43
3.2	Comparison between the rotor voltages calculated and the experimental results in the TUD test bench: (a) - TUD test bench: 85% three-phase voltage sag, 1950 RPM; (b) - UFMG test bench: 50% three-phase voltage sag, 2340 RPM. . . . .	45
3.3	Rotor voltage components during the sag obtained through Equations 3.27, 3.28 and 3.29 for: (a) - TUDb parameters (85% three-phase voltage sag, 1950 RPM); (b) - UFMGb parameters (50% three-phase voltage sag, 2340 RPM). . . . .	45
3.4	Fourier analysis of the measured rotor voltage during the sag for the TUDb(85% three-phase voltage sag, 1950 RPM). . . . .	46
3.5	Experimental result of the maximum rotor voltage during different voltage sags - UFMGb. . . . .	48

3.6	Comparison between the rotor voltage simulated and calculated with the parameters of the 2MW system (50% three-phase voltage sag, 1950 RPM). . . . .	49
3.7	Rotor voltage measured and calculated - TUDb (85% three-phase voltage sag, 1300 RPM). . . . .	51
3.8	Block diagram representation of Equations 3.37, 3.38, 3.43 and 3.44. . . . .	53
3.9	Block diagram representation of the current control. . . . .	54
3.10	Rotor equivalent circuit. . . . .	54
3.11	Bode diagram of the PI controller (2MW WECS gains). . . . .	56
3.12	Direct axis stator flux linkage (2MW WECS, 50% three-phase sag). . . . .	58
3.13	Experimental results of the phase A of the rotor currents at synchronous speed: (a) - TUD test bench (85% three-phase voltage sag, 1500 RPM); (b) - UFMG test bench (50% three-phase voltage sag, 1800 RPM). . . . .	60
3.14	Fourier analysis of the phase A rotor current at synchronous speed: (a) - TUD test bench (85% three-phase voltage sag, 1500 RPM); (b) - UFMG test bench (50% three-phase voltage sag, 1800 RPM). . . . .	61
3.15	Experimental results of the direct and quadrature axes of rotor currents at synchronous speed test: (a) - TUD test bench (85% three-phase voltage sag, 1500 RPM); (b) - UFMG test bench (50% three-phase voltage sag, 1800 RPM). . . . .	62
3.16	Experimental results of the phase A of the rotor voltages at synchronous speed test: (a) - TUD test bench (85% three-phase voltage sag, 1500 RPM); (b) - UFMG test bench (50% three-phase voltage sag, 1800 RPM). . . . .	63

- 3.17 Experimental results of the phase A of the stator currents at synchronous speed test: (a) - TUD test bench (85% three-phase voltage sag, 1500 RPM); (b) - UFMG test bench (50% three-phase voltage sag, 1800 RPM). . . . . 64
- 3.18 Experimental results of the estimated electromagnetic torque at synchronous speed test: (a) - TUD test bench (85% three-phase voltage sag, 1500 RPM); (b) - UFMG test bench (50% three-phase voltage sag, 1800 RPM). . . . . 64
- 3.19 Experimental results of the estimated active and reactive powers at synchronous speed test: (a) - TUD test bench (85% three-phase voltage sag, 1500 RPM); (b) - UFMG test bench (50% three-phase voltage sag, 1800 RPM). . . . . 65
- 3.20 Experimental results of the DC-link voltage at synchronous speed test: (a) - TUD test bench (85% three-phase voltage sag, 1500 RPM); (b) - UFMG test bench (50% three-phase voltage sag, 1800 RPM). . . . . 65
- 3.21 Experimental results of the dq GSC currents at synchronous speed test: (a) - TUD test bench (85% three-phase voltage sag, 1500 RPM); (b) - UFMG test bench (50% three-phase voltage sag, 1800 RPM). . . . . 66
- 3.22 Experimental results of the dq rotor currents at synchronous speed test with modified gains: (a) - TUD test bench (85% three-phase voltage sag, 1500 RPM); (b) - UFMG test bench (50% three-phase voltage sag, 1800 RPM). . . . . 67
- 3.23 Experimental results of the phase A of the rotor voltages at synchronous speed test with modified gains: (a) - TUD test bench (85% three-phase voltage sag, 1500 RPM); (b) - UFMG test bench (50% three-phase voltage sag, 1800 RPM). . . . . 67
- 3.24 Experimental result of the phase A of the rotor currents for slip=+0.15: (a) - TUD test bench (85% three-phase voltage sag, 1275 RPM); (b) - UFMG test bench (50% three-phase voltage sag, 1530 RPM). . . . . 68



3.25	Fourier analysis of the rotor currents for slip=+0.15: (a) - TUD test bench (85% three-phase voltage sag, 1275 RPM); (b) - UFMG test bench (50% three-phase voltage sag, 1530 RPM). . . . .	69
3.26	Experimental result of the dq rotor currents for slip=+0.15: (a) - TUD test bench (85% three-phase voltage sag, 1275 RPM); (b) - UFMG test bench (50% three-phase voltage sag, 1530 RPM). . . . .	69
3.27	Experimental result of the phase A of the rotor currents for slip=-0.15: (a) - TUD test bench (85% three-phase voltage sag, 1725 RPM); (b) - UFMG test bench (80% three-phase voltage sag, 2070 RPM). . . . .	70
3.28	Experimental result of the phase A of the rotor voltages for slip=-0.15: (a) - TUD test bench (85% three-phase voltage sag, 1725 RPM); (b) - UFMG test bench (80% three-phase voltage sag, 2070 RPM). . . . .	70
3.29	Experimental result of the TUDb, 1725 RPM, $V_{dc} = 200V$ : (a) - Rotor currents; (b) - Rotor Voltages. . . . .	71
3.30	Experimental result of the TUDb, 1725 RPM, $V_{dc} = 170V$ : (a) - Rotor currents; (b) - Rotor Voltages. . . . .	72
3.31	Maximum rotor currents: (a) - TUD test bench (85% three-phase voltage sag); (b) - UFMG test bench. . . . .	73
3.32	Simulation results of the dq rotor currents (1950 RPM, $K_p = 0.26\Omega$ and $K_i = 1.36\Omega/s$ ). . . . .	74
3.33	Simulation results of the dq rotor currents (1950 RPM, $K_p = 0.053\Omega$ and $K_i = 0.27\Omega/s$ ). . . . .	75
3.34	Simulation results of the dq rotor currents (1950 RPM, $K_p = 0.26\Omega$ and $K_i = 1.36\Omega/s$ ). . . . .	75
4.1	Stator flux linkage during a 50% phase-neutral voltage sag in the complex plane: (a) - $\theta_0 = 90^0$ - no natural component; (b) - $\theta_0 = 0^0$ - maximum natural component. . . . .	81

4.2	Open rotor experimental result for the TUDb with 90% phase-phase voltage sag, $\theta_0 = 90^0$ and 1950 RPM: (a) - Phase A of the rotor voltages; (b) - Fourier analysis of the rotor voltages. .	82
4.3	Open rotor experimental result for the TUDb with 90% phase-phase voltage sag, $\theta_0 = 0^0$ and 1950 RPM: (a) - Phase A of the rotor voltages; (b) - Fourier analysis of the rotor voltages. .	82
4.4	Open rotor experimental result for the UFMGb with 50% phase-phase voltage sag, $\theta_0 = 90^0$ and 2340 RPM: (a) - Phase A of the rotor voltages; (b) - Fourier analysis of the rotor voltages. . . . .	83
4.5	Open rotor experimental result for the UFMGb with 90% phase-phase voltage sag, $\theta_0 = 0^0$ and 2340 RPM: (a) - Phase A of the rotor voltages; (b) - Fourier analysis of the rotor voltages.	83
4.6	Maximum experimental and theoretical rotor voltage in the UFMGb for different phase-to-phase voltage sags in the case without natural component ( $\theta_0 = 90^0$ ). . . . .	85
4.7	Maximum experimental and theoretical rotor voltage in the UFMGb for different phase-to-phase voltage sags in the case with the maximum natural component ( $\theta_0 = 0^0$ ). . . . .	86
4.8	Simulated result of the stator voltage sequence components in different reference frames. . . . .	91
4.9	Bode diagram of the transfer functions in Equation 4.43 - direct voltage (continuous line) and quadrature voltage (dashed line). Parameters of the 2-MW system. . . . .	93
4.10	Bode diagram of the transfer functions 4.47 for different controller gains with the 2-MW system parameters. . . . .	95
4.11	Experimental results of the phase A of the rotor currents for a slip = -0.15, $\theta_0 = 0^0$ : (a) - TUD test bench (90% phase-to-phase voltage sag, 1725 RPM); (b) - UFMG test bench (65% phase-to-phase voltage sag, 2070 RPM). . . . .	96

- 4.12 Fourier analysis of the rotor currents for a slip = -0.15,  $\theta_0 = 0^0$ :  
 (a) - TUD test bench (90% phase-to-phase voltage sag, 1725 RPM); (b) - UFMG test bench (65% phase-to-phase voltage sag, 2070 RPM). . . . . 97
- 4.13 Experimental result of the dq rotor currents for a slip = -0.15,  $\theta_0 = 0^0$ : (a) - TUD test bench (90% phase-to-phase voltage sag, 1725 RPM); (b) - UFMG test bench (65% phase-to-phase voltage sag, 2070 RPM). . . . . 97
- 4.14 Experimental results of the phase A of the rotor voltages for a slip = -0.15,  $\theta_0 = 0^0$ : (a) - TUD test bench (90% phase-to-phase voltage sag, 1725 RPM); (b) - UFMG test bench (65% phase-to-phase voltage sag, 2070 RPM). . . . . 98
- 4.15 Experimental result of the estimated electromagnetic torque for a slip = -0.15,  $\theta_0 = 0^0$ : (a) - TUD test bench (90% phase-to-phase voltage sag, 1725 RPM); (b) - UFMG test bench (65% phase-to-phase voltage sag, 2070 RPM). . . . . 99
- 4.16 Experimental result of the active and reactive powers for a slip = -0.15,  $\theta_0 = 0^0$ : (a) - TUD test bench (90% phase-to-phase voltage sag, 1725 RPM); (b) - UFMG test bench (65% phase-to-phase voltage sag, 2070 RPM). . . . . 99
- 4.17 Experimental results of the DC-link voltage for a slip = -0.15,  $\theta_0 = 0^0$ : (a) - TUD test bench (90% phase-to-phase voltage sag, 1725 RPM); (b) - UFMG test bench (65% phase-to-phase voltage sag, 2070 RPM). . . . . 100
- 4.18 Experimental results of the dq GSC currents for slip = -0.15,  $\theta_0 = 0^0$ : (a) - TUD test bench (90% phase-to-phase voltage sag, 1725 RPM); (b) - UFMG test bench (65% phase-to-phase voltage sag, 2070 RPM). . . . . 100
- 4.19 Experimental results of the phase A of the rotor currents for a slip = +0.3,  $\theta_0 = 90^0$ : (a) - TUD test bench (90% phase-to-phase voltage sag, 1050 RPM); (b) - UFMG test bench (65% phase-to-phase voltage sag, 1260 RPM). . . . . 101

4.20	Fourier analysis of the rotor current for a slip = +0.3, $\theta_0 = 90^0$ : (a) - TUD test bench (90% phase-to-phase voltage sag, 1050 RPM); (b) - UFMG test bench (65% phase-to-phase voltage sag, 1260 RPM). . . . .	102
4.21	Experimental results of the dq rotor currents for a slip = +0.3, $\theta_0 = 90^0$ : (a) - TUD test bench (90% phase-to-phase voltage sag, 1050 RPM); (b) - UFMG test bench (65% phase-to-phase voltage sag, 1260 RPM). . . . .	102
4.22	Experimental results of the phase A of the rotor currents at synchronous speed, $\theta_0 = 0^0$ : (a) - TUD test bench (90% phase-to-phase voltage sag, 1500 RPM); (b) - UFMG test bench (65% phase-to-phase voltage sag, 1800 RPM). . . . .	103
4.23	Fourier analysis of the rotor current at synchronous speed, $\theta_0 = 0^0$ : (a) - TUD test bench (90% phase-to-phase voltage sag, 1500 RPM); (b) - UFMG test bench (65% phase-to-phase voltage sag, 1800 RPM). . . . .	103
4.24	Experimental result of the maximum rotor currents for different speeds and voltage sags: $\theta_0 = 90^0$ : (a) - no natural component $\theta_0 = 90^0$ ; (b) - maximum natural component $\theta_0 = 0^0$ .	104
4.25	Experimental result of the maximum rotor voltages for different speeds and voltage sags: $\theta_0 = 90^0$ : (a) - no natural component $\theta_0 = 90^0$ ; (b) - maximum natural component $\theta_0 = 0^0$ .	105
4.26	Simulation result of the dq rotor currents, 1950 RPM, 50% phase-neutral voltage sag: (a) - $\theta_0 = 90^0$ - no natural component; (b) - $\theta_0 = 0^0$ - maximum natural component. . . . .	107
4.27	Simulation result of the dq rotor currents, 1950 RPM, 50% phase-neutral voltage sag, recovering instant: (a) - no natural component; (b) - maximum natural component. . . . .	107
5.1	Magnetizing current control block diagram. . . . .	111

5.2	Simulation and theoretical results of the dq stator flux linkage, 50% three-phase voltage sag, 1950 RPM: (a) - Without the MCC strategy ; (b) - With the MCC strategy - $K_{p_{im}} = 15$ . . . . .	116
5.3	dq rotor currents simulated for a 50% three-phase voltage sag, rated power (no reactive power control). . . . .	117
5.4	dq rotor currents simulated for a 50% three-phase voltage sag, rated power (no reactive power control): (a) - Without the magnetizing current control; (b) - With the magnetizing current control. . . . .	118
5.5	Simulation results for 50% three-phase voltage sag, rated power, using the MCC strategy and reactive power control: (a) - dq rotor currents; (b) - Stator active and reactive powers. . . . .	118
5.6	Comparison between the rotor voltages with and without the MCC strategy - simulation result. . . . .	120
5.7	Rotor voltage calculated and simulated for different voltage sags and speeds using the MCC strategy - $K_{p_{im}} = 15$ . . . . .	121
5.8	Rotor currents simulated for different voltage sags and speeds (MCC strategy). . . . .	122
5.9	Time constant of the stator flux linkage decay varying the magnetizing current control gain - 2MW parameters. . . . .	123
5.10	Maximum rotor current simulated for different voltage sags and varying the magnetizing current control gain. . . . .	123
5.11	Maximum rotor voltage simulated for different voltage sags and varying the magnetizing current control gain. . . . .	124
5.12	Experimental results of the estimated dq stator fluxes using the MCC strategy: (a) - TUD test bench - $K_{p_{im}} = 4$ (85% three-phase voltage sag, 1500 RPM, $K_p = 100\Omega$ , $K_i = 10000\Omega/s$ ); (b) - UFMG test bench - $K_{p_{im}} = 2.5$ (50% three-phase voltage sag, 1800 RPM). . . . .	126

- 5.13 Experimental results of the dq rotor currents using the MCC strategy: (a) - TUD test bench -  $K_{p_{im}} = 4$  (85% three-phase voltage sag, 1500 RPM,  $K_p = 100\Omega$ ,  $K_i = 10000\Omega/s$ ); (b) - UFMG test bench -  $K_{p_{im}} = 2.5$  (50% three-phase voltage sag, 1800 RPM). . . . . 126
- 5.14 Experimental results of the dq rotor voltages using the MCC strategy: (a) - TUD test bench -  $K_{p_{im}} = 4$  (85% three-phase voltage sag, 1500 RPM,  $K_p = 100\Omega$ ,  $K_i = 10000\Omega/s$ ); (b) - UFMG test bench -  $K_{p_{im}} = 2.5$  (50% three-phase voltage sag, 1800 RPM). . . . . 127
- 5.15 Experimental results of the dq rotor currents using the MCC strategy: (a) - TUD test bench -  $K_{p_{im}} = 4$  (85% three-phase voltage sag, 1750 RPM,  $K_p = 100\Omega$ ,  $K_i = 10000\Omega/s$ ); (b) - UFMG test bench -  $K_{p_{im}} = 2.5$  (50% three-phase voltage sag, 2070 RPM). . . . . 128
- 5.16 Experimental results of the estimated dq stator fluxes using the MCC strategy: (a) - TUD test bench -  $K_{p_{im}} = 4$  (85% three-phase voltage sag, 1750 RPM,  $K_p = 100\Omega$ ,  $K_i = 10000\Omega/s$ ); (b) - UFMG test bench -  $K_{p_{im}} = 2.5$  (50% three-phase voltage sag, 2070 RPM). . . . . 128
- 5.17 Experimental results of the dq rotor currents using the MCC strategy and reactive power control: (a) - TUD test bench -  $K_{p_{im}} = 4$  (85% three-phase voltage sag, 1800 RPM,  $K_p = 100\Omega$ ,  $K_i = 10000\Omega/s$ ); (b) - UFMG test bench -  $K_{p_{im}} = 2.5$  (50% three-phase voltage sag, 1530 RPM). . . . . 129
- 5.18 Experimental results of the dq rotor voltages using the MCC strategy and reactive power control: (a) - TUD test bench -  $K_{p_{im}} = 4$  (85% three-phase voltage sag, 1800 RPM,  $K_p = 100\Omega$ ,  $K_i = 10000\Omega/s$ ); (b) - UFMG test bench -  $K_{p_{im}} = 2.5$  (50% three-phase voltage sag, 1530 RPM). . . . . 129

5.19	Experimental results of the active and reactive stator powers using the MCC strategy and reactive power control: (a) - TUD test bench - $K_{p_{im}} = 4$ (85% three-phase voltage sag, 1800 RPM, $K_p = 100\Omega$ , $K_i = 10000\Omega/s$ ); (b) - UFMG test bench - $K_{p_{im}} = 2.5$ (50% three-phase voltage sag, 1530 RPM). . . . .	130
6.1	Control of RSC with the strategy of compensating the torque and reactive power oscillations. . . . .	134
6.2	Simulation result of the electromagnetic torque with and without the CTRP strategy (80% phase-neutral voltage sag, $\theta_0 = 90^0$ and 1950 RPM). . . . .	136
6.3	Stator active and reactive powers with and without the CTRP strategy (80% phase-neutral voltage sag, $\theta_0 = 90^0$ and 1950 RPM). . . . .	136
6.4	Simulation results of the ABC rotor currents (80% phase-neutral voltage sag, $\theta_0 = 90^0$ and 1950 RPM): (a) - Without the CTRP strategy; (b) - With the CTRP strategy. . . . .	137
6.5	Simulation result of the ABC rotor voltages with the CTRP strategy (80% phase-neutral voltage sag, $\theta_0 = 90^0$ and 1950 RPM). . . . .	138
6.6	Simulation result of the electromagnetic torque with the CTRP strategy (80% phase-neutral voltage sag, $\theta_0 = 0^0$ and 1950 RPM). . . . .	138
6.7	Simulation results of the ABC rotor currents (80% phase-neutral voltage sag, $\theta_0 = 0^0$ and 1950 RPM): (a) - Without the CTRP strategy; (b) - With the CTRP strategy. . . . .	139
6.8	Simulation result of the electromagnetic torque with the CTRP+MCC strategy (80% phase-neutral voltage sag, $\theta_0 = 0^0$ and 1950 RPM). . . . .	140
6.9	Control of positive and negative current sequences in the RSC .	143
6.10	Control of positive and negative current sequences in the GSC.	143

6.11	Simulation results of the phase A of the rotor currents (50% phase-neutral voltage sag, $\theta_0 = 90^0$ and 1950 RPM): (a) - Without RTFC strategies; (b) - With the DPIC- <i>Target I</i> strategy. . . . .	154
6.12	Simulation results of the phase A of the rotor voltages (50% phase-neutral voltage sag, $\theta_0 = 90^0$ and 1950 RPM): (a) - Without RTFC strategies; (b) - With the DPIC- <i>Target I</i> strategy. . . . .	155
6.13	Simulation results of the ABC stator currents (50% phase-neutral voltage sag, $\theta_0 = 90^0$ and 1950 RPM): (a) - Without RTFC strategies; (b) - With the DPIC- <i>Target II</i> strategy. . . . .	156
6.14	Simulation results of the stator active and reactive powers (50% phase-neutral voltage sag, $\theta_0 = 90^0$ and 1950 RPM): (a) - Without RTFC strategies; (b) - With the DPIC- <i>Target III</i> strategy. . . . .	156
6.15	Simulation results of the electromagnetic torque (50% phase-neutral voltage sag, $\theta_0 = 90^0$ and 1950 RPM): (a) - Without RTFC strategies; (b) - With the DPIC- <i>Target IV</i> strategy. . . . .	157
6.16	Simulation results of the total active and reactive powers (50% phase-neutral voltage sag, $\theta_0 = 90^0$ and 1950 RPM): (a) - With the DPIC- <i>Target IV</i> strategy; (b) - With the DPIC- <i>Target IV</i> + GSC control strategy. . . . .	157
6.17	Simulation results with DPIC- <i>Target IV</i> (50% phase-neutral voltage sag, $\theta_0 = 0^0$ and 1950 RPM): (a) - Positive sequence rotor current; (b) - Negative sequence rotor current; (c) - Phase A of the rotor currents; (d) - Phase A of the rotor voltages; (e) - Total active and reactive powers; (f) - Electromagnetic Torque. . . . .	159
6.18	Maximum calculated rotor voltage with DPIC- <i>Target IV</i> strategy for different unbalanced voltage sags, using the 2MW WECS parameters ( $\theta_0 = 90^0$ ). . . . .	161
6.19	Scheme of the rotor current limitation. . . . .	163



6.20	Experimental result of the total dq rotor currents - TUDb (90% phase-to-phase voltage sag, $\theta_0 = 90^0$ and 1750RPM): (a) - Without the RTFC strategies; (b) - With DPIC- <i>Target I</i> strategy. . . . .	164
6.21	Experimental result of the phase A of the rotor voltages - TUDb (90% phase-to-phase voltage sag, $\theta_0 = 90^0$ and 1750RPM): (a) - Without the RTFC strategies; (b) - With DPIC- <i>Target I</i> strategy. . . . .	165
6.22	Experimental result of the ABC stator currents - TUDb (90% phase-to-phase voltage sag, $\theta_0 = 90^0$ and 1750RPM): (a) - Without the RTFC strategies; (b) - With DPIC- <i>Target II</i> strategy. . . . .	165
6.23	Experimental result of the estimated electromagnetic torque - TUDb (90% phase-to-phase voltage sag, $\theta_0 = 90^0$ and 1750RPM): (a) - Without the RTFC strategies; (b) - With DPIC- <i>Target IV</i> strategy. . . . .	166
6.24	Experimental result of the total active and reactive powers - TUDb (90% phase-to-phase voltage sag, $\theta_0 = 90^0$ and 1750 RPM): (a) - Without the RTFC strategies; (b) - With DPIC- <i>Target IV</i> + GSC control strategy. . . . .	166
6.25	Experimental result of the total dq rotor currents - TUDb (90% phase-to-phase voltage sag, $\theta_0 = 0^0$ and 1750 RPM): (a) - Without the RTFC strategies; (b) - With DPIC- <i>Target I</i> strategy. . . . .	167
6.26	Control of the RSC using the resonant control. . . . .	169
6.27	Control of the GSC using the resonant control . . . . .	170
6.28	Bode diagram of the PI+resonant controller (Equation 6.46) for different gains using the 2MW system parameters. . . . .	174

- 6.29 Simulation results using PIRC-*Target I* strategy (50% phase-neutral voltage sag,  $\theta_0 = 90^0$  and 1950 RPM): (a) - Positive sequence rotor current; (b) - Negative sequence rotor current; (c) - Phase A of the rotor currents; (d) - Phase A of the rotor voltages. . . . . 175
- 6.30 Simulation results using PIRC-*Target IV* + GSC control strategy (50% phase-neutral voltage sag,  $\theta_0 = 90^0$  and 1950 RPM): (a) - Total dq rotor currents; (b) - Electromagnetic Torque; (c) - Total dq GSC currents; (d) - Total active and reactive powers; 176
- 6.31 Simulation results using PIRC-*Target IV* strategy (50% phase-neutral voltage sag,  $\theta_0 = 0^0$  and 1950 RPM): (a) - Positive sequence rotor current; (b) - Negative sequence rotor current; (c) - Total dq rotor currents; (d) - Electromagnetic Torque. . . 177
- 6.32 Simulation results using EPIRC-*Target IV* strategy (50% phase-neutral voltage sag,  $\theta_0 = 0^0$  and 1950 RPM): (a) - Positive sequence rotor current; (b) - Negative sequence rotor current; (c) - Phase A of the rotor currents; (d) - Electromagnetic torque. 180
- 6.33 Experimental results using EPIRC-*Target I* strategy for a 50% phase-to-phase voltage sag,  $\theta_0 = 0^0$  and 2340RPM - UFMGb: (a) - Total dq rotor currents; (b) - ABC rotor currents; (c) - Electromagnetic Torque; (d) - Phase A of the rotor voltages. Straight line - voltage limits. . . . . 181
- 6.34 Experimental results for different voltage phase-to-phase voltage sags with maximum natural component ( $\theta_0 = 0^0$ ) and varying the speed - UFMGb: (a) - Maximum rotor voltages; (b) - Maximum rotor currents. . . . . 182
- 6.35 Resonant control + Magnetizing current control (RMCC). . . 184
- 6.36 Simulation results using EPIRC and the RMCC - *Target IV* strategy (50% phase-neutral voltage sag,  $\theta_0 = 0^0$  and 1950 RPM): (a) - dq rotor currents; (b) - Phase A of the rotor currents; (c) - Phase A of the rotor voltages; (d) - Electromagnetic Torque. . . . . 185

6.37	Experimental results using RMCC - <i>Target I</i> strategy for a 50% phase-to-phase voltage sag, $\theta_0 = 0^0$ and 2070RPM - UFMGb: (a) - dq rotor currents; (b) - ABC rotor currents; (c) - Phase A of the rotor voltages; (d) - Electromagnetic torque.	186
A.1	Graphical representation of Clark and Park Transforms. . . . .	206
A.2	Block diagram of the GSC current control. . . . .	210
A.3	Schematic diagram of the DC-link. . . . .	212
A.4	Block diagram representing the DC-link voltage control loop. .	213
A.5	Block diagram representation of the GSC reactive power control.	214
A.6	Vector diagram of the grid voltage and stator flux: (a) - Virtual flux orientation; (b) - Stator flux orientation. . . . .	215
A.7	Stator or grid voltage orientation. . . . .	216
A.8	Block diagram representation of the rotor currents control structure. . . . .	218
A.9	Block diagram representation of the stator active power control structure. . . . .	220
A.10	Block diagram representation of the stator reactive power control structure. . . . .	220



---

---

# Symbol List

---

## Superscript

- \* Reference values
- $r$  Variable referred to the rotor
- $g$  Variable in the synchronous reference frame
- $\rightarrow$  Vector
- + Positive Synchronous Reference Frame
- Negative Synchronous Reference Frame
- $\hat{\phantom{x}}$  Complex Conjugate

## Subscript

- $d$  Variable referred to the direct axis
- $q$  Variable referred to the quadrature axis
- $f$  Forced Component
- $n$  Natural Component
- + Positive Sequence Component
- Negative Sequence Component
- 0 Zero Sequence Component

## Variables

$\lambda_{otm}$	Optimum Speed Relation
$\psi_s$	Stator Flux Linkage
$\psi_{sv}$	Grid Virtual Flux
$\psi_r$	Rotor Flux Linkage
$\eta_g$	Generator Efficiency
$\theta$	Rotor Electrical Position
$\hat{\theta}_N$	Grid Voltage Angle
$\theta_r$	Rotor Voltages and Currents Angle
$\theta_0$	Stator Voltage Angle in the Sag Beginning
$\tau_a$	Converter Time Constant
$\tau_s$	Stator Time Constant
$\omega$	Electrical Rotor Speed (rad/s)
$\omega_m$	Mechanical Rotor Speed (rad/s)
$\omega_N$	Grid Voltage Angular Frequency (rad/s)
$\omega_s$	Stator Voltages and Currents Angular Frequency (rad/s)
$\omega_r$	Stator Voltages and Currents Angular Frequency (rad/s)
$A$	Generic Variable
$C_{p_{max}}$	Maximum Turbine Power Coefficient
$C_f$	Filter Capacitance
$f$	Electrical Rotor Speed (Hz)
$f_m$	Mechanical Rotor Speed (Hz)
$f_N$	Grid Voltage Frequency (Hz)
$f_s$	Stator Voltages and Currents Frequency (Hz)
$f_r$	Stator Voltages and Currents Frequency (Hz)
$i_n$	Filter Current
$i_s$	Stator Current
$i_r$	Rotor Current
$J$	Inertia
$K_i$	Integral Gain
$K_p$	Proportional Gain
$K_r$	Resonant Gain
$K_{p_{im}}$	Proportional Gain of the Magnetizing Current Controller
$K_{sr}$	Stator and Rotor Turns Ratio
$L_1$	Inductance of the Parallel Inductor in the VSG
$L_2$	Inductance of the Series Inductor in the VSG
$L_f$	Filter Inductance
$L_m$	Magnetizing Inductance
$L_s$	Stator Self Inductance
$L_r$	Rotor Self Inductance
$L_{\sigma s}$	Stator Leakage Inductance
$L_{\sigma r}$	Rotor Leakage Inductance

$P$	Pole Pairs
$P_e$	Electromagnetic Power
$P_s$	Stator Active Power
$Q$	Band-pass Filter Selectivity
$Q_n$	GSC Reactive Power
$Q_s$	Stator Reactive Power
$R_1$	Equivalent Resistance in the VSG
$R_f$	Filter Resistance
$R_s$	Stator Resistance
$R_r$	Rotor Resistance
$s_{lip}$	Slip
$S_s$	Stator Apparent Power
$T_d$	Converter Dead Time
$T_e$	Electromagnetic Torque
$T_{f_{Q_n}}$	Time Constant of the GSC Reactive Power Filter
$T_{f_{P_s}}$	Time Constant of the Stator Active Power Filter
$T_{f_{Q_s}}$	Time Constant of the Stator Reactive Power Filter
$T_i$	Integrative Control Time Constant
$T_{mec}$	Mechanical Torque
$T_{mec}$	Electromagnetic Torque
$T_s$	Sampling Time
$v_n$	Grid Side Converter Voltage
$v_N$	Grid Voltage
$v_s$	Stator Voltage
$v_r$	Rotor Voltage
$V_1$	Stator Voltage Before the Sag
$V_2$	Stator Voltage During the Sag
$V_{dc}$	DC-Link Voltage





---

---

# Abbreviation List

---

CNF	Compensation of the Natural Stator Flux Linkage
CNV	Compensation of the Natural Rotor Voltage
CTRP	Compensation of Torque and Reactive Power Pulsations
DFIG	Doubly-Fed Induction Generator
DPIC	Dual PI Controllers
EMF	Back Electromotive Force
GSC	Grid Side Converter
IGBT	Insulated Gate Bipolar Transistor
INV	Inverter
IPC	Industrial Power Corruptor
ISG	Impedance Sag Generator
LCCE	Laboratory of Energy Conversion and Control “Laboratório de Controle e Conversão de Energia”

MCC	Magnetizing Current Control
MO	Modulus Optimum
MPPT	Maximum Power Point Tracking
MVS	Momentary Voltage Sag
ONS	National Electric System Operator “Operador Nacional do Sistema Elétrico”
PI	Proportional-Integral Controller
PIRC	Proportional-Integral Plus Resonant Controller
PLL	Phase-Locked Loop
PSOGI	PLL with Dual Second Order Generalized Integrators
PWM	Pulse Width Modulation
RMCC Rotor Side Converter	Resonant Control + Magnetizing Current Control RSC
RTFC	Ride-through Fault Capability
SO	Symmetrical Optimum
SVPWM	Space Vector Pulse Width Modulation
TUD	“Technische Universität Dresden”
TUDb	TUD test bench
UFMG	Federal University of Minas Gerais
UFMGb	UFMG test bench
VSG	Voltage Sag Generator
WECS	Wind Energy Conversion System

# Introduction

---

## 1.1 Brief History of Wind Energy

Mankind has used the wind energy for thousands of years. Archaeological studies point out that the wind energy is employed since the beginning of the Modern Era (Heier, 2005). In the 10th century, windmills were used in Persia which were brought by the Crusaders to Europe where the technology was changed and widespread. These windmills have been used to grind grains and to pump water.

In the United States, in the 19th century, windpumps were extensively used on farms and ranches and they are still used nowadays. These mills feature a large number of blades so that they turn slowly with considerable torque in low winds and are self regulating in high winds (Clements, 2003).

The first wind turbines with aerodynamic blades constructed to produce electrical energy were introduced in the mid-twentieth century. Just in the 1950s, a German developed the first high power turbine (Heier, 2005). The grid connected wind power plants is only 25 to 30 years old (Rasmussen and Jørgensen, 2005).

In the beginning the turbines were small and with low power capability, connected just to AC distribution networks and rarely to transmission systems. Firstly, the wind generators were fixed speed and capacitors were employed to correct the power factor. When submitted to grid faults the turbines were disconnected from the grid, operating with narrow voltage and frequency limits. In the last years, new technologies of wind energy con-

version systems (WECS) have evolved, mainly because the development of power electronics. Nowadays there exist multi-megawatts turbines with high efficiency, operating with variable speed, thus, allowing maximum wind power extraction. They are connected to the grid using power converters that are also used to supply the reactive power needed by the grid. As it will be seen hereafter, the increase of the wind power plants connected to the grid leads the system operators to develop specific grid code requirements for this technology.

## 1.2 Overview of Wind Energy Nowadays

In recent years, the entire society has become increasingly concerned over the global warming and other environmental issues caused by the use of polluting energy sources like petroleum, coal, gas, etc. Thereby, the governments and companies have invested in alternative energy sources like solar, wind, biomass, etc.

The environmental impact of using WECS compared with the traditional energy sources is relatively small. During the operation, wind turbines cause virtually no emissions and very little during their manufacture, installation and removal (European Wind Energy Association - EWEA, 2009). The environmental benefits associated with the generation of electricity from renewable energy, including wind power, can be quantified in economic terms in the so-called “external costs” that include effects on human health, damage to the environment, loss of amenity as well as economic effects such as payment of subsidies and employment benefits. The most detailed analysis of external costs has been carried out through the European Commission’s ExternE project that values the external costs of wind energy at less than 0.26 euro-cents/kWh whilst those for coal-fired generation range from 2 to 15 euro-cents/kWh (European Wind Energy Association - EWEA, 2009).

Besides the environmental advantages, the electricity generation using wind energy is relatively cheaper than other renewable sources, even competing with the price of traditional power plants. For example, the auction A-3 of electric energy promoted by the Brazilian government, occurred in August 2011, the wind energy reached the minimum price of R\$96.39/MWh,

with an average value of R\$99.58/MWh, value below the average price of thermal power plants using gas (R\$103.26/MWh), and the expansion of the Jirau hydroelectric power plant (R\$102.00/MWh) (Instituto Acende Brasil, 2011). In the auction A-5, occurred in December 2012, the average price of small hydroelectric power plant was R\$93.46/MWh, while for wind energy this price was R\$87.94/MWh (Instituto Acende Brasil, 2012), confirming the continuous price decreasing.

Being a renewable, not-pollutant and cost-effective energy source, the number of wind power plants worldwide has increased so fast, as it can be seen in Figure 1.1. Brazil is one of the countries with the highest growth rates of installed wind power capacity. The country has now almost 1.96 GW of wind farms in operation (ANEEL, 2012). This number is so small when compared with other countries, but the investments are growing and so is the number of power plants.

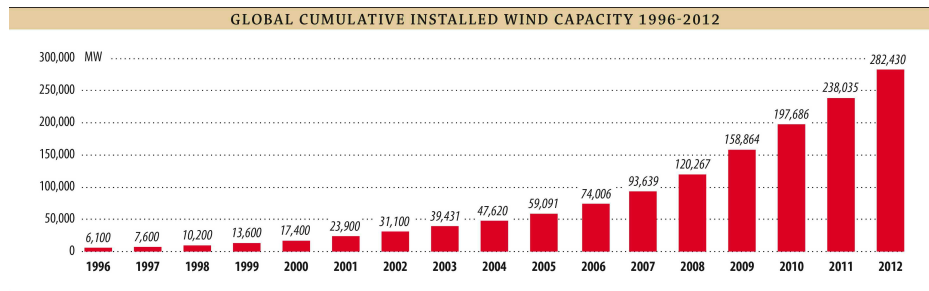


Figure 1.1: Total world installed capacity of WECS (Global Wind Energy Council, 2013).

## 1.3 Technologies of Wind Energy Conversion Systems

There exist different WECS technologies that differ in the generator technology, the mechanical connection with the turbine and the electric connection to the grid. Next, the most common topologies, depicted in Figure 1.2, are listed and shortly explained:

- Topology with generator direct connected to the grid (Blaabjerg et al.,

2006). Generally it is used a squirrel cage induction generator connected to the wind turbine using a gearbox. It is basically a fixed speed technology, because of the absence of converters, thus the efficiency of wind power extraction is low. For reactive power compensation, capacitors are used. It is also common the use of a induction machine with two speeds (different number of poles), permitting a discrete change in the speed;

- Topology with generator connected to the grid using full-scale converter (Jamil et al., 2012). The converter permits the control of active and reactive power, allowing variable speed operation and, thus, the ability of maximum wind energy extraction. Normally synchronous machines with or without a gearbox are used. In the case without gearbox, called gearless technology, the synchronous generator can be externally excited or permanent magnets can be employed;
- Topology with doubly-fed (wound rotor) induction generator (Pena et al., 1996). This is also a variable speed technology, but the converter is dimensioned just for a parcel of the rated power. As this system is the object of the present work, it is better described in this section and in the next chapter.

WECS using doubly-fed induction generators (DFIG) are one of the most commercialized topologies over the world. This technology consists of a wound rotor induction generator with the stator connected to the grid and the rotor supplied by a back-to-back converter, as depicted in Figure 1.2(d). Its main advantage is the use of converters dimensioned for a parcel of the generator rated power (normally 30%), so the equipment costs are reduced. This is a variable speed technology where the generator speed is controlled normally in the range of  $\pm 30\%$ , permitting the extraction of maximum wind power.

Figure 1.3 shows the DFIG power flow when it is operating as a generator. One can notice that, during sub-synchronous operation, the converter supplies active power to the rotor, whereas in the super-synchronous region the rotor power flow is reversed. In both conditions the stator supplies power to the grid, therefore the total generated power is the stator power minus (sub-synchronous) or plus (super-synchronous) the rotor power.

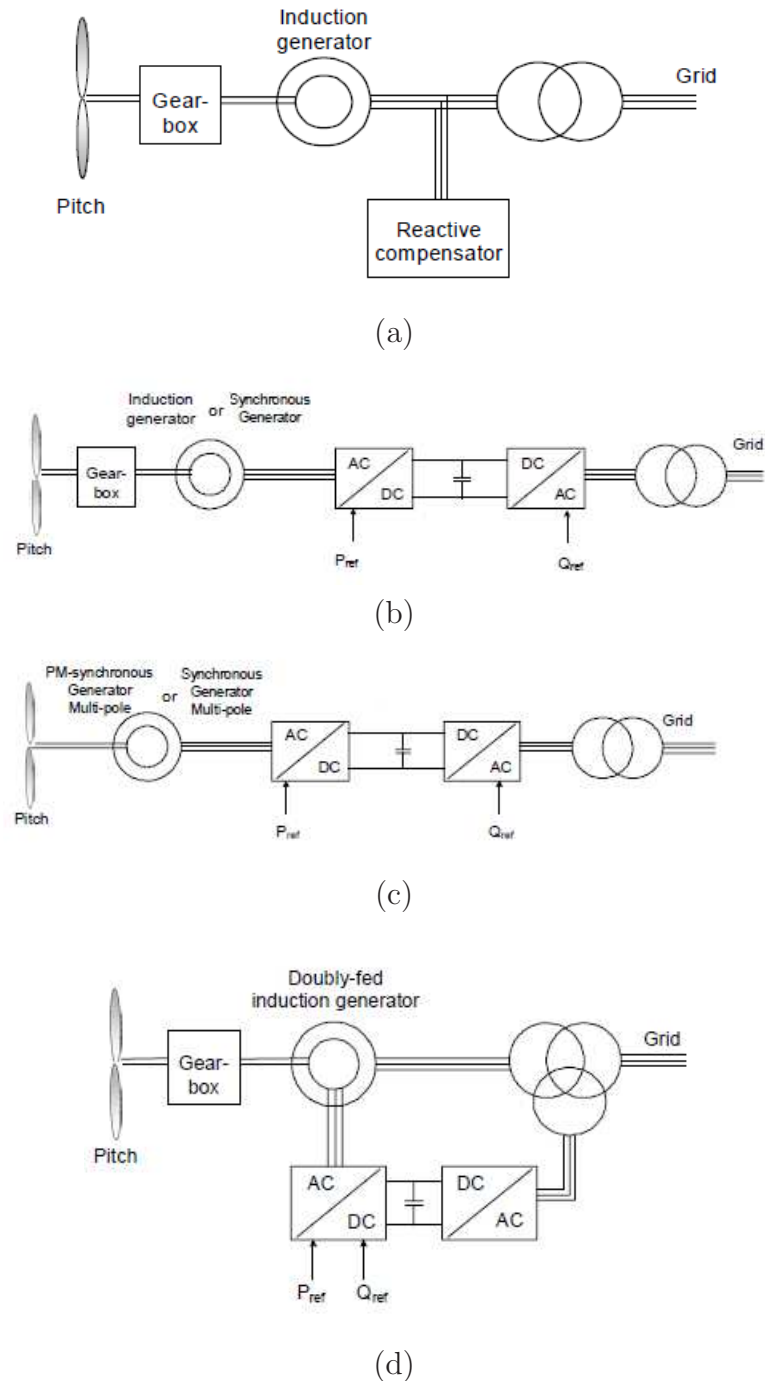


Figure 1.2: Technologies of wind energy conversion systems (Blaabjerg et al., 2006).

- (a) - Generator with direct connection to the grid;
- (b) - Generator with gearbox and full scale converter;
- (c) - Gearless generator with full-scale converter;
- (d) - Doubly-fed generator with partial converter power.

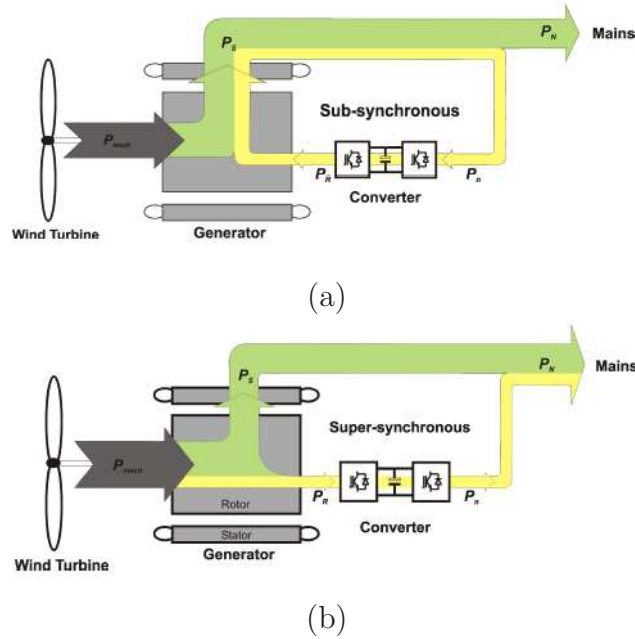


Figure 1.3: Active power flow in the DFIG technology as generator (Rabelo, 2009).

- (a) - Sub-synchronous speed operation;  
 (b) - Super-synchronous speed operation.

Nevertheless the advantages of the DFIG, due to the direct connection of the generator stator to the grid, it is more susceptible to grid disturbances than technologies which use full-scale converters. During voltage sags, over-voltages and over-currents are induced in the rotor circuit which may damage the converter (Mendes, 2009), (López et al., 2008a), (López et al., 2008b), (de Araújo Lima, 2009), (Oliveira, 2009).

In the next chapter more details about the DFIG operation are presented and the classical control strategy is briefly described.

## 1.4 Voltage Sags

WECS may produce grid disturbances, i.e, it may influence the grid power quality causing for example voltage variations, harmonics, etc., and also it may be influenced by the grid disturbances. The present work carries out an analysis of the dynamic behavior of the DFIG technology during



voltage sags and develops strategies to improve the system response during this kind of disturbance.

According to the Brazilian national grid code (PROREDE) a momentary voltage sag (MVS), phenomena analyzed in this work, is defined as an event in which the RMS voltage value is between 0.1 and 0.9pu and the duration is greater than 1 cycle ( $60 \text{ Hz} = 16.67\text{ms}$ ) and minor than 3 seconds (ONS, 2009b). Events with voltage below 0.1pu are characterized as voltage interruptions, whereas events with duration between 3 seconds and 1 minute are called temporary voltage sags. These events together with different types of voltage elevation are classified as the short duration voltage variation phenomena.

The MVS may be caused by grid faults (short-circuits), overload or direct starting of high power machines (Bollen, 2000). They are classified as phase-phase, phase-to-ground, phase-phase-to-ground or three-phase depending on the number of phases affected. The latter is a balanced or symmetrical voltage sag, whereas the others are unbalanced or asymmetrical voltage sags. The faults may occur hundreds of kilometers from the connection point of the wind farm, therefore the MVS is a common phenomena that the system has to deal with. Depending on the fault characteristics and the point of occurrence, the voltage can drop abruptly and present slower recovering. In a faulty condition, it is also possible the occurrence of phase angle jumps in the instantaneous voltage.

The international standard IEC 61400-21 (IEC, 2008) specifies measurement and assessment of power quality characteristics of grid connected wind turbines, including questions related to the WECS behavior during voltage sags. The standard recommends the MVS tests characteristics and also presents the requirements of the voltage sag generator used to test the equipment.

In this work the DFIG behavior during balanced and unbalanced voltage sags is addressed separately in Chapters 3 and 4, respectively. Details about the equipment used to produce the voltage sag and its characteristics are described in the next chapter.

## 1.5 Motivation and Objectives

With the higher penetration of wind power plants in the interconnected electrical system, power system operators have developed grid codes with specific requirements for regulating the connection of wind power plants to the electrical network (Erlich and Bachmann, 2005). One of these is the system ride-through fault capability (RTFC), i.e., the ability of the power plant to remain connected to the grid during voltage sags.

Figure 1.4 shows the RTFC curve required by the Brazilian grid code (ONS, 2009a) for balanced and unbalanced voltage sags. The vertical axis is the per unit remaining voltage in the common point of connection of the wind farm and the horizontal axis is the sag duration. The hatched area denotes the sag amplitude and duration characteristics for which the WECS must not be disconnected from the grid.

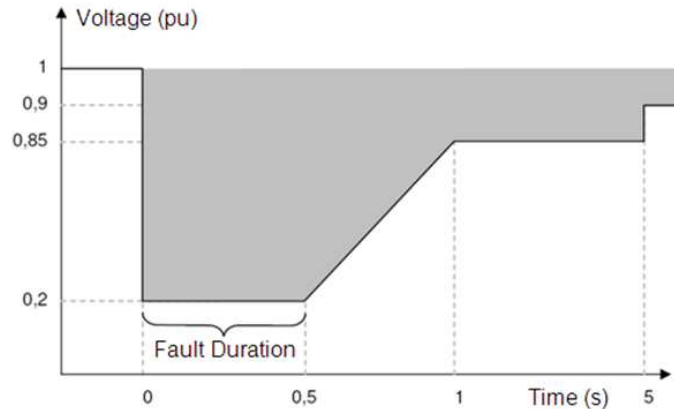


Figure 1.4: Ride-through fault capability curve required in the Brazilian grid code (ONS, 2009a).

Figure 1.5 illustrates the RTFC curve present in the German grid code (E.ON, 2006). Above the limit line 1 the system must not be disconnected and above the limit line 2 special conditions are applied, requiring a fast reconnection when the disconnection is permitted and reactive power infeed during the MVS. The capability to supply reactive power to the grid during the voltage dip is also a requirement in the modern grid codes in order to guarantee voltage support. Figure 1.6 shows the principle of voltage support required in the German grid code (E.ON, 2006).

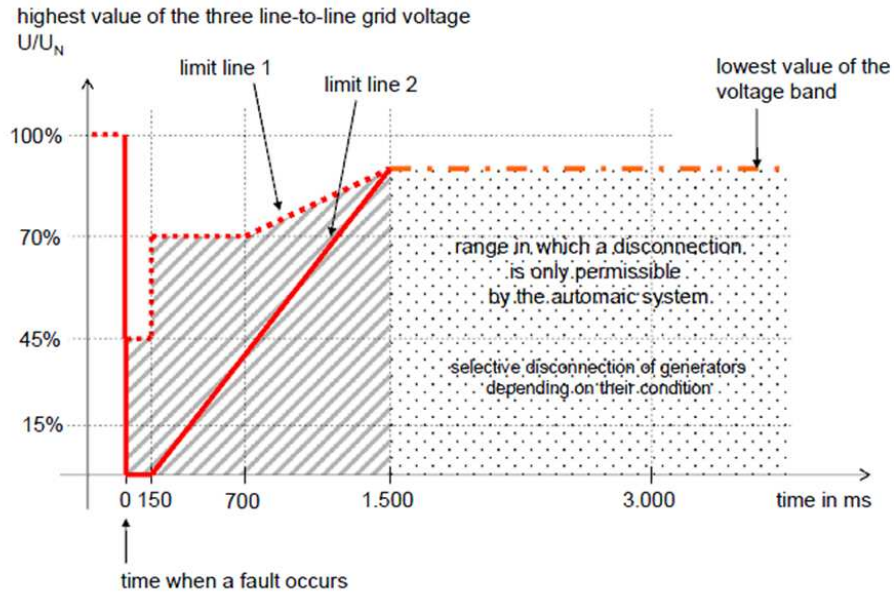


Figure 1.5: Ride-through fault capability curve required by EON-Germany grid code (E.ON, 2006).

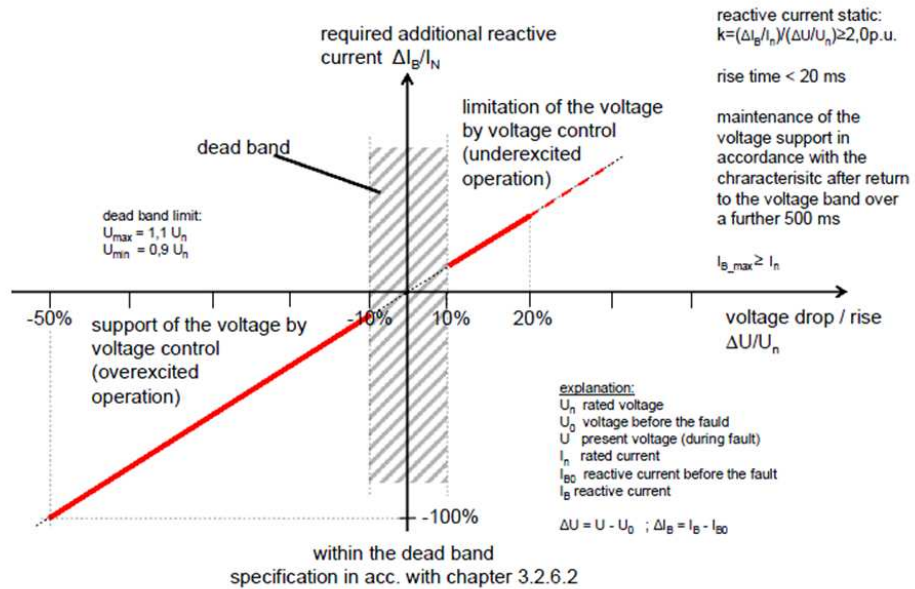


Figure 1.6: The principle of voltage support in the event of grid fault required by EON-Germany grid code (E.ON, 2006).

In this context, the present work intends to scrutinize the DFIG behavior during symmetrical and asymmetrical voltage sags using a mathematical modeling, simulation and experimental results. Analyzing these results, new control strategies to improve the system ride-through fault capability are developed. Also, some strategies present in literature are tested in order to evaluate and compare the results with the ones proposed in this work. The main objective here is not to develop a final and definitive solution, but a strategy that can be used in some situations or in conjunction with other ones.

## 1.6 Methodology

The first objective of this work is to analyze the DFIG behavior during the balanced and unbalanced voltage sags. This analysis is carried out using three methodologies:

- Mathematical modeling in the time and Laplace domains of the generator dynamic behavior during voltage sags;
- Simulation results using a computational model that represents the relevant system dynamics of a 2 MW WECS;
- Experimental results obtained in two test benches: a 4kW and a 25kW rated power.

The mathematical modeling gives the understanding of the system variables behavior and comprehension of the influence of the system parameters. The experimental results are used to observe and prove the behavior of the measured variables (voltages, currents, speed, ...). As the test benches are small-scale models of a real WECS, in order to extrapolate the results, a 2MW simulation is used.

Normally test beds with rated power below 10kW are used to test the system characteristics and new control strategies. In this work, besides a 4kW system, a 25kW test bench is fully developed and the results are compared with the simulations.

Through these results, new control strategies are proposed and their behavior are analyzed using the simulation and experimental results. The mathematical analysis of these strategies is also carried out, focusing mainly on the influence in the voltage and current behavior.

## 1.7 State of Art

With the increasing number of wind power plants worldwide, several works have been published contemplating the different aspects of WECS, like mechanical studies of the blades, electrical characteristics of the different types of generators, power electronic converters used to connect the system to the grid, etc.

The DFIG technology is one of the most studied topologies due to its high market penetration and also due to its susceptibility to grid disturbances. Wound rotor induction machines have been used for many decades. In the beginning they were used as motor with the connection of variable resistances in the rotor circuit to increase the starting torque or to vary the machine speed. Only with the development of power electronics that in the end of 1980's the wound rotor machine started to be studied and used as generator in wind conversion systems.

Tang and Xu (1992) present a system using the DFIG technology with the control implemented using the stator flux orientation. This pioneer paper shows, through simulation results, that it is possible to operate with the optimum torque and speed, extracting the maximum wind power. In Pena et al. (1996) the use of PWM converters in the rotor circuit is presented and the vector control strategy is described. The independent control of active and reactive power is demonstrated using experimental results obtained in a DFIG small-scale test bench. This paper is one of the most cited papers in this topic and it is the basis of the DFIG technology.

In the last few years, several papers have been published focusing the DFIG behavior during voltage sags. Erlich et al. (2007) presents simulation results, illustrating the DFIG behavior during balanced voltage sags, whereas Seman et al. (2006) presents experimental results in a high power test bench for the unbalanced case. Zhang et al. (2009) presents a calculation of the

short-circuit current and simulation results are shown. These and several other papers address the DFIG behavior in the time domain, but they lack of a deeper analysis that explain the variables behavior.

López et al. (2007) and López et al. (2008a) present a useful mathematical modeling, scrutinizing the behavior of the flux linkages and voltages in the generator during balanced and unbalanced voltages sags, respectively. The mathematical development is validated using experimental results. The authors simplify the analysis using the machine with open rotor circuit which is a useful tool that permits correlating the different variables behavior with the system parameters and sag severity. These papers are cited in several works, but despite the useful analysis, the current control influence in the DFIG dynamic behavior has not been analyzed.

With the development of specific grid codes to the connection of WECS in the grid including the ride-through fault capability requirements, several recent publications about the DFIG technology have focused in the development of new strategies to improve the system RTFC. The most popular solution for this problem is the crowbar device, wich is discussed in several papers. The crowbar is a switched resistance that is inserted in parallel with the rotor circuit during the sag in order to avoid that the high rotor currents damage the converter.

In their works, Lohde et al. (2007), Anaya-Lara et al. (2008) and Zhang et al. (2010) basically deal with the crowbar resistance sizing. Morren and de Haan (2005), Ling et al. (2009) and Erlich et al. (2007) show simulation results, presenting different strategies to activate and deactivate the crowbar device.

When the crowbar device is activated, the generator acts like a squirrel cage machine consuming reactive power from the grid, which is undesirable. This device is useful for the protection of the converter, but to use it for RTFC solution, modifications are necessary.

Meegahapola et al. (2010) uses the grid side converter (GSC) to supply reactive power to the grid, compensating the consumed reactive power and acting as a STATCOM. Similarly, in Kasem et al. (2008), the rotor side converter (RSC) is disconnected from the machine and used in parallel with the GSC, both injecting reactive power into the grid.

In order to avoid the disconnection of the RSC during the dip, Yang et al. (2009) proposes the use of series resistances, instead of using the crowbar in parallel with the rotor. In this paper, a method for calculating the currents during the sag is developed and simulation results are used to validate the modeling and the proposed strategy. Rahimi and Parniani (2010) uses the resistances in series with the stator instead of the rotor.

The solutions using the crowbar or series resistances require the addition of extra hardware, increasing system complexity and costs. Therefore, software modifications in the control strategy are preferred, enhancing the system behavior during the dips. The crowbar may be used just as a protection device to avoid high currents in the converters.

In Xiang et al. (2006) the stator flux linkage is used to calculate the rotor current reference during the sags and an analysis of the feasible conditions when the strategy can ride-through the sag is shown. Using experimental and simulation results the strategy feasibility is demonstrated for balanced and unbalanced voltage sags.

The stator flux linkage is also used to generate the rotor current references during balanced voltage sags in López et al. (2008b). Through simulation results it is demonstrated that the strategy increase the flux damping, but the rotor currents, the most important variable, are not analyzed in this work. Probably, to damp the flux as shown, extremely high rotor currents are necessary.

The reduction of the rotor currents during the sag is performed in Liang et al. (2010) using feed-forward compensators to deal with the rotor voltages and currents transients caused by the voltage sag, but it is shown that the stator flux damping is reduced.

Ling et al. (2009) compares two strategies to control the rotor current using the reference values calculated through the stator flux linkage. Simulations results are shown, but the analysis of the rotor current is missing.

In Xiang et al. (2006), López et al. (2008b), Liang et al. (2010) and Ling et al. (2009), the flux estimation is necessary which is a great disadvantage, because it depends on the machine parameters. The feed-forward compensator proposed by Lima et al. (2010) is simpler, since only the stator currents are used as the new control references. The experimental results for balanced



voltage sags shows that the strategy reduces the rotor overcurrents, but the stator flux linkage oscillations are not analyzed. The authors also develop a modeling in the Laplace domain to describe the behavior of the voltage and currents during the voltage sags.

The control strategies proposed in the discussed papers show results for symmetrical voltage sags, but the majority of the dips in the power system are unbalanced. The DFIG ride-through during unbalanced conditions is a little more complicated, because, as it will be demonstrated in this work, negative sequence current arise.

In Brekken and Mohan (2004) and Brekken and Mohan (2007) a feed-forward compensation is employed in the classic current control in order to decrease the torque and power oscillations caused by the negative sequence current during unbalanced voltage sags. Simulation and experimental results are presented to validate the proposed strategy and a mathematical model is used to tune the filters used for the compensation.

Several works in the literature present the use of a dual-PI structure to control separately the current positive and negative sequence components. Xu and Wang (2007), Park et al. (2007), Kearney and Conlon (2008) and Hu et al. (2009b) show the mathematical modeling of the machine under grid voltage unbalance and demonstrate the use of the dual-PI structure to control the RSC currents. Navarro and Richter (2007), Abo-Khalil et al. (2007), Zhou et al. (2007), Qiao and Harley (2008), Xu (2008), Wang et al. (2008), Zhou et al. (2009), Fan et al. (2009) and Wang and Xu (2010) extend the analysis and the use of this control structure also for the GSC. It is presented the coordinate control of the RSC and GSC in order to reduce the grid power oscillation.

The works cited in the last paragraph deal just with the DFIG control when there is a small grid voltage unbalance. The transient caused during voltage sags is not analyzed. Gomis-Bellmunt et al. (2008) analyzes the same control structure showing results also for asymmetrical voltage sags. Wang et al. (2009) proposes the use of the dual-PI control with the addition of a compensation term to deal with the voltage transient.

Based on the same principle of controlling the negative sequence, Hu et al. (2009a), Hu and He (2009a) and Hu and He (2011) propose the use of



a PI-resonant control structure. Resonant controllers are also employed in Hu and He (2009b) and Luna et al. (2009) in a stationary reference frame. All these papers show the reduction in the electromagnetic torque pulsation due to the negative sequence, but the transient caused by the voltage sag is not analyzed since just long term voltage unbalances in the network are addressed.

The works presented in this section are deeper analyzed in the following chapters. Some of the control strategies proposed in the literature are implemented and analyzed for the sake of comparison.

To finish the presentation of the state of art, it is important to mention the large experience of the “Laboratório de Controle e Conversão de Energia” (LCCE) studying wind energy conversion systems. In the last three years four Master dissertation and one PhD thesis were developed about different aspects of the doubly-fed technology: Ramos (2009), Mendes (2009), da Silva (2009), Liu (2011) and Oliveira (2009). Other technologies are also studied as synchronous machines with permanent magnets. The research group experience contributed for the development of the present work.

## 1.8 Contributions

The core of this work is the analysis of the DFIG behavior during voltage sags and the development of new ride-through control strategies, but it intends to go one step further to the works presented in the previous section. The following new contributions can be listed:

- The development of a mathematical modeling in the Laplace domain which permits the inclusion of the control effect in the machine dynamic behavior during voltage sags;
- Extension of the proposed Laplace domain mathematical modeling with separation in positive and negative sequence components;
- The effect of the voltage sag transient during symmetrical and asymmetrical voltage sags is deep analyzed;

- Development of new control strategies to improve the DFIG ride-through fault capability during balanced and unbalanced voltage sags, including the analysis of the voltage sag transient.

All the analysis carried out is validated using mathematical demonstration, simulation results in a Simulink model and experimental results.

Besides the contributions cited, the author gives the contribution of design and assembly of the 25kW test bench which could be used in several other works to be developed in the LCCE. A system like that, with all its functionality and such rated power, probably is unique in Brazil, contributing with the national science development.

The results produced in this work originated five conference papers and one paper in a journal. They are cited below per chronological order:

- V. F. Mendes, B. Rabelo, C. V. Sousa, F. F. Matos, W. Hofmann and S. R. Silva (2010). Comportamento de Aerogeradores de Dupla Excitação Frente a Afundamentos de Tensão. *III Simpósio Brasileiro de Sistemas Elétricos - SBSE*, pages 1-6.
- V. F. Mendes, C. V. Sousa, S. R. Silva, B. Rabelo, S. Krauss and W. Hofmann (2010). Behavior of Doubly-Fed Induction Generator During Symmetrical Voltage Dips Experimental Results. *IEEE International Symposium on Industrial Electronics - ISIE*, pages 2345-2350.
- V. F. Mendes, W. Hofmann, S. R. Silva (2010). Control of Doubly-Fed Induction Generator during Symmetrical Voltage Sags. *IEEE Power & Energy Student Summit - PESS*, pages 26-29.
- V. F. Mendes, C. V. Sousa, S. R. Silva, B. Rabelo, S. Krauss and W. Hofmann (2011). Modeling and Ride-Through Control of Doubly Fed Induction Generators During Symmetrical Voltage Sags. *IEEE Transactions on Energy Conversion*, v.26, issue4, pages 1161 - 1171.
- V. F. Mendes, S. Y. Liu, S. R. Silva (2012). Controle de Aerogeradores Duplamente Excitados Durante Afundamentos Momentâneos de Tensão Desequilibrados. *IV Simpósio Brasileiro de Sistemas Elétricos*, v. 1, p. 1-7.

- V. F. Mendes, C. V. Sousa, G. M. Rezende, S. Y. Liu, S. R. Silva (2012). Estratégias de Controle Aplicadas a Aerogeradores Duplamente Excitados Durante Afundamentos de Tensão Desequilibrados. *XIX Congresso Brasileiro de Automática*, v. 1, p. 3118-3125.

The journal of the publication is classified as Qualis A by CAPES and this paper has been cited 9 times according to Scopus and 5 times according IEEE. The paper presented in the PESS (IEEE Power & Energy Student Summit) received the 2nd Best Paper Award Prize. This publications and this prize contribute to the divulgation of the work results and the evaluation by the scientific community.

The author has also contributed in areas related to this work, publishing seven papers as co-author in national and international conferences during the doctorate.

It is important to mention that this work was developed in cooperation between the Federal University of Minas Gerais (UFMG) and Dresden Technological University (TUD - “Technische Universität Dresden”) in Germany. Part of the studies presented in this document was developed during the sandwich doctorate realized during 2010 under supervision of Prof. Dr. Ing-Wilfried Hofmann.

## 1.9 Text Organization

In this first chapter an overview of the use of wind energy is presented and the technology studied in this work is briefly described. The motivation and objectives of the present dissertation is clarified, as well as the methodology used in order to reach these aims. A bibliographic review is presented, emphasizing the present state of art. Finally the intended contributions are set.

The second chapter is dedicated to describe the DFIG control topology. The simulation model and the test benches used to analyze and validate the results are also described.

Since symmetrical and asymmetrical voltage sags cause slightly different

effect on the DFIG behavior, these two cases are analyzed separately in Chapters 3 and 4, respectively. The analysis is carried out using in both cases a mathematical approach, simulation and experimental results.

The proposed ride-through control strategies for symmetrical and asymmetrical case are presented in Chapter 5 and 6, respectively. The simulation and experimental are shown in order to validate the strategies.

In the last chapter, the conclusions are presented and the proposals for continuation are listed.

# Doubly-Fed Wind Energy Conversion System

---

## 2.1 Introduction

Wind energy conversion systems are constituted of a wind turbine that converts the kinetic wind energy into mechanical power in the generator shaft. There are technologies with a gearbox between the turbine and the generator, as the DFIG, and others called gearless technologies. The mechanical power is converted by the generator into electric power which is supplied to the grid using or not using power converters.

This chapter is dedicated to briefly describe the energy conversion process in the DFIG technology, explaining the generator classical control strategies. Furthermore, the simulation model and test benches are also presented.

As the objective of the present work is to analyze the electrical behavior of the machine which is much faster than the mechanical dynamics, the latter is not described here. Details about the turbine, the gearbox and a simple mechanical modeling can be found in Mendes (2009) and Rabelo (2009).

## 2.2 The DFIG Technology

As stated previously, in the DFIG technology a wound rotor induction generator is connected to the turbine through a gearbox that raises the slow

turbine speed to a higher speed in the generator shaft. The stator circuit of the generator is directly connected to the grid, therefore, under normal operation, it is supplied by a constant voltage amplitude and frequency. The rotor circuit is supplied by converters through slip rings. The Figure 2.1 depicts the schematic diagram of the DFIG drive topology.

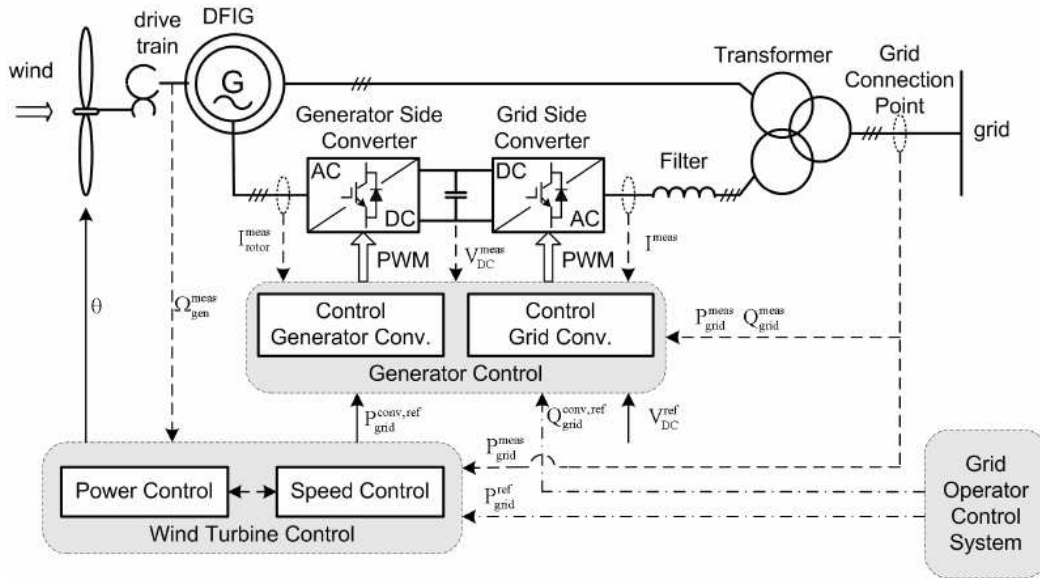


Figure 2.1: DFIG drive topology (Blaabjerg et al., 2006).

Two voltage source converters (VSC) connected using a DC-link in the so-called back-to-back configuration are used. Generally, these converters use IGBTs (Insulated Gate Bipolar Transistor) commanded using PWM (Pulse Width Modulation) switching method.

The grid side converter (GSC) is connected to the grid through a filter used to reduce the harmonics due to the converter switching. A transformer can be used or not for the connection of the filter to the grid. When the transformer is used, its role is to decrease the rotor circuit voltage, decreasing the DC-link voltage. The GSC controls the DC-link voltage and can be also used to control the reactive power flowing from or to the grid.

The rotor side converter (RSC) is connected to the rotor circuit and it controls the rotor currents. As mentioned in the previous chapter, when the converter takes out active power from the rotor circuit, the machine operates

on supersynchronous speeds, whereas the active power injection results in subsynchronous operation. The changing in the rotor current represents a changing in the stator power flow, therefore the RSC is used to control the stator active and reactive powers.

In the next subsections, the electric components of the technology are mathematically modeled. Based on this modeling the GSC and RSC classical control strategies are presented in the following sections.

### 2.2.1 Wound rotor induction generator

The construction of the wound rotor induction machine is similar to the squirrel cage one. The stator windings are supplied by alternating voltage and currents, in such a way that the spatial winding distribution produces a rotating magnetic flux in the machine air gap. The windings in the rotor end up on copper slip-rings mounted to the shaft that permits the use of an external source to supply rotor circuits. The rotor currents also impose a rotating flux in the air gap whose frequency depends on the currents frequency, defining the machine speed in such a value that warrants the production of continuous torque.

In this section, the classical induction motor model in a synchronous reference frame is presented. The stator and rotor differential equations in the synchronous reference frame are written as (Kovács, 1984):

$$\vec{v}_s = R_s \vec{i}_s + \frac{d}{dt} \vec{\psi}_s + j\omega_s \vec{\psi}_s, \quad (2.1)$$

$$\vec{v}_r = R_r \vec{i}_r + \frac{d}{dt} \vec{\psi}_r + j\omega_r \vec{\psi}_r, \quad (2.2)$$

where the variables are in the synchronous reference frame and the parameters are referred to the stator. The meanings are clarified below:

- $v_s$  and  $v_r$  are the stator and rotor voltages, respectively;
- $i_s$  and  $i_r$  are the stator and rotor currents, respectively;

- $\omega_s$  and  $\omega_r$  are the voltages and currents angular speed in the stator and rotor, respectively, where:

$$\omega_r = \omega_s - \omega; \quad (2.3)$$

- $\omega$  is the electrical rotor speed given by:

$$\omega = P\omega_m, \quad (2.4)$$

where  $P$  is the number of pole pairs and  $\omega_m$  is the mechanical speed;

- $\psi_s$  and  $\psi_r$  are the stator and rotor flux linkages, respectively;
- $R_s$  and  $R_r$  are the stator and rotor resistances, respectively.

The stator and rotor flux linkages,  $\psi_s$  e  $\psi_r$ , are given as:

$$\vec{\psi}_s = L_s \vec{i}_s + L_m \vec{i}_r = (L_{\sigma s} + L_m) \vec{i}_s + L_m \vec{i}_r, \quad (2.5)$$

$$\vec{\psi}_r = L_r \vec{i}_r + L_m \vec{i}_s = (L_{\sigma r} + L_m) \vec{i}_r + L_m \vec{i}_s. \quad (2.6)$$

where  $L_s$ ,  $L_r$  are, respectively, the stator and rotor self inductances,  $L_{\sigma s}$  and  $L_{\sigma r}$  are the stator and rotor leakage inductances and  $L_m$  is the magnetizing inductance.

The mechanical differential equation is written as:

$$J \frac{d\omega_m}{dt} + k_f \omega_m = T_e - T_{mec}, \quad (2.7)$$

where  $J$  is the inertia constant  $k_a$  is the friction coefficient and  $T_{mec}$  is the mechanical torque provided by the wind turbine through the gearbox expressed in the generator shaft.  $T_e$  is the machine electromagnetic torque calculated through:

$$T_e = \frac{3}{2} P \frac{L_m}{L_s} \text{Im} \left( \vec{\psi}_s \vec{i}_r^* \right), \quad (2.8)$$



where the superscript “ $\wedge$ ” indicates the complex conjugate.

These equations are important to explain the control and they will be also useful to model the generator behavior during voltage sags, as presented in the following chapters.

### 2.2.2 LCL Filter

In order to minimize the grid harmonics injected by the GSC, it is common to use a LCL (inductor-capacitor-inductor) filter to connect the converter to the grid. The Figure 2.2 represents the schematic diagram of the LCL filter.

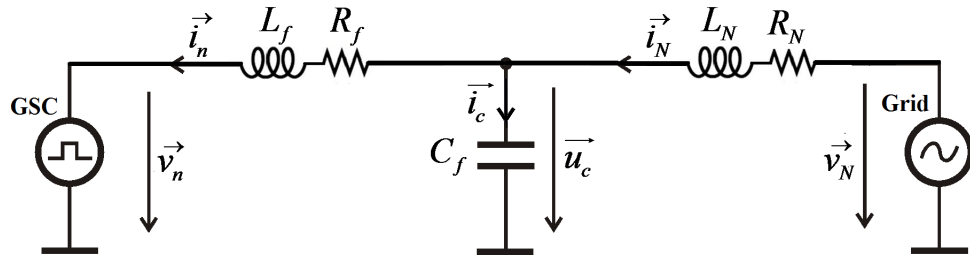


Figure 2.2: LCL filter schematic circuit.

In Figure 2.2  $L_f$  and  $R_f$  represent the filter inductance and resistance at the converter side, respectively, and  $L_N$  and  $R_N$  are the filter inductance and resistance at the grid side which can also include the grid impedance. It is common the use of a resistor in series with the capacitor, not represented in the circuit, to increase the filter damping. Details about the filter design can be found in Liserre et al. (2005).

The capacitor voltage is approximately equal to the grid voltage. Using the vector notation and considering a three-phase balanced system, the filter response, evaluated in the grid frequency, can be modeled as simple LR circuit:

$$\vec{v}_N = R_f \vec{i}_n + L_f \frac{d\vec{i}_n}{dt} + \vec{v}_n, \quad (2.9)$$

where  $i_n$  is the filter current,  $v_N$  is the grid voltage,  $v_n$  is the voltage imposed by the converter.

Rewriting the Equation (2.9) in the synchronous reference frame rotating with the grid voltage angular frequency ( $\omega_N$ ), yields:

$$\vec{v}_N^g = R_f \vec{i}_n^g + L_f \frac{d\vec{i}_n^g}{dt} + j\omega_N L_f \vec{i}_n^g + \vec{v}_n^g. \quad (2.10)$$

### 2.2.3 Converters

As mentioned previously, the DFIG technology uses a back-to-back converter, depicted in Figure 2.1. In this work, the so called space vector modulation is used for the command of the converters (der Broeck et al., 1988).

The complete modeling of the converters requires studies that are out of the scope of the present work, therefore it will be presented just the employed control strategies described in next section.

## 2.3 Classical Control Strategy

Previously, the mathematical modeling of the main components of the DFIG technology were presented. Based on the dynamic equations, this section is dedicated to describe briefly the classical control strategies. Deeper explanations of the control orientation and controller tuning methods are presented in Appendix A and can also be found in Mendes (2009).

### 2.3.1 GSC control

The classical GSC control strategy uses internal loops controlling the grid (filter) currents, which are oriented in the angle of the grid voltage. This orientation permits a decoupled control of active and reactive power (Pena et al., 1996). External to the direct axis current loop it is implemented the DC-link voltage control, because with this orientation the direct axis

component (d) is responsible for the active power. The reactive power is controlled by a controller external to the quadrature (q) current control loop.

Figure 2.3 depicts the block diagram representation of the GSC control. One can see that PI controllers are used and compensators are employed in the output of the current controllers to improve the control response.

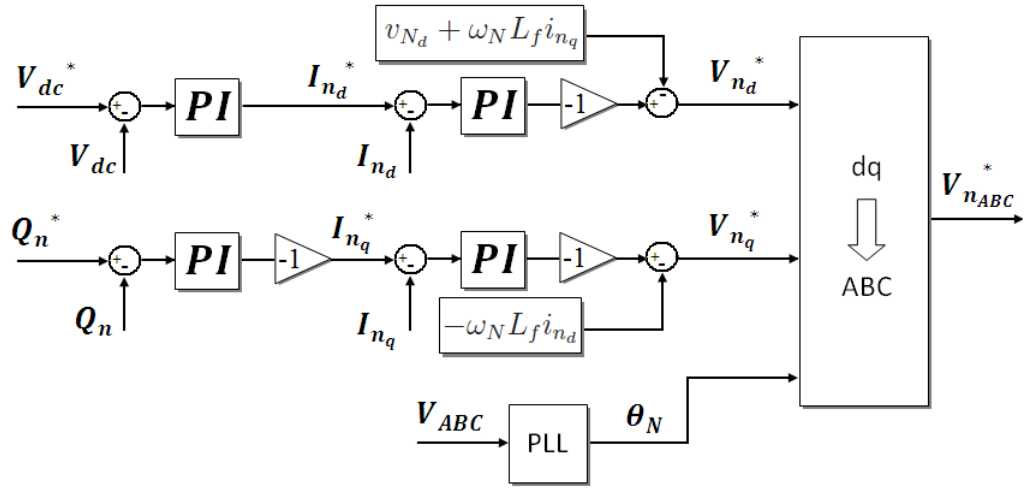


Figure 2.3: Block diagram representation of the GSC control structure.

The methods of Modulus Optimum (MO) and Symmetrical Optimums (SO), which are described in the Appendix A, are used to tune the GSC controllers gains.

### 2.3.2 Phase-Locked Loop (PLL)

As illustrated in Figure 2.3, the angle of the grid voltage vector ( $\hat{\theta}_N$ ), which is used in the orientation of the converter currents, is estimated using the so-called phase-locked loop (PLL).

The classical PLL (Kaura and Blasko, 1997) uses a control loop to adjust the estimated angle in such a way that, when the phase is “locked”, the quadrature component is null. This simple structure has good accuracy for three-phase balanced voltages, but it is not suitable for unbalanced conditions.

Rodriguez et al. (2006) proposes a PLL based on the use of a “Dual Second Order Generalized Integrator” (PSOGI), demonstrating the fast and accurate response of this PLL during voltage unbalances. Indeed this PLL is similar to the classical one, but a decoupling structure is used for the separation of positive and negative sequence components of the voltages. Figure 2.4 shows the block diagram of the PSOGI.

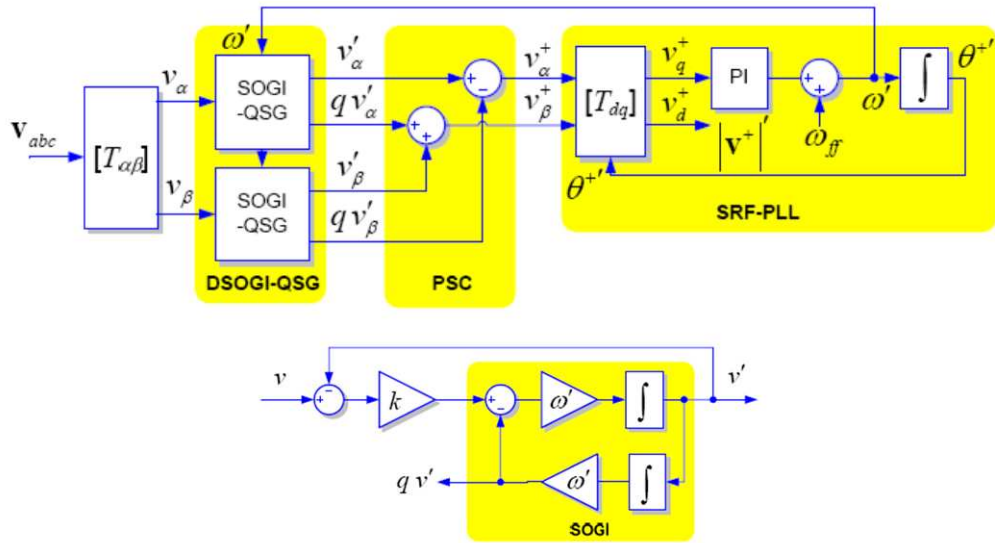


Figure 2.4: PLL topology - PSOGI (Rodriguez et al., 2006).

The PSOGI is used in this work, because it will be useful when developing control strategies for the unbalanced voltage sags.

### 2.3.3 RSC control

The GSC control keeps a constant DC-link voltage, permitting the generator control through the RSC which regulates the rotor currents.

For the orientation of rotor currents the angle of the stator voltage is used (Petersson et al., 2004). Therefore, the angle used for the transformation is given by:

$$\theta_r = \theta_s - \theta, \quad (2.11)$$

where  $\theta_r$  is the rotor voltages and currents angle and  $\theta$  is the rotor electrical position. The angle  $\theta_s$  is obtained through the PLL and  $\theta$  is measured using an incremental encoder.

Using this orientation, described in Appendix A, is easy to demonstrate that the active and reactive powers are calculated as (Oliveira, 2009):

$$P_s = \frac{3}{2}v_{sd}i_{sd} = -\frac{3}{2}\frac{L_m}{L_s}v_{sd}i_{rd}, \quad (2.12)$$

$$Q_s = -\frac{3}{2}v_{sd}i_{sq} = \frac{3}{2}\frac{v_{sd}^2}{\omega_s L_s} + \frac{3}{2}\frac{L_m}{L_s}v_{sd}i_{rq}. \quad (2.13)$$

One can notice that the active stator power depends on the direct axis rotor current and the reactive power depends on the quadrature axis rotor current. Therefore, decoupled rotor currents internal control loops with external active and reactive power control loops are used in the RSC, as depicted in Figure 2.5.

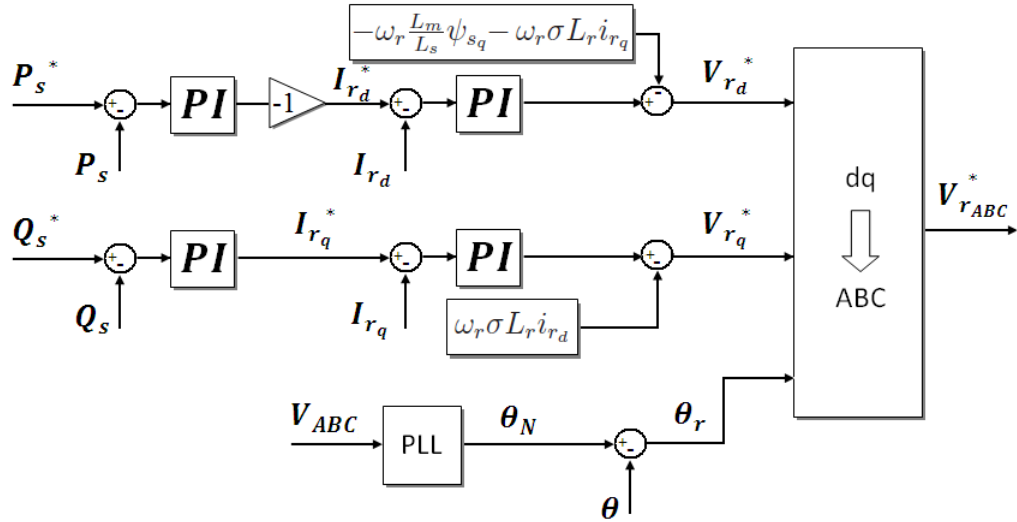


Figure 2.5: Block diagram representation of the RSC control structure.

The active stator power reference is calculated in such a way that the maximum wind power extraction is attained. This calculation algorithm is called maximum power point tracking (MPPT) and is given by:

$$P_s^* = \frac{1}{2} \rho A \left( \frac{\omega_r R}{k \lambda_{otm}} \right)^3 C_{p_{\max}} \eta_g, \quad (2.14)$$

where  $\eta_g$  includes the generator efficiency and the parcel of power that flows through the stator. The latter is dependent on the generator slip. The term  $\lambda_{otm}$  is the optimum tip speed ratio which results the maximum turbine power coefficient ( $C_{p_{\max}}$ ), that is, the maximum possible wind energy is converted into mechanical power to drive the generator. More details about the turbine modeling and the MPPT algorithm can be found in Mendes (2009).

The method of Modulus Optimum (MO) is also used to tune the PI controllers of the RSC. One can also see in Figure 2.5 the use of cross-coupling compensators, which are described in the Appendix A.

## 2.4 The Simulation Model

In the previous sections the DFIG technology and its main components were presented and mathematically modeled. Through the developed equations, a computational model representing the main electrical dynamics of the DFIG drive was implemented using the MATLAB/Simulink, depicted in Figure 2.6.

Commonly it is used the library “SimPowerSystems” to simulate electrical components in the Simulink, but to have a better comprehension and easier manipulation of the model, instead of using predefined electrical components, own components were created. The implementation of the main components of the DFIG drive are briefly described below:

- Grid: represented by ideal three-phase voltage sources with infinite short-circuit capability. Ideal balanced and unbalanced voltage sags can be simulated or it is also possible to simulate the sag through switching impedances, as used in the test bench and described hereafter;
- PLL: implemented as depicted in Figure 2.4;
- Transformer: ideally represented considering just the turns ratio;

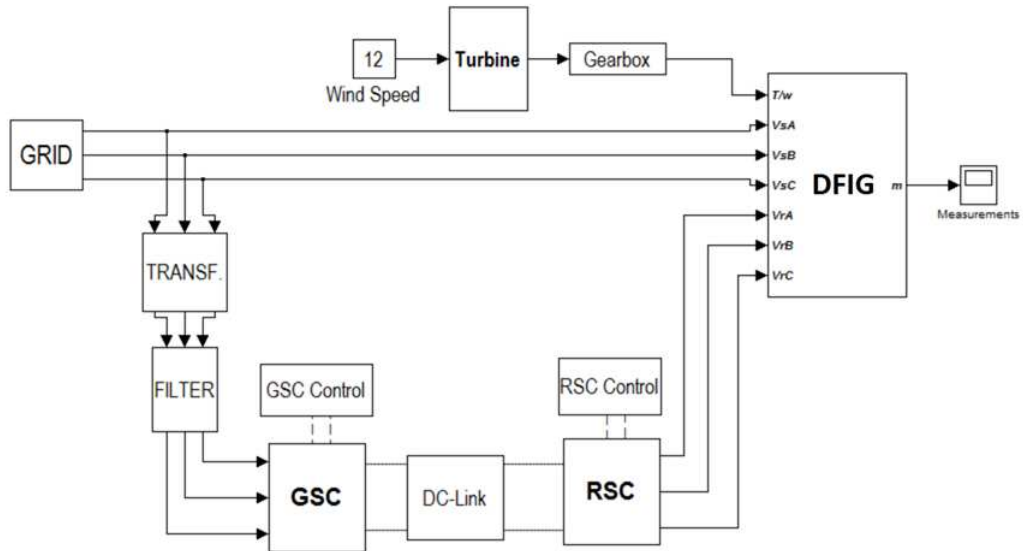


Figure 2.6: Simulation model implemented in Simulink.

- Filter: represented by the Equation 2.9 in the Laplace domain;
- RSC and GSC converters: implemented neglecting the delays involved in the switching process;
- Pulse Width Modulator: based on the voltage space vectors (SVPWM) (der Broeck et al., 1988);
- RSC and GSC control: as described previously and depicted in the Figures 2.3 and 2.5;
- Wound Induction Generator: implemented in the Laplace domain using the Equations 2.1 to 2.8 and considering the orientation of the rotating frame in the stator voltage angle;
- Wind turbine and gearbox: for the studies carried out here the mechanical modeling is no so important, but simple models of the turbine and the gearbox were included in the simulation. Details about these models can be found in Mendes (2009).

The studies carried out here intend to analyze the DFIG behavior generically, so the simulation model is supposed to work with any set of parameters.

The model was validated using the parameters of the 4kW test bench, comparing the simulation results with the experimental ones, but these results are not shown here.

Since the test benches have small power, in order to extrapolate the results for a real scale unit, the simulations studies were performed for a model using the parameters of a 2MW turbine, which are shown in Annex D.

It is important to highlight that, for a better visualization of the variables behavior, for all simulation results presented in this work, the Pulse Width Modulator was neglected, that is, the control voltage reference is the real voltage imposed in the machine. This assumption does not commit the results, since just the high frequency harmonics are neglected.

## 2.5 The Test Benches

All analysis carried out in this work are validated using experimental results obtained in two small scale test benches: a 4kW system localized in TU Dresden (Germany), which was developed by students of this university, and a 25kW test bed projected and built by the author, which is localized in the LCCE-CPH UFMG.

Both test rigs share the same general structure whose schematic diagram is shown in Figure 2.7. Each component is described in this section and the voltage sag generator is characterized in the next subsection.

The wind turbine is represented by a turbine simulator that uses a speed controlled induction motor (IM) drive to emulate the static and dynamic wind turbine characteristics. The simulated turbine characteristics are calculated in a DSpace 1103 platform which generates the speed reference for commercial inverters, responsible for the control of the IM.

The DFIG converters control scheme, depicted in the Figures 2.3 and 2.5, is also implemented in the same DSpace platform, generating PWM signals to the RSC and GSC gate drivers. The 4kW test bench, called from now on TUDb, has a switching frequency of 4kHz and in the 25kW system, called from now on UFMGb, the switching frequency is 6kHz.



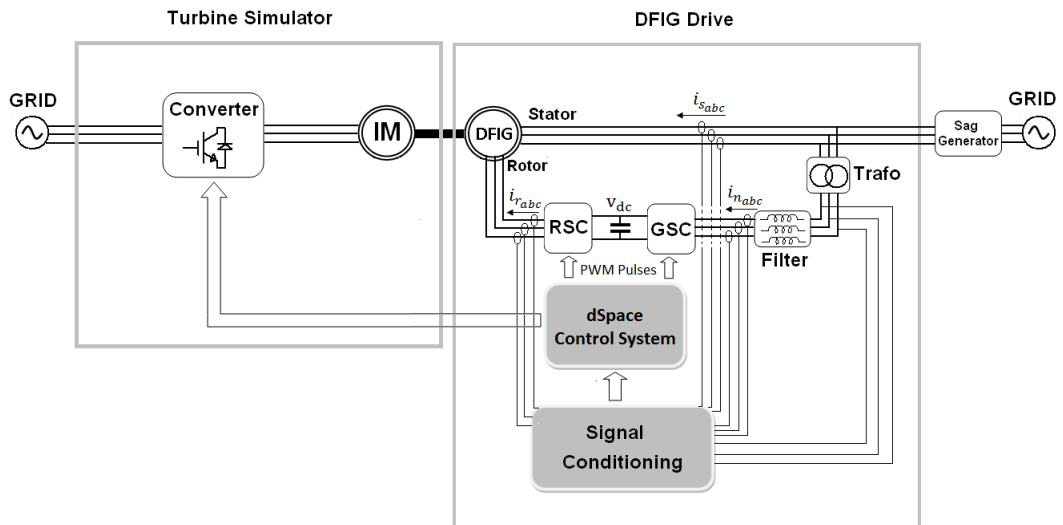


Figure 2.7: Diagram of the test benches that emulate DFIG systems.

The currents and voltages necessary to the control are measured using proper transducers, conditioned to a voltage range compatible with the dSpace input (-10V to +10V). The sampling frequency of the AD converters is equal to the switching frequency. In the UFMGb the measured signals are filtered using a anti-aliasing filter with a cut-off frequency of 2.5kHz.

The control and supervision of the test benches is done through a personal computer, using the software ControlDesk. This software permits the implementation of a supervisory which is used to change the control references, actuate the system contactors and also view and record the variables involved in the process.

Figure 2.8 shows a picture of the TUDb and Figure 2.9 of the UFMGb. The parameters of these test benches are presented in Appendices B and C.

As the main aim of this work is to study the effects of voltage dips on the DFIG, the voltage sag generator (VSG) is a important part of the test benches. It is connected between the grid and the DFIG drive terminals. Two devices are used for this purpose: the sag generator using impedances (ISG) and the “Industrial Power Corruptor” (IPC). They are described in the following subsections.

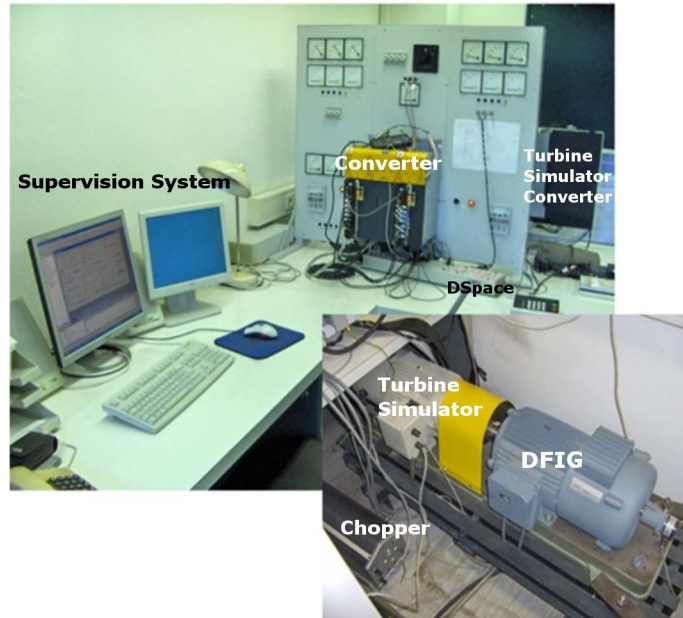


Figure 2.8: Picture of the TU Dresden test bench - 4kW system.

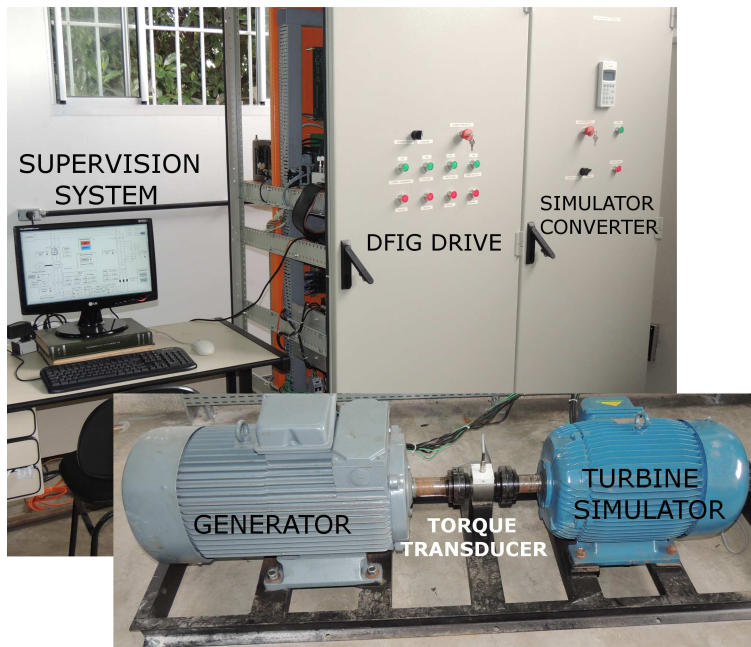


Figure 2.9: Picture of the UFMG test bench - 25kW system.

### 2.5.1 Sag generator using impedances (ISG)

A voltage sag can be emulated using a voltage divider with inductors. This device is recommended in standard IEC61400-21 (IEC, 2008) and its circuit is depicted in the Figure 2.10. The ISG is composed of series and parallel inductors. When the switch is closed, the currents flowing to the short-circuited parallel inductors cause a voltage drop across the series inductors, acting as a voltage dip at the DFIG drive terminals.

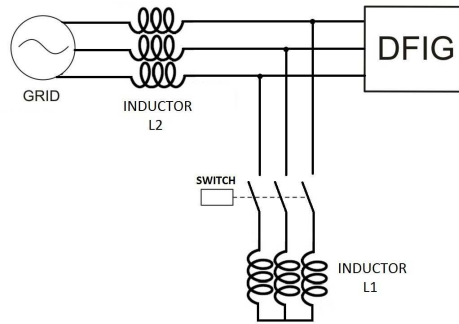


Figure 2.10: Schematic diagram of the ISG voltage sag generator.

The impedances  $Z_1$  and  $Z_2$  are chosen according to the desired voltage drop. The following equation defines the amplitude (%) of the remaining voltage:

$$AMT(\%) = \frac{Z_1}{Z_1 + Z_2} \cdot 100\%. \quad (2.15)$$

The standard (IEC, 2008) defines that the amplitude of the AMT is measured for the ISG isolated from the system to be tested. Nevertheless, when the DFIG is operating the AMT amplitude may be changed from the first adjusted value. Furthermore, this standard permits a small amplitude variation and also a tolerance for the slope of the voltage drop and rise, as depicted in Figure 2.11.

In the TUDb it was available just the configuration of  $Z_1 = 6.28\Omega$  and  $Z_2 = 0.94\Omega$ , thus, three-phase voltage sags with remaining voltage of approximately 85% were tested. This voltage sag is depicted in Figure 2.12(a).

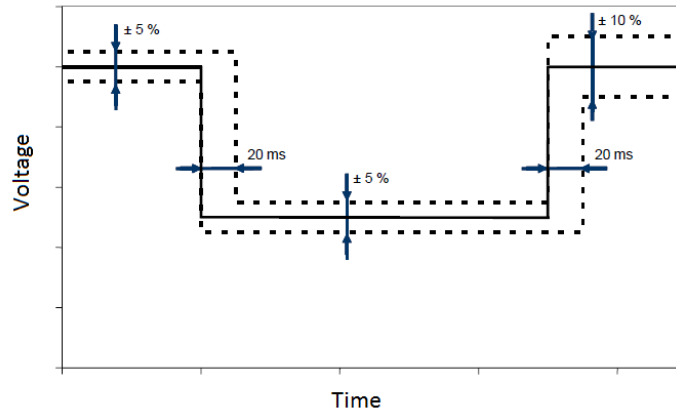


Figure 2.11: Tolerance of voltage drop (IEC, 2008).

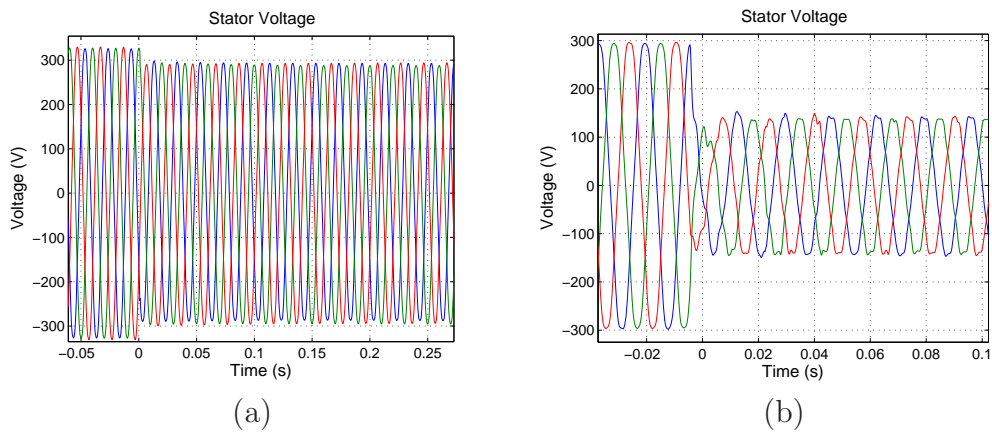


Figure 2.12: Experimental results of the stator voltage for three-phase voltage sags:  
 (a) - TUD test bench: 85%;  
 (b) - UFMG test bench 50%.

Looking at the graph of Figure 2.12(a), it seems that the voltage sag has a rectangular profile, but actually the voltage presents an exponential transient in the beginning. This behavior happens because the inductances has an associated resistance ( $= 0.3\Omega$ ), thus, when the switch is closed the currents present a transient before reaching the steady state. As it will be shown in the next chapter, this transient affects the machine behavior, thus, it must be modeled.

In the UFMGb three three-phase inductors were designed to the ISG:

two with 1.2mH and one with 0.3mH. All these inductors have central point taps which allows the use of half value of the inductances. Therefore, a considerable number of voltage sags can be emulated, but the maximum grid current and the inductors saturation has to be considered. Figure 2.12(b) shows a 50% three-phase voltage sag ( $Z_1 = 0.45\Omega$  and  $Z_2 = 0.45\Omega$ ).

Figure 2.12(b) shows that in the voltage sag beginning there is a transient before the voltage reach the “steady-state” during the sag for the UFMGb. This transient is a little different from the transient previously described for the TUDb. The latter is due to the RL circuit transient. In the UFMGb the main issue is caused by the inductor saturation. Immediately after the switch is closed extremely high inrush currents ( $\approx 2000A$ ) flow through the inductors, saturating them. The unequal saturation of the inductors causes a deeper voltage drop, in the sag beginning, than expected, as depicted in Figure 2.12(b). Both effects have a similar influence on the machine which will be analyzed in the next chapter.

An unbalanced voltage drop can be emulated removing one phase of the parallel inductor on ISG. This solution is used in the TUDb and Figure 2.13(a) shows the voltage behavior for a sag with 90% remaining voltage. For the UFMGb other equipment is used for the asymmetrical voltage sag which is described in the next subsection.

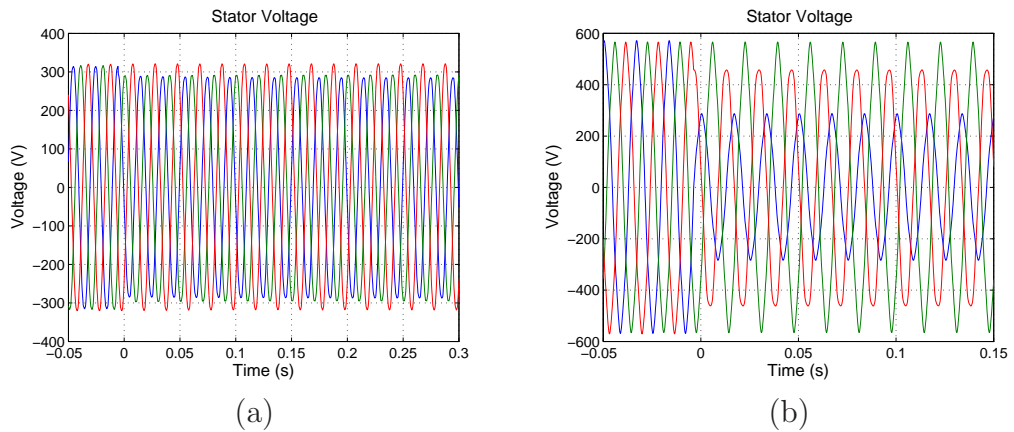


Figure 2.13: Experimental results of the stator voltage for phase-phase voltage sags:

- (a) - TUD test bench: 90%;
- (b) - UFMG test bench 50%.

### 2.5.2 Industrial Power Corruptor (IPC)

In order to have more flexibility in the asymmetrical voltage sag tests, a equipment called “Industrial Power Corruptor” (IPC) is used. It is commercialized by “Power Standard Labs” and the model is IPC-480V-100A.

This device is constituted of a three-phases transformer with many taps which are switched using IGBT’s, thus, varying the output voltage. The IPC allows phase-to-phase and phase-to-neutral voltage sags following the standard IEC61000 (IEC, 2009). The output voltage can also be varied from 0% to 125% with 5% steps and the sag duration can be varied from 1 cycle to 30s. The sag entry instant can also be defined: for  $\theta_0 = 0^0$  the phase A voltage is passing for zero and for  $\theta_0 = 90^0$  it is passing for a maximum value. Figure 2.13(b) depicts a phase-to-phase voltage sag produced by the IPC.

## 2.6 Final Considerations

In this chapter the details of the DFIG technology were discussed. The system components were presented and were mathematically modeled. Control strategies were explained and the methods used in this work for the gains adjustment were highlighted. Finally, the simulation model and the test benches were briefly described. With the knowledge of the DFIG drive topology, in the next chapters will be possible to develop the studies regarding the system behavior under balanced and unbalanced voltage sags.

---

# DFIG Behavior During Balanced Voltage Sags

---

## 3.1 Introduction

In the last chapter the wind generation system using the DFIG technology was described, giving the understanding of the system operation under normal conditions. The present chapter is dedicated to analyze the DFIG behavior during balanced voltage sags. First, the system response is analyzed using a mathematical modeling and after the experimental and simulation results are presented.

## 3.2 Mathematical Modeling

Normally the DFIG behavior during voltage sags is modeled using the differential equations of induction machines, that is, using time domain analysis, as in the following works: Seman et al. (2006), López et al. (2007), López et al. (2008a), Zhang et al. (2009), Peng et al. (2009) and Zhang et al. (2010). Lima et al. (2010) uses the Laplace domain analysis to model the DFIG system during voltage sags.

Time and Laplace domains modeling have their own advantages and application issues, therefore in the present work both are used and described separately in the next subsections.

### 3.2.1 Time domain model

For the theoretical development it is used the classical induction motor equations in the reference frame fixed in the stator (Kovács, 1984):

$$\vec{v}_s = R_s \vec{i}_s + \frac{d\vec{\psi}_s}{dt}, \quad (3.1)$$

$$\vec{v}_r = R_r \vec{i}_r + \frac{d\vec{\psi}_r}{dt} - j\omega \vec{\psi}_r, \quad (3.2)$$

$$\vec{\psi}_s = L_s \vec{i}_s + L_m \vec{i}_r, \quad (3.3)$$

$$\vec{\psi}_r = L_r \vec{i}_r + L_m \vec{i}_s. \quad (3.4)$$

In order to model the voltage applied to the system, the following equation is used:

$$\vec{v}_s = \begin{cases} V_s e^{j\omega_s t} = V_1 e^{j\omega_s t} & t < t_0 \\ V_2 e^{j\omega_s t} + V_{tr} e^{-t/\tau_{tr}} & t \geq t_0 \end{cases}, \quad (3.5)$$

where  $V_s = V_1$  is the rated stator voltage,  $V_2$  is the stator voltage during the sag and  $t_0$  is the instant of the sag beginning, always considered the 0s instant in the graphs presented in this work. The term  $V_{tr}$ , which was added to the voltage during the sag, represents the transient caused by the ISGs. As mentioned in the last chapter, this term has different behaviors in the 4kW and the 25kW test benches:

- In the TUDb the ISG transient is due to the inductor  $L_1$  inrush currents. This transient decays according to the time constant  $\tau_{tr}$ , that can be approximated by the value  $L_1/R_1$ . In this case  $V_{tr}$  is F positive value, representing that the voltage decays slowly until reaching its final value during the sag;



- In the UFMGb  $V_{tr}$  is a negative value, because the inductor saturation causes a deeper voltage drop in the sag beginning, as depicted in Figure 2.12(b). This transient is fast and the  $\tau_{tr}$  is few milliseconds. Due to the difficulty to model the inductor saturation, the complete characteristic of this transient term can be determined just experimentally.

In spite of being two different causes of the transient in the sag beginning, this term can be modeled in the same manner, because the effect on the machine is similar, as will be shown hereafter.

Through Equations 3.2, 3.3 and 3.4, the rotor voltage can be represented by:

$$\vec{v}_r = \frac{L_m}{L_s} \left( \frac{d}{dt} - j\omega \right) \vec{\psi}_s + \left[ R_r + \sigma L_r \left( \frac{d}{dt} - j\omega \right) \right] \vec{i}_r. \quad (3.6)$$

In this equation, the second term, dependent on the rotor current, is smaller than the first one, because generally the rotor resistance ( $R_r$ ) and transient inductance ( $\sigma L_r$ ) have small values. Thereby, a first approximation is possible assuming rotor currents equal to zero, that is, to consider the open rotor circuit case (López et al., 2007). Before starting the open rotor analysis, the representation in the Laplace domain model is presented.

### 3.2.2 Laplace domain model

In this case the induction motor equations are used in the synchronous reference frame (Kovács, 1984), rewriting Equations 3.1 and 3.2 as:

$$\vec{v}_s = R_s \vec{i}_s + \frac{d\vec{\psi}_s}{dt} + j\omega_s \vec{\psi}_s, \quad (3.7)$$

$$\vec{v}_r = R_r \vec{i}_r + \frac{d\vec{\psi}_r}{dt} + j\omega_r \vec{\psi}_r. \quad (3.8)$$

Decomposing the machine equations in real(d axis) and imaginary(q axis) components and applying the Laplace transformation, yields:

$$V_{s_d} = R_s I_{s_d} + s\psi_{s_d} - \omega_s \psi_{s_q}, \quad (3.9)$$

$$V_{s_q} = R_s I_{s_q} + s\psi_{s_q} + \omega_s \psi_{s_d}, \quad (3.10)$$

$$V_{r_d} = R_r I_{r_d} + s\psi_{r_d} - \omega_r \psi_{r_q}, \quad (3.11)$$

$$V_{r_q} = R_r I_{r_q} + s\psi_{r_q} + \omega_r \psi_{r_d}, \quad (3.12)$$

$$\psi_{s_d} = L_s I_{s_d} + L_m I_{r_d}, \quad (3.13)$$

$$\psi_{s_q} = L_s I_{s_q} + L_m I_{r_q}, \quad (3.14)$$

$$\psi_{r_d} = L_r I_{r_d} + L_m I_{s_d}, \quad (3.15)$$

$$\psi_{r_q} = L_r I_{r_q} + L_m I_{s_q}. \quad (3.16)$$

The dependence “(s)” in variables was omitted to simplify the notation, i.e.,  $A(s)=A$ . The initial conditions of the Laplace Transform were considered equal to zero to simplify the analysis. Actually the initial conditions affect the system behavior, but in the analysis just the dynamic behavior is of interest, as demonstrated hereafter.

From Equations 3.13 and 3.14 the stator currents can be expressed as:

$$I_{s_d} = \frac{\psi_{s_d} - L_m I_{r_d}}{L_s}, \quad (3.17)$$

$$I_{s_q} = \frac{\psi_{s_q} - L_m I_{r_q}}{L_s}. \quad (3.18)$$

In order to evaluate the behavior of the stator flux linkage during the sag, it is considered the stator voltage angle orientation, that is, the quadrature axis of the stator voltage is zero. Substituting Equation 3.18 in 3.10 yields:

$$\psi_{s_q} = \frac{(R_s L_m / L_s)}{s + R_s / L_s} I_{r_q} - \frac{\omega_s}{s + R_s / L_s} \psi_{s_d}. \quad (3.19)$$

Using Equation 3.17 in 3.9:

$$V_{s_d} = R_s \left( \frac{\psi_{s_d} - L_m I_{r_d}}{L_s} \right) + s \psi_{s_d} - \omega_s \psi_{s_q}, \quad (3.20)$$

and Equation 3.19 in 3.20:

$$\begin{aligned} \psi_{s_d} = & \frac{(s + R_s / L_s)}{\left( s^2 + 2 \frac{R_s}{L_s} s + \frac{R_s^2}{L_s^2} + \omega_s^2 \right)} V_{s_d} + \frac{L_m \frac{R_s}{L_s} (s + R_s / L_s)}{\left( s^2 + 2 \frac{R_s}{L_s} s + \frac{R_s^2}{L_s^2} + \omega_s^2 \right)} I_{r_d} \\ & - \frac{\omega_s L_m \frac{R_s}{L_s}}{\left( s^2 + 2 \frac{R_s}{L_s} s + \frac{R_s^2}{L_s^2} + \omega_s^2 \right)} I_{r_q}. \end{aligned} \quad (3.21)$$

Generally  $(R_s^2 / L_s^2) \ll \omega_s^2$ , therefore it is possible to neglect  $(R_s^2 / L_s^2)$ . The gain of the last term is small when compared with the other terms, so it can also be neglected. Making these assumptions and doing  $\tau_s = L_s / R_s$ , called the stator time constant, the direct axis stator flux linkage is:

$$\psi_{s_d}(s) = \frac{(s + 1/\tau_s)}{\left( s^2 + 2 \frac{1}{\tau_s} s + \omega_s^2 \right)} V_{s_d}(s) + \frac{L_m / \tau_s (s + 1/\tau_s)}{\left( s^2 + 2 \frac{1}{\tau_s} s + \omega_s^2 \right)} I_{r_d}(s). \quad (3.22)$$

Similarly, it is possible to deduce the quadrature axis stator flux linkage:

$$\psi_{s_q}(s) = \frac{-\omega_s}{\left( s^2 + 2 \frac{1}{\tau_s} s + \omega_s^2 \right)} V_{s_d}(s) + \frac{L_m / \tau_s (s + 1/\tau_s)}{\left( s^2 + 2 \frac{1}{\tau_s} s + \omega_s^2 \right)} I_{r_q}(s). \quad (3.23)$$

Through Equations 3.22 and 3.23 it is seen that the stator flux linkage depends on the stator voltage and the rotor current. During a voltage sag if the rotor current is kept constant, the flux starts to oscillate with the stator frequency ( $\omega_s$ ) and the oscillation damping depends on the stator time constant ( $\tau_s$ ). Through Equation 3.6 one can notice that the stator flux linkage induces a rotor voltage. Depending on the the control action (rotor current control), the stator flux linkage oscillation frequency and damping can be modified, as will be demonstrated hereafter.

### 3.2.3 Open rotor circuit analysis in time domain

As mentioned previously, a first approximation considers the machine with a open rotor circuit, and then the analysis in the time domain is carried out.

From Equations 3.1 and 3.3:

$$\frac{d\vec{\psi}_s}{dt} = \vec{v}_s - \frac{R_s}{L_s} \vec{\psi}_s \quad (3.24)$$

Considering that before the voltage sag the machine is in steady state and that the stator resistance is negligible, the stator flux linkage is:

$$\vec{\psi}_{sf1} = \frac{V_1 e^{j\omega_s t}}{j\omega_s}. \quad (3.25)$$

Using this flux as initial condition to solve the differential Equation 3.24, the stator flux linkage during the sag is given by:

$$\begin{aligned} \vec{\psi}_s &= \frac{V_2}{j\omega_s} e^{j\omega_s t} + \frac{(V_1 - V_2)}{j\omega_s} e^{-\frac{(t-t_0)}{\tau_s}} + \frac{V_{tr}}{1/\tau_s - 1/\tau_{tr}} \left( e^{-\frac{(t-t_0)}{\tau_{tr}}} - e^{-\frac{(t-t_0)}{\tau_s}} \right) \\ &= \vec{\psi}_{sf2} + \vec{\psi}_{sn} + \vec{\psi}_{str} \end{aligned} \quad (3.26)$$

The stator flux presents three components:  $\vec{\psi}_{sf2}$  is the forced response

during the sag,  $\vec{\psi}_{sn}$  is the natural response that appears when the stator voltage changes and  $\vec{\psi}_{str}$  is the response due to the voltage transient caused by the ISG. Actually, the latter component is also a natural one, but to simplify the analysis  $\vec{\psi}_{sn}$  is considered the natural component when the voltage sag is rectangular whereas  $\vec{\psi}_{str}$  represents the non-rectangular behavior of the voltage sag. Therefore, the transient term is used to model the ISG behavior, but it can also represent the sag behavior in a real grid.

Through Equation 3.26 one can notice that the forced component has constant amplitude and rotates with the stator frequency while the natural component is a fixed vector whose amplitude decays exponentially according to the stator time constant. Figure 3.1 illustrates the stator flux linkage behavior during a three-phase voltage sag when its vector is analyzed in the complex plane.

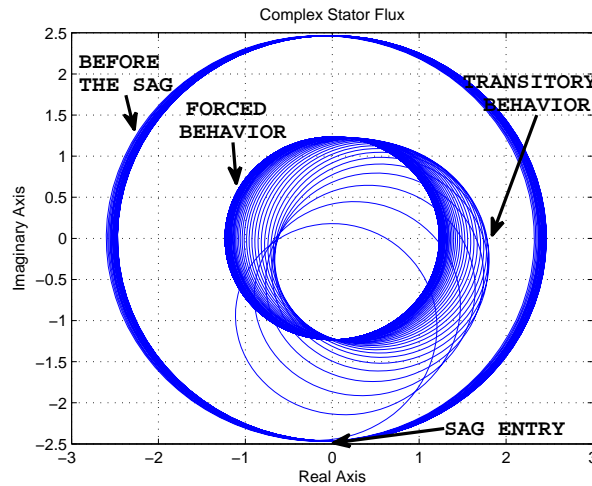


Figure 3.1: Complex plane representation of the stator flux linkage during a 50% three-phase voltage sag.

In Figure 3.1 the transient behavior of the ISG of the TUDb is emphasized, because it takes some time to extinguish. In the case of the ISG of the UFMGb this term decays faster.

Each part of the stator flux linkage induces a correspondent rotor voltage. Substituting Equation 3.26 in 3.6, considering  $\vec{i}_r = 0$ , the three components of the induced rotor voltage, in the rotor referential frame, are given as:

- The forced response:

$$\vec{v}_{r_f}^r = \frac{L_m}{L_s} s_{lip} V_2 e^{j\omega_r t}, \quad (3.27)$$

where  $s_{lip} = \omega_r / \omega_s$  is the slip.

- The natural response:

$$\vec{v}_{r_n}^r = -\frac{L_m}{L_s} \left( \frac{1}{\tau_s} - j\omega \right) \frac{V_1 - V_2}{j\omega_s} e^{-\frac{(t-t_0)}{\tau_s}} e^{-j(\omega t - \theta_0)}, \quad (3.28)$$

where  $\theta_0 = \omega t_0$  is the angle of the stator voltage vector in the instant of the sag entry.

- The “transient” natural response:

$$\vec{v}_{r_{tr}}^r = \frac{L_m}{L_s} \left( \frac{1}{\tau} - j\omega \right) \left( e^{-\frac{(t-t_0)}{\tau_{tr}}} - e^{-\frac{(t-t_0)}{\tau_s}} \right) \tau V_{tr} e^{-j(\omega t - \theta_0)}, \quad (3.29)$$

where  $1/\tau = 1/\tau_s - 1/\tau_{tr}$ .

Through Equations 3.27, 3.28 and 3.29 it is seen that the rotor voltage has two frequency components: a small frequency equal to the rotor frequency ( $\omega_r$ ) and a higher frequency equal to the machine electrical frequency ( $\omega$ ). The natural components have amplitude significantly higher than the forced component, thus, the natural components dominate the rotor voltage behavior, as it will be proved hereafter.

In order to validate the theoretical development, the generators of the test benches were left with open rotor circuits and it was imposed with the turbine simulator a slip of -0.3 (worst case). Figures 3.2(a) and (b) show the experimental results for both test benches. One phase of the rotor voltage is compared with the result obtained through Equations 3.27, 3.28 and 3.29. Both responses are in good agreement. The small difference observed can be explained by the fact that the term produced by the VSG is not a perfect exponential as modeled, but this fact does not commit the analysis.

Figures 3.3 (a) and (b) shows separately the amplitude of the rotor voltage components obtained in the Equations 3.27, 3.28 and 3.29, evidencing

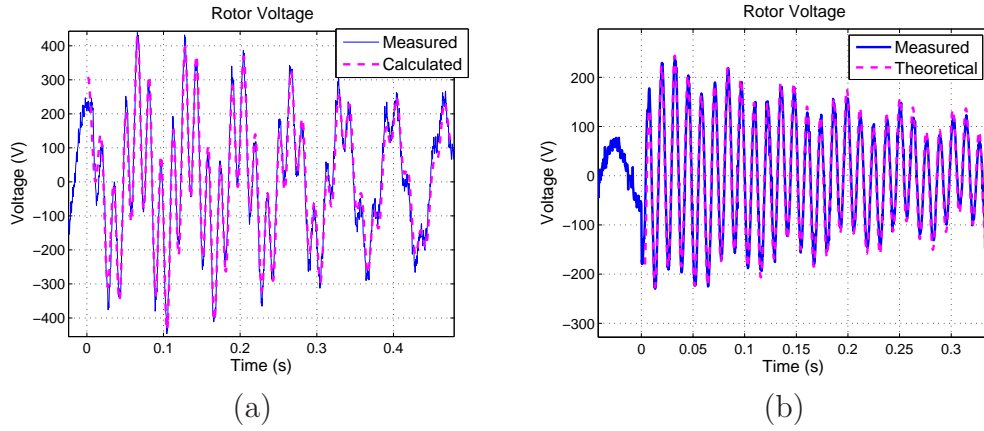


Figure 3.2: Comparison between the rotor voltages calculated and the experimental results in the TUD test bench:

- (a) - TUD test bench: 85% three-phase voltage sag, 1950 RPM;
- (b) - UFMG test bench: 50% three-phase voltage sag, 2340 RPM.

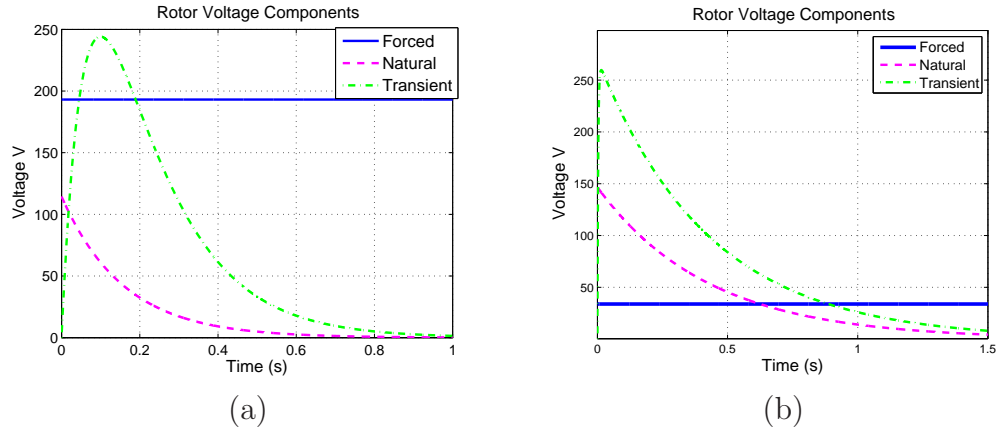


Figure 3.3: Rotor voltage components during the sag obtained through Equations 3.27, 3.28 and 3.29 for:

- (a) - TUDb parameters (85% three-phase voltage sag, 1950 RPM);
- (b) - UFMGb parameters (50% three-phase voltage sag, 2340 RPM).

the behavior of each one. It is seen that the transient response has a huge impact on the amplitude of the rotor voltage.

Before proceed the analysis, it is important to note that the results of both test benches are analyzed for sake of comparison. The two results are not shown just in cases when the responses are similar.

In order to verify the presence of the components with different frequencies in the measured rotor voltage, the Fourier analysis of this variable is shown in Figure 3.4 for the TUDb. The behavior for the UFMGb is similar, with the difference that its supply frequency is 60Hz, whereas for the TUDb is 50Hz. Below each component is analyzed:

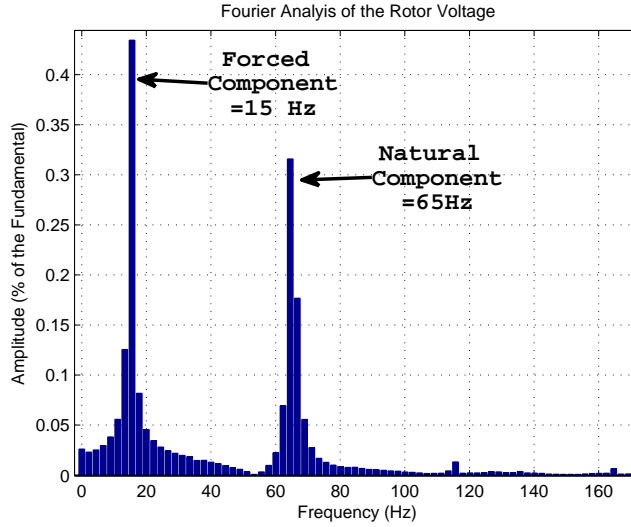


Figure 3.4: Fourier analysis of the measured rotor voltage during the sag for the TUDb(85% three-phase voltage sag, 1950 RPM).

- The forced component has frequency equal to the rotor frequency ( $f_r$ ). The amplitude of this component is constant and can be calculated through:

$$|v_{r_{f_{\max}}}| = \frac{L_m}{L_s} |s_{lip}| V_2, \quad (3.30)$$

so dependent on the slip magnitude and the remaining stator voltage;

- The natural component has frequency equal to the rotor electrical frequency ( $f$ ). It is seen that this component decay according the stator time constant. The maximum natural component may be approximated by:

$$|v_{r_{n_{\max}}}| = \frac{L_m}{L_s} (1 - s_{lip}) (V_1 - V_2), \quad (3.31)$$



and happens in the sag beginning. Through Equation 3.31 one can notice that the amplitude is proportional to the per unit machine speed and the voltage sag depth;

- The so called transient component has frequency equal to the natural component, because in fact it is also part of the natural component, as already stated. It is seen that this component presents a first rising, dependent on the transitory time constant ( $\tau_{tr}$ ), and after it decays according the stator time constant. Taking the derivative of Equation 3.29 it is calculated that the maximum value of the component occurs in the instant  $t_p$ :

$$t_p = -\tau \ln \left( \frac{\tau_s}{\tau_{tr}} \right). \quad (3.32)$$

For the TUDb this rising time takes some cycles and for the UFMGb it is fast. The maximum amplitude of this term is equal to:

$$|v_{r_{tr\max}}| = \frac{L_m}{L_s} \omega \tau V_{tr} \left[ \left( \frac{\tau_s}{\tau_{tr}} \right)^{\tau/\tau_{tr}} - \left( \frac{\tau_s}{\tau_{tr}} \right)^{\tau/\tau_s} \right], \quad (3.33)$$

showing that it is proportional to the electrical frequency and also the constant  $\tau$ .

The dependence of the transitory response amplitude on the constant  $\tau$ , thus, on the  $\tau_{tr}$  is an interesting fact that comes from Equation 3.33. This conclusion demonstrates that the doubly-fed generator is affected not just by the remaining voltage, but also on the voltage dip shape. Figures 3.3 (a) and (b) show that the transient response in those cases are worse than the natural response.

The results presented in this work are dependent on the ISG characteristics. The ISG may not reproduce the characteristics of a real voltage sag mainly because the impedances are changed for different voltage depths. Although, the study is not invalidated, because a complete analysis is carried out, therefore each effect can be easily separated. This discussion points two important facts:

- actually, a real grid voltage sag is not rectangular as commonly studied, therefore the impact on the DFIG may be much worse than expected;
- the ISG parameters may affect the system under test. As this structure is recommended on the standard IEC61400-21 for voltage sag tests, it is important to evaluate this effect.

Continuing the open rotor analysis, in order to verify the behavior of the machine in different speeds and voltage sags depth, Figure 3.5 shows the maximum rotor voltages measured in the UFMGb. The results for the TUDb is not shown, because it is possible to test just a unique voltage sag. In this bench, for the 85% three-phase voltage sag, the maximum rotor voltage is 450V in 1950RPM.

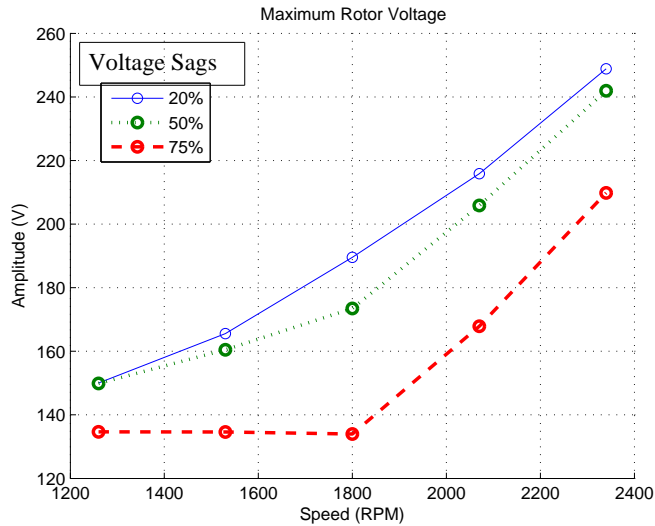


Figure 3.5: Experimental result of the maximum rotor voltage during different voltage sags - UFMGb.

The characteristic of the curve shown in Figure 3.5 can be explained analyzing Equations 3.30, 3.31 and 3.33. Unfortunately, the maximum rotor voltage cannot be calculated adding the three values given by these equations, because the components are not in phase. Although, the equations give an idea about the influence of the speed and the voltage depth in the maximum rotor voltage. For small sag depths, the forced response represents the largest part of the rotor voltage, so it is seen a high dependence of the slip modulus.

Increasing the voltage sag depth, the natural and the transitory component becomes the largest component. As these components depend on the speed, one can notice in Figure 3.5, that for higher speeds it is induced higher voltages.

Comparing the curves in Figure 3.5, it is seen that the distance between the 75% and 50% curves is greater than the distance between the 50% and 20% curves. This fact is justified not by the machine behavior, but by the ISG behavior. Different sags mean different impedances, thus, the voltage sag shape also changes due to the inductor saturation, as previously stated.

Until now just the results of the test benches were shown. In order to extrapolate the results for a high power system, Figure 3.6 show the comparison between the rotor voltage calculated and the one obtained using the complete 5th order model implemented in the MATLAB/Simulink. The theoretical result is calculated using just Equations 3.27 and 3.28, since the sag is considered perfectly rectangular in the simulation.

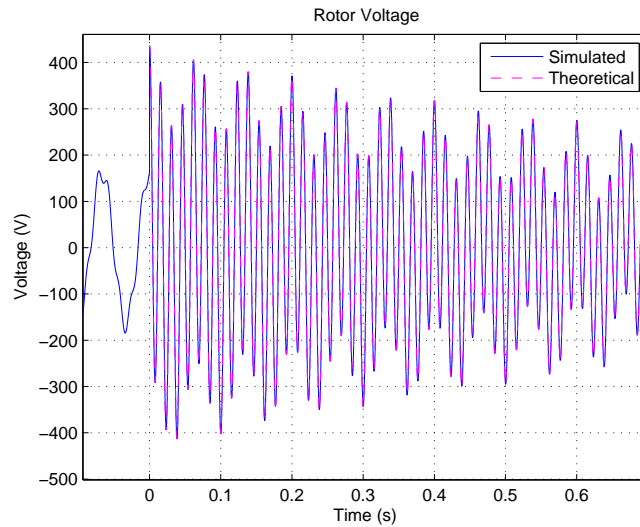


Figure 3.6: Comparison between the rotor voltage simulated and calculated with the parameters of the 2MW system (50% three-phase voltage sag, 1950 RPM).

Comparing Figures 3.2 and 3.6 one can notice that the natural component decays much more slowly in the 2MW system. This behavior is explained by the fact that high power generator generally has a small stator resistance

and then the stator time constant is higher than in small generators. Comparing the results of Figures 3.2 (a) and (b) for the test benches, this fact can also be noticed. The 30kW generator (UFMGb) has higher time constant than the 4kW one (TUDb). It is necessary to pay attention in this fact when the results of the test bench are analyzed and RTFC strategies are developed.

### 3.2.4 Open rotor circuit analysis in Laplace domain

Considering the rotor current equal to zero, substituting Equations 3.15, 3.17 and 3.22 in Equation 3.11, the direct axis rotor voltage equation is:

$$V_{r_d}(s) = \frac{L_m}{L_s} \left( \frac{s^2 + \frac{1}{\tau_s}s + \omega_r\omega_s}{s^2 + 2\frac{1}{\tau_s}s + \omega_s^2} \right) V_{s_d}(s). \quad (3.34)$$

Similarly using Equations 3.16, 3.18 and 3.23 in Equation 3.12, the quadrature rotor voltage is given by:

$$V_{r_q}(s) = \frac{L_m}{L_s} \left( \frac{(\omega_r - \omega_s)s + \omega_r/\tau_s}{s^2 + 2\frac{1}{\tau_s}s + \omega_s^2} \right) V_{s_d}(s). \quad (3.35)$$

In these equations it is possible to see that the rotor voltage dynamic behavior is represented by a second order transfer function with time constant equal to  $\tau_s$  and angular frequency equal to  $\omega_s$ . This fact confirms the results obtained in Equations 3.27, 3.28 and 3.29.

Figure 3.7 shows the comparison between the measured rotor voltage in the TUDb and the results obtained using equations in the time and Laplace domains. Now a sub-synchronous speed was tested and again the theoretical and experimental results are in good agreement.

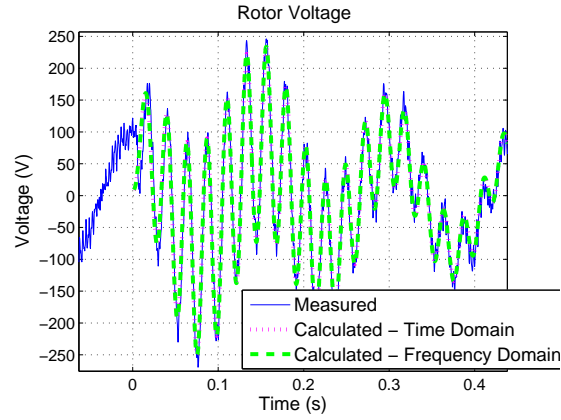


Figure 3.7: Rotor voltage measured and calculated - TUDb (85% three-phase voltage sag, 1300 RPM).

### 3.2.5 Complete analysis in Laplace domain

The open rotor analysis is a good mathematical approximation if the rotor current is kept under acceptable values, but generally that is not true during voltage sags due to the high induced rotor voltage, as demonstrated in the previous subsections. Furthermore, the RSC control influences the rotor currents behavior, thus, the flux linkage transient response.

The stator flux linkage differential equation, obtained from Equations 3.1 and 3.3, is:

$$\frac{d\vec{\psi}_s}{dt} = \vec{v}_s - \frac{R_s}{L_s} \vec{\psi}_s + \frac{L_m}{L_s} \vec{i}_r. \quad (3.36)$$

The analysis of the stator flux linkage response in the time domain is not a simple task, thereby the Laplace domain is used. Equations 3.22 and 3.23 show the influence of the rotor currents in the stator flux linkage in the Laplace domain. To simplify the notation these equations are rewritten below:

$$\psi_{s_d}(s) = G_{\langle \psi_{s_d} V_{s_d} \rangle}(s) \cdot V_{s_d}(s) + G_{\langle \psi_{s_d} I_{r_d} \rangle}(s) \cdot I_{r_d}(s), \quad (3.37)$$

$$\psi_{s_q}(s) = G_{\langle \psi_{s_q} V_{s_d} \rangle}(s) \cdot V_{s_d}(s) + G_{\langle \psi_{s_q} I_{r_q} \rangle}(s) \cdot I_{r_q}(s). \quad (3.38)$$

The stator voltage depends on the sag behavior, but the rotor current depends on the control action and also on the stator flux linkage. In order to deduce this dependence, Equation 3.17 is substituted in 3.15 and Equation 3.18 in 3.16, resulting:

$$\psi_{r_d} = L_r I_{r_d} + \frac{L_m}{L_s} (\psi_{s_d} - L_m I_{r_d}), \quad (3.39)$$

$$\psi_{r_q} = L_r I_{r_q} + \frac{L_m}{L_s} (\psi_{s_q} - L_m I_{r_q}) \quad (3.40)$$

From the substitution of Equations 3.39 and 3.40 in 3.11, yields:

$$\begin{aligned} I_{r_d}(s) = & \frac{1}{\sigma L_r s + R_r} V_{r_d}(s) - \frac{(L_m/L_s)}{\sigma L_r s + R_r} s \psi_{s_d}(s) \\ & + \frac{\omega_r [\sigma L_r I_{r_q}(s) + (L_m/L_s) \psi_{s_q}(s)]}{\sigma L_r s + R_r} \end{aligned} \quad (3.41)$$

Similarly substituting Equations 3.39 and 3.40 in Equation 3.12:

$$\begin{aligned} I_{r_q}(s) = & \frac{1}{\sigma L_r s + R_r} V_{r_q}(s) - \frac{(L_m/L_s)}{\sigma L_r s + R_r} s \psi_{s_q}(s) \\ & - \frac{\omega_r [\sigma L_r I_{r_d}(s) + (L_m/L_s) \psi_{s_d}(s)]}{\sigma L_r s + R_r} \end{aligned} \quad (3.42)$$

Simplifying the notation of Equations 3.41 and 3.42:

$$I_{r_d}(s) = G_{\langle I_{r_d} V_{r_d} \rangle}(s) \cdot \{V_{r_d}(s) - s(L_m/L_s) \cdot \psi_{s_d}(s) + CC_d\}, \quad (3.43)$$

$$I_{r_q}(s) = G_{\langle I_{r_q} V_{r_q} \rangle}(s) \cdot \{V_{r_q}(s) - s(L_m/L_s) \cdot \psi_{s_q}(s) + CC_q\}. \quad (3.44)$$

In these equations the cross coupling terms ( $CC_d$  and  $CC_q$ ) may be neglected, because their effects are generally reduced using compensators which were described in last chapter. Therefore, it is seen that the rotor current depends on the stator flux linkage and the rotor voltage, which is imposed by the converter and depends on the gains of the rotor current control loop. The parcel dependent on the stator flux linkage is the voltage induced in the rotor circuit or the so called electromotive force (emf).

The block diagram shown in Figure 3.8 represents the Equations 3.37, 3.38, 3.43 and 3.44. In Figure 3.9 this block diagram is simplified and the rotor current control loop is included. The subscripts d and q were suppressed,  $G_c$  is the controller transfer function and “INV” is the inverter. One can notice that the rotor current influences the stator flux linkage, but the stator flux linkage is also influenced by the rotor current, that is, the state variables are dependent.

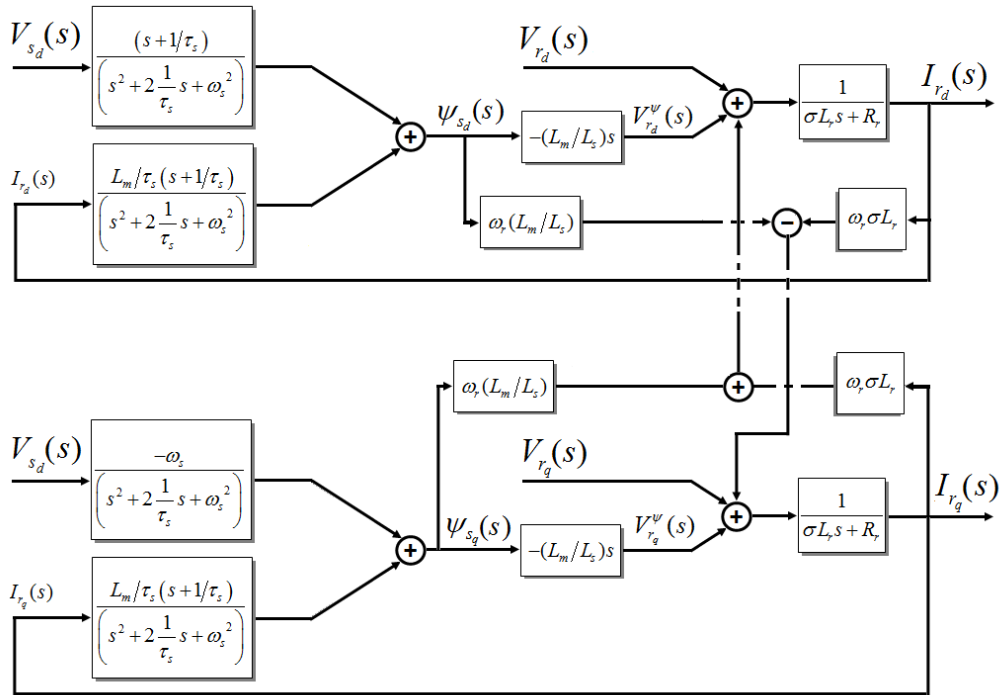


Figure 3.8: Block diagram representation of Equations 3.37, 3.38, 3.43 and 3.44.

In the time domain the correspondent differential equation of the transfer functions given in Equations 3.41 and 3.42 is:

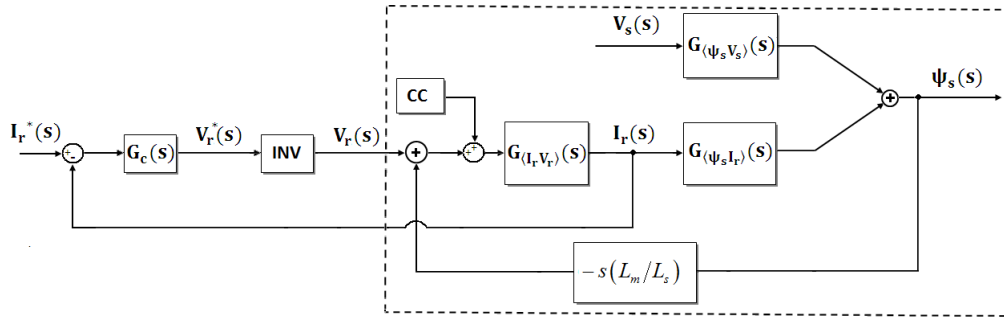


Figure 3.9: Block diagram representation of the current control.

$$\vec{v}_r^r = \vec{v}_{r_\psi}^r + R_r \vec{i}_r + \sigma L_r \frac{d}{dt} \vec{i}_r, \quad (3.45)$$

where  $\vec{v}_{r_\psi}^r$  is the open rotor voltage or the emf calculated summing the components given in Equations 3.27 to 3.29. This equation can be represented by an equivalent RL circuit depicted in Figure 3.10. The inverter is represented using an ideal current source, because it is current controlled. This consideration is only valid if the inverter is capable of synthesizing the voltage  $\vec{v}_r^r$ . On the contrary, high currents take place.

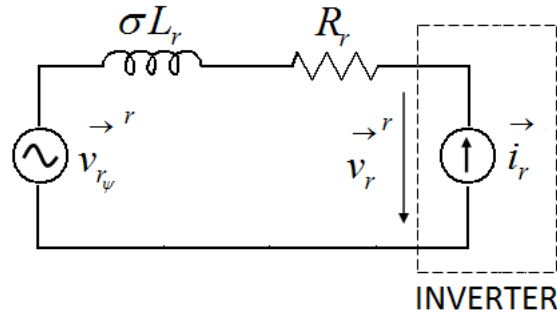


Figure 3.10: Rotor equivalent circuit.

Considering an ideal inverter, i.e., without delays and without saturation, neglecting the cross coupling terms and using a PI controller, Equations 3.41 and 3.42 can be written as:



$$I_{r_d}(s) = \frac{1}{\sigma L_r s + R_r} \left( \frac{K_p s + K_i}{s} \right) (I_{r_d}^*(s) - I_{r_d}(s)) - \frac{s(L_m/L_s)}{\sigma L_r s + R_r} \psi_{s_d}(s), \quad (3.46)$$

$$I_{r_q}(s) = \frac{1}{\sigma L_r s + R_r} \left( \frac{K_p s + K_i}{s} \right) (I_{r_q}^*(s) - I_{r_q}(s)) - \frac{s(L_m/L_s)}{\sigma L_r s + R_r} \psi_{s_q}(s). \quad (3.47)$$

It is interesting to analyze only the stator flux linkage and rotor current natural components (oscillatory response) since the forced component can be easily obtained from the steady-state analysis. Therefore, null rotor current reference ( $I_r^*(s)$ ) can be assumed and from Equations 3.46 and 3.47 the natural rotor currents are given by:

$$I_{r_d}^n(s) = \frac{-s^2 (L_m/L_s)}{\sigma L_r s^2 + (K_p + R_r) s + K_i} \psi_{s_d}^n(s), \quad (3.48)$$

$$I_{r_q}^n(s) = \frac{-s^2 (L_m/L_s)}{\sigma L_r s^2 + (K_p + R_r) s + K_i} \psi_{s_q}^n(s), \quad (3.49)$$

where the superscript “n” represents the natural or oscillatory response. Substituting Equations 3.48 and 3.49 in 3.22 and 3.23, the natural stator flux linkage is calculated through:

$$\psi_{s_d}^n(s) = \frac{(s + 1/\tau_s) (\sigma L_r s^2 + (K_p + R_r) s + K_i)}{\left( s^2 + 2\frac{1}{\tau_s} s + \omega_s^2 \right) (\sigma L_r s^2 + (K_p + R_r) s + K_i) + \frac{1}{\tau_s} \frac{L_m^2}{L_s} s^2 \left( s + \frac{1}{\tau_s} \right)} V_{s_d}(s), \quad (3.50)$$

$$\psi_{s_q}^n(s) = \frac{-\omega_s (\sigma L_r s^2 + (K_p + R_r) s + K_i)}{\left( s^2 + 2\frac{1}{\tau_s} s + \omega_s^2 \right) (\sigma L_r s^2 + (K_p + R_r) s + K_i) + \frac{1}{\tau_s} \frac{L_m^2}{L_s} s^2 \left( s + \frac{1}{\tau_s} \right)} V_{s_d}(s). \quad (3.51)$$

Equations 3.50 and 3.51 show two fourth order transfer functions relating

the stator voltage with the natural stator flux linkage. It is not a easy task to simplify these equations using the literal form, but substituting real numeric values of a typical DFIG generator and choosing adequate controllers gains, one can notice that the system may be reduced to second-order transfer functions. Through the analysis of these transfer functions one can notice that the control parameters' values ( $K_p$ ,  $K_i$ ) affect the stator flux linkage damping and oscillation.

If the controller zero ( $K_i/K_p$ ) is much smaller than the grid frequency  $\omega_s$ , the controller will not affect the phase angle between the input and output, so the rotor current will be lagging the voltage by  $180^\circ$  (negative feedback). In this situation, the flux damping depends on the controller gain evaluated in the grid frequency. The smaller the gain, the higher the flux damping. Cases 1 and 2 in Figure 3.11 illustrate the Bode diagram of the PI controller with high and small gains, respectively, in the cases when current and voltage vectors have no phase difference when evaluated in the frequency  $\omega_s$ . The gains for the 2MW system listed in the Appendix D were used as base values.

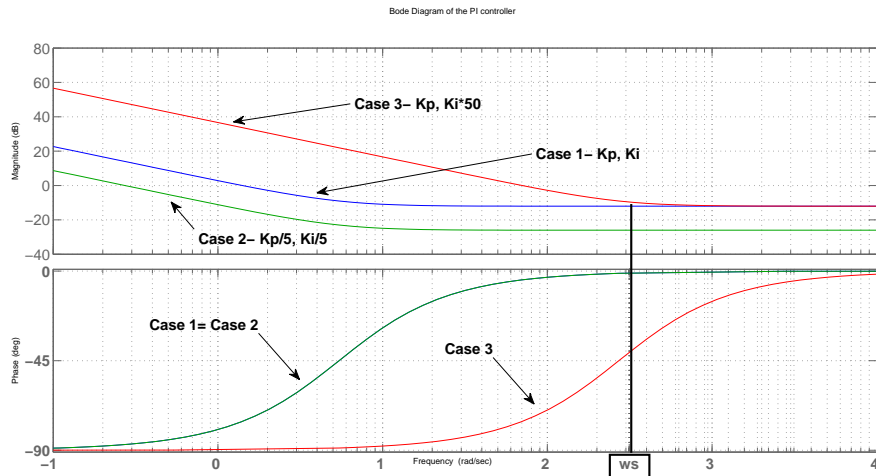


Figure 3.11: Bode diagram of the PI controller (2MW WECS gains).

When the controller zero is higher than the frequency  $\omega_s$ , the controller inserts a phase angle between the rotor current and voltage. In this case, the flux damping is slowed down. The higher the phase shift, the smaller the damping. The worst case happens when there is a phase lag of  $90^\circ$ . This situation is depicted as Case 3 in Figure 3.11 where one can see that the

gain evaluated in the grid frequency is similar to the Case 1, but the phase approximately  $45^\circ$ .

Figure 3.12 depicts the natural direct axis stator flux linkage in the three cases mentioned earlier. These graphs were obtained using Equation 3.50 with the 2-MW system parameters. The results of Figure 3.12 and the pole analysis of Equations 3.50 and 3.51 lead to important conclusions:

- The flux damping is accelerated when the current control is adjusted to a small bandwidth. Although, a small control bandwidth means a slow system response, therefore during voltage sags the currents will be extremely high, because the inverter will not answer fast to counteract the high emf induced in the rotor. In this situation, the RSC may be destroyed.
- A priori, for normal operation the implementation of fast controllers is desirable, because it can reject the system disturbances, but during the voltage sags a fast controller implies a slower flux damping. Although the rotor currents are smaller than those in the case with slow control, a decrease in the flux damping is not desirable, because the flux oscillations reflect on the electromagnetic torque causing high mechanical stresses in the drive train.

In order to avoid problems like those, it is necessary to implement control strategies in such a way that the system behavior is not dependent on the current control adjustment. It is also mandatory to limit the rotor current to avoid the damage of the RSC. In Chapter 5 strategies based on these conclusions are developed.

It is important to highlight that in the mathematical development it was assumed a generator with stator and rotor turns ratio unitary. Generally in real systems this relation is not unitary, so Equations 3.50 and 3.51 referred to the rotor can be rewritten as:

$$\psi_{sd}^n|_r = \frac{(s + 1/\tau_s)(\sigma L_r s^2 + (K_{sr} K_p + R_r) s + K_{sr} K_i)}{\left(s^2 + 2\frac{1}{\tau_s} s + \omega_s^2\right)(\sigma L_r s^2 + (K_{sr} K_p + R_r) s + K_{sr} K_i) + \frac{1}{K_{sr}} \frac{L_m^2}{\tau_s L_s} s^2 \left(s + \frac{1}{\tau_s}\right)} V_{sd}, \quad (3.52)$$

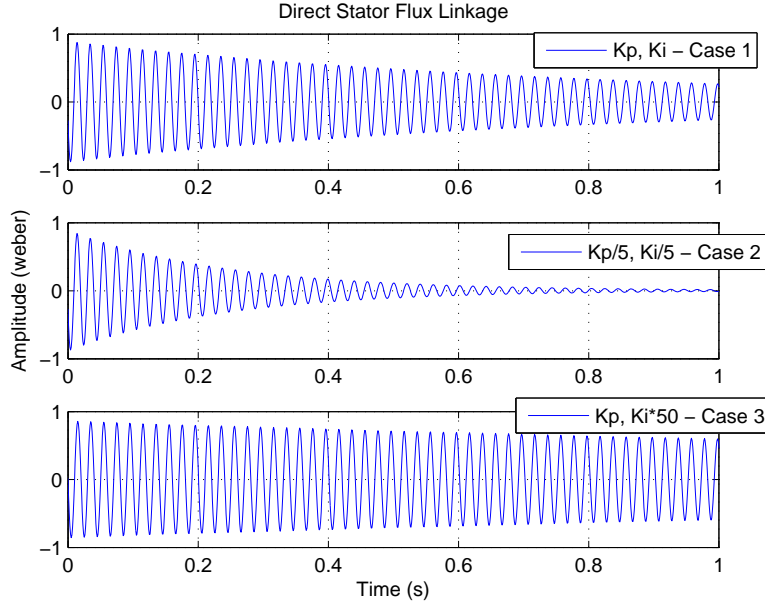


Figure 3.12: Direct axis stator flux linkage (2MW WECS, 50% three-phase sag).

$$\psi_{sq}^n \Big|_r = \frac{-\omega_s (\sigma L_r s^2 + (K_{sr} K_p + R_r) s + K_{sr} K_i)}{\left( s^2 + 2 \frac{1}{\tau_s} s + \omega_s^2 \right) (\sigma L_r s^2 + (K_{sr} K_p + R_r) s + K_{sr} K_i) + \frac{1}{K_{sr}} \frac{L_m^2}{\tau_s L_s} s^2 \left( s + \frac{1}{\tau_s} \right)} V_{sd}, \quad (3.53)$$

where  $K_{sr} = \frac{V_s}{V_r}$  is the relation between stator and rotor voltages.

Another important assumption is that the converter is capable of imposing the voltages required by the control. In the case when the converter saturates (maximum voltage is reached), the system response may be worse, because high uncontrolled rotor currents may take place.

The mathematical modeling developed in this section is also valid for the voltage recovering after the sag. In the voltage recovering transient, the stator flux natural component is present, and it induces high rotor voltages and currents. This situation is not addressed here, because it is similar to the voltage drop transient.

## 3.3 Experimental Results

In the previous section the mathematical analysis was developed in order to understand the behavior of the DFIG during the voltage sags. The comparison between the theoretical and experimental results, for the open rotor case, have been already shown, therefore here the effect of the control in the system behavior is analyzed comparing the experimental results with the mathematical prediction.

In this section, some experimental results are presented for both test rigs. The following conditions were considered during the tests:

- The DC-link voltage controlled in 450 V;
- The quadrature axis of the grid and rotor current references are equal to zero, i.e, no reactive power control. This assumption does not impact the currents dynamics, just the amplitude;
- The stator active power reference follows the maximum power point tracking (MPPT) curve;
- During the voltage sag, the active power control is deactivated and the current reference is kept constant. This procedure is used in order to avoid the influence of the power control that can difficult the analysis. Furthermore the power control is slow, therefore its influence can be neglected without significant errors in the analysis;
- In the TUDb an 85% (remaining voltage) three-phase voltage sag is applied, whereas in the UFMGb an 50% sag is tested. In both situations the sag starting time is  $t_0 = 0s$  and it lasts 1s.

The following subsections show the experimental results for different operation conditions.

### 3.3.1 Test 1: Synchronous Speed

In the first test, the generators are operating at the synchronous speed. This is not a typical speed for the operation of the DFIG, because in this

point some problems arise, like the unequal heating of the RSC's IGBTs. Nevertheless, this is the condition first analyzed, because it is the simplest case. In the next subsections other speeds are analyzed.

During the tests, the proportional and integral gains of the rotor current control were set according to the tables presented in the Appendices B and C.

The most important variable to be analyzed is the rotor currents, shown in Figures 3.13 (a) and (b). During the sag these currents reach high peak values that may destroy the RSC. For better visualization, when it is necessary just one phase of the ABC currents and voltages is shown.

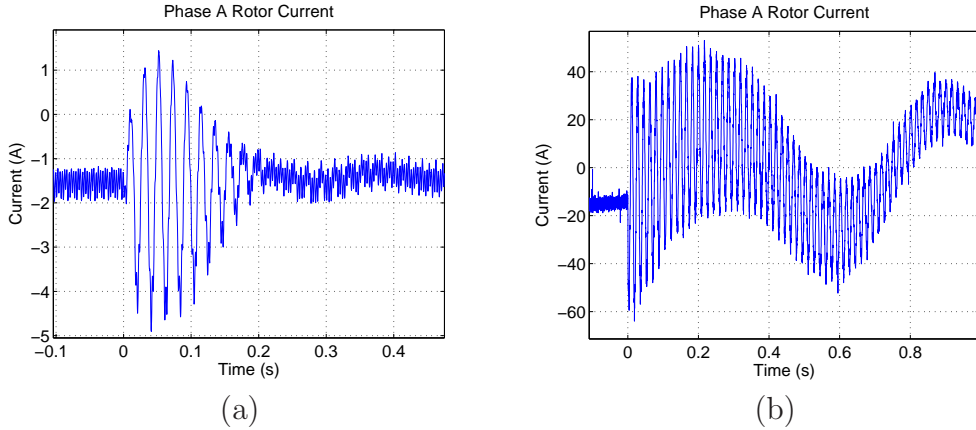


Figure 3.13: Experimental results of the phase A of the rotor currents at synchronous speed:

- (a) - TUD test bench (85% three-phase voltage sag, 1500 RPM);
- (b) - UFMG test bench (50% three-phase voltage sag, 1800 RPM).

Through the Fourier analysis of the rotor currents (Figures 3.14 (a) and (b)) it is possible to identify the components. The forced component is  $f_r = 0$ , since the synchronous speed was considered during the tests. For the UFMGb this component is not exactly null, because during the test the machine deviates a little from the synchronous speed. The natural components are also highlighted in these graphs and they have a frequency close to the grid frequency.

As seen in Figures 3.13 (a) and (b), the natural component causes high rotor currents compared with the normal operation. In the open rotor circuit

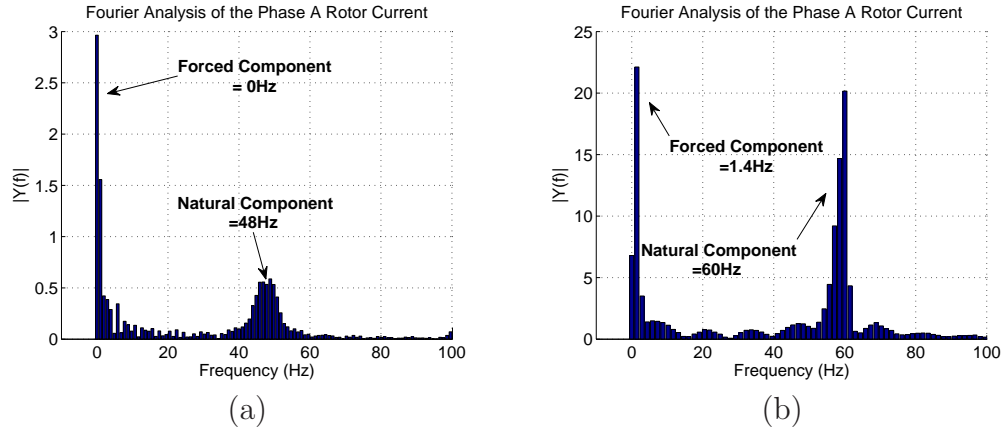


Figure 3.14: Fourier analysis of the phase A rotor current at synchronous speed:  
 (a) - TUD test bench (85% three-phase voltage sag, 1500 RPM);  
 (b) - UFMG test bench (50% three-phase voltage sag, 1800 RPM).

case, the natural flux decays according to the stator time constant. The test benches presents different behaviors:

- For the TUDb one can notice, analyzing the rotor currents, that the control action increases the flux damping. The stator time constant is  $\tau_s = 0.158s$  and through Figure 3.13(a) it is seen that the natural component decays to 0 in approximately 0.2s. The control action also changes the natural component frequency, which in this case lies around 48Hz, deviating from the stator frequency (50Hz).
- For the UFMGb, the control action does not affects the stator flux damping compared with the open rotor analysis ( $\tau_s = 0.426s$ ). The currents frequency is 59Hz, 1Hz below the grid frequency.

The influence of the control in the rotor currents can be calculated using Equations 3.48 to 3.51. Substituting the TUDb parameters in these equations, it is calculated that the decay time constant is reduced to 86.5ms, because the controller gain evaluated in 50Hz is relatively small and the rotor current is opposite to the voltage. The natural frequency is also changed to 48Hz. Figure 3.15(a) shows the dq currents measured and calculated.

Figure 3.15(a) shows that there is a small difference between the responses, mainly in the phase, but this does not commit the modeling, since it

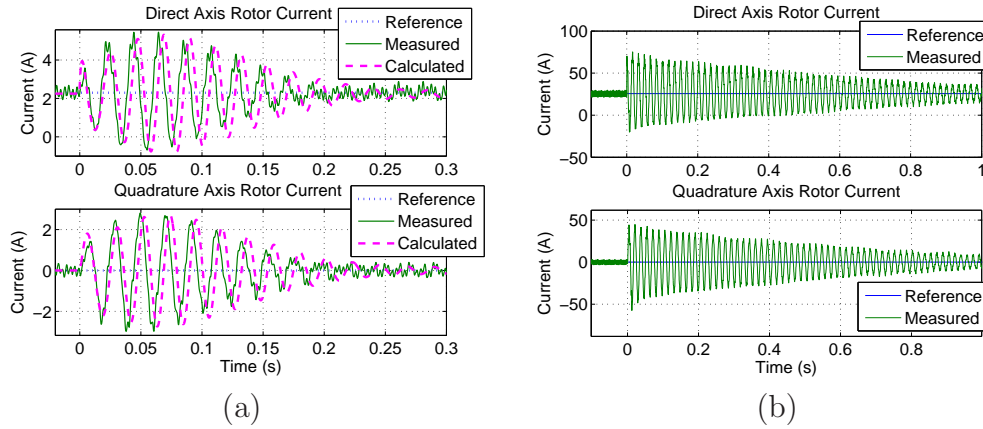


Figure 3.15: Experimental results of the direct and quadrature axes of rotor currents at synchronous speed test:  
 (a) - TUD test bench (85% three-phase voltage sag, 1500 RPM);  
 (b) - UFMG test bench (50% three-phase voltage sag, 1800 RPM).

is important to calculate the maximum current values and approximate the damping. The shift error probably is from the assumed approximations. It is important to highlight that Equations 3.48 to 3.51 give just the natural response, so in order to compare the graphics the forced current was added to the calculated result.

In Figure 3.15(b) the dq rotor currents for the UFMGb is shown. The comparison between the experimental and the theoretical results was not possible, because the dynamical behavior of the ISG affects so much the response of the rotor currents and this effect is complex to be modeled. Although, it is possible to see through this figure and Figure 3.14(b) that the natural component is more relevant in the UFMGb. This fact is explained first because the voltage sag is deeper and second because the stator time constant is higher. The latter fact is important to be analyzed, because the rotor currents will be in high values longer, thus, they are potentially more dangerous for the converter.

Another important variable is the rotor voltage imposed by the converter, shown in Figures 3.16 (a) and (b). If the voltage demanded by the control exceeds the converter limits, the rotor currents may increase very much. In both cases, one can notice that the rotor voltages are below the limits. Despite the fact that the TUDb voltage sag is less deep than the sag in



UFMGB, the voltage maximum values are similar, because in the TUDb the rated rotor voltage is higher.

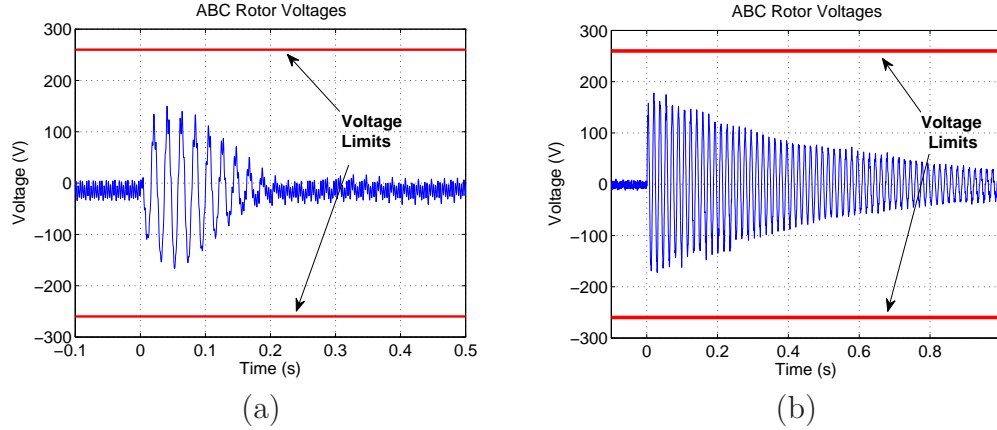


Figure 3.16: Experimental results of the phase A of the rotor voltages at synchronous speed test:

- (a) - TUD test bench (85% three-phase voltage sag, 1500 RPM);
- (b) - UFMG test bench (50% three-phase voltage sag, 1800 RPM).

Comparing Figures 3.16 and 3.15, it is possible to see that in both cases the rotor currents are in anti-phase with the voltages. For the TUDb the gain in the grid frequency is high (Case 1 of Figure 3.11), thus, the flux damping is increased. For the UFMGB this gain is small (Case 2 of Figure 3.11) in such a way that the damping is not changed.

Figures 3.17 (a) and (b) show the phase A of the stator currents. The deviation of the natural flux frequency from the stator frequency, 2Hz in the TUDb and 1Hz in the UFMGB, caused by the control action, appears in the stator current.

The rotor currents and stator flux linkage oscillations due to the natural component cause vibration in the machine electromagnetic torque, causing mechanical stresses. These oscillations also reflect in the power supplied to the grid, causing a decrease in the system power quality. Figures 3.18 and 3.19 show the estimated electromagnetic torque and power where it is seen the oscillations in these variables and a decrease in their mean values. One can notice that the natural component in the UFMGB is longer, therefore it has a greater effect in the whole system.

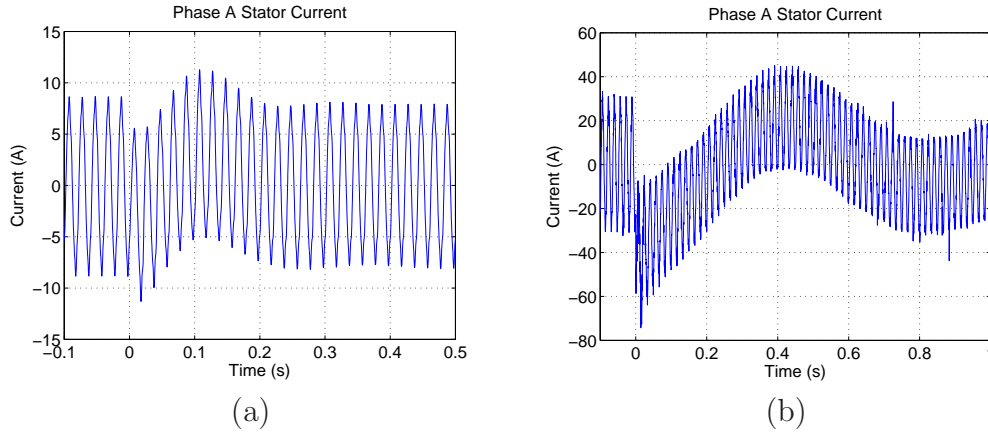


Figure 3.17: Experimental results of the phase A of the stator currents at synchronous speed test:  
 (a) - TUD test bench (85% three-phase voltage sag, 1500 RPM);  
 (b) - UFMG test bench (50% three-phase voltage sag, 1800 RPM).

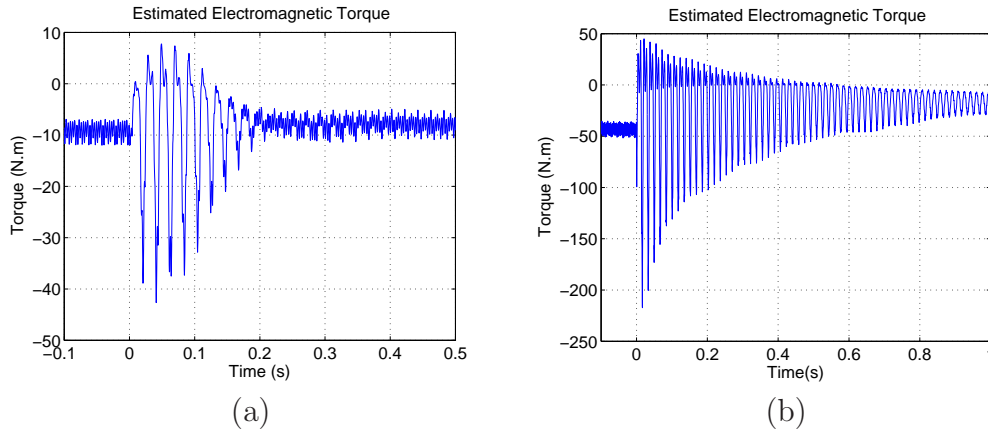


Figure 3.18: Experimental results of the estimated electromagnetic torque at synchronous speed test:  
 (a) - TUD test bench (85% three-phase voltage sag, 1500 RPM);  
 (b) - UFMG test bench (50% three-phase voltage sag, 1800 RPM).

During the sag the DC-link voltage (Figure 3.20) tends to increase, because the high rotor currents flow to the capacitor, thus the grid side currents also increase (Figure 3.21) in order to keep the DC-link voltage constant and to keep the same power transfer. In the case of the TUDb, as the sag is smooth, the grid side converter is capable of controlling the grid currents

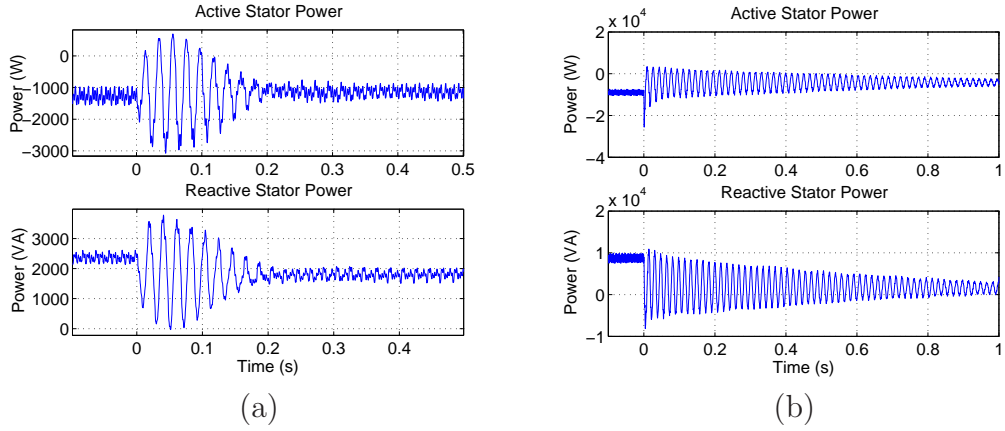


Figure 3.19: Experimental results of the estimated active and reactive powers at synchronous speed test:  
 (a) - TUD test bench (85% three-phase voltage sag, 1500 RPM);  
 (b) - UFMG test bench (50% three-phase voltage sag, 1800 RPM).

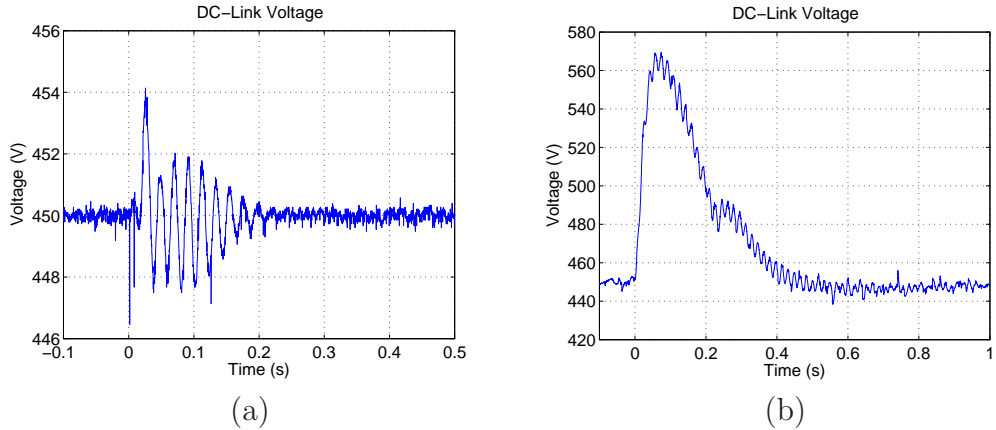


Figure 3.20: Experimental results of the DC-link voltage at synchronous speed test:  
 (a) - TUD test bench (85% three-phase voltage sag, 1500 RPM);  
 (b) - UFMG test bench (50% three-phase voltage sag, 1800 RPM).

and keeping the DC-link voltage mean value constant. For the UFMGb the control grid currents limit is reached (35A), therefore the DC-link voltage rises. To avoid the damage of the converter, a break chopper is used to limit the DC-link voltage (maximum 540V). In both cases, the rotor currents oscillations reflect on the DC-link voltage and GSC currents.

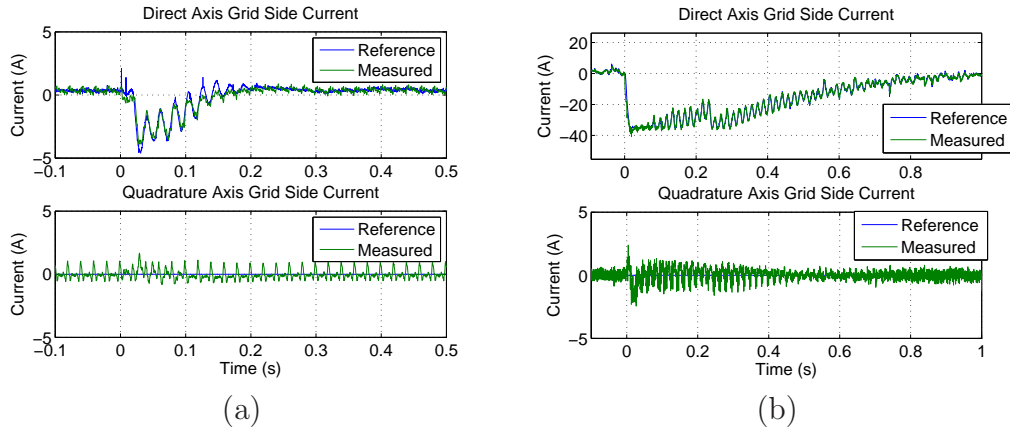


Figure 3.21: Experimental results of the dq GSC currents at synchronous speed test:

- (a) - TUD test bench (85% three-phase voltage sag, 1500 RPM);
- (b) - UFMG test bench (50% three-phase voltage sag, 1800 RPM).

### 3.3.2 Test 2: Synchronous Speed, Modifying the Control Gains

In order to verify the influence of the rotor current controllers gains on the DFIG behavior, the same conditions of the previous test are considered, but the controller is changed in such a way that now the control shifts the phase between the rotor voltages and currents. In the TUDb the calculated project value of the integral gain is increased of 3.33 times and in the UFMGb 6.66 times.

Figure 3.22 depicts the dq rotor currents during the voltage sag. It is seen in both cases that compared with the open rotor case and with the previous test, the natural component decays is much slower. The increase in the natural oscillation causes higher rotor currents and voltages (Figure 3.23), increasing the IGBT's heating and the system mechanical stresses.

Comparing the results of this section with the previous one, it is seen that if no ride-through strategies are implemented, the adjustment of the control may decrease so much the flux damping, even leading the system to instable operation. Of course the tested gains are not optimized, but the objective is to show that the gains can affect the system behavior.

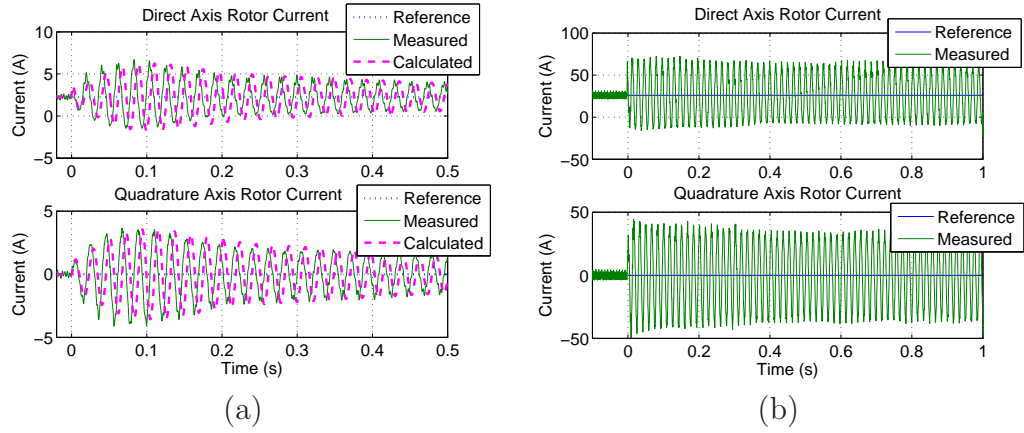


Figure 3.22: Experimental results of the dq rotor currents at synchronous speed test with modified gains:  
 (a) - TUD test bench (85% three-phase voltage sag, 1500 RPM);  
 (b) - UFMG test bench (50% three-phase voltage sag, 1800 RPM).

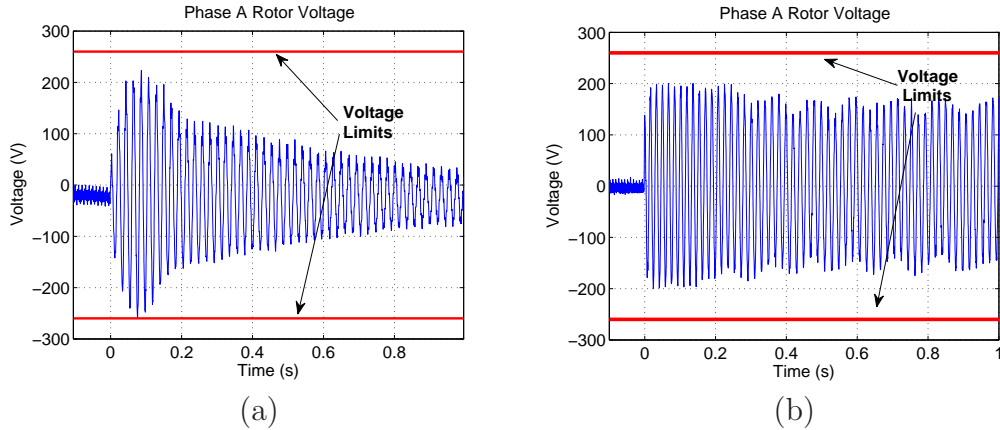


Figure 3.23: Experimental results of the phase A of the rotor voltages at synchronous speed test with modified gains:  
 (a) - TUD test bench (85% three-phase voltage sag, 1500 RPM);  
 (b) - UFMG test bench (50% three-phase voltage sag, 1800 RPM).

### 3.3.3 Test 3: Slip = +0.15

In order to evaluate the system behavior for different operating conditions, the controller gains are set again for the same value of the Test 1. It is first tested a sub-synchronous speed in such a way that the machines are

operating with a slip equal to 0.15.

Figure 3.24 show the results for the phase A of the rotor currents and Figure 3.25 shows the Fourier analysis. The rotor current has a forced component with frequency equal to the rotor frequency ( $f_r$ ) and a natural component. It is clearly seen how the natural component has a high value.

For the TUDb, as the controller gains are the same of the Test 1, the calculated natural frequency (47Hz) and the decay time constant (86.5 ms) are equal. The natural frequency calculated from Equations 3.48 to 3.51 is given in the rotating synchronous reference frame, so in the fixed referential the natural component is supposed to be 39.5Hz, this is the natural frequency(47Hz) minus the rotor electrical frequency( $f_r = 7.5Hz$ ), value close to the value shown in Figure 3.25(a). For the UFMGb  $f_r = 9Hz$  the same analysis can be done and one can notice that the the natural component in the fixed referential frame is 50Hz.

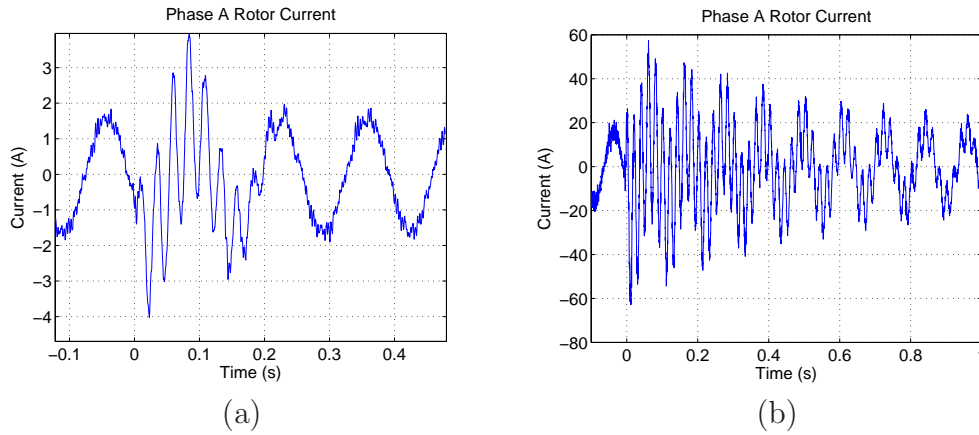


Figure 3.24: Experimental result of the phase A of the rotor currents for slip=+0.15:

- (a) - TUD test bench (85% three-phase voltage sag, 1275 RPM);
- (b) - UFMG test bench (50% three-phase voltage sag, 1530 RPM).

The Figure 3.26 depicts the rotor currents in the synchronous reference frame. In Figure 3.26(a) the theoretical result is also plotted, showing good agreement between the responses. It is interesting to note that, as in the previous tests, the mean value of the currents (forced component) is controlled, but the peak values of the oscillatory part (natural component) is almost not affected by the control.

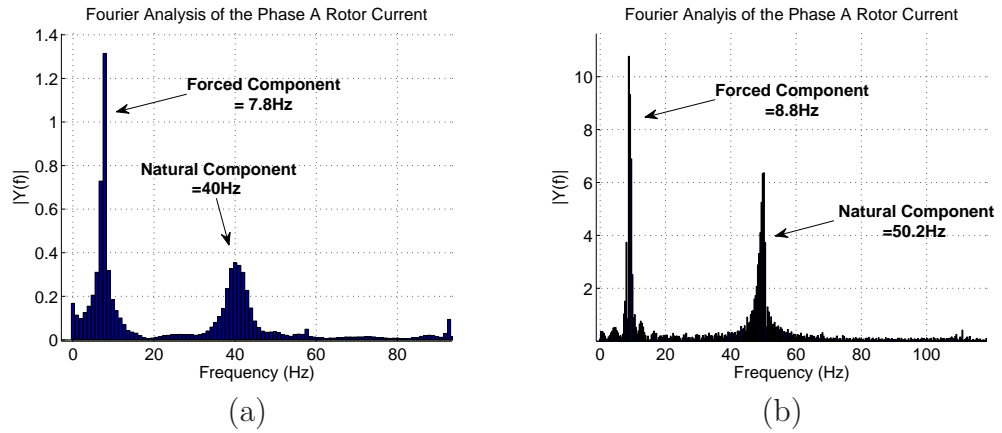


Figure 3.25: Fourier analysis of the rotor currents for slip=+0.15:  
 (a) - TUD test bench (85% three-phase voltage sag, 1275 RPM);  
 (b) - UFMG test bench (50% three-phase voltage sag, 1530 RPM).

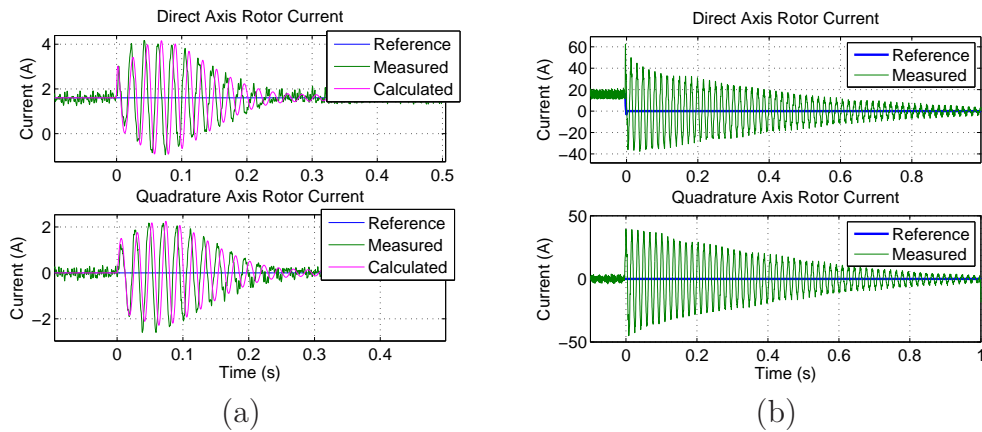


Figure 3.26: Experimental result of the dq rotor currents for slip=+0.15:  
 (a) - TUD test bench (85% three-phase voltage sag, 1275 RPM);  
 (b) - UFMG test bench (50% three-phase voltage sag, 1530 RPM).

### 3.3.4 Test 4: Slip = -0.15

The results for the test of a super-synchronous speed (slip=-0.15) is discussed in this subsection. The UFMG test bench cannot tolerate a 50% voltage sag with this speed, because the converter current protection activate. Therefore, an voltage drop with 80% remaining voltage is considered.

Figures 3.27 and 3.28 shows the phase A of the rotor currents and voltages. With the increasing of the speed, the risk for the system is increased, because of two facts: the induced rotor voltage is higher, thus, the currents tend to be higher and also because the currents is already higher before the sag.

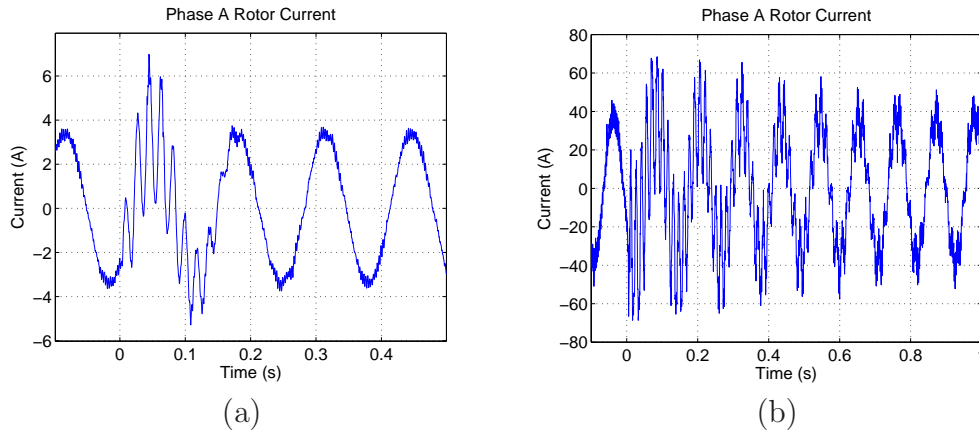


Figure 3.27: Experimental result of the phase A of the rotor currents for slip=-0.15:  
 (a) - TUD test bench (85% three-phase voltage sag, 1725 RPM);  
 (b) - UFMG test bench (80% three-phase voltage sag, 2070 RPM).

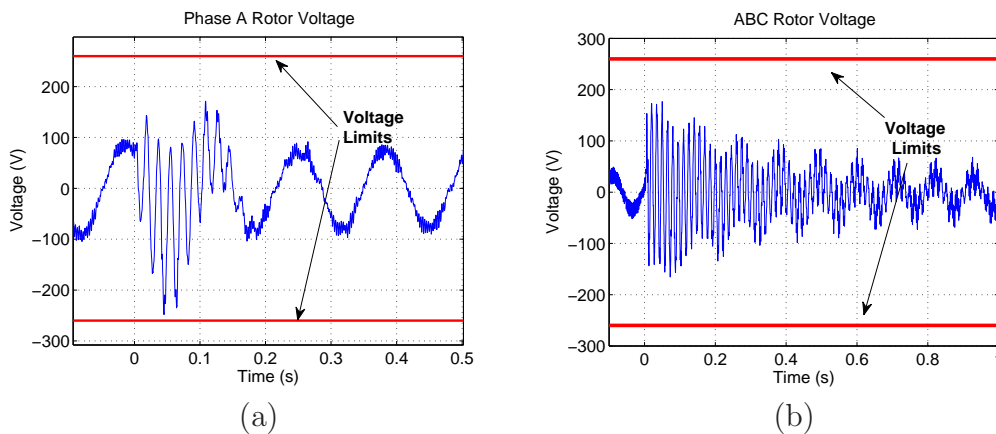


Figure 3.28: Experimental result of the phase A of the rotor voltages for slip=-0.15:  
 (a) - TUD test bench (85% three-phase voltage sag, 1725 RPM);  
 (b) - UFMG test bench (80% three-phase voltage sag, 2070 RPM).



### 3.3.5 Test 5: Slip = -0.15 - Control Saturation

Until now the analysis were carried out for the cases where the control does not saturate, i.e., the converter imposes the required voltage. Here the same conditions of the Test 4 are used, but the DC-link voltage is changed, reducing the converter voltage limits capability. The results for the UFMGb is not shown, because the effect to be demonstrated is similar in both test benches.

Figures 3.29(a) and 3.30(a) show the rotor currents during the sag when DC-link voltage is 200V and 170V, respectively. Figures 3.29(b) and 3.30(b) depict the correspondent rotor voltage. Comparing the current peaks, one can see that the increase in the voltage saturation increases the rotor currents. There is also a small change in the damping and frequency of the natural component.

Through these results one can conclude that the maximum rotor current during the sag depends on the converter voltage capability. Without ride-through strategies the rotor currents may reach unacceptable values tripping the converter or even damaging it.

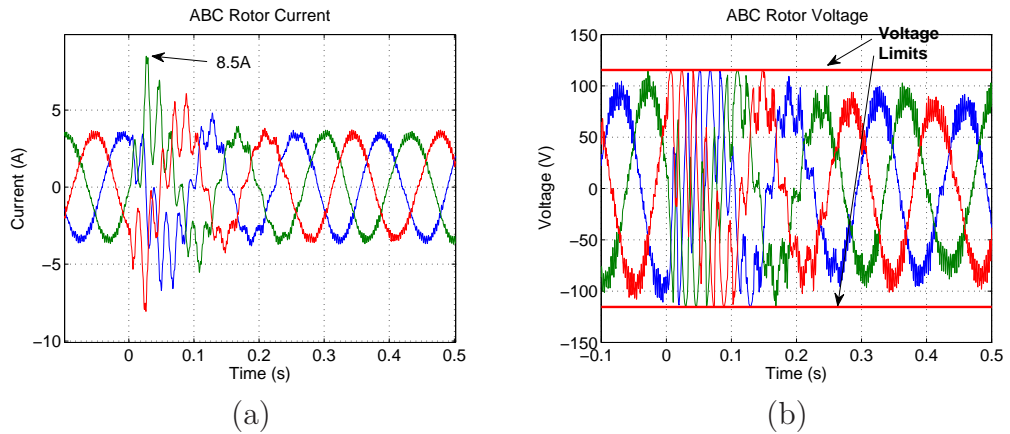


Figure 3.29: Experimental result of the TUDb, 1725 RPM,  $V_{dc} = 200V$ :

- (a) - Rotor currents;
- (b) - Rotor Voltages.

It is expected that in the voltage recovering after the sag the natural component also arises and system behavior is similar to the voltage sag beginning transient. This instant is briefly analyzed for the simulation results.

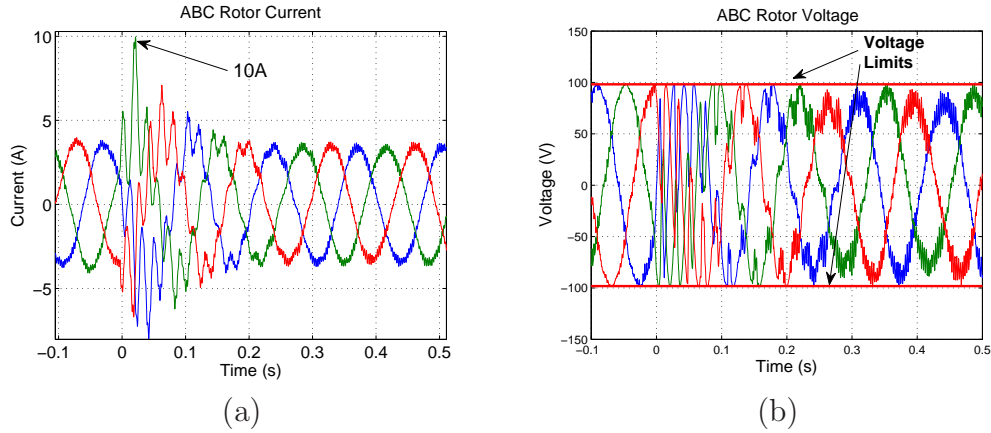


Figure 3.30: Experimental result of the TUDb, 1725 RPM,  $V_{dc} = 170V$ :

- (a) - Rotor currents;
- (b) - Rotor Voltages.

### 3.3.6 Rotor currents excursion

In the previous subsections the transient behavior of the rotor voltage and current were analyzed in different operation conditions. Here the amplitude behavior of such variables varying with the speed is shown in Figures 3.31 (a) and (b). These graphs were obtained with the machine controlled following the MPPT curve. Furthermore, in order to avoid high rotor currents, immediately after the sag the stator active power reference was decreased to zero.

For the TUDb it is shown the result of the 85% voltage sag and for UFMGb three sags are evaluated: 80%, 50% and 20%. Through Figures 3.31 (a) and (b) it is seen the increasing of the maximum rotor current with the speed increasing, because of the increasing in the generated power.

For the UFMGb (Figure 3.31(b)) the increase of rotor currents with the increasing of the voltage sag depth is demonstrated. Unfortunately it was not possible to complete the entire curves for all speeds, because currents above 70A causes the trip of the converter protection. The curves are not equally separated from each other, because, as stated previously, changing the voltage sag also change the ISG behavior. Nevertheless, the arising of high currents is clearly seen, therefore strategies to avoid them are necessary.

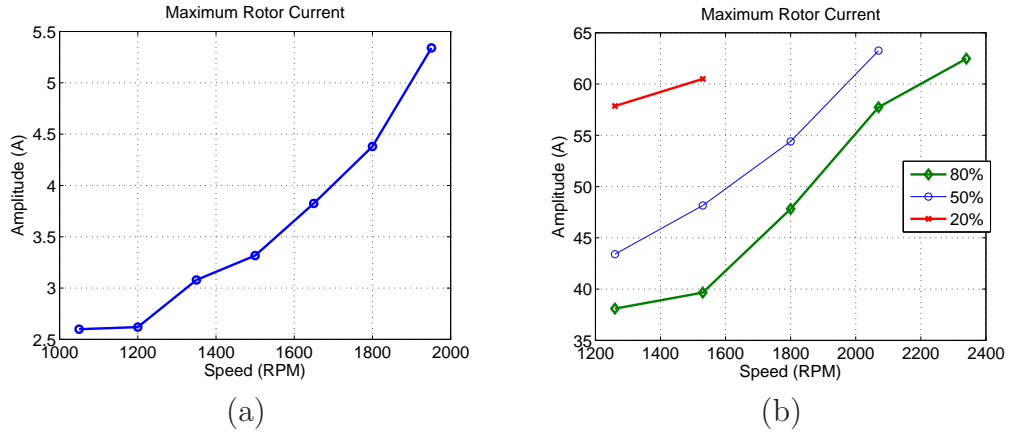


Figure 3.31: Maximum rotor currents:  
 (a) - TUD test bench (85% three-phase voltage sag);  
 (b) - UFMG test bench.

### 3.4 Simulation Results

In the previous section the experimental results were presented and analyzed. These results were obtained in small scales test benches, therefore to extrapolate the results for a high power WECS the simulation model is used. It is important to mention that the objective here is not prove the validity of the simulation model, but to show the difference between the responses of the low and high power WECS.

In the simulation of the 2MW system a 50% three-phase voltage sag was tested with the machine operating at rated power (1950RPM). First the control is adjusted with a bandwidth approximately 400Hz, in such a way that the voltage is lagging  $180^\circ$  the current in 50Hz, i.e., the flux damping is not changed when compared with the open rotor case.

Figure 3.32 shows the dq rotor currents simulated and calculated using Equations 3.48 to 3.51. The results calculated and simulated are in good agreement presenting a small difference in the damping. As already stated in the open rotor analysis, it is seen that the natural component damping in the 2 MW system is much smaller than in the test bench, so the rotor currents oscillate for longer time, reflecting in torque and power oscillations.

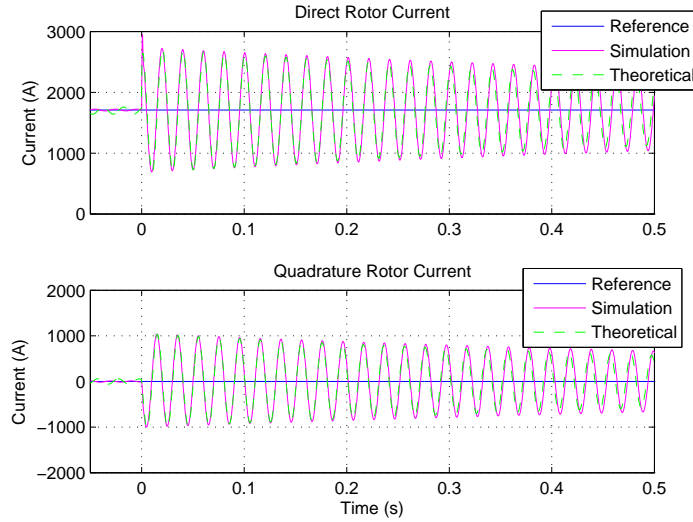


Figure 3.32: Simulation results of the dq rotor currents (1950 RPM,  $K_p = 0.26\Omega$  and  $K_i = 1.36\Omega/s$ ).

Figure 3.33 depicts the rotor currents when the control bandwidth is reduced to 80Hz. It is seen that the flux damping is increased, but on the other hand the rotor currents in beginning of the sag suffers a considerable increment. The theoretical result differs a little more from the simulation, but the maximum current and the damping are still well approximated.

Setting again the controller gains for its normal values, Figure 3.34 shows the simulation result for a 50% three-phase voltage sag with 1s duration. In this figure the sag recovering instant is presented, showing that in this moment natural component also arise, as stated before.

In Figure 3.34 comparing the maximum rotor current when the voltage drops and rise, one can notice that the voltage recovering is worse for the system. This fact occurs, because in spite of being the natural component equal, the forced component is obviously higher after the voltage sag end than during the sag.

These results show that studies of voltage sags carried out in small scale test rigs can be used for the analysis, but the difference in the stator time constants should be considered. This remark is important mainly when developing ride-through strategies. None of the papers investigated in the recent literature considers this fact.

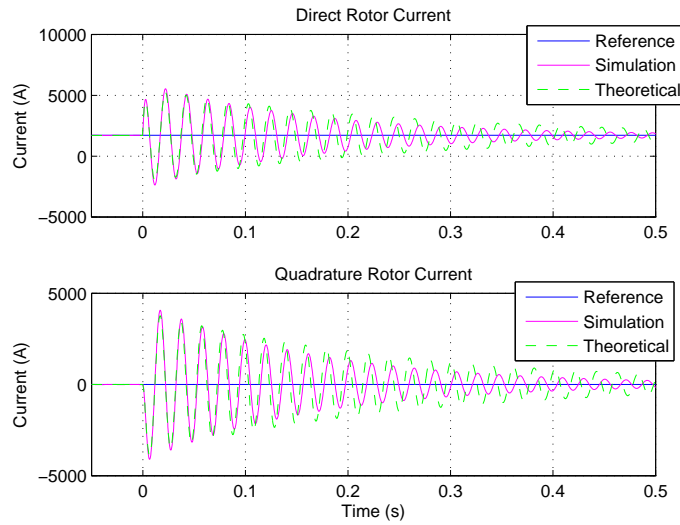


Figure 3.33: Simulation results of the dq rotor currents (1950 RPM,  $K_p = 0.053\Omega$  and  $K_i = 0.27\Omega/s$ ).

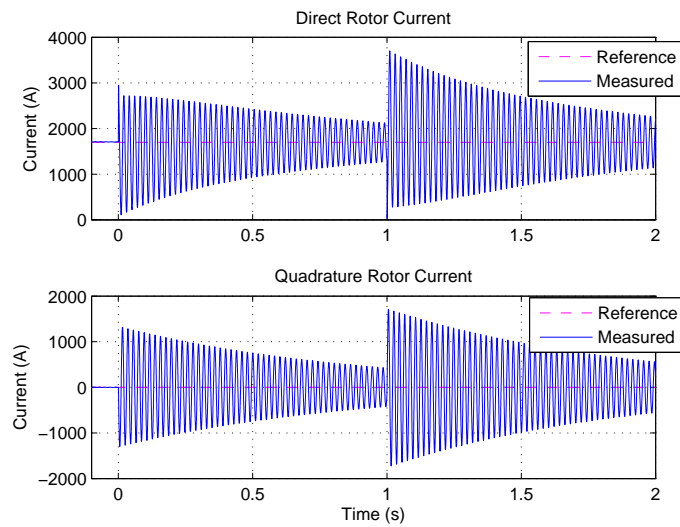


Figure 3.34: Simulation results of the dq rotor currents (1950 RPM,  $K_p = 0.26\Omega$  and  $K_i = 1.36\Omega/s$ ).

## 3.5 Final Considerations

In this chapter the behavior of the DFIG technology during balanced voltage sags was analyzed. The theoretical analysis and the experimental

and simulation results show that, during balanced voltage sags, the natural stator flux linkage induces high rotor voltages and currents. The natural component causes torque and power oscillations that are prejudicial to the system. Furthermore, the high voltage and currents are harmful for the converter, because the IGBT's heating is increased.

It was demonstrated through the mathematical modeling that the rotor current control tuning affects the damping of the stator flux linkage natural component. Therefore, the natural component in the rotor voltages and currents are also affected increasing or decreasing the electrical and mechanical stresses, depending on the control action. This fact was proved through the experimental and simulation results.

The flux damping is also dependent on the stator time constant. The comparison between the simulation and experimental results evidences that in high power systems the damping is smaller, because higher the generator rated power smaller the stator resistance and higher the time constant. This remark is important when analyzing the results of scaled small power test benches.

Another fact that affects the electrical and mechanical stresses of the system is the converter voltage capability. If the voltage command set by the controller is not imposed by the converter, that is, the voltage control output saturates, the amplitude of the rotor currents will be high and may destroy the converter. To avoid the damage of the converters it is necessary to implement ride-through strategies. In Chapter 5 new strategies to improve the behavior of the DFIG during balanced voltage sags are proposed.

# DFIG Behavior During Unbalanced Voltage Sags

---

## 4.1 Introduction

The previous chapter analyzed the behavior of the doubly-fed induction generator during balanced voltage sags. In the present chapter, the unbalanced voltage sags case is scrutinized. Actually, this type of voltage sag represents 90% of all voltage dips (Bollen, 2000), therefore it is important to analyze the DFIG behavior for this situation.

Most of the grid codes do not distinguish the system RTFC requirements between symmetrical and asymmetrical faults, but some of them require the injection of reactive power for voltage support during voltage dips. Furthermore, generated power quality restrictions are mandatory (ONS, 2009a), (E.ON, 2006). Therefore, the analysis carried out in this chapter is important in order to develop strategies to improve system RTFC.

Similar to the balanced case analysis, first the mathematical modeling is developed and after the experimental and simulation results are presented and analyzed.

## 4.2 Mathematical Modeling

In order to develop the mathematical analysis of the DFIG during asymmetrical voltage sags, as previously, the analysis in the time domain and in the Laplace domain are carried out.

### 4.2.1 Time domain model

Balanced three-phase systems have only positive sequence component, whereas during voltage unbalances negative sequence components also arise (Bollen, 2000). Thus, for the temporal analysis, the symmetrical components theory is employed (Wagner and Evans, 1933) in such a way that the variables can be divided in positive, negative and zero sequence. The stator variables can be represented by:

$$\vec{A}_s = \vec{A}_0 + \vec{A}_+ e^{j\omega_s t} + \vec{A}_- e^{-j\omega_s t}, \quad (4.1)$$

where  $A_s$  represents a generic stator variable ( $v_s, i_s, \psi_s$ ), the subscripts +, - and 0 are, respectively, the positive, negative and zero sequence components. Analogously, the rotor variables can be calculated through:

$$\vec{A}_r = \vec{A}_0 + \vec{A}_+ e^{j\omega_{r+} t} + \vec{A}_- e^{j\omega_{r-} t}, \quad (4.2)$$

where  $\omega_{r+} = \omega_s - \omega$  and  $\omega_{r-} = -\omega_s - \omega$  are the angular frequency of the rotor currents due to the positive and negative sequences, respectively.

Using Fortescue Transform (Fortescue, 1918), the sequence components are calculated through:

$$\begin{bmatrix} \vec{A}_+ \\ \vec{A}_- \\ \vec{A}_0 \end{bmatrix} = \frac{1}{3} \begin{bmatrix} 1 & a & a^2 \\ 1 & a^2 & a \\ 1 & 1 & 1 \end{bmatrix} \begin{bmatrix} \vec{A}_a \\ \vec{A}_b \\ \vec{A}_c \end{bmatrix}, \quad (4.3)$$

with  $a = e^{j\frac{2\pi}{3}}$ .

Using Equations 4.1 and 4.2, the equations of induction machines can also be divided in positive and negative sequence. These equations in the fixed stator reference frame are given by:

$$\vec{v}_{s\pm} = R_s \vec{i}_{s\pm} + \frac{d\vec{\psi}_{s\pm}}{dt}, \quad (4.4)$$



$$\vec{v}_{r\pm} = R_r \vec{i}_{r\pm} + \frac{d\vec{\psi}_{r\pm}}{dt} - j\omega \vec{\psi}_{r\pm}, \quad (4.5)$$

$$\vec{\psi}_{s\pm} = L_s \vec{i}_{s\pm} + L_m \vec{i}_{r\pm}, \quad (4.6)$$

$$\vec{\psi}_{r\pm} = L_r \vec{i}_{r\pm} + L_m \vec{i}_{s\pm}, \quad (4.7)$$

Considering a machine with symmetric impedances, the positive and negative components produce fluxes that rotate in opposition to each other, whereas the zero component does not produce flux (López et al., 2008a). The stator flux during the sag is given by the positive and negative sequences of the forced response plus the natural component induced during the voltage transient, as stated for the symmetrical case:

$$\vec{\psi}_s = \vec{\psi}_{s+} + \vec{\psi}_{s-} + \vec{\psi}_{s_n}. \quad (4.8)$$

The stator flux linkage components induce correspondent rotor voltage components:

$$\vec{v}_r = \vec{v}_{r+} + \vec{v}_{r-} + \vec{v}_{r_n}. \quad (4.9)$$

As in the balanced case and based in López et al. (2008a), the first approximation adopted is to analyze the open rotor circuit case. Before starting the development, it is important to highlight that the transient component, which depends on the ISG and was modeled for the symmetrical case, is neglected in the present modeling, because the main component is the negative sequence, as shown during the development.

### 4.2.2 Open rotor circuit analysis in time domain

Considering that before the voltage sag the machine is in steady state and the stator resistance is negligible, the stator flux linkage symmetric components during the sag are given by:

$$\vec{\psi}_{s+} = \frac{V_+ e^{j\omega_s t}}{j\omega_s}. \quad (4.10)$$

$$\vec{\psi}_{s-} = -\frac{V_- e^{-j\omega_s t}}{j\omega_s}. \quad (4.11)$$

Through these equations one can notice that the positive and negative sequence vectors of the flux rotate in opposition to each other in such a way that twice per period the flux components are aligned in the same direction and twice are aligned but in opposition. If in the instant of the sag beginning the latter condition occurs, there is no natural component induced, whereas for the first condition the maximum natural component appears and it is calculated through:

$$\vec{\psi}_{s_n} = \frac{(V_1 - V_+ - V_-)}{j\omega_s} e^{-t/\tau_s}, \quad (4.12)$$

remembering that  $V_1$  is the stator voltage before the sag.

Considering phase-neutral voltage sags, Figures 4.1 (a) and (b) show the complex diagram of the stator flux linkage for both cases described earlier. It is noticeable that, for this kind of sag, the maximum natural component appears when in the instant of the sag entry the stator voltage vector is passing for a zero ( $\theta_0 = 0^\circ$ ). When the stator voltage vector is passing for a maximum ( $\theta_0 = 90^\circ$ ) there is no natural component. The stator flux behavior for the phase-phase voltage sags is similar.

Figure 4.1(a) shows that in the case without natural component immediately after the sag entry the stator flux vector leaves its circular trajectory and change to a elliptical trajectory, evidencing the counter-rotating behavior of the negative and positive sequences. Figure 4.1(b) depicts the natural component decay before the flux reaches its steady-state during the sag.

Similarly to the balanced case, the rotor voltage positive and negative components can be calculated through:

$$v_{r+}^r = \frac{L_m}{L_s} s_{lip} V_+ e^{j\omega_{r+} t}, \quad (4.13)$$

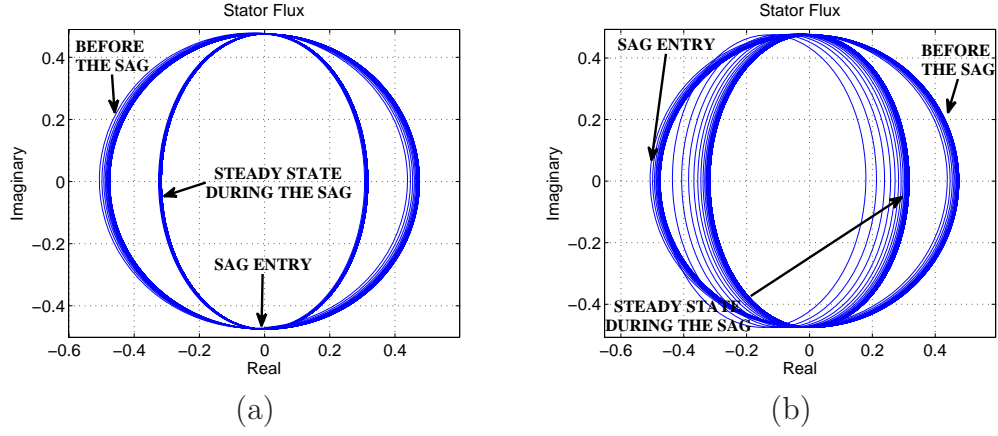


Figure 4.1: Stator flux linkage during a 50% phase-neutral voltage sag in the complex plane:

- (a) -  $\theta_0 = 90^\circ$  - no natural component;
- (b) -  $\theta_0 = 0^\circ$  - maximum natural component.

$$\vec{v}_{r-} = \frac{L_m}{L_s} (2 - slip) V_- e^{-j(2-slip)\omega_s t} = \frac{L_m}{L_s} (2 - slip) V_- e^{j\omega_{r-} t}. \quad (4.14)$$

Analyzing these equations it is seen that the amplitude of the positive sequence is proportional to the slip, therefore relatively small, and its angular frequency is also small. The negative sequence voltage includes a factor of 2, therefore can be high if the asymmetry is high. The frequency of the latter is almost twice the stator frequency, so it is high compared to the frequency of the positive sequence.

The maximum rotor voltage natural component, i.e., when in the instant of the sag entry the positive and negative components are aligned, is given by:

$$\vec{v}_{r_n} = -\frac{L_m}{L_s} \left( \frac{1}{\tau_s} + j\omega \right) \frac{V_1 - V_+ - V_-}{j\omega_s} e^{-t/\tau_s} e^{-j(\omega t - \pi/2)}. \quad (4.15)$$

Figures 4.2(a) and 4.3(a) show the open rotor experimental result for the TUDb for two sag instants entry. In the first graph there is no natural

component and during the sag is present a higher frequency due to the negative sequence and a smaller frequency due to the positive sequence. In the second graph the positive and negative sequences are also present, but now the natural component is superimposed. In the Figures 4.4(a) and 4.5(a) the results for the UFMGb are presented, showing the similar behavior.

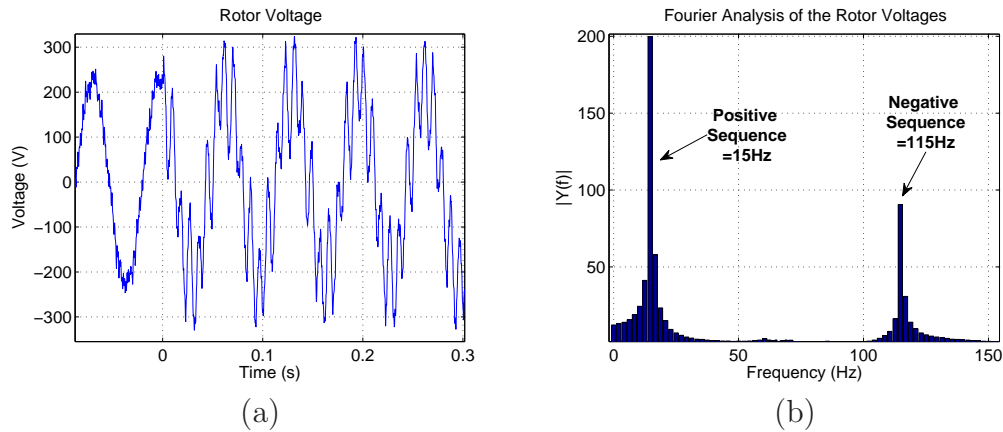


Figure 4.2: Open rotor experimental result for the TUDb with 90% phase-phase voltage sag,  $\theta_0 = 90^\circ$  and 1950 RPM:  
 (a) - Phase A of the rotor voltages;  
 (b) - Fourier analysis of the rotor voltages.

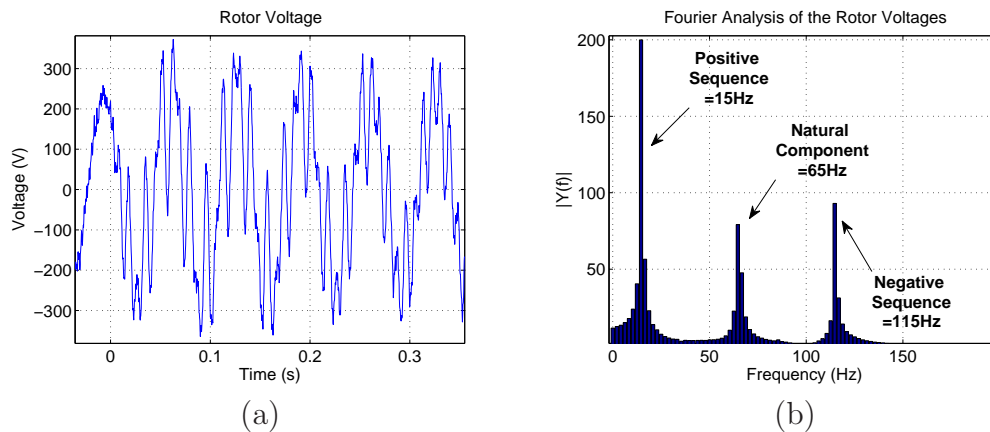


Figure 4.3: Open rotor experimental result for the TUDb with 90% phase-phase voltage sag,  $\theta_0 = 0^\circ$  and 1950 RPM:  
 (a) - Phase A of the rotor voltages;  
 (b) - Fourier analysis of the rotor voltages.

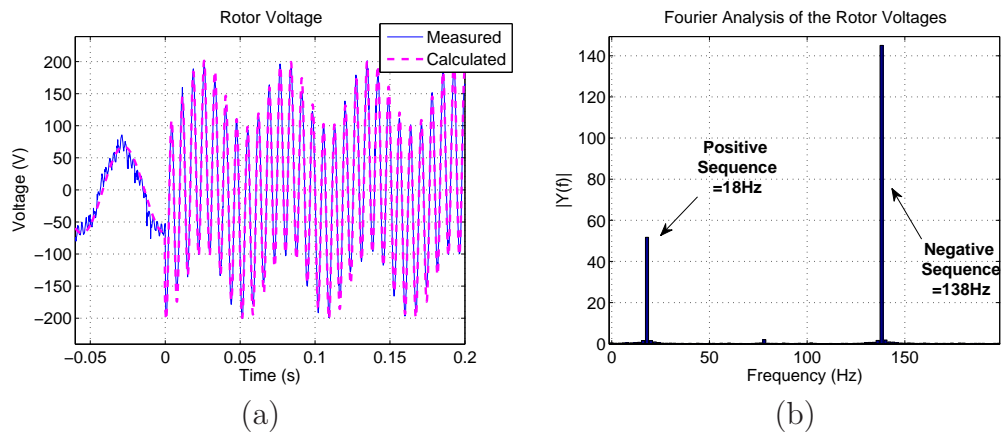


Figure 4.4: Open rotor experimental result for the UFMGb with 50% phase-phase voltage sag,  $\theta_0 = 90^0$  and 2340 RPM:  
 (a) - Phase A of the rotor voltages;  
 (b) - Fourier analysis of the rotor voltages.

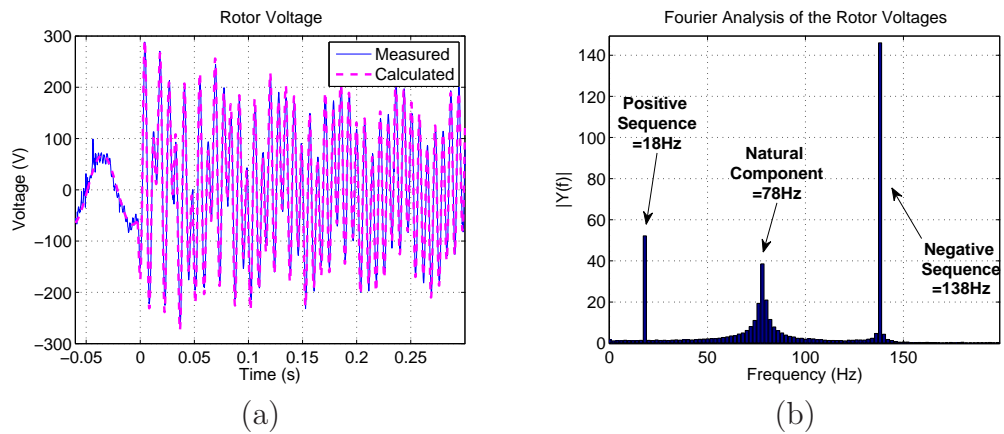


Figure 4.5: Open rotor experimental result for the UFMGb with 90% phase-phase voltage sag,  $\theta_0 = 0^0$  and 2340 RPM:  
 (a) - Phase A of the rotor voltages;  
 (b) - Fourier analysis of the rotor voltages.

In order to verify the presence of each component in the measured rotor voltages, the Fourier analysis of these voltages are shown in Figures 4.3(b), 4.4(b), 4.5(b) and 4.6(b). It is clearly seen the presence of three different frequency components:

- The positive sequence component has frequency equal to the rotor frequency ( $f_{r+} = f_s - f$ ). The amplitude of this component is constant and can be calculated similarly to the balanced case through:

$$|v_{r+\max}| = \frac{L_m}{L_s} |s_{lip}| V_+, \quad (4.16)$$

so it depends on the slip magnitude and the positive sequence stator voltage;

- The frequency of the negative sequence component is the machine electrical frequency plus the stator frequency ( $f_{r-} = f_s + f$ ). This component is present during all the sag with constant amplitude given by:

$$|v_{r-\max}| = \frac{L_m}{L_s} |(s_{lip} - 2) V_-|; \quad (4.17)$$

- The natural component is dependent on the sag entry instant. The frequency is always equal to the machine electrical frequency ( $f$ ). In the worst case, the maximum value of the natural component may be approximated by:

$$|v_{r_{n\max}}| = \frac{L_m}{L_s} |(1 - s_{lip}) (V_1 - V_+ - V_-)|, \quad (4.18)$$

and it happens in the sag beginning. Through Equation 4.18 one notice that the amplitude is proportional to the per unit machine speed and the stator voltage positive and negative sequences.

Figures 4.4(a) and 4.5(a) also present the theoretical result of the rotor voltage obtained from Equations 4.13, 4.14 and 4.15. The responses are in good agreement, proving the mathematical development.

In order to observe the behavior of the machine in different speeds, Figure 4.6 shows the maximum theoretical rotor voltages for different phase-to-phase voltage sag, without natural component. Since in the TUDb it is possible to test only one voltage depth, just the results for the UFMGb is shown. The theoretical points were obtained from Equations 4.16 and 4.17. One can notice that the calculated maximum voltages do not differs so much from the experimental results.

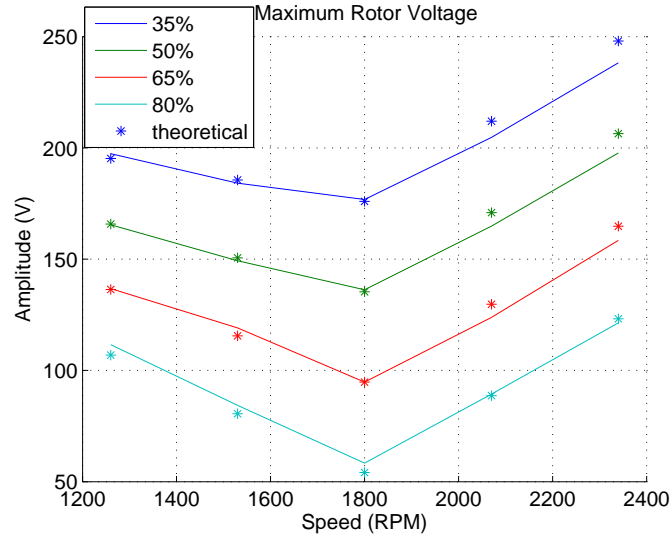


Figure 4.6: Maximum experimental and theoretical rotor voltage in the UFMGb for different phase-to-phase voltage sags in the case without natural component ( $\theta_0 = 90^0$ ).

The Figure 4.7 shows the maximum rotor voltages in the UFMGb for the case with the maximum natural component. The theoretical results were obtained from Equations 4.13, 4.14 and 4.15. Through Equations 4.16 to 4.18 it is possible to have an idea of the magnitude of the rotor voltage, but they cannot be summed directly, because the components are not in phase.

It is seen in Figure 4.6 that for small unbalances the rotor voltage depends approximately on the slip magnitude, because the response is dominated by the positive sequence (Equation 4.16). With the unbalance increasing, the negative sequence (Equation 4.18) becomes more significant and then there is higher voltages in the supersynchronous speeds. Through Figure 4.7 one can notice that, with the presence of the natural component, the rotor voltage increases dramatically. The curves show that, the higher the voltage unbalance, the higher is the dependence of the rotor voltage on the speed.

One can see that extremely high voltages may take place during the unbalanced voltage sags. These voltages may cause high rotor currents that could destroy the converter. It is important to highlight that the peak values shown in Figure 4.7 are transitory and vary depending on the sag entry instant, but the values shown in Figure 4.6 are present during all the sag.

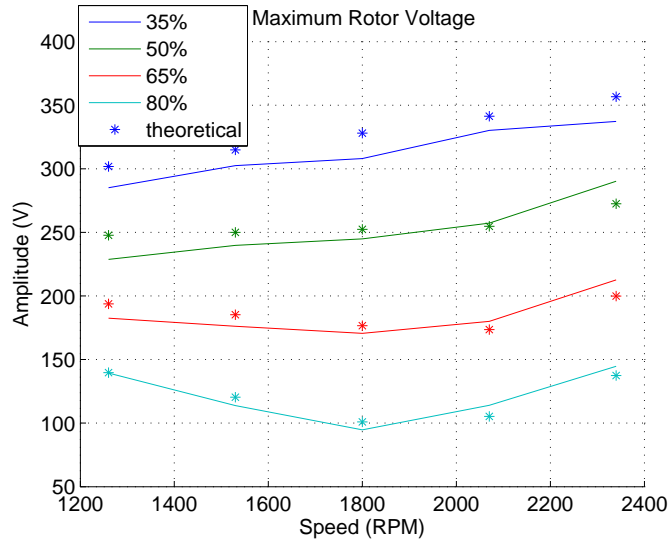


Figure 4.7: Maximum experimental and theoretical rotor voltage in the UFMGB for different phase-to-phase voltage sags in the case with the maximum natural component ( $\theta_0 = 0^0$ ).

### 4.2.3 Laplace domain model

For the Laplace domain modeling the induction motor equations in the synchronous reference frame are used, as in the previous chapter, but now the equations are divided in positive and negative sequence components (Wang et al., 2009):

$$\vec{v}_{s\pm} = R_s \vec{i}_{s\pm} + \frac{d\vec{\psi}_{s\pm}}{dt} \pm j\omega_s \vec{\psi}_{s\pm}, \quad (4.19)$$

$$\vec{v}_{r\pm} = R_r \vec{i}_{r\pm} + \frac{d\vec{\psi}_{r\pm}}{dt} + j\omega_{r\pm} \vec{\psi}_{r\pm}, \quad (4.20)$$

$$\vec{\psi}_{s\pm} = L_s \vec{i}_{s\pm} + L_m \vec{i}_{r\pm}, \quad (4.21)$$

$$\vec{\psi}_{r\pm} = L_r \vec{i}_{r\pm} + L_m \vec{i}_{s\pm}. \quad (4.22)$$



The positive and negative sequences differential equations are jointly represented in order to get a compact expression. The variables can be decomposed in dq components and expressed in terms of the positive and negative sequences in different reference frames in such a way that:

$$A_{dq}^+ = A_{dq+}^+ + A_{dq-}^+ = A_{dq+}^+ + A_{dq-}^- e^{-j2\omega_s t}. \quad (4.23)$$

It is important to clarify the notation utilized. The superscript indicates the reference frame of the variable and the subscript represents the component. For example: the variable  $A_{d-}^+$  represents the direct negative sequence component referred to the frame which rotates with the positive synchronous angular frequency ( $\omega_s$  for the stator variables and  $\omega_{r+}$  for the rotor variables), whereas the  $A_{q+}^-$  variable represents the quadrature positive sequence component referred to the frame which rotates with the negative synchronous angular frequency ( $-\omega_s$  and  $\omega_{r-}$ ).

With the equations decomposed in positive and negative sequences and in dq components, applying the Laplace Transform in Equations 4.19 to 4.22, yields:

$$V_{sd\pm}^\pm = R_s I_{sd\pm}^\pm + s\psi_{sd\pm}^\pm \mp \omega_s \psi_{sq\pm}^\pm, \quad (4.24)$$

$$V_{sq\pm}^\pm = R_s I_{sq\pm}^\pm + s\psi_{sq\pm}^\pm \pm \omega_s \psi_{sd\pm}^\pm, \quad (4.25)$$

$$V_{rd\pm}^\pm = R_r I_{rd\pm}^\pm + s\psi_{rd\pm}^\pm - \omega_{r\pm} \psi_{rq\pm}^\pm, \quad (4.26)$$

$$V_{rq\pm}^\pm = R_r I_{rq\pm}^\pm + s\psi_{rq\pm}^\pm + \omega_{r\pm} \psi_{rd\pm}^\pm, \quad (4.27)$$

$$\psi_{sd\pm}^\pm = L_s I_{sd\pm}^\pm + L_m I_{rd\pm}^\pm, \quad (4.28)$$

$$\psi_{sq\pm}^\pm = L_s I_{sq\pm}^\pm + L_m I_{rq\pm}^\pm, \quad (4.29)$$

$$\psi_{rd\pm}^{\pm} = L_r I_{rd\pm}^{\pm} + L_m I_{sd\pm}^{\pm}, \quad (4.30)$$

$$\psi_{rq\pm}^{\pm} = L_r I_{rq\pm}^{\pm} + L_m I_{sq\pm}^{\pm}, \quad (4.31)$$

where the dependence “(s)” was omitted to simplify the notation.

Proceeding in the same way as in the balanced analysis, the stator flux components are expressed as:

$$\psi_{sd\pm}^{\pm}(s) = \frac{(s + 1/\tau_s)}{\left(s^2 + 2\frac{1}{\tau_s}s + \omega_s^2\right)} V_{sd\pm}^{\pm}(s) + \frac{L_m/\tau_s (s + 1/\tau_s)}{\left(s^2 + 2\frac{1}{\tau_s}s + \omega_s^2\right)} I_{rd\pm}^{\pm}(s), \quad (4.32)$$

$$\psi_{sq\pm}^{\pm}(s) = \frac{\mp\omega_s}{\left(s^2 + 2\frac{1}{\tau_s}s + \omega_s^2\right)} V_{sd\pm}^{\pm}(s) + \frac{L_m/\tau_s (s + 1/\tau_s)}{\left(s^2 + 2\frac{1}{\tau_s}s + \omega_s^2\right)} I_{rq\pm}^{\pm}(s). \quad (4.33)$$

Through Equations 4.32 and 4.33 it is possible to see that the dynamic behavior of the positive and negative sequences of stator flux linkage components are similar, but, as already shown, they rotate in opposition to each other. In the following subsection the open rotor analysis for the Laplace domain is analyzed.

#### 4.2.4 Open rotor circuit analysis in Laplace domain

Using Equations 4.28 to 4.32 in 4.26 and considering the rotor current equal to zero, the direct rotor voltage sequence components are given by:

$$V_{rd\pm}^{\pm}(s) = \frac{L_m}{L_s} \left( \frac{s^2 + \frac{1}{\tau_s}s \pm \omega_{r\pm}\omega_s}{s^2 + 2\frac{1}{\tau_s}s + \omega_s^2} \right) V_{sd\pm}^{\pm}(s). \quad (4.34)$$

Similarly, the quadrature sequence components are:

$$V_{r_{q\pm}}^{\pm}(s) = \frac{L_m}{L_s} \left( \frac{(\omega_{r\pm} \mp \omega_s) s + \omega_{r\pm}/\tau_s}{s^2 + 2\frac{1}{\tau_s}s + \omega_s^2} \right) V_{s_{d\pm}}^{\pm}(s). \quad (4.35)$$

Using Equations 4.23, 4.34 and 4.35, the rotor voltages can be represented just in the synchronous positive reference frame:

$$V_{r_d}^+(s) = \frac{L_m}{L_s} \left( \frac{s^2 + \frac{1}{\tau_s}s \pm \omega_{r\pm}\omega_s}{s^2 + 2\frac{1}{\tau_s}s + \omega_s^2} \right) \left( V_{s_{d+}}^+ + e^{-j2\omega_s t} V_{s_{d-}}^- \right) (s), \quad (4.36)$$

$$V_{r_q}^+(s) = \frac{L_m}{L_s} \left( \frac{(\omega_{r\pm} \mp \omega_s) s + \omega_{r\pm}/\tau_s}{s^2 + 2\frac{1}{\tau_s}s + \omega_s^2} \right) \left( V_{s_{d+}}^+ + e^{-j2\omega_s t} V_{s_{d-}}^- \right) (s). \quad (4.37)$$

Equations 4.36 and 4.37 show that the induced rotor voltage depends on the direct stator voltage positive and negative sequences. In the positive synchronous frame the positive stator voltage induces a constant component in the rotor voltage, whereas the negative sequence induces an oscillatory component with angular frequency  $2\omega_s$ .

In these equations it is possible to see that the rotor voltage dynamics is represented by a second order transfer function with time constant equal  $\tau_s$  and frequency equal to  $\omega_s$ , as in the balanced case. Therefore, during a voltage transient, besides the positive and negative sequences, there is a natural component. If no negative sequence is present, these equations become the Equations 3.34 and 3.35 deduced in last chapter.

Instead of a deeper analysis of the open rotor case in the Laplace domain, more attention is given for the complete modeling presented in the next subsection.

### 4.2.5 Complete analysis in Laplace domain

As already developed for the balanced case, the rotor current in the synchronous positive reference frame can be calculated through:

$$I_{r_{dq}^+}^+(s) = \frac{1}{\sigma L_r s + R_r} \left( \frac{K_p s + K_i}{s} \right) \left( I_{r_{dq}^+}^{+*}(s) - I_{r_{dq}^+}^+(s) \right) - \frac{s(L_m/L_s)}{\sigma L_r s + R_r} \psi_{s_{dq}^+}^+(s). \quad (4.38)$$

The classical control of the DFIG generator is implemented only in the synchronous positive reference frame without any sequence decomposition. Therefore, the dq rotor currents used to feedback the control contain positive and negative sequences, both oriented in the positive reference frame. Through Equation 4.23 it is seen that the negative sequence oriented in the positive frame oscillates with angular frequency  $2\omega_s$ . Thereby, one of the objectives of the present modeling is to analyze the influence of the classical control on the negative sequence.

Rewriting Equation 4.38 and dividing the positive and negative sequence components, both oriented in the positive synchronous reference frame, yields:

$$I_{r_{dq+}^+}^+(s) = \frac{1}{\sigma L_r s + R_r} \left( \frac{K_p s + K_i}{s} \right) \left( I_{r_{dq+}^+}^{+*}(s) - I_{r_{dq+}^+}^+(s) \right) - \frac{s(L_m/L_s)}{\sigma L_r s + R_r} \psi_{s_{dq+}^+}^+(s), \quad (4.39)$$

$$I_{r_{dq-}^+}^+(s) = \frac{1}{\sigma L_r s + R_r} \left( \frac{K_p s + K_i}{s} \right) \left( I_{r_{dq-}^+}^{+*}(s) - I_{r_{dq-}^+}^+(s) \right) - \frac{s(L_m/L_s)}{\sigma L_r s + R_r} \psi_{s_{dq-}^+}^+(s). \quad (4.40)$$

Just the oscillatory response is analyzed, thus, the rotor current reference is set equal to zero in such a way that the rotor current sequence components are given by:

$$I_{r_{dq+}^+}^{+t}(s) = \frac{-s^2(L_m/L_s)}{\sigma L_r s^2 + (K_p + R_r)s + K_i} \psi_{s_{dq+}^+}^{+t}(s), \quad (4.41)$$

$$I_{r_{dq-}^+}^{+t}(s) = \frac{-s^2(L_m/L_s)}{\sigma L_r s^2 + (K_p + R_r)s + K_i} \psi_{s_{dq-}^+}^{+t}(s), \quad (4.42)$$

where the superscript “t” represents the transient or oscillatory response, that is, the natural component and the negative sequence.

The dq stator flux linkage positive sequence in the positive reference frame is given by Equations 4.32 and 4.33. The dq stator flux linkage negative sequence in the negative frame is also given in these equations. When the negative flux sequence is referred to the positive frame, the Equations 4.32 and 4.33 change. This occurs because the quadrature stator voltage negative sequence is not zero as in the balanced case. For a better understanding, Figure 4.8 shows the stator voltage components in different reference frames.

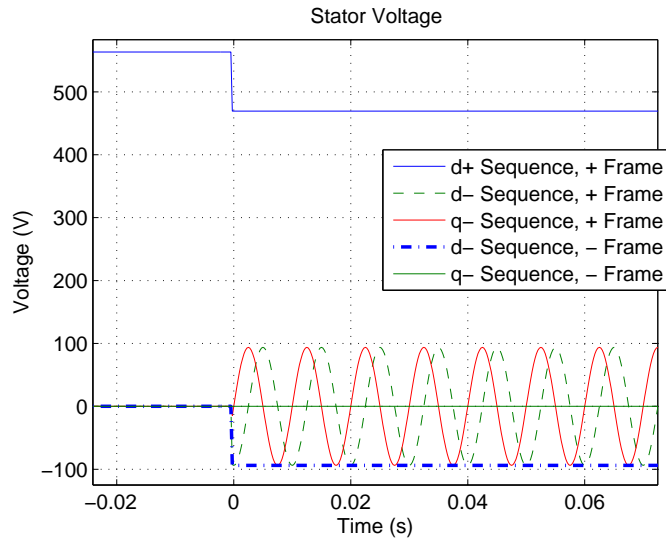


Figure 4.8: Simulated result of the stator voltage sequence components in different reference frames.

One can notice through Figure 4.8 that the stator voltage negative sequence components, when referred to positive reference frame, oscillate with twice the grid frequency, as already stated and mathematically demonstrated in Equation 4.23. Assuming nonzero quadrature components, the flux equations can be rewritten as:

$$\begin{aligned} \psi_{s_{d\pm}}^+(s) &= \frac{(s+1/\tau_s)}{(s^2+2\frac{1}{\tau_s}s+\omega_s^2)} V_{s_{d\pm}}^+(s) + \frac{\omega_s}{(s^2+2\frac{1}{\tau_s}s+\omega_s^2)} V_{s_{q\pm}}^+(s) \\ &\quad + \frac{L_m/\tau_s(s+1/\tau_s)}{(s^2+2\frac{1}{\tau_s}s+\omega_s^2)} I_{r_{d\pm}}^+(s) \end{aligned} \quad , \quad (4.43)$$

$$\begin{aligned} \psi_{s_{q\pm}}^+(s) &= \frac{-\omega_s}{(s^2+2\frac{1}{\tau_s}s+\omega_s^2)} V_{s_{d\pm}}^+(s) + \frac{(s+1/\tau_s)}{(s^2+2\frac{1}{\tau_s}s+\omega_s^2)} V_{s_{q\pm}}^+(s) \\ &\quad + \frac{L_m/\tau_s(s+1/\tau_s)}{(s^2+2\frac{1}{\tau_s}s+\omega_s^2)} I_{r_{q\pm}}^+(s) \end{aligned} \quad . \quad (4.44)$$

Substituting Equations 4.41 and 4.42 in 4.43 and 4.44, the complete stator flux linkage dq components are given by:

$$\begin{aligned} \psi_{s_d}^{+t}(s) &= \psi_{s_{d+}}^{+t}(s) + \psi_{s_{d-}}^+(s) \\ &= \frac{(s+1/\tau_s)(\sigma L_r s^2 + (K_p + R_r)s + K_i)}{(s^2+2\frac{1}{\tau_s}s+\omega_s^2)(\sigma L_r s^2 + (K_p + R_r)s + K_i) + \frac{1}{\tau_s} \frac{L_m^2}{L_s} s^2 (s + \frac{1}{\tau_s})} (V_{s_{d+}}^+ + V_{s_{d-}}^+)(s) \quad , \\ &\quad + \frac{\omega_s(\sigma L_r s^2 + (K_p + R_r)s + K_i)}{(s^2+2\frac{1}{\tau_s}s+\omega_s^2)(\sigma L_r s^2 + (K_p + R_r)s + K_i) + \frac{1}{\tau_s} \frac{L_m^2}{L_s} s^2 (s + \frac{1}{\tau_s})} V_{s_{q-}}^+(s) \end{aligned} \quad (4.45)$$

$$\begin{aligned} \psi_{s_q}^{+t}(s) &= \psi_{s_{q+}}^{+t}(s) + \psi_{s_{q-}}^+(s) \\ &= \frac{-\omega_s(\sigma L_r s^2 + (K_p + R_r)s + K_i)}{(s^2+2\frac{1}{\tau_s}s+\omega_s^2)(\sigma L_r s^2 + (K_p + R_r)s + K_i) + \frac{1}{\tau_s} \frac{L_m^2}{L_s} s^2 (s + \frac{1}{\tau_s})} (V_{s_{d+}}^+ - V_{s_{d-}}^+)(s) \quad . \\ &\quad + \frac{(s+1/\tau_s)(\sigma L_r s^2 + (K_p + R_r)s + K_i)}{(s^2+2\frac{1}{\tau_s}s+\omega_s^2)(\sigma L_r s^2 + (K_p + R_r)s + K_i) + \frac{1}{\tau_s} \frac{L_m^2}{L_s} s^2 (s + \frac{1}{\tau_s})} V_{s_{q-}}^+(s) \end{aligned} \quad (4.46)$$

Through these transfer functions, it is seen that the stator voltage positive sequence affects the flux exactly in the same way as calculated for the balanced case, but now the effect of the direct and quadrature negative sequence components of the stator voltage is present. These components have frequency equal to  $2\omega_s$ , causing oscillations in the this frequency in the stator flux linkage components. In the ABC stator flux these oscillations appear as an unbalance between the phases and induce oscillations in the rotor voltage, consequently in the rotor currents, electromagnetic torque and generated power.

Figure 4.9 shows the Bode diagram of the two transfer functions in Equation 4.43 with the 2-MW system parameters, evidencing the frequency of the negative component. Analyzing the Bode diagrams and the root locus (omitted) for different control adjustments, one can notice that the changing in the controller gains only affect a little the resonant frequency and the damping, as already stated for the symmetrical case. For acceptable PI gains the closed loop response evaluated in the negative sequence frequency ( $2\omega_s$ ) is not affected with the change in the gains. It is necessary too high gains, that is, large bandwidth for a significant changing in the rotor current negative sequence.

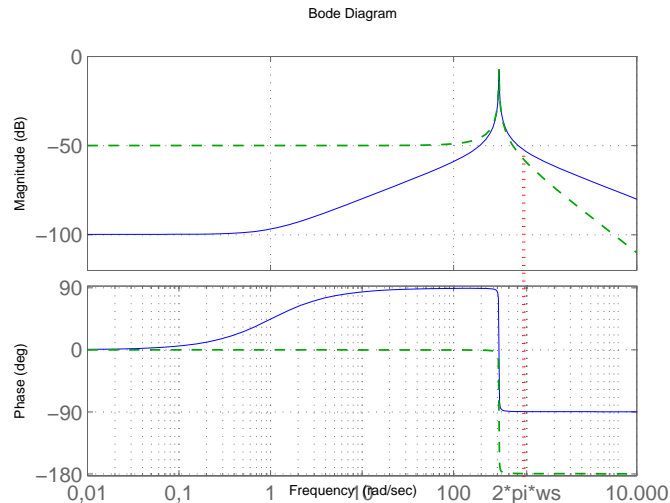


Figure 4.9: Bode diagram of the transfer functions in Equation 4.43 - direct voltage (continuous line) and quadrature voltage (dashed line). Parameters of the 2-MW system.

Although the stator flux is not changed with the control, it is possible to change the behavior of the rotor currents, consequently of the stator currents, the electromagnetic torque and the stator power. Using Equations 4.41, 4.42, 4.45 and 4.46, the rotor current is written as:

$$\begin{aligned}
I_{r_d}^{+t}(s) &= I_{r_{d+}}^{+t}(s) + I_{r_{d-}}^{+t}(s) \\
&= \frac{-s^2(L_m/L_s)(s+1/\tau_s)}{(s^2+2\frac{1}{\tau_s}s+\omega_s^2)(\sigma L_r s^2+(K_p+R_r)s+K_i)+\frac{1}{\tau_s}\frac{L_m^2}{L_s}s^2(s+\frac{1}{\tau_s})}(V_{s_{d+}}^{+t} + V_{s_{d-}}^{+t})(s) , \\
&+ \frac{-s^2(L_m/L_s)\omega_s}{(s^2+2\frac{1}{\tau_s}s+\omega_s^2)(\sigma L_r s^2+(K_p+R_r)s+K_i)+\frac{1}{\tau_s}\frac{L_m^2}{L_s}s^2(s+\frac{1}{\tau_s})}V_{s_{q-}}^{+t}(s)
\end{aligned} \tag{4.47}$$

$$\begin{aligned}
I_{r_q}^{+t}(s) &= I_{r_{q+}}^{+t}(s) + I_{r_{q-}}^{+t}(s) \\
&= \frac{s^2\omega_s(L_m/L_s)(s+1/\tau_s)}{(s^2+2\frac{1}{\tau_s}s+\omega_s^2)(\sigma L_r s^2+(K_p+R_r)s+K_i)+\frac{1}{\tau_s}\frac{L_m^2}{L_s}s^2(s+\frac{1}{\tau_s})}(V_{s_{q+}}^{+t} + V_{s_{q-}}^{+t})(s) . \\
&+ \frac{-s^2(L_m/L_s)(s+1/\tau_s)}{(s^2+2\frac{1}{\tau_s}s+\omega_s^2)(\sigma L_r s^2+(K_p+R_r)s+K_i)+\frac{1}{\tau_s}\frac{L_m^2}{L_s}s^2(s+\frac{1}{\tau_s})}V_{s_{q-}}^{+t}(s)
\end{aligned} \tag{4.48}$$

Figure 4.10 shows the Bode plot of the first transfer function in Equation 4.47 for different controller gains. It is seen that increasing the bandwidth of the controllers it is possible to reduce the effect of the negative sequence stator voltage in the rotor current, but for a small change in the answer it is necessary a high increase in the gains of a simple PI, what is most of the times unrealizable.

In order to increase the gain of the controllers in such a way that the negative sequence is controlled it is proposed in the literature the addition of a resonant part in the PI controller. Another strategy is the independent control of the rotor current negative sequence. These strategies are analyzed in the Chapter 6 using the mathematical equations developed here.



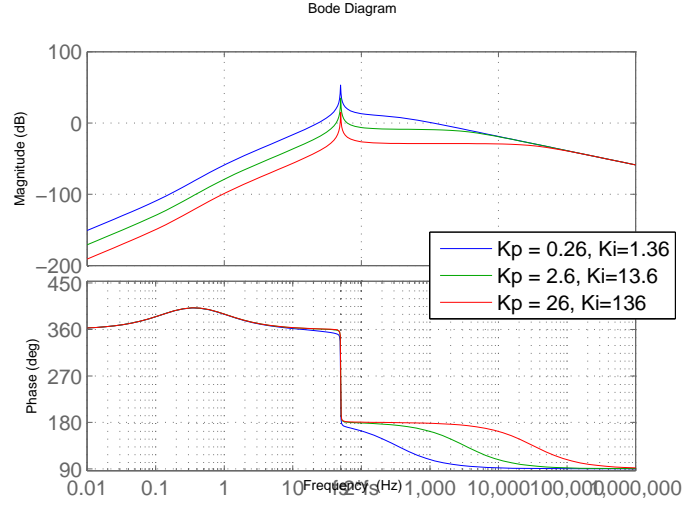


Figure 4.10: Bode diagram of the transfer functions 4.47 for different controller gains with the 2-MW system parameters.

## 4.3 Experimental Results

In the previous section the theoretical analysis was developed in order to understand the behavior of the DFIG during the unbalanced voltage sags. The comparison between the theoretical and the experimental results for the open rotor case has already been shown. In this section, the experimental results with the control of the rotor currents for different operating conditions are presented.

For all the tests described in the next subsections, similar conditions used for the balanced voltage sags case (Section 3.3) were considered.

### 4.3.1 Test 1: Slip = -0.15, maximum natural component ( $\theta_0 = 0^0$ )

For the first test both test benches are operating with a -0.15 slip (super-synchronous speed). The voltage sag entry instant was set in such a way that appears the maximum natural component ( $\theta_0 = 0^0$ ).

Figure 4.11 depicts one phase of the rotor currents, showing that in the instant of the voltage transient it is induced a natural component superimposed to the negative sequence component. The natural component behavior is similar to the balanced case and the decay depends on the control adjustment, as already stated, and reinforced in Equations 3.45 and 3.46. Changing the control gains, as in the previous chapter, the damping can also be changed. These results are not shown here, because the focus now is on the negative sequence. After the extinction of the natural component, it remains just the negative sequence component. This component is higher in the UFMGb, since the voltage unbalance tested is higher.

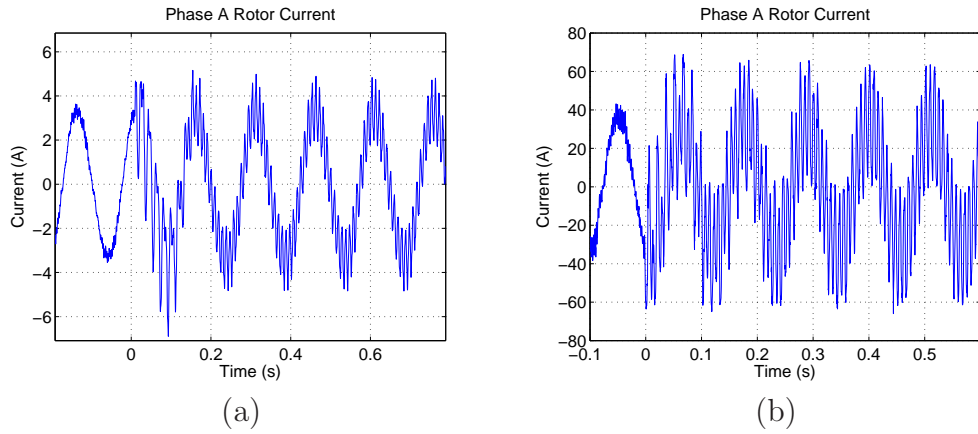


Figure 4.11: Experimental results of the phase A of the rotor currents for a slip =  $-0.15$ ,  $\theta_0 = 0^0$ :  
 (a) - TUD test bench (90% phase-to-phase voltage sag, 1725 RPM);  
 (b) - UFMG test bench (65% phase-to-phase voltage sag, 2070 RPM).

The Figure 4.12 shows the Fourier analysis of the rotor currents, evidencing the three components:

- Positive sequence which has the slip frequency ( $f_r$ );
- Natural component with frequency approximately  $f_s + f_r$ . The deviation from this frequency is due to the control action, as discussed in the last chapter;
- Negative sequence with  $2f_s$ . The control does not affect this component, because of the narrow bandwidth.

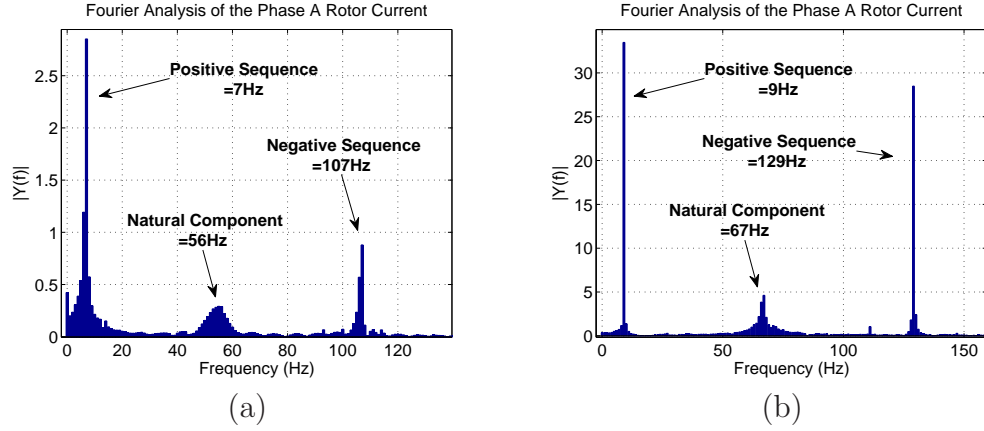


Figure 4.12: Fourier analysis of the rotor currents for a slip = -0.15,  $\theta_0 = 0^0$ :  
 (a) - TUD test bench (90% phase-to-phase voltage sag, 1725 RPM);  
 (b) - UFMG test bench (65% phase-to-phase voltage sag, 2070 RPM).

The behavior of the rotor current sequence components is also noticed when this variable is referred in the synchronous reference frame, as shown in Figure 4.13. One can notice that the mean value (positive sequence component) is well controlled, but neither the natural component nor the negative sequence are controlled.

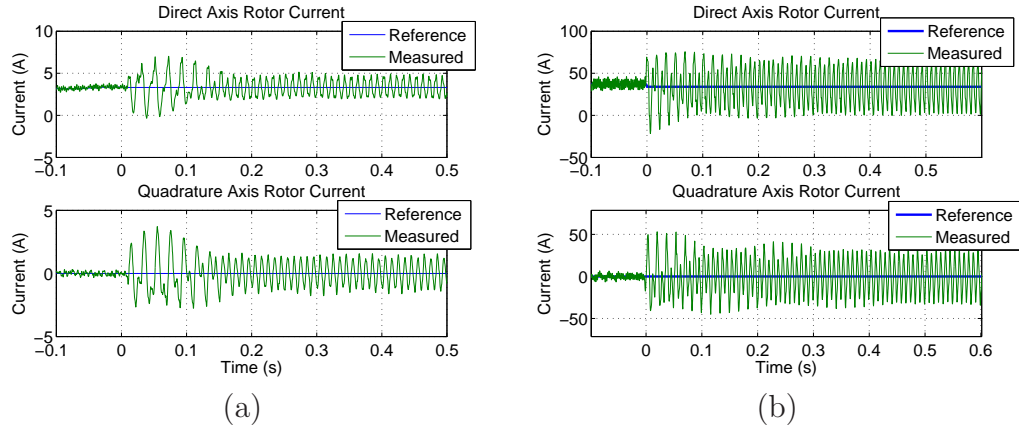


Figure 4.13: Experimental result of the dq rotor currents for a slip = -0.15,  $\theta_0 = 0^0$ :  
 (a) - TUD test bench (90% phase-to-phase voltage sag, 1725 RPM);  
 (b) - UFMG test bench (65% phase-to-phase voltage sag, 2070 RPM).

One phase of the voltages imposed by the RSC converter is illustrated in Figure 4.14, showing the voltage is below the converter voltage limits. If

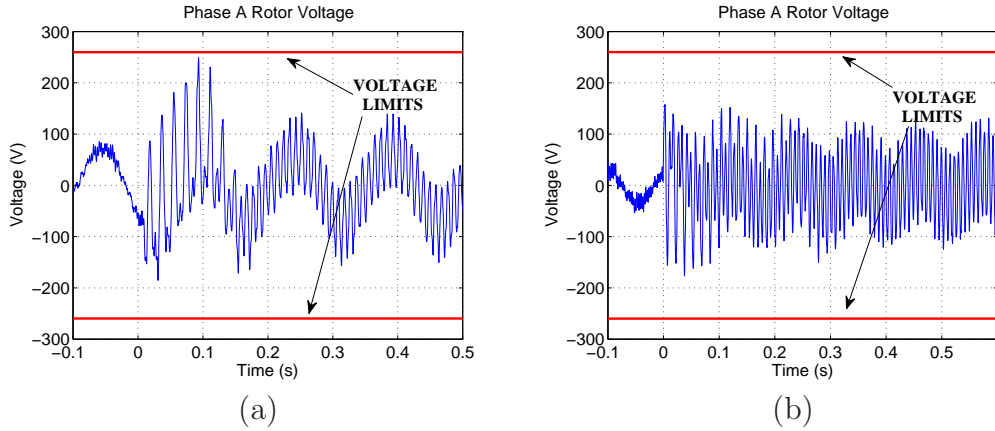


Figure 4.14: Experimental results of the phase A of the rotor voltages for a slip =  $-0.15$ ,  $\theta_0 = 0^0$ :  
 (a) - TUD test bench (90% phase-to-phase voltage sag, 1725 RPM);  
 (b) - UFMG test bench (65% phase-to-phase voltage sag, 2070 RPM).

the voltage limit is exceeded, the rotor current increasing may be higher.

The major drawback of the pulsation in the rotor currents is the increasing in their amplitude that can damage the converter. Furthermore, the pulsation in the electromagnetic torque (Figure 4.15) can be dangerous for the mechanical part and the oscillations in the stator power (Figure 4.16) degrade the system power quality, already degraded by the voltage dip.

The DC-link voltage tends to increase during the voltage sag and the natural component and negative sequence oscillations also affect this voltage. Figure 4.17(a) depicts the DC-link voltage in the TUDb, evidencing the oscillations which can also affect the harmonics in the grid and rotor currents. In this case the DC voltage does not increase, because the GSC control action is effective, as shown in Figure 4.18(a). In the UFMGb, the GSC current control saturate in the sag beginning (Figure 4.18(b)), therefore the DC-link voltage increases (Figure 4.17(b)).

In Figure 4.18 is evident that the classical control of the GSC cannot control the negative sequence of the currents. Thereby, ride-through strategies have to be employed not just in the RSC, but also in the GSC.

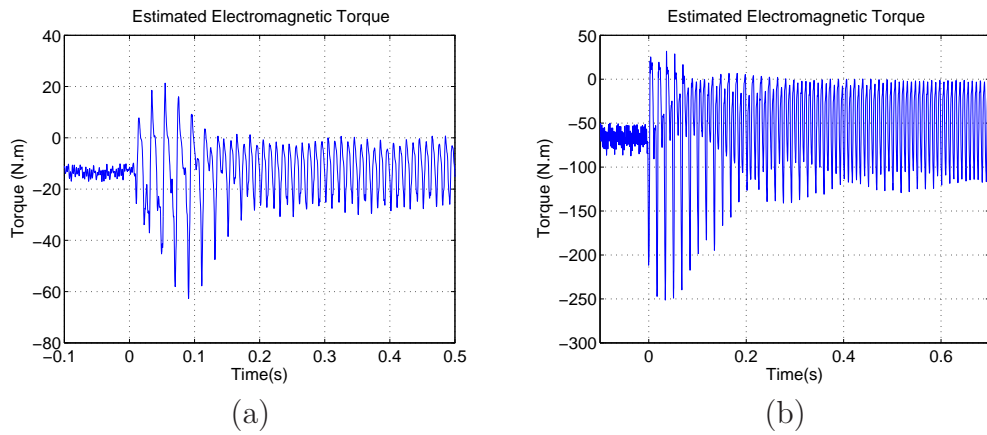


Figure 4.15: Experimental result of the estimated electromagnetic torque for a slip =  $-0.15$ ,  $\theta_0 = 0^0$ :  
 (a) - TUD test bench (90% phase-to-phase voltage sag, 1725 RPM);  
 (b) - UFMG test bench (65% phase-to-phase voltage sag, 2070 RPM).

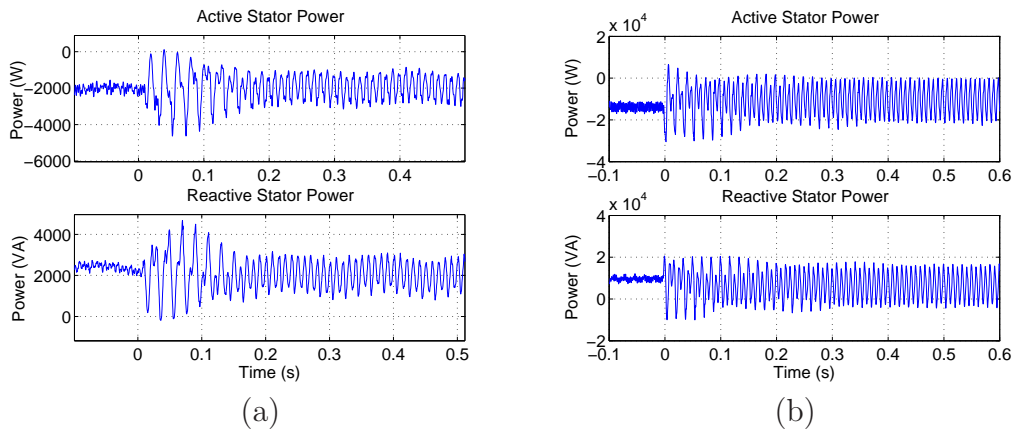


Figure 4.16: Experimental result of the active and reactive powers for a slip =  $-0.15$ ,  $\theta_0 = 0^0$ :  
 (a) - TUD test bench (90% phase-to-phase voltage sag, 1725 RPM);  
 (b) - UFMG test bench (65% phase-to-phase voltage sag, 2070 RPM).

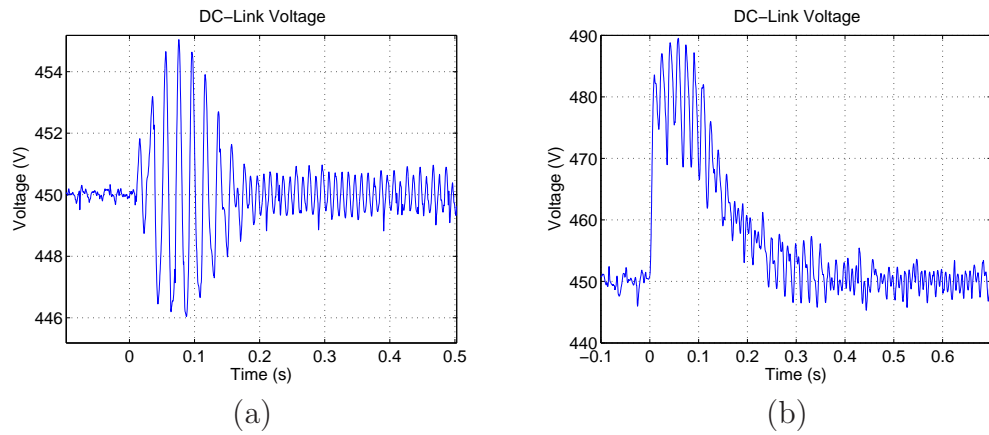


Figure 4.17: Experimental results of the DC-link voltage for a slip  $= -0.15$ ,  $\theta_0 = 0^0$ :  
 (a) - TUD test bench (90% phase-to-phase voltage sag, 1725 RPM);  
 (b) - UFMG test bench (65% phase-to-phase voltage sag, 2070 RPM).

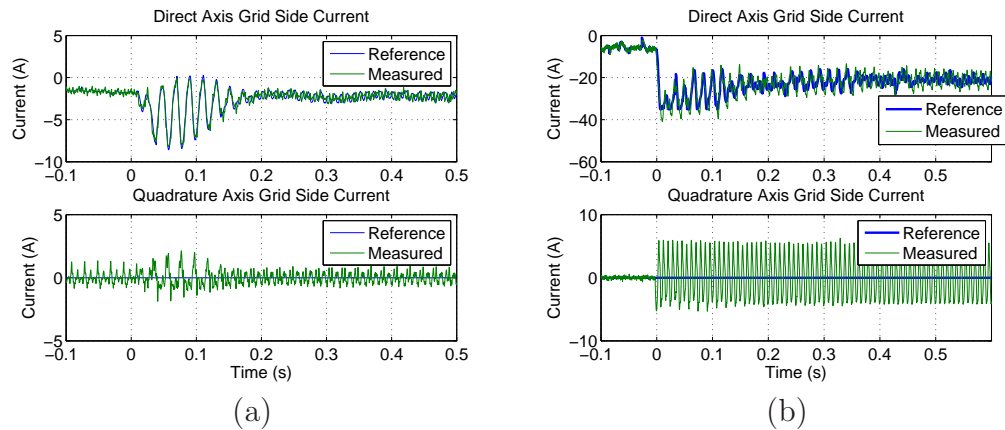


Figure 4.18: Experimental results of the dq GSC currents for slip  $= -0.15$ ,  $\theta_0 = 0^0$ :  
 (a) - TUD test bench (90% phase-to-phase voltage sag, 1725 RPM);  
 (b) - UFMG test bench (65% phase-to-phase voltage sag, 2070 RPM).

### 4.3.2 Test 2: Slip = +0.3, no natural component ( $\theta_0 = 90^\circ$ )

Changing the speed for the sub-synchronous region, Figure 4.19 shows the rotor currents in the case when there is no natural component. Without natural component the rotor currents are smaller than in the case with this component. The Fourier analysis of these currents are shown in Figure 4.20, evidencing the two components.

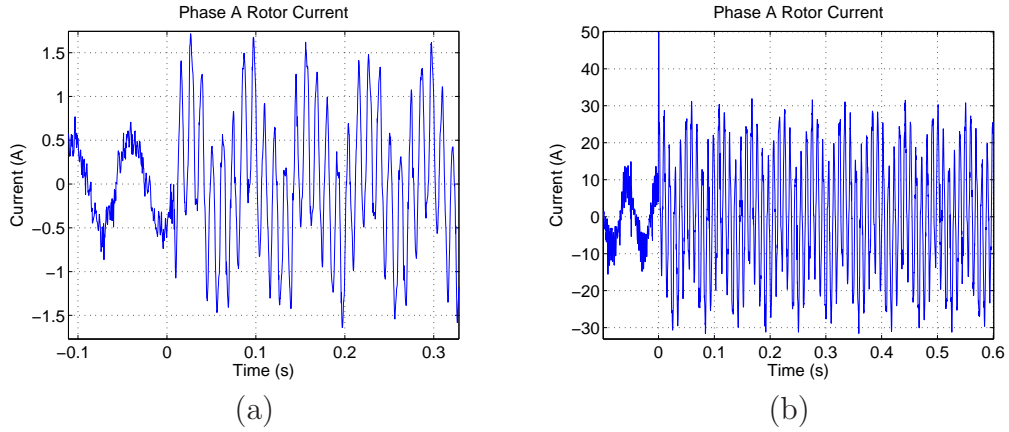


Figure 4.19: Experimental results of the phase A of the rotor currents for a slip = +0.3,  $\theta_0 = 90^\circ$ :  
 (a) - TUD test bench (90% phase-to-phase voltage sag, 1050 RPM);  
 (b) - UFMG test bench (65% phase-to-phase voltage sag, 1260 RPM).

Figure 4.21 shows the rotor currents in the synchronous reference frame. In this frame the oscillations due to the negative sequence is always equal to  $2f_s$ . One can see that the negative sequence is not controlled.

The electromagnetic torque, the active and reactive powers and DC-link behavior are similar to the previous case, but without the natural component. The graphs of these variables are omitted.

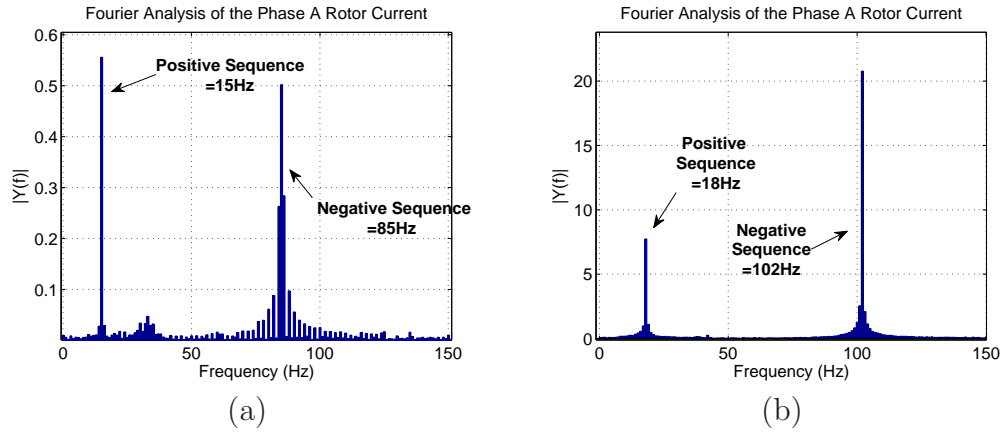


Figure 4.20: Fourier analysis of the rotor current for a slip = +0.3,  $\theta_0 = 90^\circ$ :  
 (a) - TUD test bench (90% phase-to-phase voltage sag, 1050 RPM);  
 (b) - UFMG test bench (65% phase-to-phase voltage sag, 1260 RPM).

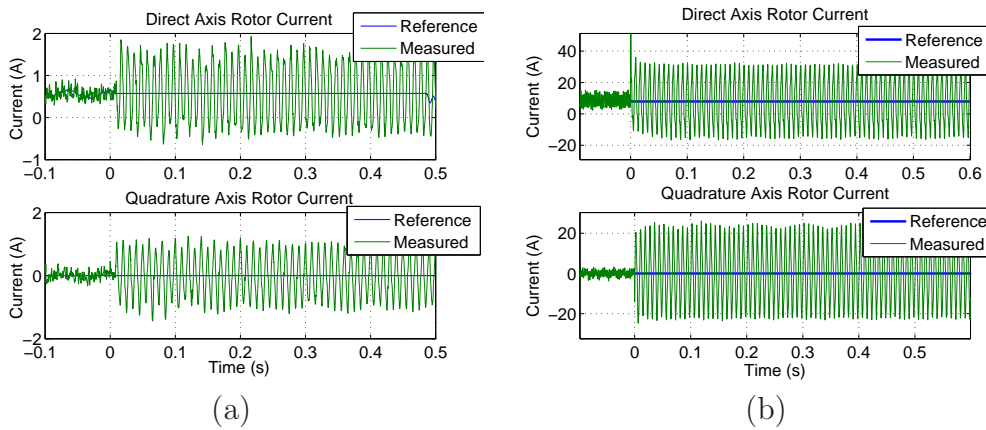


Figure 4.21: Experimental results of the dq rotor currents for a slip = +0.3,  $\theta_0 = 90^\circ$ :  
 (a) - TUD test bench (90% phase-to-phase voltage sag, 1050 RPM);  
 (b) - UFMG test bench (65% phase-to-phase voltage sag, 1260 RPM).



### 4.3.3 Test 3: synchronous speed - maximum natural component ( $\theta_0 = 0^0$ )

Testing the synchronous speed in such a way that the maximum natural component appears, Figure 4.22 shows the rotor currents and Figure 4.23 shows the Fourier analysis of these currents.

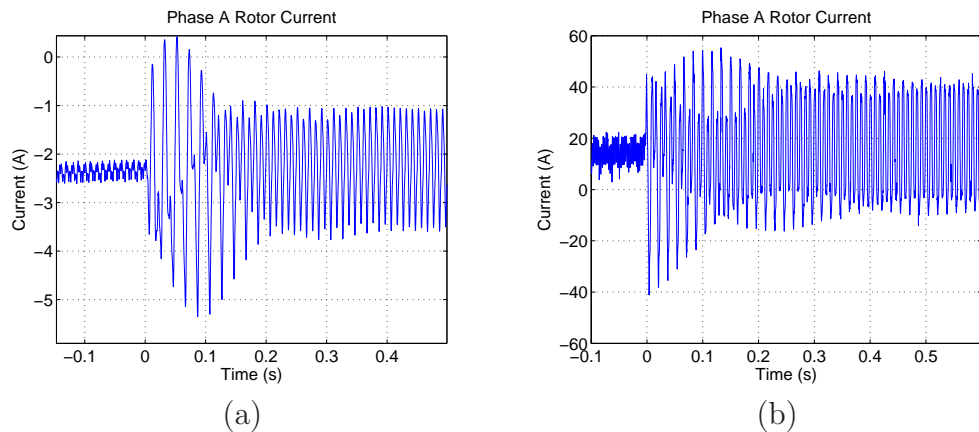


Figure 4.22: Experimental results of the phase A of the rotor currents at synchronous speed,  $\theta_0 = 0^0$ :  
 (a) - TUD test bench (90% phase-to-phase voltage sag, 1500 RPM);  
 (b) - UFMG test bench (65% phase-to-phase voltage sag, 1800 RPM).

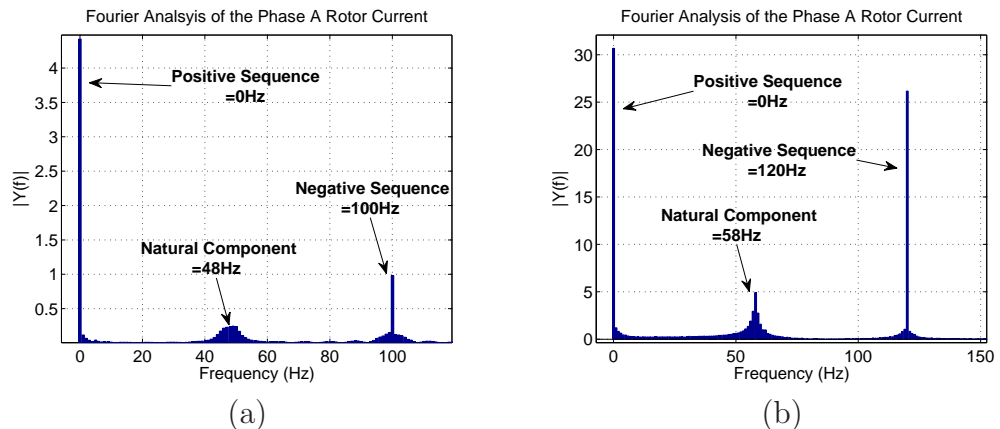


Figure 4.23: Fourier analysis of the rotor current at synchronous speed,  $\theta_0 = 0^0$ :  
 (a) - TUD test bench (90% phase-to-phase voltage sag, 1500 RPM);  
 (b) - UFMG test bench (65% phase-to-phase voltage sag, 1800 RPM).

One can notice that the frequency of the natural component and the negative sequence of the rotor currents change with the speed (slip). Thereby, it is necessary to develop control strategies effective for any slip. Fortunately, in the synchronous reference frame these components have constant frequencies. This fact will be helpful, as will be demonstrated in Chapter 6.

#### 4.3.4 Rotor voltage and current excursion

After showing separately the behavior of the DFIG during unbalanced voltage sags for different operating conditions, in this section the behavior of the rotor current and voltage using excursion charts is analyzed. Just the results for the UFMGb is shown, because in this test bench is possible to test different sag depths. The same strategy of reducing the active reference to zero, utilized in the balanced case is adopted here.

Figure 4.24(a) shows the behavior of the maximum rotor currents for the case without natural component and Figure 4.24(b) depicts the case with maximum natural component.

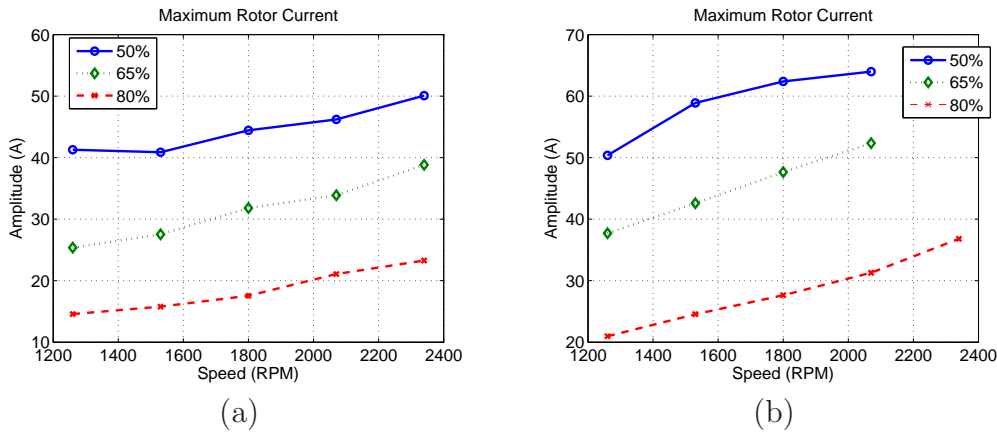


Figure 4.24: Experimental result of the maximum rotor currents for different speeds and voltage sags:  $\theta_0 = 90^0$ :

- (a) - no natural component  $\theta_0 = 90^0$ ;
- (b) - maximum natural component  $\theta_0 = 0^0$ .

One can notice that the rotor currents present a behavior almost linear with the increase of the speed. It is clearly seen that when the natural

component is induced, the rotor currents is much higher than in the other case. In this situation it is noticeable that is necessary to control both natural and negative sequence in order to improve the system behavior.

Figure 4.25 illustrates the maximum rotor voltages, showing both results without (a) and with (b) natural component. Comparing both graphs, it is noticed that in the latter case the rotor voltages are higher. These graphs are similar to the ones shown in Figures 4.6 and 4.7 for the open rotor case. Actually the open rotor voltage values differ from the case with the control just of the voltage drop in the rotor impedance, which generally is small.

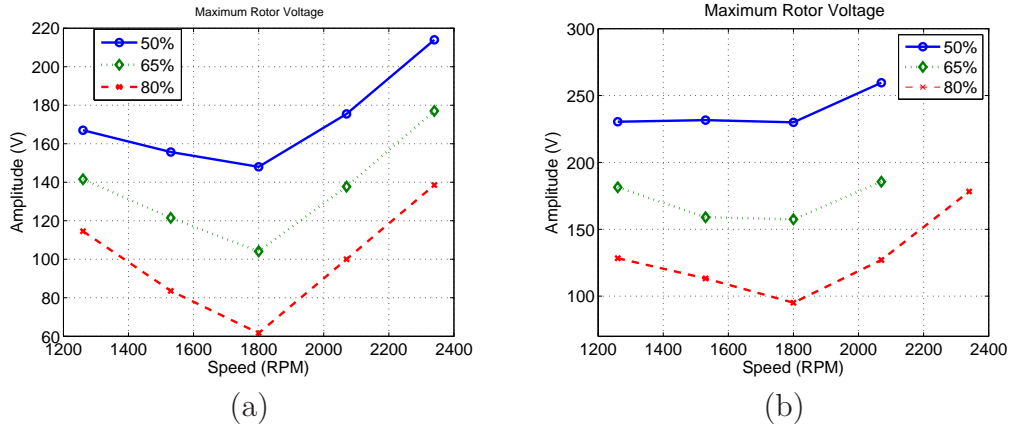


Figure 4.25: Experimental result of the maximum rotor voltages for different speeds and voltage sags:  $\theta_0 = 90^\circ$ :  
 (a) - no natural component  $\theta_0 = 90^\circ$ ;  
 (b) - maximum natural component  $\theta_0 = 0^\circ$ .

These graphs are useful for the obtainment of the ride-through capability of the system for the classical control strategy. One can see that even reducing the active power, in the 50% phase-to-phase sag the rotor currents reach values close to the nominal RSC current (62A). Deeper sags cannot be supported by the system, therefore with the classical control the system cannot comply with the grid codes (Figures 1.4 and 1.5). These curves will be used to compare with the results using the RTFC strategies, proposed in Chapter 6.

## 4.4 Simulation Results

In the simulation of the 2MW system it was tested a 50% phase-neutral voltage, considering the rated operation (1950 RPM). For sake of simplicity, just the dq rotor currents will be analyzed, because they are the most important variables in the RSC point of view and their shape reflect the behavior of other variables, as torque and power.

Figure 4.26(a) shows the rotor currents in the case without natural component. In these graphs it is seen just the positive sequence (constant value) and the negative sequence that oscillates with 100Hz ( $2f_s$ ). The negative sequence produces extremely high oscillatory currents, causing torque and power oscillations, as obtained in the experimental results. The rotor voltages also increase very much, therefore it is necessary a high DC-link voltage which sometimes is not possible.

Simulating the same conditions, but with the sag entry instant causing the highest natural component, Figure 4.26(b) shows the rotor currents. In this case the currents increase even more due to the natural component superimposed to the negative sequence. Due to the relatively high stator time constant in high power generators, the natural component decay is slower than the experimental results analyzed. This component increases the system electrical and mechanical stresses.

The experimental results just show the DFIG behavior in the the sag beginning. In order to analyze the system behavior during the voltage recovering, Figures 4.27 (a) and (b) depict the simulation results for a 50% phase-neutral voltage sag with approximately 0.2s duration. In both cases the sag entry was considered  $\theta_0 = 0^0$ , therefore during the sag there is just positive and negative sequences.

As in the sag beginning, the instant that the voltage rises back to its normal value influences the system behavior. In Figure 4.27(b) during the voltage sag recovering the maximum natural component is induced and the negative sequence disappears instantly after the sag. One can notice that depending on the sag depth, the recovering transient can be worse than the voltage drop transient. Figure 4.27(a) shows the case when no natural component is induced after the sag.

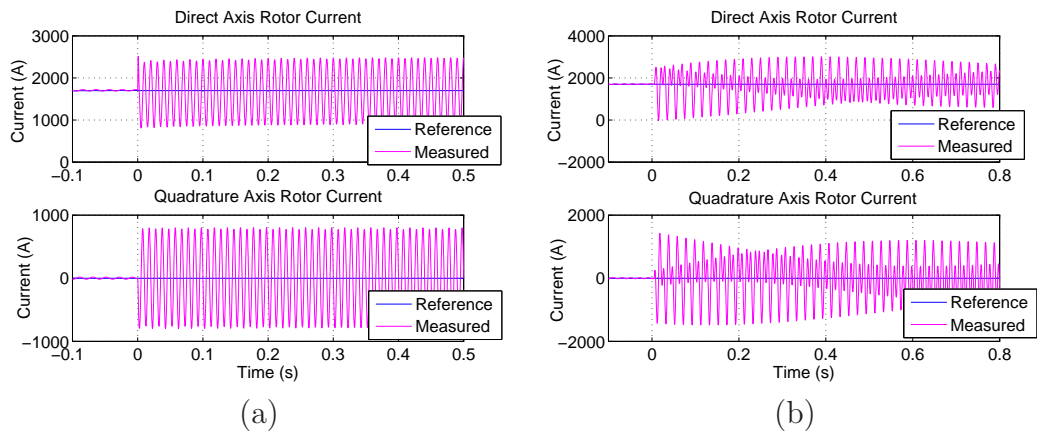


Figure 4.26: Simulation result of the dq rotor currents, 1950 RPM, 50% phase-neutral voltage sag:  
 (a) -  $\theta_0 = 90^\circ$  - no natural component;  
 (b) -  $\theta_0 = 0^\circ$  - maximum natural component.

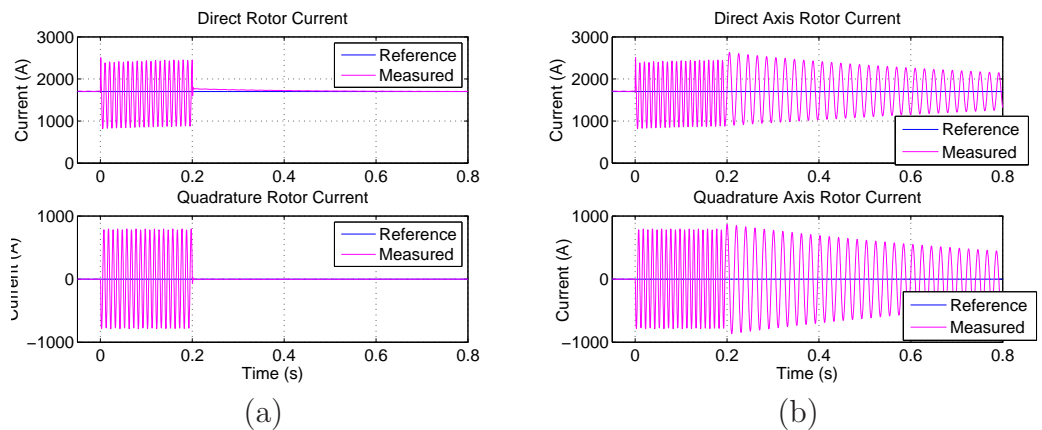


Figure 4.27: Simulation result of the dq rotor currents, 1950 RPM, 50% phase-neutral voltage sag, recovering instant:  
 (a) - no natural component;  
 (b) - maximum natural component.

Through Figure 4.27 one can see that during the voltage sag recovering transient is also necessary to implement ride-through strategies to avoid high rotor currents and voltages. In this moment the negative sequence disappears, but the natural component is still a problem.

## 4.5 Final Considerations

The theoretical analysis and the experimental results show that during unbalanced voltage sags, the stator flux linkage induces high rotor voltages and currents, due to the natural and negative sequence components. These components cause undesired torque and power oscillations. Furthermore, the high voltage and currents are harmful for the converter, because the IGBT's heating is increased.

In the simulation and experimental results it was demonstrated that high rotor currents take place during asymmetrical voltage sags. In the sag entry and also in recovering there are high rotor currents, thus, in order to avoid the damage of the converters it is necessary to implement ride-through strategies which are presented in the following chapters.

---

# **Ride-Through Strategies - Symmetrical Voltage Sags Case**

---

## **5.1 Introduction**

Several papers in the literature propose strategies to improve the DFIG ride-through fault capability during symmetrical voltage sags. Most of these strategies use passive solutions, as the crowbar and its variations (Lohde et al., 2007), (Anaya-Lara et al., 2008), (Zhang et al., 2010), (Morren and de Haan, 2005), (Ling et al., 2009), (Erlich et al., 2007), (Meegahapola et al., 2010), (Kasem et al., 2008), (Yang et al., 2009), (Rahimi and Parniani, 2010). In this work, alternative solutions using just control strategies are developed.

As shown in Chapter 3, during the balanced voltage sags the induced natural component causes two undesirable DFIG behaviors: high rotor currents and torque and power oscillations. In the present chapter, it is proposed a strategy to deal specifically with the natural component. The next chapter is dedicated to develop strategies for the general case, that is, the asymmetrical voltage sags.

## **5.2 Magnetizing Current Control (MCC)**

The proposed control strategy intends to control the magnetizing current in order to increase the damping of the stator flux linkage oscillations, so reducing the torque and power pulsation during the voltage sags.

Using the synchronous reference frame with orientation in the angle of the grid voltage, as employed in the control strategy (Appendix A), in such a way that the stator flux linkage vector is oriented in the quadrature axis, the magnetizing current is calculated by:

$$I_m = -(I_{r_q} + I_{s_q}). \quad (5.1)$$

Equation 5.1 points out that the magnetizing current is defined by the quadrature axis of the stator and rotor currents. Since the RSC controls the rotor currents, one can notice that the magnetizing current can be changed by the manipulation of the quadrature rotor current. Its magnitude can be approximated by:

$$I_m^* \approx \frac{\psi_{s_q}}{L_m} \approx -\frac{V_{s_d}}{L_m \omega_s}. \quad (5.2)$$

As the aim of the magnetizing current control (MCC) is to control the oscillations that appear in this current due to the stator flux natural component, it is necessary to control just this component. For the extraction of the natural component of the magnetizing current it is possible to use a band-pass filter adjusted for the stator electrical frequency with the following transfer function:

$$G_f(s) = \frac{\omega_s s}{s^2 + \omega_s s + \omega_s^2} \quad (5.3)$$

This filter is useful because the high frequency harmonics and noise is removed and the DC component is also removed and the reference of the magnetizing current can be set to zero. Figure 5.1 shows the structure of the MCC. As depicted, this control works in cascade with the reactive power control, in such a way that, during the sag, the reactive power can be controlled independently. Using this feedback structure, it is not necessary to detect the voltage sag and adopt a different control strategy during the dip, because the magnetizing control is always active.

Since just the oscillatory part of the magnetizing current is controlled, the control structure shown in Figure 5.1 can be modified in such a way that



the reactive power control and the magnetizing current control are in parallel. Both strategies have the same behavior because the reactive power control is much slower than the other control loops.

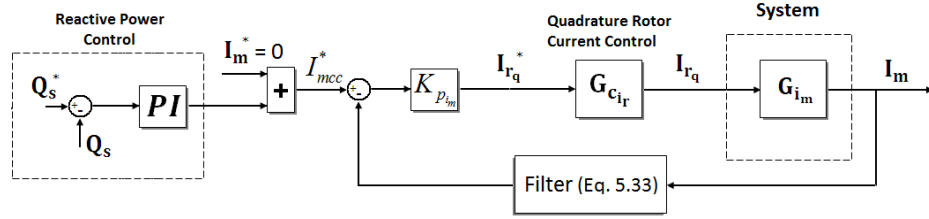


Figure 5.1: Magnetizing current control block diagram.

The main objective of the MCC is to increase the stator flux linkage damping, but the effects on the rotor currents and voltages have to be analyzed. In the following subsections the different effects are mathematically modeled and checked with simulation results. Next the experimental results are shown in order to prove the effectiveness of the proposed strategy.

### 5.2.1 Influence of magnetizing current on stator flux linkage

The mathematical development carried out here is based on the equations presented in Chapter 3, but now the magnetizing current is considered for the development. Using Equation 5.1 in 3.14, yields:

$$I_{s_q} = \frac{\psi_{s_q} - L_m I_m}{L_s - L_m}. \quad (5.4)$$

Substituting Equation 5.4 in 3.10:

$$\psi_{s_q} = \frac{\frac{R_s L_m}{L_s - L_m}}{s + \frac{R_s}{L_s - L_m}} I_m - \frac{\omega_s}{s + \frac{R_s}{L_s - L_m}} \psi_{s_d}, \quad (5.5)$$

and using this equation and Equation 3.17 in 3.9:

$$\begin{aligned}
\psi_{s_d} = & \frac{\left(s + \frac{R_s}{L_s - L_m}\right)}{\left[s^2 + \left(\frac{R_s}{L_s - L_m} + \frac{R_s}{L_s}\right)s + \frac{R_s^2}{L_s(L_s - L_m)} + \omega_s^2\right]} V_{s_d} + \frac{\omega_s L_m \frac{R_s}{L_s - L_m}}{\left[s^2 + \left(\frac{R_s}{L_s - L_m} + \frac{R_s}{L_s}\right)s + \frac{R_s^2}{L_s(L_s - L_m)} + \omega_s^2\right]} I_m \\
& + \frac{L_m \frac{R_s}{L_s} \left(s + \frac{R_s}{L_s - L_m}\right)}{\left[s^2 + \left(\frac{R_s}{L_s - L_m} + \frac{R_s}{L_s}\right)s + \frac{R_s^2}{L_s(L_s - L_m)} + \omega_s^2\right]} I_{r_d}
\end{aligned} \tag{5.6}$$

It is possible to neglect the term  $R_s^2/[L_s(L_s - L_m)]$ , much smaller than  $\omega_s^2$ , and considering  $\tau_{\sigma s} = \frac{L_s - L_m}{R_s} = \frac{L_{\sigma s}}{R_s}$ , since  $L_s = L_{\sigma s} + L_m$  and  $L_{\sigma s}$  is the stator linkage inductance. The last term, which is dependent on  $I_{r_d}$ , can also be neglected because the transfer function gain is small when compared with the other two terms. With these considerations:

$$\psi_{s_d}(s) = \frac{\left(s + \frac{1}{\tau_{\sigma s}}\right)}{\left[s^2 + \left(\frac{1}{\tau_s} + \frac{1}{\tau_{\sigma s}}\right)s + \omega_s^2\right]} V_{s_d}(s) + \frac{\frac{\omega_s L_m}{\tau_{\sigma s}}}{\left[s^2 + \left(\frac{1}{\tau_s} + \frac{1}{\tau_{\sigma s}}\right)s + \omega_s^2\right]} I_m(s). \tag{5.7}$$

Similarly, it is possible to deduce the quadrature stator flux linkage:

$$\psi_{s_q}(s) = \frac{-\omega_s}{\left[s^2 + \left(\frac{1}{\tau_s} + \frac{1}{\tau_{\sigma s}}\right)s + \omega_s^2\right]} V_{s_d}(s) + \frac{\frac{L_m}{\tau_{\sigma s}} \left(s + \frac{1}{\tau_s}\right)}{\left[s^2 + \left(\frac{1}{\tau_s} + \frac{1}{\tau_{\sigma s}}\right)s + \omega_s^2\right]} I_m(s). \tag{5.8}$$

Equations 5.7 and 5.8 show how the magnetizing current influence the stator flux linkage, however the objective of the development is to evaluate the flux behavior when this current is controlled.

As the control acts only in the current oscillations, it is necessary just a proportional controller ( $K_{p_{i_m}}$ ), since zero steady-state error is not of interest. In this situation, for sake of simplicity in the analysis, the following simplifications are considered:

- Neglecting the reactive power control, because generally it has a nar-

row bandwidth, hence during the transient the controller output varies slowly. For the test benches the cut-off frequency of this control is 5Hz;

- Just the natural (oscillatory) flux response is analyzed, since the control reference is zero. This assumption is represented by the superscript “n” in the flux variables;
- The rotor current control (internal loop) is much faster than the magnetizing current control and has no limitations, therefore the rotor current reference generated by the external loop can be reached immediately.

Assuming these simplifications, the rotor current can be written as:

$$I_{r_q} = -\frac{K_{p_{im}} I_{s_q}}{1 + K_{p_{im}}}. \quad (5.9)$$

Substituting Equation 5.9 in 3.14 yields:

$$I_{s_q} = \frac{\psi_{s_q}^n (1 + K_{p_{im}})}{K_{p_{im}} L_s + L_s - K_{p_{im}} L_m}, \quad (5.10)$$

and this equation in Equation 3.10:

$$\psi_{s_q}^n = \frac{-\omega_s \psi_{s_d}^n}{s + \frac{R_s(1+K_{p_{im}})}{K_{p_{im}} L_s + L_s - K_{p_{im}} L_m}}. \quad (5.11)$$

Using Equations 5.11 and 3.17 in 3.9, the result is:

$$\psi_{s_d}^n = \frac{\left[ s + \frac{R_s(1+K_{p_{im}})}{K_{p_{im}} L_s + L_s - K_{p_{im}} L_m} \right] V_{s_d} + \left[ L_m \frac{R_s}{L_s} \left( s + \frac{R_s(1+K_{p_{im}})}{K_{p_{im}} L_s + L_s - K_{p_{im}} L_m} \right) \right] I_{r_d}}{\left[ s^2 + \left( \frac{R_s}{L_s} + \frac{R_s(1+K_{p_{im}})}{K_{p_{im}} L_s + L_s - K_{p_{im}} L_m} \right) s + \frac{R_s^2(1+K_{p_{im}})}{L_s(K_{p_{im}} L_s + L_s - K_{p_{im}} L_m)} + \omega_s^2 \right]}. \quad (5.12)$$

The parcel  $[R_s^2(1+K_{p_{im}})]/[L_s(K_{p_{im}} L_s + L_s - K_{p_{im}} L_m)]$  is much smaller than  $\omega_s^2$  and can be neglected. The second term, which is dependent on

$I_{r_d}$ , is small when compared with the first one, therefore can also be neglected. Assuming  $\tau_m = \frac{K_{p_{im}} L_s + L_s - K_{p_{im}} L_m}{R_s(1+K_{p_{im}})}$  and the simplifications, the direct stator flux linkage is:

$$\psi_{s_d}^n(s) = \frac{\left(s + \frac{1}{\tau_m}\right)}{s^2 + \left(\frac{1}{\tau_s} + \frac{1}{\tau_m}\right)s + \omega_s^2} V_{s_d}(s). \quad (5.13)$$

Similarly, the quadrature stator flux can be written as:

$$\psi_{s_q}^n(s) = \frac{-\omega_s}{s^2 + \left(\frac{1}{\tau_s} + \frac{1}{\tau_m}\right)s + \omega_s^2} V_{s_d}(s). \quad (5.14)$$

Comparing Equations 5.13, 5.14 and 3.22, 3.23 it is possible to realize that the flux damping is increased, because  $1/\tau_m$  can be high depending on the controller adjustment, as following demonstrated:

- In the case that  $K_{p_{im}} = 0$ :

$$1/\tau_m = 1/\tau_s,$$

therefore the damping is not modified;

- In the case that  $K_{p_{im}} \rightarrow \infty$ :

$$\lim_{K_{p_{im}} \rightarrow \infty} \left(\frac{1}{\tau_m}\right) = \frac{R_s}{L_s - L_m} = \frac{R_s}{L_{\sigma s}}.$$

Generally  $L_{\sigma s}$  is too small, therefore  $1/\tau_m$  is higher than  $1/\tau_s$ , so the flux damping is increased.

Theoretically, the maximum damping obtained using the magnetizing current control is  $\frac{R_s}{2\omega_s} \left(\frac{1}{L_s} + \frac{1}{L_{\sigma s}}\right)$ . Of course for choosing  $K_{p_{im}}$  it is necessary to consider the rotor current control loop dynamics in such a way that the magnetizing current control is not faster than the internal control, avoiding instability.

Equations 5.13 and 5.14 represent just the oscillatory part of the stator flux, as described previously. For the complete flux representation it is necessary to consider also the forced response:

$$\psi_{s_d}(s) = \psi_{s_d}^n(s) + c_{i_{m_d}}, \quad (5.15)$$

$$\psi_{s_q}(s) = \psi_{s_q}^n(s) + c_{i_{m_q}}, \quad (5.16)$$

where  $c_{i_{m_d}}$  and  $c_{i_{m_q}}$  are forced responses of the flux and they can be calculated through the gains of the transfer functions 5.13 and 5.14. Obviously, if the magnitude of the current magnetizing is not modified by the control action, the gain of Equation 5.15 must be equal to gain of the transfer function 5.7 and then:

$$c_{i_{m_d}} = \frac{(\tau_m - \tau_{\sigma s}) V_{s_d} + \omega_s L_m \tau_m I_m}{\tau_m \tau_{\sigma s} \omega_s^2}. \quad (5.17)$$

Substituting the value of magnetizing current, given in Equation 5.2, in the Equation 5.17, yields:

$$c_{i_{m_d}} = \frac{-\tau_{\sigma s}}{\tau_m \tau_{\sigma s} \omega_s^2} V_{s_d}. \quad (5.18)$$

Similarly, the gain of the transfer function 5.16 must also be equal to gain of Equation 5.8, resulting:

$$c_{i_{m_q}} = \frac{1}{\tau_s \tau_{\sigma s} \omega_s^3} V_{s_d}. \quad (5.19)$$

One can notice that Equations 5.18 and 5.19 have no dynamics. Equation 5.19 represents a too small value, therefore it can be neglected.

In order to check the mathematical development, a 50% three-phase voltage sag was simulated and the results are compared with the ones obtained from Equations 5.15 and 5.16. Two results are presented: without the MCC and using the MCC with a proportional gain  $K_{p_{i_m}} = 15$ . More details about the control tuning are described hereafter.

Comparing Figure 5.2(a) and (b) one can notice that the MCC increases the flux damping. It is also demonstrated a good agreement between the

theoretical (Equations 5.15 and 5.16) and the simulation results. The small difference between the responses can be justified by the fact that the internal control current loop has a dynamic that is fast but not instantaneous as assumed in the mathematical development.

Through the mathematical development and the simulation result one can notice that the MCC is capable of decrease the natural component faster, but in order to do so it is necessary to analyze the influence on the rotor currents and voltages.

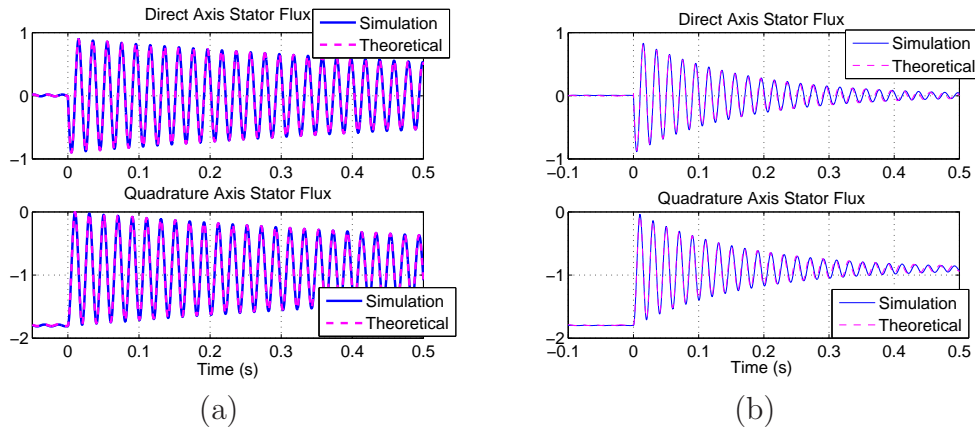


Figure 5.2: Simulation and theoretical results of the dq stator flux linkage, 50% three-phase voltage sag, 1950 RPM:  
 (a) - Without the MCC strategy ;  
 (b) - With the MCC strategy -  $K_{p_{im}} = 15$ .

### 5.2.2 Influence of MCC on the rotor currents

In the previous subsection it was analyzed just the influence of the MCC on the stator flux linkage, because the behavior of this variable determines the rotor voltages and currents behavior. However, the most important variable to be analyzed during the sag is the rotor current, since the high current transient can damage the RSC. Figure 5.3 shows the comparison of the dq rotor currents simulated with and without the magnetizing current control.

As depicted in Figure 5.3, when the magnetizing current control is used, the quadrature rotor current in the sag beginning is higher than the case

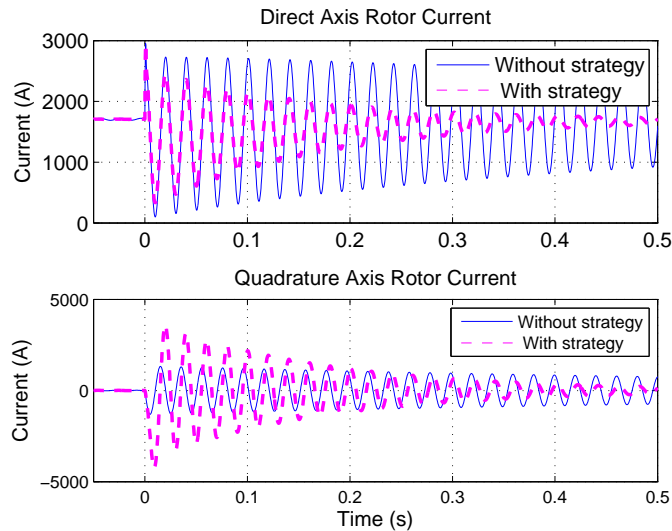


Figure 5.3: dq rotor currents simulated for a 50% three-phase voltage sag, rated power (no reactive power control).

without the control, due to the control action. However, the natural component extinguishes faster, being possible the control of the current in such a way that reactive power is supplied to the grid. In the direct axis rotor current, the attenuation of the natural component with the use of the MCC is clearly observed. The effect of the MCC on the ABC rotor currents is illustrated in Figure 5.4 where it is seen the increasing in the rotor currents.

In the previous test no strategy was implemented in the stator power control. The ideal strategy is to reduce the active power and start the control of reactive power. Figures 5.5(a) and (b) show the simulation results of the rotor currents and the stator power, when the magnetizing current control is used. One can notice that reducing the direct axis current it is possible to increase the reactive power. With the use of the control strategy the mechanical stresses are decreased and the power quality is improved.

Hereafter it will be demonstrated that the current increasing is affected by the MCC adjustment, therefore choosing an adequate gain and references it is possible to increase the damping without increasing the currents too much.

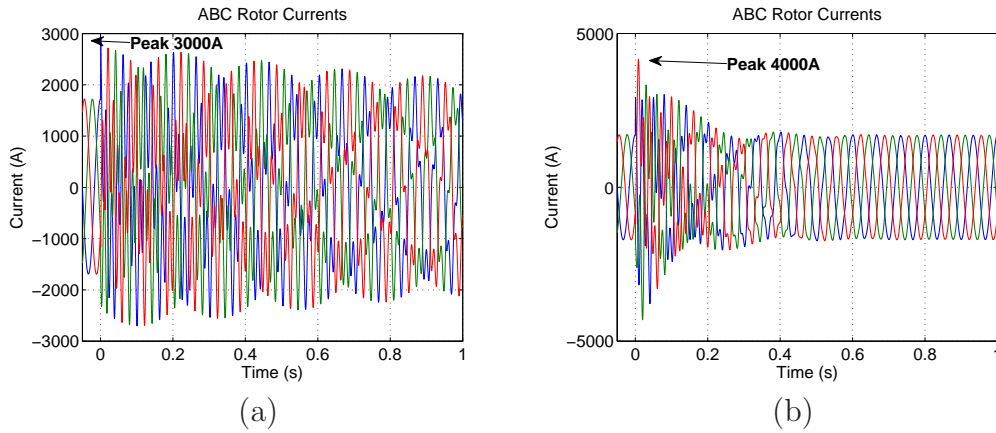


Figure 5.4: dq rotor currents simulated for a 50% three-phase voltage sag, rated power (no reactive power control):  
 (a) - Without the magnetizing current control;  
 (b) - With the magnetizing current control.

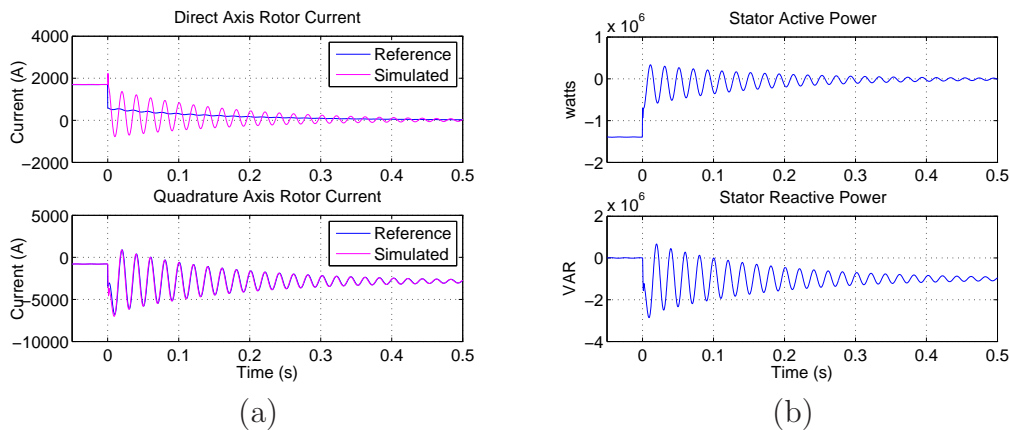


Figure 5.5: Simulation results for 50% three-phase voltage sag, rated power, using the MCC strategy and reactive power control:  
 (a) - dq rotor currents;  
 (b) - Stator active and reactive powers.

### 5.2.3 Influence of the MCC on the rotor voltages

If during the sag the converter voltage output saturate, that is, the converter is not capable of imposing the demanded voltage, high currents may take place. Therefore, it is important to analyze the behavior of the rotor



voltages.

Proceeding in the same manner as in the previous sections and using the Equations 5.13 and 5.14, it is possible to demonstrate that using the MCC the rotor voltages can be approximated by:

$$\begin{aligned}
V_{r_d}(s) &= \left[ \frac{\frac{L_m}{L_s} s^2 + \frac{L_m}{L_s \tau_m} s - \frac{\omega_r \omega_s [L_m(1+K_{p_{im}}) - L_r K_{p_{im}}]}{K_{p_{im}} L_m - L_s(1+K_{p_{im}})}}{s^2 + \left(\frac{1}{\tau_s} + \frac{1}{\tau_m}\right) s + \omega_s^2} \right] V_{s_d}(s) \\
&\quad - \left( \frac{\omega_r (K_{p_{im}} L_m^2 - K_{p_{im}} L_s L_r)}{K_{p_{im}} L_m - L_s(1+K_{p_{im}})} \right) I_{mcc}^*(s) \\
V_{r_q}(s) &= \left[ \frac{\frac{L_m \omega_s (1+K_{p_{im}}) - \omega_s L_r K_{p_{im}} + \omega_r (L_m/L_s)}{K_{p_{im}} L_m - L_s(1+K_{p_{im}})} s - \frac{\omega_s R_r K_{p_{im}}}{K_{p_{im}} L_m - L_s(1+K_{p_{im}})} + \frac{\omega_r L_m}{L_s \tau_m}}{s^2 + \left(\frac{1}{\tau_s} + \frac{1}{\tau_m}\right) s + \omega_s^2} \right] V_{s_d}(s) \\
&\quad + \left[ \frac{K_{p_{im}} L_m^2 - K_{p_{im}} L_s L_r}{K_{p_{im}} L_m - L_s(1+K_{p_{im}})} s - \frac{R_r K_{p_{im}} L_s}{K_{p_{im}} L_m - L_s(1+K_{p_{im}})} \right] I_{mcc}^*(s)
\end{aligned} \tag{5.20}$$

$$\tag{5.21}$$

Equations 5.20 and 5.21 shows that the rotor voltage depends on the stator voltage and it is influenced by control adjustment ( $K_{p_{im}}$ ). The reference of the magnetizing current control ( $I_{mcc}^*$ ) appears in these equations, because it is not zero when the reactive stator power is controlled, as can be seen in Figure 5.1. One can notice that this reference cannot be changed abruptly, because there is an derivative term in the quadrature voltage transfer function (Equation 5.21).

Figure 5.6 shows the comparison between the rotor voltages with and without the MCC strategy. As expected, it is necessary smaller rotor voltages when the strategy is utilized and the oscillations due to the natural component disappear faster.

Using the Equations 5.20 and 5.21, the maximum rotor voltage in dif-

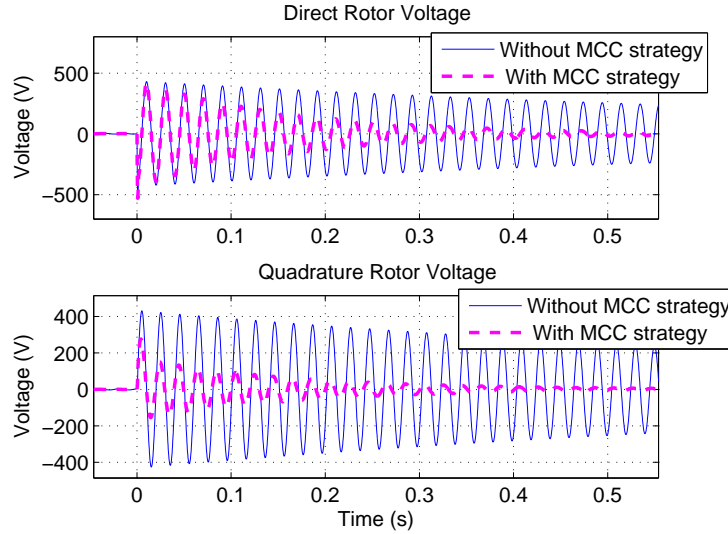


Figure 5.6: Comparison between the rotor voltages with and without the MCC strategy - simulation result.

ferent operation conditions is calculated for the 2MW WECS. Figure 5.7 shows the magnitude of the maximum rotor voltage reached during the sag. Furthermore, this figure plots the points obtained from the simulation model to show that the values calculated are consistent. The simulation results represents the system following the MPPT curve and with unitary power factor in the stator.

Through Figure 5.7, it is seen that for a fixed generator speed, the higher is the voltage sag depth, the higher is the rotor voltage demanded, a result easily observed also in the equations. For the correct control of the magnetizing current, the converter needs to impose the voltages presented in this figure. Varying the speed, the figure shows that the rotor voltage magnitude is dependent on the slip. In the supersynchronous region the increase in the rotor voltage is higher than the subsynchronous region.

In the previous tests it was considered just a fixed magnetizing control adjustment, so the next step in the development will be to analyze the influence of the control gain on the rotor currents and voltages.

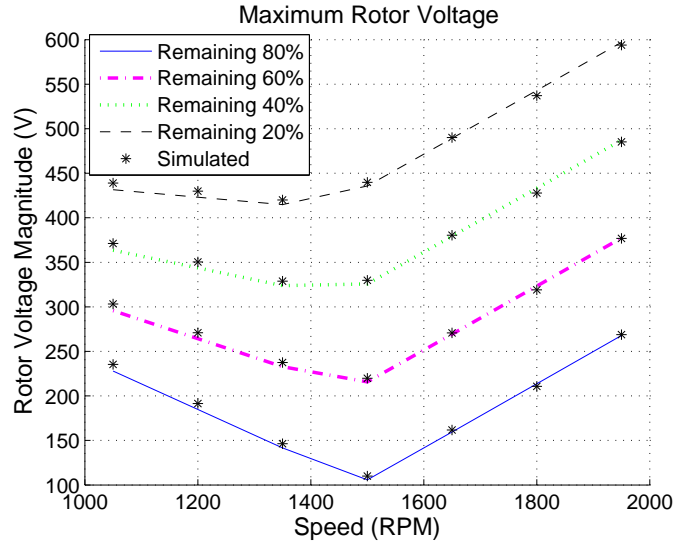


Figure 5.7: Rotor voltage calculated and simulated for different voltage sags and speeds using the MCC strategy -  $K_{p_{im}} = 15$ .

#### 5.2.4 Influence of the MCC gain on the rotor currents and voltages

Using the same conditions and the same MCC gain ( $K_{p_{im}} = 15$ ) of the last section, the simulation is carried out for different speeds and voltage depths.

Figure 5.8 shows the normalized maximum rotor currents magnitude (1 pu  $\approx 2000A$ ). It is seen that the rotor current maximum value depends basically on the sag amplitude. Furthermore, for the control adjustment utilized, the magnetizing current control requires a high instantaneous rotor current immediately after the sag entry. In order to use this strategy in safety conditions it is necessary to increase the converter rated power, what is not desirable, or decrease the MCC gain, causing a reduction in the control performance.

Using Equations 5.13 and 5.14 the time constant of the stator flux linkage decay versus the MCC gain is plotted in Figure 5.9. One can notice that the controller gain utilized earlier ( $K_{p_{im}} = 15$ ) results in a good flux attenuation when compared with the case without control ( $K_{p_{im}} = 0$ ), but, as shown

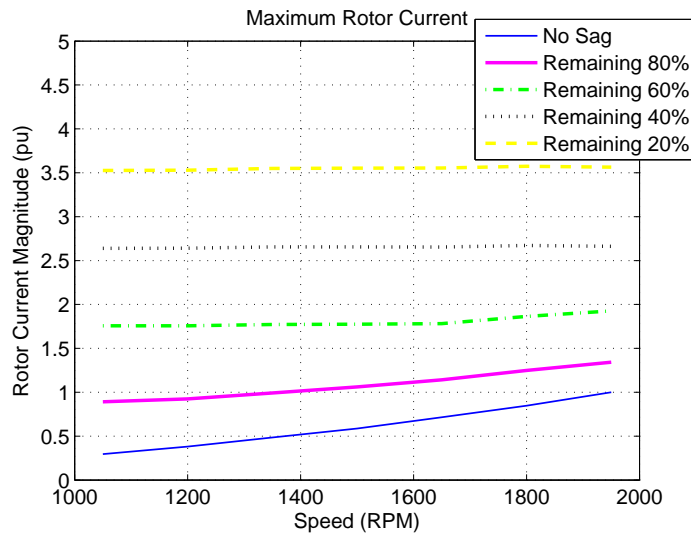


Figure 5.8: Rotor currents simulated for different voltage sags and speeds (MCC strategy).

previously, a high rotor current is required.

It is possible to decrease the rotor peak currents decreasing the control gain, but, as can be seen in Figure 5.9, the decay time constant of the natural stator flux linkage is increased. Figure 5.10 shows the relation between the maximum rotor current and the control gain for the rated operation (speed 1950 RPM, generating 2MW).

Analyzing Figure 5.10 it is perceived the remarkable dependence of the rotor current on the control gain and the voltage sag depth. The constant level seen in the beginning of each curve can be explained by the fact that in these conditions the direct axis rotor current (load current) has more influence than the quadrature axis rotor current (magnetizing current).

Through Figures 5.9 and 5.10 one can notice that even if the controller gain is decreased for decreasing the rotor currents, the stator flux linkage damping may be significantly increased when compared with the case in which the control strategy is not used. For example, if the proportional gain is set to 4, the rotor currents will be not higher than 2 pu and the time constant of the stator flux linkage will be reduced to 35% of the time constant when the control is not used.

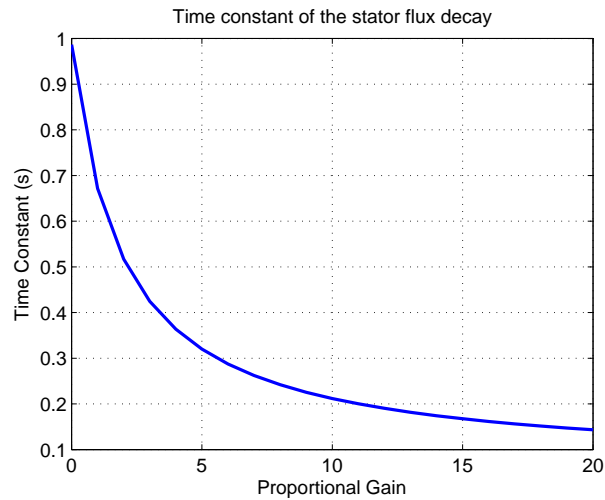


Figure 5.9: Time constant of the stator flux linkage decay varying the magnetizing current control gain - 2MW parameters.

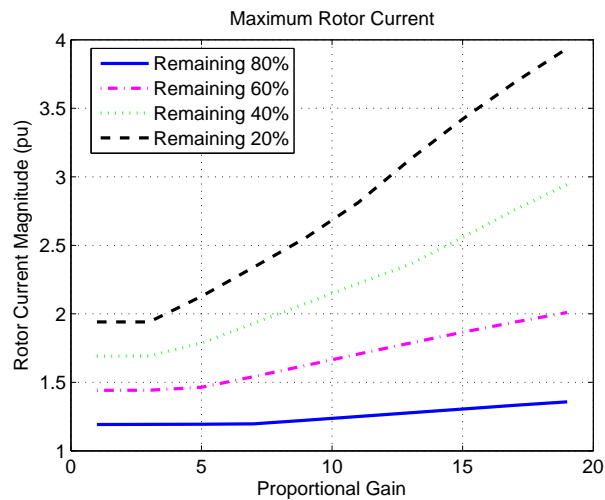


Figure 5.10: Maximum rotor current simulated for different voltage sags and varying the magnetizing current control gain.

Figure 5.11 depicts the maximum rotor voltage in per unit when the gain is varied, showing that the gain has a small influence on the rotor voltage. For more severe voltage dips the influence of the gain increases. As the rotor voltage is almost constant, the power flowing through the rotor is more dependent on the current.

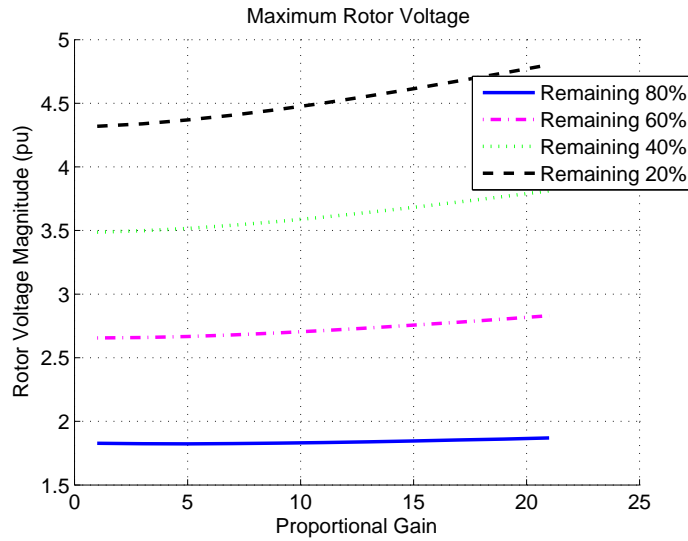


Figure 5.11: Maximum rotor voltage simulated for different voltage sags and varying the magnetizing current control gain.

It is important to highlight that in the previous tests the active and reactive power were kept constant. It is possible to reduce the rotor currents if the active power reference is set to zero during the sag. Setting the active power to zero leads the system to increase its speed, but as the inertia of the turbine is huge and the sag is fast, this increasing may be not substantial. The reactive power reference has to be adjusted depending on the converter limits and the grid codes requirements. In the next chapter an strategy is presented to deal with the active power decrease and reactive increase.

### 5.2.5 Experimental results

In order to validate experimentally the control of the magnetizing current the following conditions are used during the first tests:

- TUDb => 85% three-phase voltage sag, UFMGb => 50% three-phase voltage sag;
- Synchronous speed;
- The active power is controlled following the MPPT curve;

- During the sag the active power reference is set to zero in order to diminish the rotor currents;
- The control of the reactive stator power is disabled;
- The MCC gain is set to 4 in the TUDb and 2.5 in the UFMGb;

In order to better visualize the control effect on the system behavior, the gains of the rotor current control of the TUDb were purposely set to  $K_p = 50\Omega$  and  $K_i = 10000\Omega/s$ , similar to the tests presented in Chapter 3. In the UFMGb the gains were kept in the normal values.

Figures 5.12 (a) and (b) show the comparison between the estimated dq stator fluxes with and without the use of the MCC strategy. It is clearly seen that the use of the control strategy increase the flux damping, proving the effectiveness of such strategy.

The increasing in the flux damping is higher for the TUDb, because the sag is smaller, therefore the demanded current is smaller, permitting an higher MCC gain. In the UFMGb the current supported by the converter is just 10% higher than the rotor nominal current (generating 25kW). This fact difficults the increasing of the MCC gain, therefore the damping increasing is limited.

Figures 5.13 and 5.14 depict the behavior of the dq rotor currents and voltages. One can notice that the quadrature rotor current increases for a short time in the sag beginning, but after the transient it is smaller than the case without strategy. As stated earlier, the rotor voltage is reduced with the use of the MCC. The use of the strategy increases the damping of the natural flux component, so reducing the oscillations of the rotor currents and voltages, consequently the pulsation in the electromagnetic torque and generated power.

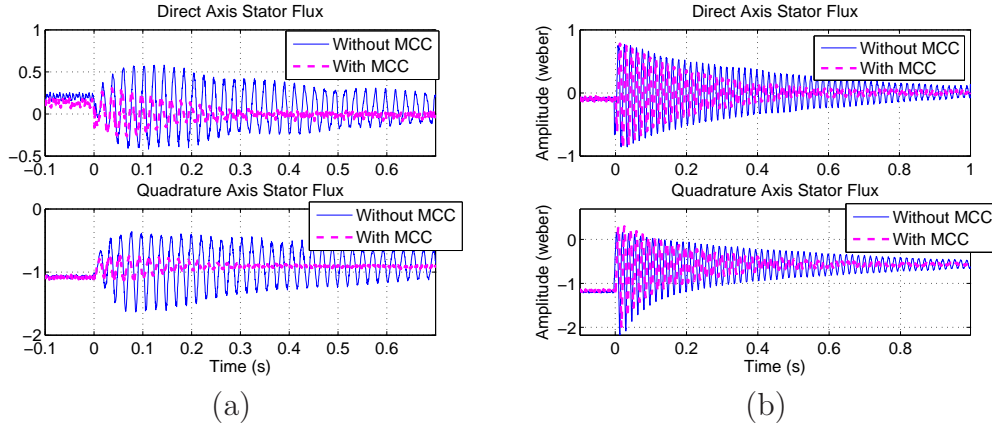


Figure 5.12: Experimental results of the estimated dq stator fluxes using the MCC strategy:

- (a) - TUD test bench -  $K_{p_{im}} = 4$  (85% three-phase voltage sag, 1500 RPM,  $K_p = 100\Omega$ ,  $K_i = 10000\Omega/s$ );  
 (b) - UFMG test bench -  $K_{p_{im}} = 2.5$  (50% three-phase voltage sag, 1800 RPM).

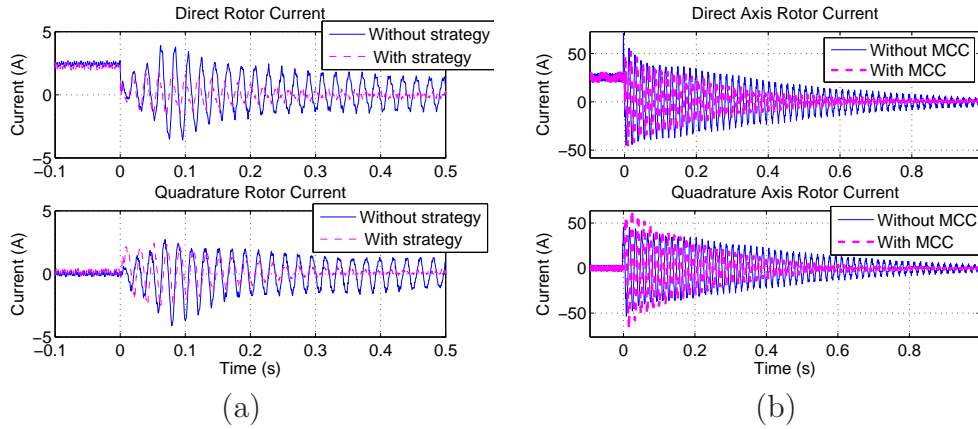


Figure 5.13: Experimental results of the dq rotor currents using the MCC strategy:  
 (a) - TUD test bench -  $K_{p_{im}} = 4$  (85% three-phase voltage sag, 1500 RPM,  $K_p = 100\Omega$ ,  $K_i = 10000\Omega/s$ );  
 (b) - UFMG test bench -  $K_{p_{im}} = 2.5$  (50% three-phase voltage sag, 1800 RPM).

In the tests carried out previously it was considered the machine operating in the synchronous speed that is a special case because the rotor voltages and currents are DC values. This condition was used in most of the tests due



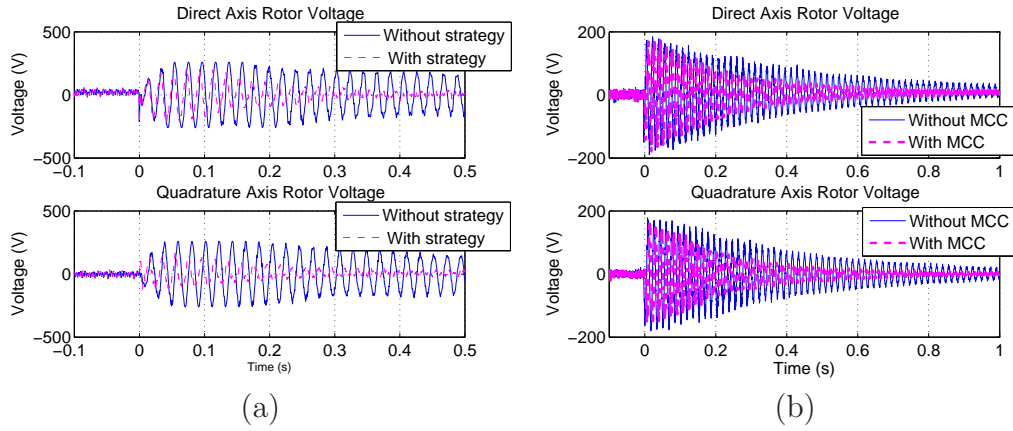


Figure 5.14: Experimental results of the dq rotor voltages using the MCC strategy:  
 (a) - TUD test bench -  $K_{p_{im}} = 4$  (85% three-phase voltage sag, 1500 RPM,  $K_p = 100\Omega$ ,  $K_i = 10000\Omega/s$ );  
 (b) - UFMG test bench -  $K_{p_{im}} = 2.5$  (50% three-phase voltage sag, 1800 RPM).

to power limitations of the RSC in the test benches. In order to prove that this strategy is also effective for nonzero slips, Figures 5.15 and 5.16 show the dq rotor currents and stator flux linkages for the systems operating with slip=-0.15.

Observing the MCC structure, shown in Figure 5.1, it is seen the possibility of controlling the reactive stator power simultaneously with the magnetizing current. This feature is important because during the sag it is possible to supply reactive power to the grid, helping in the voltage support and attending the modern grid codes. Figures 5.17 and 5.18 show the dq rotor currents and voltages and Figure 5.19 depicts the reactive stator power when the reactive power is controlled during the voltage sag in both test benches.

Through Figures 5.19(a) and (b) it is possible to verify that before the sag the system is operating with unity power factor ( $Q_s = 0$ ). During all the voltage dip in the TUDb the reference is set to supply 1000VAR to the grid. In the UFMGb the reference is set to 5000VAR just after 0.5s, when the currents are in acceptable values, permitting the reactive power control. Of course such time to start to control the reactive power is not acceptable in the grid codes, but this time was chosen to avoid dangerous operation of the test bench because of the converter limitation, as already stated. Nevertheless, it

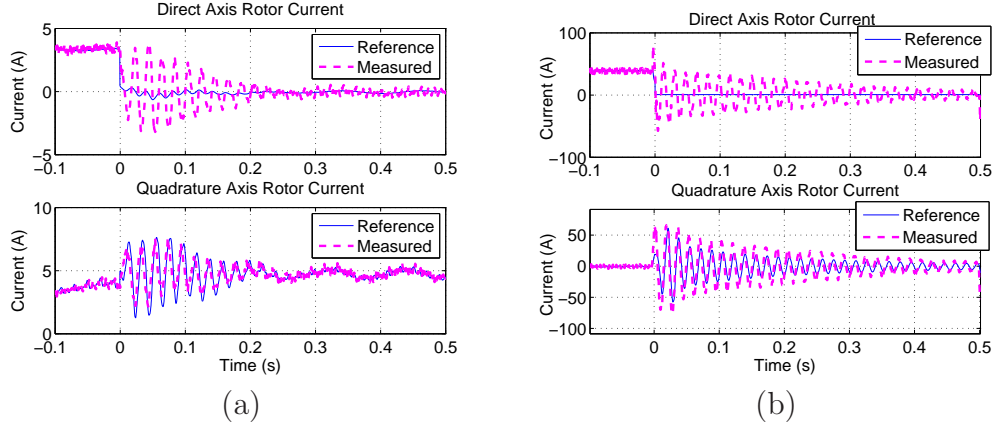


Figure 5.15: Experimental results of the dq rotor currents using the MCC strategy:  
 (a) - TUD test bench -  $K_{p_{i_m}} = 4$  (85% three-phase voltage sag, 1750 RPM,  $K_p = 100\Omega$ ,  $K_i = 10000\Omega/s$ );  
 (b) - UFMG test bench -  $K_{p_{i_m}} = 2.5$  (50% three-phase voltage sag, 2070 RPM).

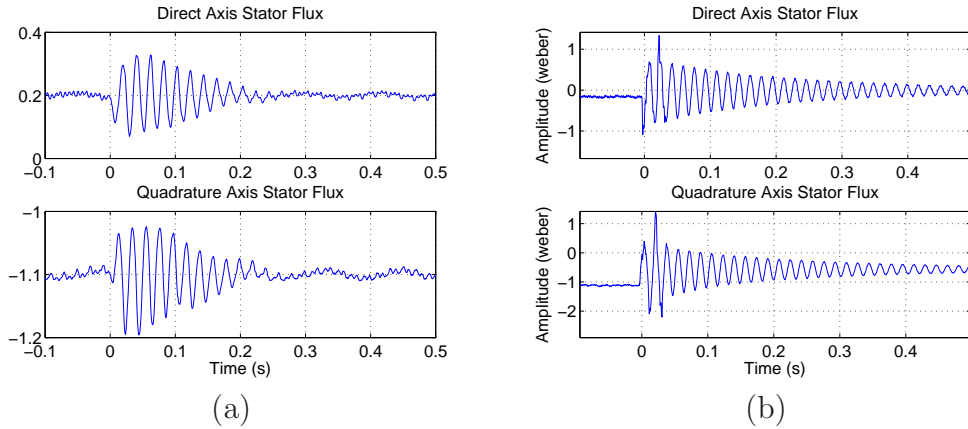


Figure 5.16: Experimental results of the estimated dq stator fluxes using the MCC strategy:  
 (a) - TUD test bench -  $K_{p_{i_m}} = 4$  (85% three-phase voltage sag, 1750 RPM,  $K_p = 100\Omega$ ,  $K_i = 10000\Omega/s$ );  
 (b) - UFMG test bench -  $K_{p_{i_m}} = 2.5$  (50% three-phase voltage sag, 2070 RPM).

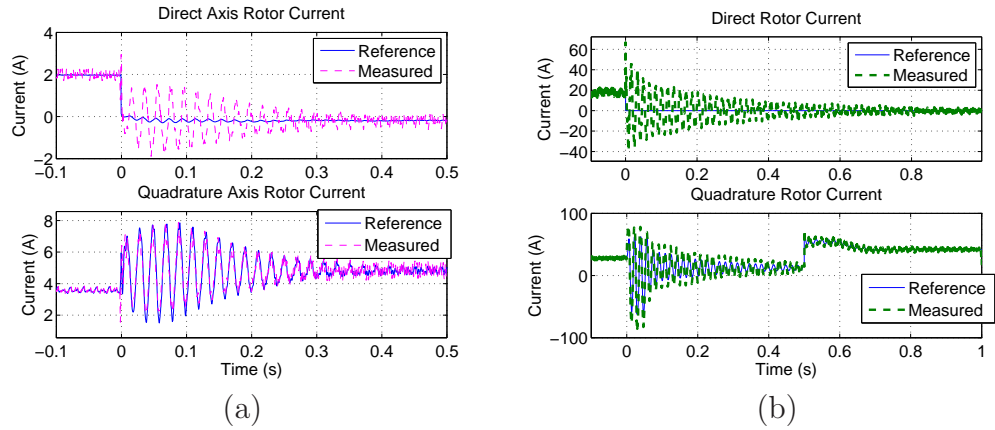


Figure 5.17: Experimental results of the dq rotor currents using the MCC strategy and reactive power control:

- (a) - TUD test bench -  $K_{p_{im}} = 4$  (85% three-phase voltage sag, 1800 RPM,  $K_p = 100\Omega$ ,  $K_i = 10000\Omega/s$ );  
 (b) - UFMG test bench -  $K_{p_{im}} = 2.5$  (50% three-phase voltage sag, 1530 RPM).

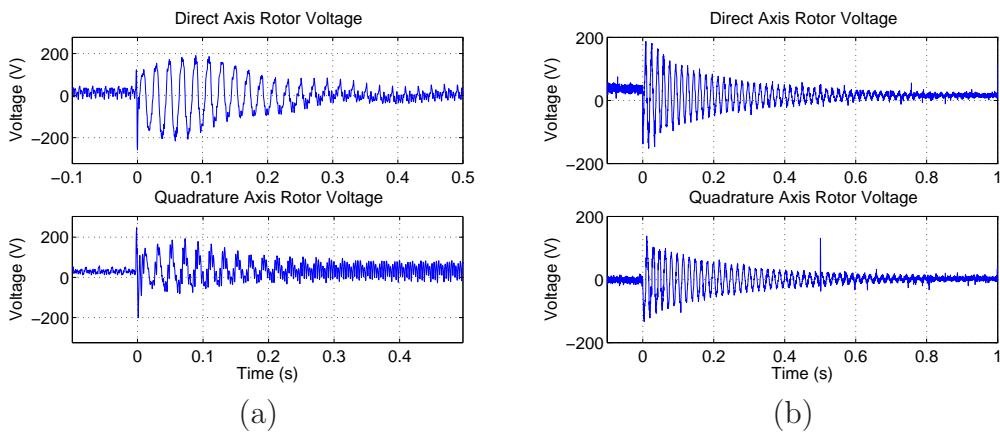


Figure 5.18: Experimental results of the dq rotor voltages using the MCC strategy and reactive power control:

- (a) - TUD test bench -  $K_{p_{im}} = 4$  (85% three-phase voltage sag, 1800 RPM,  $K_p = 100\Omega$ ,  $K_i = 10000\Omega/s$ );  
 (b) - UFMG test bench -  $K_{p_{im}} = 2.5$  (50% three-phase voltage sag, 1530 RPM).

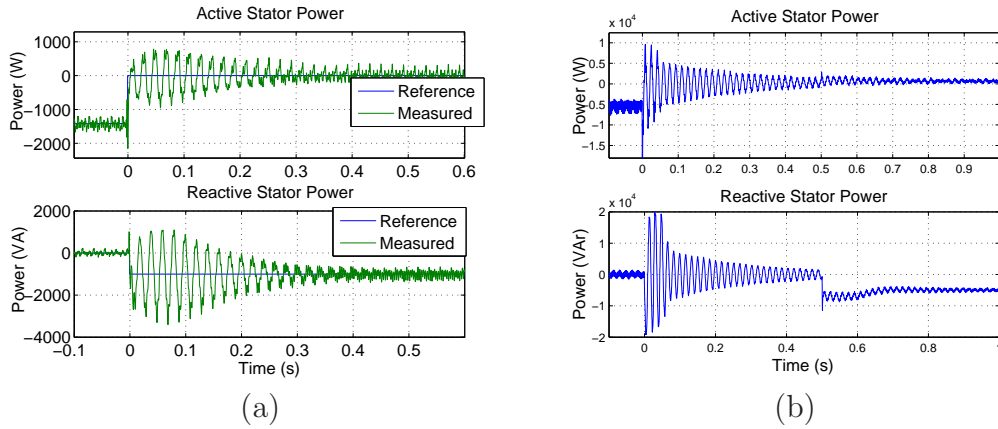


Figure 5.19: Experimental results of the active and reactive stator powers using the MCC strategy and reactive power control:

- (a) - TUD test bench -  $K_{p_{im}} = 4$  (85% three-phase voltage sag, 1800 RPM,  $K_p = 100\Omega$ ,  $K_i = 10000\Omega/s$ );  
 (b) - UFMG test bench -  $K_{p_{im}} = 2.5$  (50% three-phase voltage sag, 1530 RPM).

is demonstrated the capability of changing the converter power from active to reactive power. Furthermore the MCC is still effective, thus, the increasing in the flux damping is warranted.

Here just the behavior of the strategy in the sag beginning was demonstrated, but it is also useful during the voltage recovering in the end of voltage sag, because in this instant also appears the natural response of the stator flux linkage. Furthermore the MCC can also be employed during the connection of the generator to the grid, because the voltage transient in the machine stator also causes oscillatory flux response, causing undesired torque and power oscillations.

## 5.2.6 Application issues

Figures 5.7 to 5.11 indicate that the use of the MCC strategy is restrictive due to the high demanded RSC currents and voltages.

In fact the Figure 5.10 is plotted for the rated operation without changing in the direct (active) current reference during the sag. It is possible to

reduce the maximum rotor current by reducing the active power reference, as demonstrated in the simulation and experimental results. Even with this reduction, the demanded rotor current may be high depending on the MCC adjustment, so it is necessary to choose the gain in such a way that the flux damping is increased without a prohibitive current rising. Another fact to be evaluated is the capability of the converter to supply reactive power to the grid. The reactive power control also increases the rotor current.

The main issue for the application of the MCC strategy lies in the RSC voltage capability. The observations done for the currents are generally true in the case when the converter voltage limits is not exceeded. As shown in Figure 5.7 the RSC has to apply high voltages depending on the voltage sag amplitude and the machine speed. If the converter is not capable of imposing the demanded voltage, the correct control of the magnetizing control may not be attained, reducing the strategy effectiveness. Furthermore, as described in Chapter 3, the rotor currents will also increase, increasing the probability of the system to trip.

In order to use the MCC strategy, theoretically is not necessary to increase the converter current limits if the methodologies mentioned above are used, but the voltage limits must be high to improve the system performance for deep voltage sags. The RSC voltage capability may be improved, increasing the DC-link voltage until the IGBT's limit voltage. If it is necessary to increase the voltage beyond this limit, the strategy becomes economically unviable and it can be used just to shallow voltage sags or the transient during the connection of the generator to the grid. A deep analysis of the converter capability is necessary in order to check the conditions when the use of the MCC can be effective.

It is important to highlight that the proposed strategy does not intend to be a unique solution of ride-through, but it can improve the system performance and it may be combined to others strategies.

## 5.3 Final Considerations

In this chapter an specific strategy for the symmetrical voltage sags was presented in order to reduce the effect of the stator flux natural component.

The mathematical, simulation and experimental results demonstrate that the magnetizing current control is effective in the increasing of the flux damping, but high rotor voltages and currents are necessary.

As the balanced voltage sags are particular cases of the unbalanced ones, the strategies presented in the next chapter, for the asymmetrical sags, can also be employed for the symmetrical one. Furthermore, the MCC can also be useful for the unbalanced case and it will be evaluated again in the next chapter.

# Ride-Through Strategies - Asymmetrical Voltage Sags Case

---

## 6.1 Introduction

In the Chapter 4, it was shown that during unbalanced voltage sags high rotor voltages take place due to the stator flux linkage negative sequence component and, depending on the instant of the sag entry, natural component also arises. These components cause high rotor currents, which can damage the converter, and also torque and power oscillations that may be harmful for the system. Therefore, it is necessary to use strategies to improve the DFIG behavior during the grid faults.

In the last few years, several papers proposed the use of different control strategies in order to mitigate the effect of the negative sequence in the doubly-fed induction generators. Most of these papers deal just with the system control under long term grid voltage unbalances. The converter limits are also not well explored, because generally the long term voltage unbalances have small amplitude, thereby the demanded rotor currents and voltages are small. Therefore, the use of such control strategies during voltage sags has two points that have to be analyzed: the natural component of the rotor currents and voltages that may be induced during the sag transient and the converter limitation that can be exceeded depending on the sag magnitude.

In this chapter, some of the control strategies found in the literature are

presented and simulation results of the 2MW system are analyzed for the asymmetrical voltage sags. Based on these strategies and those presented in the last chapter, novel control methodologies are proposed and validated using simulation and experimental results.

## 6.2 Compensation of Torque and Reactive Power Pulsations (CTRP)

In order to reduce the torque and the stator reactive power oscillations papers Brekken and Mohan (2004) and Brekken and Mohan (2007) propose the compensation of such variables in the output of the rotor current control, as illustrated in Figure 6.1. The compensations are just activated in the presence of a voltage unbalance and supplement the output of the PI controllers to remove the  $2\omega_s$  disturbance due to the negative sequence component.

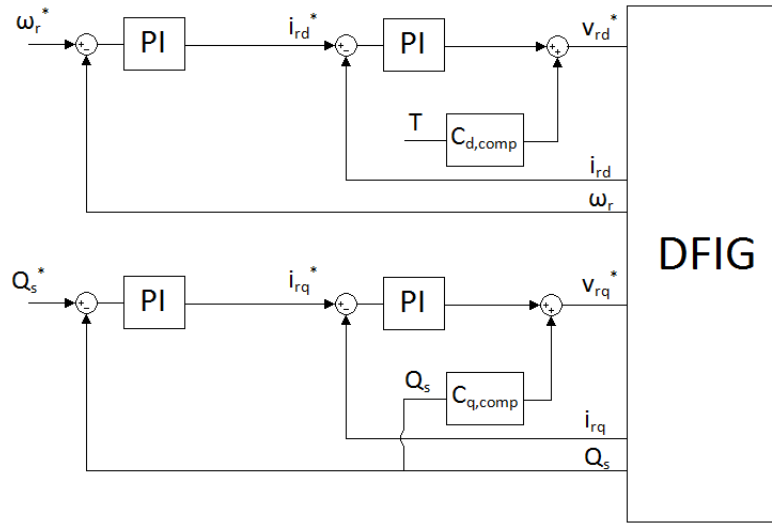


Figure 6.1: Control of RSC with the strategy of compensating the torque and reactive power oscillations.

The  $C_{d,comp}$  and  $C_{q,comp}$  terms are designed to have a high gain in the frequency of the disturbance and are implemented using resonant filters. In the present case of study, the compensation transfer functions used are:



$$C_{comp} = \frac{A_{comp}s}{s^2 + \frac{2}{\tau_{comp}}s + (2\omega_s)^2}, \quad (6.1)$$

where  $A_{comp}$  is the filter gain and  $\tau_{comp}$  is time constant. The compensations are tuned to have a high gain in the double of the grid frequency without pushing the system to the instability. More details about the influence of the resonant filter parameters is not described here, since the main goal is to verify the improvement in the DFIG response during the voltage sags and to expand the analysis done in Brekken and Mohan (2004) and Brekken and Mohan (2007).

Simulating an 80% phase-neutral voltage sag with entry  $\theta_0 = 90^\circ$  (no natural component), Figures 6.2 to 6.5 show the result of the main interested variables for the simulation with and without the CTRP strategy for the system in the rated operation (1950 RPM).

Figure 6.2 shows that the use the strategy reduces drastically the electromagnetic torque oscillations, thus, reducing the mechanical stresses. Through Figure 6.3 it is seen that the reactive power oscillation are also reduced. One can notice that the remaining oscillations depend on the compensation gain in the 100Hz ( $2f_s$ ) frequency. The strategy has a small effect in the active power oscillations, because it is impossible to eliminate the oscillation in the torque and the active power simultaneously, as will be shown hereafter. If the compensation gain is set smaller, it is possible to decrease the active power oscillation, but in the other hand the torque pulsation is increased. Other possibility is to reduce the oscillation in the total active power supplied to the grid through the control coordinated of the GSC, strategy discussed in the following sections.

Comparing the rotor currents in Figures 6.4a and 6.4b it is seen that the amplitude of the current is reduced with the CTPR strategy. Furthermore, the 100Hz harmonic is almost eliminated from the rotor currents.

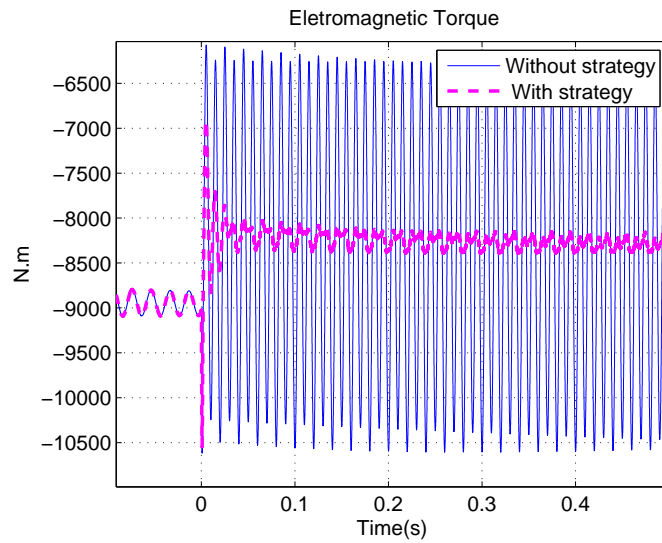


Figure 6.2: Simulation result of the electromagnetic torque with and without the CTRP strategy (80% phase-neutral voltage sag,  $\theta_0 = 90^\circ$  and 1950 RPM).

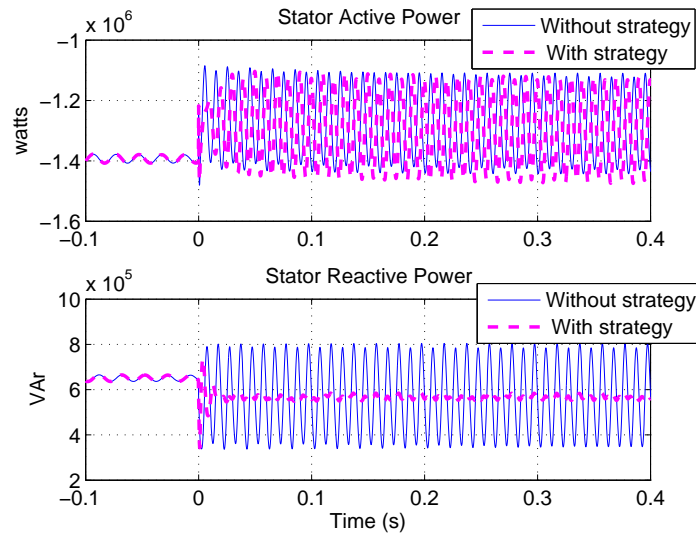


Figure 6.3: Stator active and reactive powers with and without the CTRP strategy (80% phase-neutral voltage sag,  $\theta_0 = 90^\circ$  and 1950 RPM).

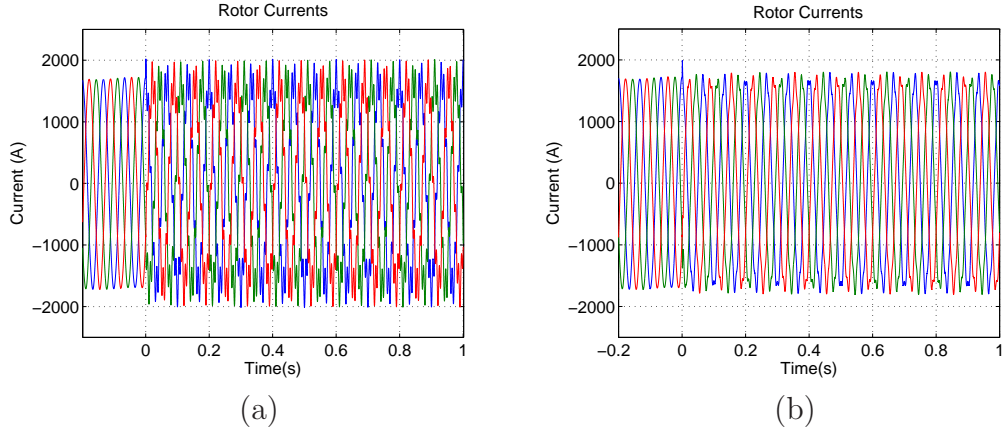


Figure 6.4: Simulation results of the ABC rotor currents (80% phase-neutral voltage sag,  $\theta_0 = 90^\circ$  and 1950 RPM):  
 (a) - Without the CTRP strategy;  
 (b) - With the CTRP strategy.

Of course the effectiveness of the compensation depends on the RSC voltage capability. Observing the rotor voltages in Figure 6.5, it is clearly seen an increase in the amplitude due to the 100Hz component (negative sequence). As the rotor currents are kept under control without high transient, it is possible to decrease the current reference maintaining the converter in safety operation conditions if the demanded voltage is not higher than the maximum RSC limit.

Considering that the rotor currents are under control, the voltage drop in the rotor transient inductance ( $\sigma Lr$ ) is generally small, therefore the maximum converter voltage is given by the open rotor voltage calculated through Equations 4.16 and 4.17. The maximum voltage calculated for the present case (80% phase-neutral sag, 1950 RPM) is 236 V and the simulated result is 242V, as shown in Figure 6.5.

Until now just the case without natural flux component ( $\theta_0 = 90^\circ$ ) was analyzed. Figures 6.6 and 6.7 show the simulation results when appears the maximum natural component ( $\theta_0 = 0^\circ$ ). It is seen that there is no oscillations due to the negative sequence (100Hz) in electromagnetic torque and in the reactive stator power, but the oscillation due to the natural component (50Hz) is not affected.

In the rotor currents, shown in Figure 6.7(b), the positive and the natural

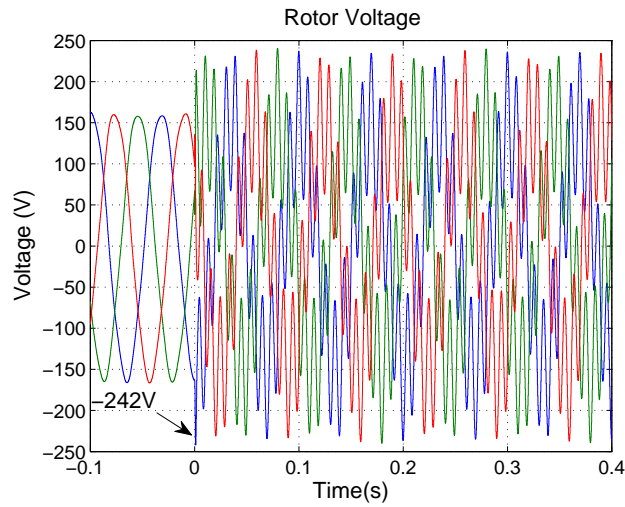


Figure 6.5: Simulation result of the ABC rotor voltages with the CTRP strategy (80% phase-neutral voltage sag,  $\theta_0 = 90^\circ$  and 1950 RPM).

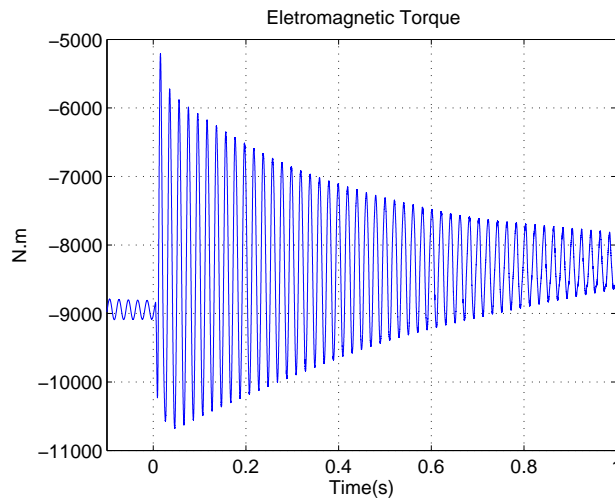


Figure 6.6: Simulation result of the electromagnetic torque with the CTRP strategy (80% phase-neutral voltage sag,  $\theta_0 = 0^\circ$  and 1950 RPM).

components are predominant with small influence of the negative sequence. Even with the elimination of the negative sequence, the rotor currents continue to be high.

The improvement of the response just in the negative sequence were expected because the compensation is tuned just for the  $2\omega_s$ . In order to

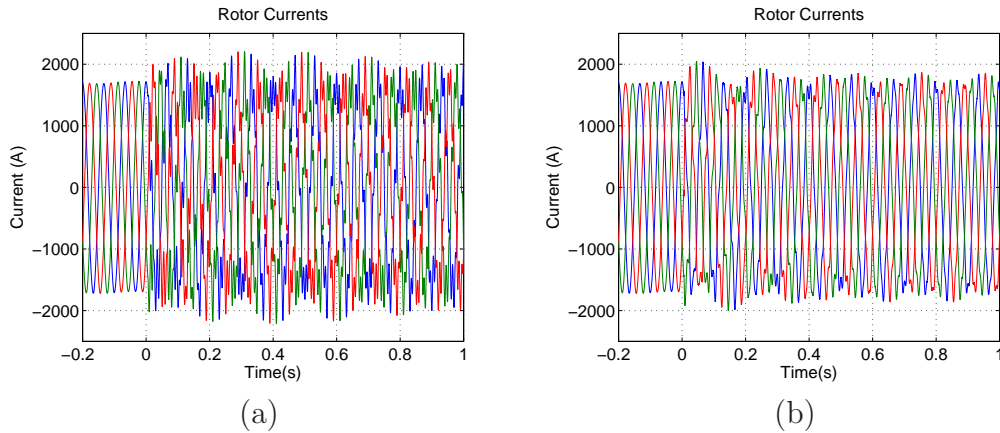


Figure 6.7: Simulation results of the ABC rotor currents (80% phase-neutral voltage sag,  $\theta_0 = 0^\circ$  and 1950 RPM):  
 (a) - Without the CTRP strategy;  
 (b) - With the CTRP strategy.

deal with the natural component it is possible to use the MCC strategy described in Chapter 5.

For example, the Figure 6.8 shows the torque when the CTPR strategy is used in conjunction with the magnetizing current control (MCC). It is seen that the damping of the natural component is increased, similar to the balanced case. The same voltage and current converter restrictions, already analyzed in the balanced case, apply for this case, but now the demanded voltage is higher due to the addition of the compensating terms.

This strategy seems to be simple and efficient, but its performance depends on the compensation transfer functions. The stability of the system is a critical point that must be considered in the control and compensation adjustment. Therefore, several papers in the literature propose the direct control of the negative sequence, as discussed in the following sections.

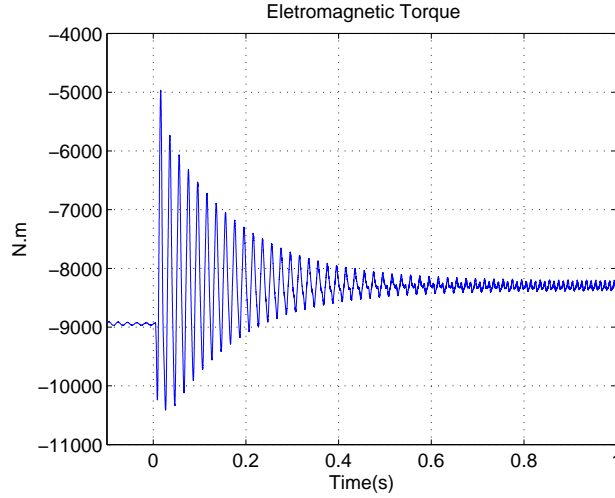


Figure 6.8: Simulation result of the electromagnetic torque with the CTRP+MCC strategy (80% phase-neutral voltage sag,  $\theta_0 = 0^0$  and 1950 RPM).

### 6.3 Dual PI Controllers (DPIC)

The study of the improvement of PWM voltage converters performance during grid voltage unbalances is the aim of some papers in the literature as Song and Nam (1999), Xu et al. (2005), Yin et al. (2008) and Hu and He (2008). These papers propose the independent control of the positive and negative sequences in such a way that average unity power factor is maintained, sinusoidal currents are injected into the grid and the DC-link voltage oscillations are reduced.

In this sense, in the last few years several works extended the use of this control, called dual PI controller (DPIC), to the DFIG topology (Wang et al., 2009), (Xu and Wang, 2007), (Xu, 2008), (Wang et al., 2008), (Wang and Xu, 2010), (Zhou et al., 2009), (Zhou et al., 2007), (Park et al., 2007), (Abokhalil et al., 2007), (Qiao and Harley, 2008), (Fan et al., 2009), (Navarro and Richter, 2007), (Kearney and Conlon, 2008), (Gomis-Bellmunt et al., 2008), (Hu et al., 2009b). These papers present basically the same mathematical development and control structure, which has independent control of the positive and negative rotor current sequences. The coordinated control of the RSC and GSC is also proposed to enhance the system behavior.

With exception of Wang et al. (2009), the other papers analyze the DFIG behavior during long term voltage unbalances, not dealing with the voltage sag transient. Therefore, this section discusses the DPIC strategy behavior during voltage sags.

For the sake of organization, this section is divided in the description of the control strategy, the mathematical modeling during the sag, the calculation of the references, the presentation of simulation results, the analysis of the converter limitations and finally the experimental results are shown.

### 6.3.1 The DPIC strategy

Different from the presented papers, which model the machine in the time domain, here the Laplace domain analysis is carried out. As already shown in Section 4.2, the equations can be separated in positive and negative sequence. Manipulating the machine equations similarly to the balanced case, yields:

$$I_{rdq+}^+(s) = \frac{1}{\sigma L_r s + R_r} V_{rdq+}^+(s) - \frac{s(L_m/L_s)}{\sigma L_r s + R_r} \psi_{sdq+}^+(s) \pm \frac{\omega_{r+} [\sigma L_r I_{rqd+}^+(s) + (L_m/L_s) \psi_{sqd+}^+(s)]}{\sigma L_r s + R_r}, \quad (6.2)$$

$$I_{rdq-}^-(s) = \frac{1}{\sigma L_r s + R_r} V_{rdq-}^-(s) - \frac{s(L_m/L_s)}{\sigma L_r s + R_r} \psi_{sdq-}^-(s) \pm \frac{\omega_{r-} [\sigma L_r I_{rqd-}^-(s) + (L_m/L_s) \psi_{sqd-}^-(s)]}{\sigma L_r s + R_r}. \quad (6.3)$$

Through Equations 6.2 and 6.3 one can notice that it is possible to control the negative sequence of the rotor currents imposing with the converter negative sequence voltages, similar to the positive sequence. The second term on these equations depends on the derivative of the stator flux, therefore they are different from zero just during stator voltage transients. The last terms are the cross coupling ( $cc_{r+}$  and  $cc_{r-}$ ) terms and can be used as a compensators similar to the classical control strategy.

In order to control independently the current positive and negative sequences it is necessary to “extract” them from the measured signal. There are

many ways to realize this separation (Zhou et al., 2009). Based on the fact that the negative sequence appears as a pulsation with the double of the grid frequency in the positive synchronous rotating frame and that the positive sequence appears as a pulsation with the double of the grid frequency in the negative synchronous rotating frame, band-trap filters are used to separate the sequence components. The filters are adjusted to reject the frequencies in the vicinity of  $2\omega_s$ . In this work the following filter is used:

$$Filter(s) = \frac{s^2 + (2\omega_s)^2}{s^2 + 2\frac{\omega_s}{q}s + (2\omega_s)^2}, \quad (6.4)$$

where the factor  $q$  defines the selectivity of the filter and also affects the response speed. It is important to remove the  $2\omega_s$  frequency as fast as possible, thus a  $q$  equal to 1 is used.

Using Equation 4.23, the total rotor voltage to be imposed by the converter is given as:

$$V_{r_{dq}}^+ = V_{r_{dq+}}^+ + V_{r_{dq-}}^+ = V_{r_{dq+}}^+ + V_{r_{dq-}}^- e^{-j2\omega_s t}. \quad (6.5)$$

Figure 6.9 depicts the control structure used in the RSC. The references of the positive sequences are given by the power control external loops and the negative sequence references are calculated in such a way that some targets are accomplished. The control of the GSC is similar to the RSC and it is shown in Figure 6.10. Details about the references calculation are described hereafter.

The gains of the negative sequence control are equal to the positive control, because the dynamics of both are similar, as shown in Equations 6.2 and 6.3.

Besides the filter, another factor that affects the control performance is the correct estimation of the voltage angle used for the orientation. For a good estimation of the grid and stator voltage angles even during unbalanced conditions, the ‘‘Dual Second Order Generalized Integrator’’ (PSOGI) is used (Rodriguez et al., 2006). The PSOGI was described in Chapter 2 and its block diagram was presented in Figure 2.4.



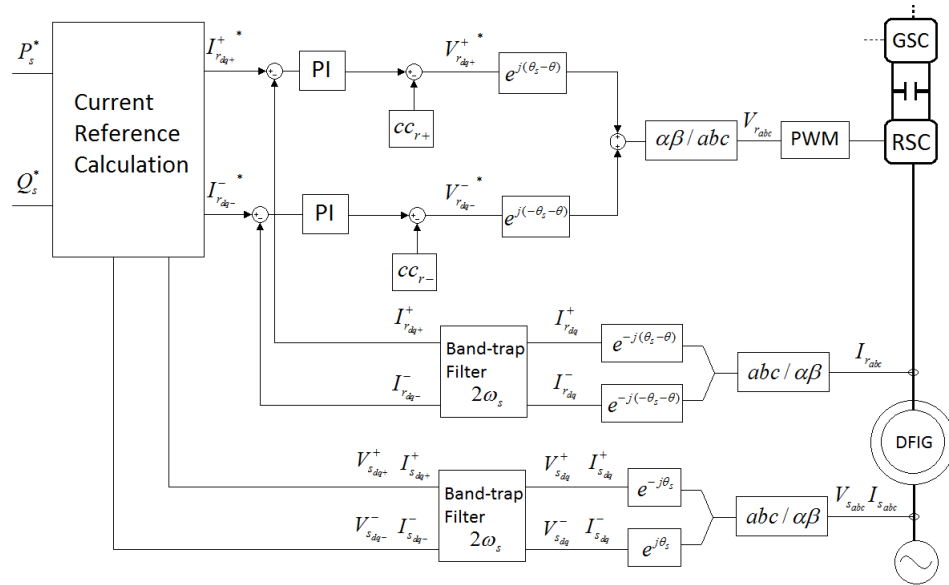


Figure 6.9: Control of positive and negative current sequences in the RSC .

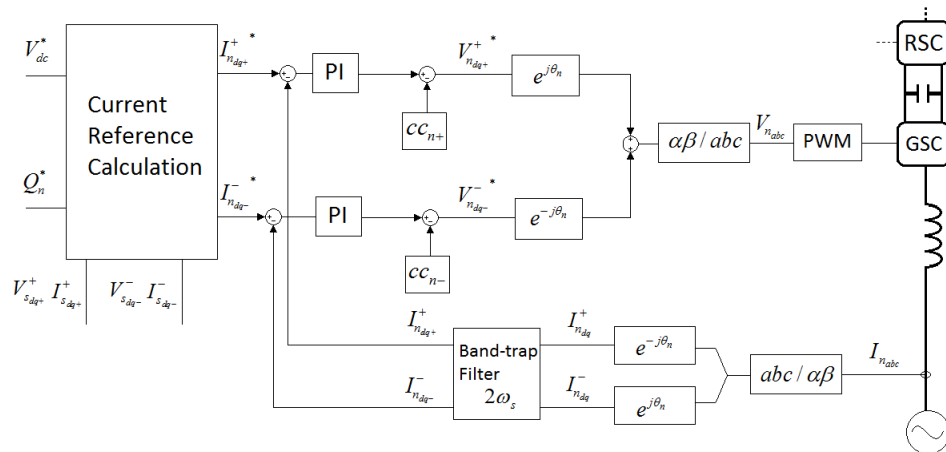


Figure 6.10: Control of positive and negative current sequences in the GSC.

### 6.3.2 Mathematical modeling during the voltage sags

In Chapter 4 the stator flux linkage and the rotor current transfer functions were calculated for the classical control structure. In this section a similar development is carried out, but in spite of using both sequence components in the positive synchronous reference frame, the equations are divided in positive and negative reference frames.

With the DPIC strategy both sequence components are controlled independently, thus Equations 4.39 and 4.40 can be rewritten as:

$$I_{r_{dq+}}^+(s) = \frac{1}{\sigma L_r s + R_r} \left( \frac{K_p s + K_i}{s} \right) \left( I_{r_{dq+}}^{+*}(s) - I_{r_{dq+}}^+(s) \right) - \frac{s(L_m/L_s)}{\sigma L_r s + R_r} \psi_{sdq+}^+(s), \quad (6.6)$$

$$I_{r_{dq-}}^-(s) = \frac{1}{\sigma L_r s + R_r} \left( \frac{K_p s + K_i}{s} \right) \left( I_{r_{dq-}}^{-*}(s) - I_{r_{dq-}}^-(s) \right) - \frac{s(L_m/L_s)}{\sigma L_r s + R_r} \psi_{sdq-}^-(s). \quad (6.7)$$

Considering the rotor current references null, as previously, the transient response of the rotor current components are given as follows:

$$I_{r_{dq+}}^{+t}(s) = \frac{-s^2(L_m/L_s)}{\sigma L_r s^2 + (K_p + R_r)s + K_i} \psi_{sdq+}^{+t}(s) \quad (6.8)$$

$$I_{r_{dq-}}^{-t}(s) = \frac{-s^2(L_m/L_s)}{\sigma L_r s^2 + (K_p + R_r)s + K_i} \psi_{sdq-}^{-t}(s) \quad (6.9)$$

Substituting Equations 6.8 and 6.9 in 4.32 and 4.33, yields:

$$\psi_{sd\pm}^{\pm t} = \frac{(s + 1/\tau_s)(\sigma L_r s^2 + (K_p + R_r)s + K_i)}{\left(s^2 + 2\frac{1}{\tau_s}s + \omega_s^2\right)(\sigma L_r s^2 + (K_p + R_r)s + K_i) + \frac{1}{\tau_s} \frac{L_m^2}{L_s} s^2 \left(s + \frac{1}{\tau_s}\right)} V_{sd\pm}^{\pm}, \quad (6.10)$$

$$\psi_{s_{q\pm}}^{\pm t} = \frac{\mp\omega_s (\sigma L_r s^2 + (K_p + R_r) s + K_i)}{\left(s^2 + 2\frac{1}{\tau_s} s + \omega_s^2\right) (\sigma L_r s^2 + (K_p + R_r) s + K_i) + \frac{1}{\tau_s} \frac{L_m^2}{L_s} s^2 \left(s + \frac{1}{\tau_s}\right)} V_{s_{d\pm}}^{\pm}, \quad (6.11)$$

where the dependence “(s)” was omitted to simplify the notation. As expected, the positive sequence components oriented in the positive synchronous frame have the same dynamics of the balanced case. The negative sequence components oriented in the negative synchronous frame also have a similar dynamics. Therefore, the control gains may affect the frequency oscillation of the natural stator flux response and the flux damping in both positive and negative sequences.

Although positive and negative sequence have the same dynamics in their respective reference frames, when they are referred to a common reference in order to reconstruct the total response, their frequencies are different. Equation 6.12 shows that in the synchronous frame the total stator flux linkage has a DC component due to the positive sequence and the negative sequence appears as an oscillation with the double of the grid frequency, exactly as in the classical strategy.

$$\psi_{s_{dq}}^+ = \psi_{s_{dq+}}^+ + \psi_{s_{dq-}}^+ = \psi_{s_{dq+}}^+ + \psi_{s_{dq-}}^- e^{-j2\omega_s t} \quad (6.12)$$

One can notice that the flux oscillations caused by the negative sequences are not affected by the control action, but, as previously stated, the rotor currents depends on the control adjustment.

### 6.3.3 Calculation of the rotor current references

The development carried out in the last subsection represents the condition where the rotor current references are set to zero. Choosing the references equal to zero the currents flowing through the converter are decreased, avoiding the RSC to trip or be damaged. This strategy, which will be called *Target I*, is useful as a protection, but has the drawback that the torque and power oscillations continue to exist, as will be shown in the simulation results. To deal with these issues Xu and Wang (2007) and Hu et al. (2009b)

propose different methods to calculate the current references.

Before showing the calculation of the references, it is necessary to present the modeling of the power and torque during a voltage unbalance. The apparent stator power is calculated using:

$$S_s = P_s + jQ_s = \frac{3}{2} \vec{v}_s \cdot \vec{\hat{i}}_s = \frac{3}{2} \left\{ \left( V_{s_d}^+ I_{s_d}^+ + V_{s_q}^+ I_{s_q}^+ \right) + j \left( V_{s_q}^+ I_{s_d}^+ - V_{s_d}^+ I_{s_q}^+ \right) \right\} \quad (6.13)$$

where “ $\hat{\phantom{x}}$ ” represents the complex conjugate. In this equation the negative signal of the power indicates that the machine is in the generation mode. Using Equation 4.23 to decompose the sequence components and using the Euler identity, Equation 6.13 can be rewritten as (Gomis-Bellmunt et al., 2008):

$$P_s = P_{s_0} + P_{s_{\cos}} \cos(2\omega_s t) + P_{s_{\sin}} \sin(2\omega_s t) \quad (6.14)$$

$$Q_s = Q_{s_0} + Q_{s_{\cos}} \cos(2\omega_s t) + Q_{s_{\sin}} \sin(2\omega_s t) \quad (6.15)$$

where:

$$\begin{bmatrix} P_{s_0} \\ P_{s_{\cos}} \\ P_{s_{\sin}} \\ Q_{s_0} \\ Q_{s_{\cos}} \\ Q_{s_{\sin}} \end{bmatrix} = \frac{3}{2} \begin{bmatrix} V_{s_{d+}}^+ & V_{s_{q+}}^+ & V_{s_{d-}}^- & V_{s_{q-}}^- \\ V_{s_{d-}}^- & V_{s_{q-}}^- & V_{s_{d+}}^+ & V_{s_{q+}}^+ \\ V_{s_{q-}}^- & -V_{s_{d-}}^- & -V_{s_{q+}}^+ & V_{s_{d+}}^+ \\ V_{s_{q+}}^+ & -V_{s_{d+}}^+ & V_{s_{q-}}^- & -V_{s_{d-}}^- \\ V_{s_{q-}}^- & -V_{s_{d-}}^- & V_{s_{q+}}^+ & -V_{s_{d+}}^+ \\ -V_{s_{d-}}^- & -V_{s_{q-}}^- & V_{s_{d+}}^+ & V_{s_{q+}}^+ \end{bmatrix} \begin{bmatrix} I_{s_{d+}}^+ \\ I_{s_{q+}}^+ \\ I_{s_{d-}}^- \\ I_{s_{q-}}^- \end{bmatrix}. \quad (6.16)$$

In these equations it is clearly seen the oscillations in the active and reactive power due to the voltage and current negative sequences. Using Equations 4.24, 4.25, 4.28 and 4.29, if the voltage drop in the stator resistance is neglected, one can notice that, in steady state, the stator currents are related to the rotor currents according to:

$$I_{s_{d\pm}}^{\pm} = \pm \frac{V_{s_{q\pm}}^{\pm}}{\omega_s L_s} - \frac{L_m I_{r_{d\pm}}^{\pm}}{L_s}, \quad (6.17)$$

$$I_{s_{d\pm}}^{\pm} = \pm \frac{V_{s_{q\pm}}^{\pm}}{\omega_s L_s} - \frac{L_m I_{r_{d\pm}}^{\pm}}{L_s}. \quad (6.18)$$

Therefore, Equation 6.16 can be rewritten as following:

$$\begin{aligned} \begin{bmatrix} P_{s_0} \\ P_{s_{\cos}} \\ P_{s_{\sin}} \\ Q_{s_0} \\ Q_{s_{\cos}} \\ Q_{s_{\sin}} \end{bmatrix} &= -\frac{3L_m}{2L_s} \begin{bmatrix} V_{s_{d+}}^+ & V_{s_{q+}}^+ & V_{s_{d-}}^- & V_{s_{q-}}^- \\ V_{s_{d-}}^- & V_{s_{q-}}^- & V_{s_{d+}}^+ & V_{s_{q+}}^+ \\ V_{s_{q-}}^- & -V_{s_{d-}}^- & -V_{s_{q+}}^+ & V_{s_{d+}}^+ \\ V_{s_{q+}}^+ & -V_{s_{d+}}^+ & V_{s_{q-}}^- & -V_{s_{d-}}^- \\ V_{s_{q-}}^- & -V_{s_{d-}}^- & V_{s_{q+}}^+ & -V_{s_{d+}}^+ \\ -V_{s_{d-}}^- & -V_{s_{q-}}^- & V_{s_{d+}}^+ & V_{s_{q+}}^+ \end{bmatrix} \begin{bmatrix} I_{r_{d+}}^+ \\ I_{r_{q+}}^+ \\ I_{r_{d-}}^- \\ I_{r_{q-}}^- \end{bmatrix} \\ &+ \frac{3}{2\omega_s L_s} \begin{bmatrix} V_{s_{d+}}^+ & -V_{s_{q+}}^+ & -V_{s_{d-}}^- & V_{s_{q-}}^- \\ V_{s_{d-}}^- & -V_{s_{q-}}^- & -V_{s_{d+}}^+ & V_{s_{q+}}^+ \\ V_{s_{q-}}^- & V_{s_{d-}}^- & V_{s_{q+}}^+ & V_{s_{d+}}^+ \\ V_{s_{q+}}^+ & V_{s_{d+}}^+ & -V_{s_{q-}}^- & -V_{s_{d-}}^- \\ V_{s_{q-}}^- & V_{s_{d-}}^- & -V_{s_{q+}}^+ & -V_{s_{d+}}^+ \\ -V_{s_{d-}}^- & V_{s_{q-}}^- & -V_{s_{d+}}^+ & V_{s_{q+}}^+ \end{bmatrix} \begin{bmatrix} V_{s_{q+}}^+ \\ V_{s_{d+}}^+ \\ V_{s_{q-}}^- \\ V_{s_{d-}}^- \end{bmatrix}. \end{aligned} \quad (6.19)$$

Similarly the electromagnetic power is given by (Hu et al., 2009b):

$$\begin{aligned} P_e &= \frac{3}{2} \text{Re} \left[ j\omega_s \vec{\psi}_s \cdot \vec{\hat{i}}_s + j\omega_r \vec{\psi}_r \cdot \vec{\hat{i}}_r \right] = -\frac{3}{2} \frac{L_m}{L_s} \omega \text{Re} \left[ j \vec{\psi}_s \cdot \vec{\hat{i}}_r \right], \\ &= P_{e_0} + P_{e_{\sin}} \sin(2\omega_s t) + P_{e_{\cos}} \cos(2\omega_s t) \end{aligned} \quad (6.20)$$

with

$$\begin{bmatrix} P_{e0} \\ P_{e\sin} \\ P_{e\cos} \end{bmatrix} = -\frac{3 L_m \omega}{2 L_s \omega_s} \begin{bmatrix} V_{sd+}^+ & V_{sq+}^+ & -V_{sd-}^- & -V_{sq-}^- \\ -V_{sq-}^- & V_{sd-}^- & -V_{sq+}^+ & V_{sd+}^+ \\ -V_{sd-}^- & -V_{sq-}^- & V_{sd+}^+ & V_{sq+}^+ \end{bmatrix} \begin{bmatrix} I_{rd+}^+ \\ I_{rq+}^+ \\ I_{rd-}^- \\ I_{rq-}^- \end{bmatrix}. \quad (6.21)$$

The electromagnetic torque is calculated through:

$$T_e = \frac{P_e}{\omega_m}. \quad (6.22)$$

Using the orientation in the angle of the grid voltage  $V_{sq+}^+ = 0$ , thus further simplifications can be made in the previous equations.

Through Equations 6.19 to 6.21 it is seen that the rotor current components  $(I_{rd+}^+, I_{rq+}^+, I_{rd-}^-, I_{rq-}^-)$  affect the torque and power oscillation. Therefore, these currents can be controlled independently in order to reduce the oscillations. It is noticeable that due to the limited number of controlled variables it is not possible to achieve the elimination of both power and torque oscillations (Xu and Wang, 2007). Different control targets are proposed in Xu and Wang (2007) and Hu et al. (2009b).

*Target I* was already defined and it intends to reduce the rotor currents setting the references of the negative sequence to zero:

$$I_{rd-}^{*} = 0 \quad I_{rq-}^{*} = 0. \quad (6.23)$$

The references of the positive sequence can be adjusted in such a way that the converter limits are not exceeded and supplying the desired mean active or reactive power. Using Equation 6.19, these references are given as:

$$I_{rd+}^{*} = \frac{2 L_s P_{s0}^*}{3 L_m V_{sd+}^+} \quad I_{rq+}^{*} = -\frac{L_s \left( \frac{2}{3} Q_{s0}^* + \frac{D_1}{\omega_s L_s} \right)}{L_m V_{sd+}^+}, \quad (6.24)$$

where  $D_1 = V_{sd+}^{+2} - (V_{sd-}^{-2} + V_{sq-}^{-2})$ .

*Target II* intends to warrant balanced stator currents in order to ensure balanced heating in the stator windings. For this purpose is necessary to eliminate the stator currents negative sequence. Through Equations 6.17 and 6.18, setting  $I_{s_{d-}}^- = 0$  and  $I_{s_{q-}}^- = 0$ , yields:

$$I_{r_{d-}}^{-*} = -\frac{V_{s_{q-}}^-}{L_m \omega_s} \quad I_{r_{q-}}^{-*} = \frac{V_{s_{d-}}^-}{L_m \omega_s}. \quad (6.25)$$

Through Equation 6.19 the positive sequence references are calculated as:

$$I_{r_{d+}}^{+*} = \frac{2}{3} \frac{L_s P_{s_0}^*}{L_m V_{s_{d+}}^+} \quad I_{r_{q+}}^{+*} = -\frac{L_s \left( \frac{2}{3} Q_{s_0}^* + \frac{D_1}{\omega_s L_s} \right)}{L_m V_{s_{d+}}^+}. \quad (6.26)$$

With *Target III* the objective is to eliminate the pulsation in the active stator power, improving the system power capability. Making  $P_{s_{\sin}} = 0$  and  $P_{s_{\cos}} = 0$  in Equation 6.19, the references of the positive and negative sequence are calculated through:

$$I_{r_{d-}}^{-*} = -\frac{2V_{s_{q-}}^-}{L_m \omega_s} - k_{dd} I_{r_{d+}}^+ - k_{qd} I_{r_{q+}}^+ \quad I_{r_{q-}}^{-*} = \frac{2V_{s_{d-}}^-}{L_m \omega_s} - k_{qd} I_{r_{d+}}^+ + k_{dd} I_{r_{q+}}^+, \quad (6.27)$$

$$I_{r_{d+}}^{+*} = \frac{2}{3} \frac{L_s P_{s_0}^* V_{s_{d+}}^+}{L_m D_1} \quad I_{r_{q+}}^{+*} = -\frac{2}{3} \frac{L_s V_{s_{d+}}^+ Q_{s_0}^*}{L_m D_2} - \frac{V_{s_{d+}}^+}{L_m \omega_s}, \quad (6.28)$$

where  $k_{dd} = V_{s_{d-}}^- / V_{s_{d+}}^+$ ,  $k_{qd} = V_{s_{q-}}^- / V_{s_{d+}}^+$  and  $D_2 = V_{s_{d+}}^{+2} + V_{s_{d-}}^{-2} + V_{s_{q-}}^{-2}$ .

Using *Target IV* the electromagnetic torque is reduced, reducing the mechanical stresses in the system. For this, it is necessary to do  $P_{e_{\sin}} = 0$  and  $P_{e_{\cos}} = 0$  in the Equation 6.21, giving the following references:

$$I_{r_{d-}}^{-*} = k_{dd} I_{r_{d+}}^+ + k_{qd} I_{r_{q+}}^+ \quad I_{r_{q-}}^{-*} = k_{qd} I_{r_{d+}}^+ - k_{dd} I_{r_{q+}}^+. \quad (6.29)$$

$$I_{r_{d+}}^{+*} = \frac{2 L_s V_{s_{d+}}^+ P_{s_0}^*}{3 L_m D_2} \quad I_{r_{q+}}^{+*} = -\frac{2 L_s V_{s_{d+}}^+ Q_{s_0}^*}{3 L_m D_1} - \frac{V_{s_{d+}}^+}{L_m \omega_s}. \quad (6.30)$$

The target should be chosen accordingly to the desired objective, but the converter limitations, which is analyzed hereafter, must not be exceeded.

### 6.3.4 Calculation of the grid current references

As in the RSC, it is also possible to use in the GSC the decoupled control of positive and negative sequences. Wang et al. (2008), Wang and Xu (2010) and Pena et al. (2007) propose the use of the GSC to inject into the grid negative sequence currents, permitting the rebalance of the voltages in the common connection point. The rebalance of the grid voltages through control normally is just possible when the unbalance is small and/or the grid has low short-circuit (weak grid). These are specific situations and are not treated in this work.

The proposed GSC control studied in this section intends to reduce the oscillations in the total active power supplied to the grid, as presented in Xu (2008), Zhou et al. (2007), Qiao and Harley (2008) and Fan et al. (2009).

As in the generator stator, the power flowing through the GSC is given by:

$$P_n = P_{n_0} + P_{n_{\cos}} \cos(2\omega_s t) + P_{n_{\sin}} \sin(2\omega_s t), \quad (6.31)$$

$$Q_n = Q_{n_0} + Q_{n_{\cos}} \cos(2\omega_s t) + Q_{n_{\sin}} \sin(2\omega_s t), \quad (6.32)$$

where:



$$\begin{bmatrix} P_{n_0} \\ P_{n_{\cos}} \\ P_{n_{\sin}} \\ Q_{n_0} \\ Q_{n_{\cos}} \\ Q_{n_{\sin}} \end{bmatrix} = \frac{3}{2} \begin{bmatrix} V_{n_{d+}}^+ & V_{n_{q+}}^+ & V_{n_{d-}}^- & V_{n_{q-}}^- \\ V_{n_{d-}}^- & V_{n_{q-}}^- & V_{n_{d+}}^+ & V_{n_{q+}}^+ \\ V_{n_{q-}}^- & -V_{n_{d-}}^- & -V_{n_{q+}}^+ & V_{n_{d+}}^+ \\ V_{n_{q+}}^+ & -V_{n_{d+}}^+ & V_{n_{q-}}^- & -V_{n_{d-}}^- \\ V_{n_{q-}}^- & -V_{n_{d-}}^- & V_{n_{q+}}^+ & -V_{n_{d+}}^+ \\ -V_{n_{d-}}^- & -V_{n_{q-}}^- & V_{n_{d+}}^+ & V_{n_{q+}}^+ \end{bmatrix} \begin{bmatrix} I_{n_{d+}}^+ \\ I_{n_{q+}}^+ \\ I_{n_{d-}}^- \\ I_{n_{q-}}^- \end{bmatrix}. \quad (6.33)$$

Through Equations 6.14 and 6.31 the total active power flowing to the grid is calculated as:

$$P_{total} = P_n + P_s = (P_{s_0} + P_{n_0}) + (P_{s_{\cos}} + P_{n_{\cos}}) \cos(2\omega_s t) + (P_{s_{\sin}} + P_{n_{\sin}}) \sin(2\omega_s t). \quad (6.34)$$

Therefore, to minimize the oscillations in the total active power it is necessary to make:

$$\begin{aligned} P_{s_{\cos}} + P_{n_{\cos}} &= 0 \\ P_{s_{\sin}} + P_{n_{\sin}} &= 0 \end{aligned}. \quad (6.35)$$

Combining Equations 6.33 and 6.35, the grid current negative sequence references are given as:

$$I_{n_{d-}}^{-*} = \frac{3 P_{s_{\cos}}}{2 V_{s_{d+}}^+} - k_{dd} I_{n_{d+}}^+ - k_{qd} I_{n_{q+}}^+ \quad I_{n_{q-}}^{-*} = \frac{3 P_{s_{\sin}}}{2 V_{s_{d+}}^+} - k_{qd} I_{n_{d+}}^+ + k_{dd} I_{n_{q+}}^+, \quad (6.36)$$

where  $P_{s_{\sin}}$  and  $P_{s_{\cos}}$  are calculated using Equation 6.19.

If the GSC is capable of eliminating the oscillations in the total power flowing to the grid, it is interesting to use the *Target IV* in the RSC, because the mechanical stresses are reduced through the RSC control and the power quality are increased with the GSC control.

### 6.3.5 Simulation results

For the simulation of the 2-MW system, the following conditions were considered:

- Rated operation, i.e., machine rotating with fixed 1950 RPM and supplying 2 MW to the grid;
- Unity power factor, i.e.,  $Q_s = 0$ ;
- The DC-link voltage was set high enough (1200V) to ensure the operation of the control strategies without saturation;
- As proposed by Xu (2008), the feedback of the positive sequence controls is given by the total current without sequence decomposition. Using this artifice the positive control “helps” the negative sequence control;
- During the sag the reference of the rotor current positive sequences are set equal to the value immediately before the voltage drop. This strategy was employed to avoid other transients that not the ones caused by the voltage unbalance.

Before starting the analysis, it is necessary to clarify some definitions. There are different ways to measure the current and voltage unbalance. Here the definition used in Brekken and Mohan (2007) is applied, which says that the percentage of unbalance is given by the negative sequence component divided by the positive one:

$$VUF(\%) = \left| \frac{A_-}{A_+} \right| * 100\% \quad (6.37)$$

Another important value is the percentage of the oscillations for the power, torque and DC-link voltage. In this work this value is defined as the amplitude of the 100Hz oscillation component normalized by the DC component.

Simulating the case when there is no natural component ( $\theta_0 = 90^\circ$ ), Table 6.1 shows the percentage of unbalance for the currents and voltages,

the percentage of the 100Hz oscillations in the power, torque and DC-link voltage for different voltage sags and different control targets. Furthermore, the maximum rotor voltage absolute value is given.

Table 6.1: Percentage of unbalance and of oscillations for different simulated voltage sags ( $\theta_0 = 90^\circ$ ).

	<i>No strategy</i>			<i>Target I</i>			<i>Target II</i>		
<i>VUF</i> (%)	7.12	20	50	7.12	20	50	7.12	20	50
<i>I<sub>rd</sub></i> (%)	29.2	73.2	146	<b>0.03</b>	<b>0.07</b>	<b>0.15</b>	0.03	0.08	0.16
<i>I<sub>rq</sub></i> (%)	25.9	64.9	129	<b>0.51</b>	<b>1.28</b>	<b>2.56</b>	6.982	17.46	34.93
<i>I<sub>sd</sub></i> (%)	29.3	73.3	146	0.01	0.04	0.08	<b>0.026</b>	<b>0.066</b>	<b>0.134</b>
<i>I<sub>sq</sub></i> (%)	493	492	491	92.3	92.4	92.4	<b>5.79</b>	<b>5.80</b>	<b>5.81</b>
<i>T<sub>e</sub></i> (%)	26.9	45.1	53.0	6.01	12.2	18.7	5.577	11.34	17.31
<i>P<sub>s</sub></i> (%)	20.5	40.2	60.5	6.65	15.2	29.1	6.293	14.72	28.59
<i>Q<sub>s</sub></i> (%)	87.3	83.7	78.1	67.1	66.7	56.6	65.56	65.06	61.70
<i>P<sub>t</sub></i> (%)	15.2	24.6	13.1	5.89	13.2	23.1	5.377	12.53	23.01
<i>V<sub>dc</sub></i> (%)	0.04	0.12	0.27	0.03	0.08	0.17	0.034	0.087	0.181
<i>V<sub>r</sub></i> (V)	244	347	519	244	353	535	249	366	560
	<i>Target III</i>			<i>Target IV</i>			<i>Target. IV+GSC</i>		
<i>VUF</i> (%)	7.12	20	50	7.12	20	50	7.12	20	50
<i>I<sub>rd</sub></i> (%)	6.95	19.4	48.7	7.01	19.6	49.0	7.016	19.63	49.07
<i>I<sub>rq</sub></i> (%)	6.47	14.1	18.4	7.49	20.8	51.4	7.491	20.81	51.40
<i>I<sub>sd</sub></i> (%)	6.95	19.4	48.7	7.01	19.6	49.0	7.010	19.62	49.03
<i>I<sub>sq</sub></i> (%)	1.10	13.6	43.0	12.7	25.2	54.6	12.70	25.29	54.66
<i>T<sub>e</sub></i> (%)	10.4	19.3	23.3	<b>0.13</b>	<b>0.27</b>	<b>0.40</b>	<b>0.139</b>	<b>0.271</b>	<b>0.400</b>
<i>P<sub>s</sub></i> (%)	<b>0.37</b>	<b>1.57</b>	<b>6.31</b>	11.9	25.6	40.1	11.91	25.65	40.15
<i>Q<sub>s</sub></i> (%)	84.5	81.7	65.7	43.5	40.5	29.7	43.50	40.59	29.76
<i>P<sub>t</sub></i> (%)	1.27	3.97	17.0	9.47	20.1	25.8	<b>0.750</b>	<b>1.870</b>	<b>3.057</b>
<i>V<sub>dc</sub></i> (%)	0.03	0.09	0.22	0.03	0.07	0.13	0.015	0.037	0.056
<i>V<sub>r</sub></i> (V)	249	364	550	252	374	589	252	374	589

As described earlier, each target aims the reduction of the unbalance or pulsation in a specific variable. Therefore, in the Table 6.1 the values referent to each target is bolded, showing the reduction in its values when compared with the other cases.

Figures 6.11 to 6.16 show some simulation results for the different targets, testing a 50% phase-neutral sag ( $VUF = 20\%$ ). For each variable plotted,

it is shown just the result for the target that change the behavior of this variable.

Figure 6.11 shows the rotor currents without ride-through strategies and using the DPIC-*Target I* strategy. There is an initial transient that increases momentarily the currents, but after a short time it is seen that the negative sequence disappears. These transients come from the dynamics imposed by the filter that delays the decomposition in positive and negative sequence. With the use of the *Target I*, the negative sequence (100Hz oscillation) is eliminated after the transient, thus it is seen smaller currents compared with the case without strategies. In order to protect the converter, it is interesting to control the negative sequence to zero during the transient and after one of the other targets can be set, limiting the reference according to the RSC capability.

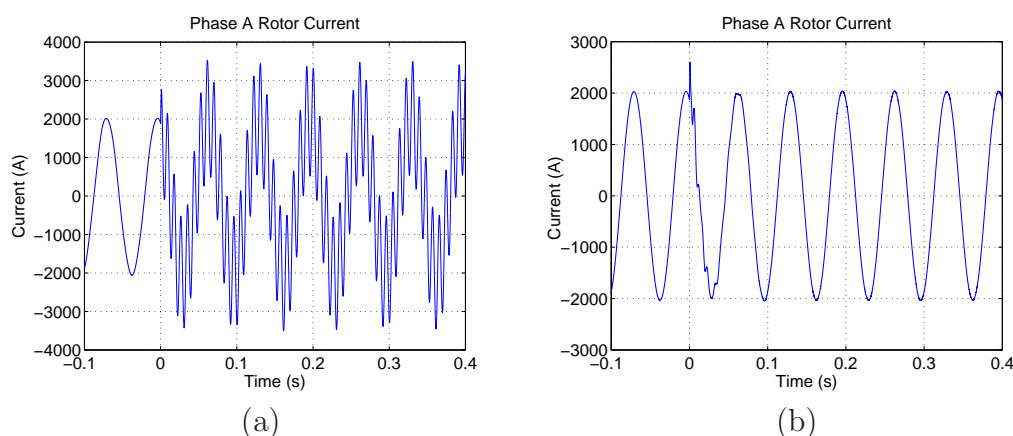


Figure 6.11: Simulation results of the phase A of the rotor currents (50% phase-neutral voltage sag,  $\theta_0 = 90^\circ$  and 1950 RPM):

- (a) - Without RTFC strategies;
- (b) - With the DPIC-*Target I* strategy.

Observing Figure 6.12 one can notice that the use of the strategy increases the rotor voltages imposed by the RSC of just 10V. Table 6.1 show that for the same voltage sag amplitude, the rotor voltage maximum values for the different targets do not differ so much. It is clearly seen in the rotor voltage the presence of the positive sequence superimposed to the negative one. In the next subsection the theoretical value of the maximum rotor voltage is deduced.

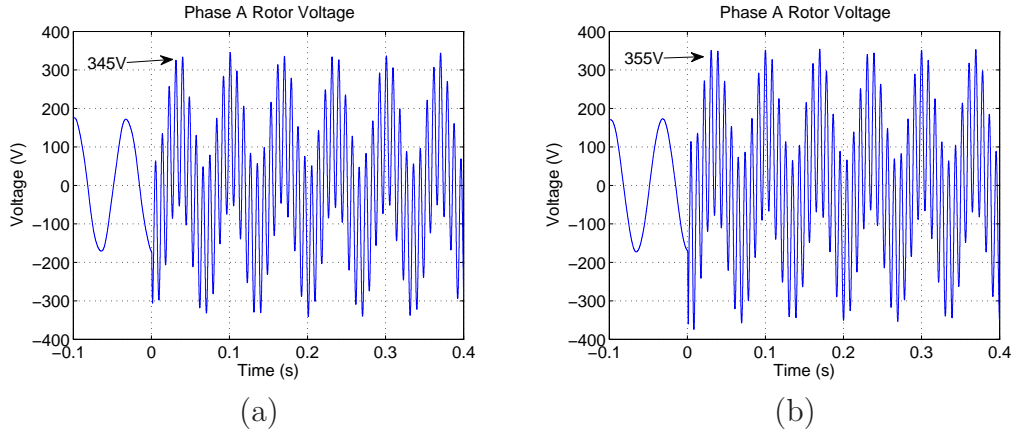


Figure 6.12: Simulation results of the phase A of the rotor voltages (50% phase-neutral voltage sag,  $\theta_0 = 90^\circ$  and 1950 RPM):  
 (a) - Without RTFC strategies;  
 (b) - With the DPIC-*Target I* strategy.

With the use of the *Target II* the unbalance in the stator currents is almost eliminated, as shown Figure 6.13. The Table 6.1 indicates that the Target I also reduces much the stator currents unbalance, whilst the Target III and Target VI the unbalance is higher, but even less than the classical control. It is important to reduce the unbalance in the currents mostly for the permanent voltage unbalances, but during voltage sags, which generally have duration less than 2 seconds, the unequal heating in the windings is not an issue.

The *Target III*, as expected, reduces the active stator power oscillations, as demonstrated in Figure 6.14. In the other hand, the oscillation in the reactive power continues to be high. During voltage sags maybe it is more important to reduce the oscillation in the reactive power and reduce the active power supplied to the grid.

With the guaranty of safety operation of the RSC, probably the most important oscillations to be mitigated is the electromagnetic torque, because the mechanical stresses in the drive train reduces its life time, increasing the cost of maintenance. It is seen in Figure 6.15 that the use of the DPIC with the *Target IV* reduces considerably the torque oscillations. In the sag beginning the transient continues to cause high torque oscillations, therefore some extra strategy should be used.

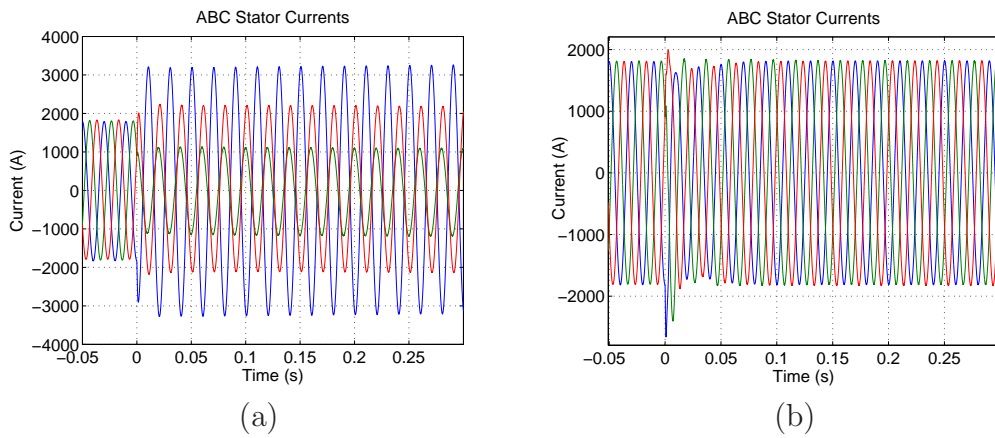


Figure 6.13: Simulation results of the ABC stator currents (50% phase-neutral voltage sag,  $\theta_0 = 90^\circ$  and 1950 RPM):  
 (a) - Without RTFC strategies;  
 (b) - With the DPIC-*Target II* strategy.

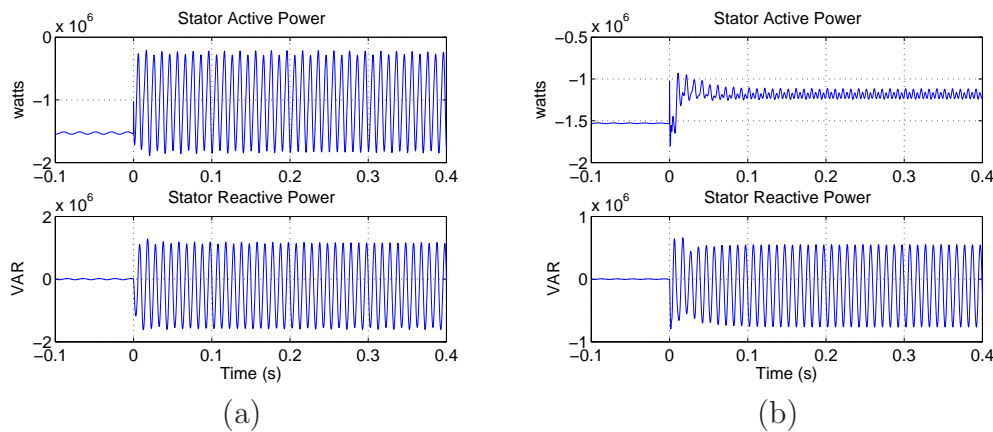


Figure 6.14: Simulation results of the stator active and reactive powers (50% phase-neutral voltage sag,  $\theta_0 = 90^\circ$  and 1950 RPM):  
 (a) - Without RTFC strategies;  
 (b) - With the DPIC-*Target III* strategy.

Figure 6.16 shows the simulation result when the *Target IV* is used coordinated with the control of the GSC. One can notice that injection of negative sequence currents into the grid compensates the stator active power oscillations, therefore reducing the total active power.

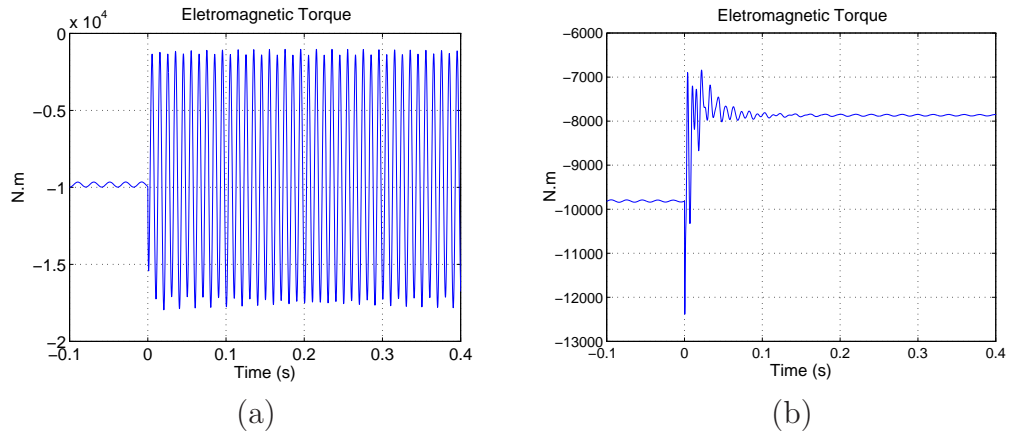


Figure 6.15: Simulation results of the electromagnetic torque (50% phase-neutral voltage sag,  $\theta_0 = 90^\circ$  and 1950 RPM):  
 (a) - Without RTFC strategies;  
 (b) - With the DPIC-Target IV strategy.

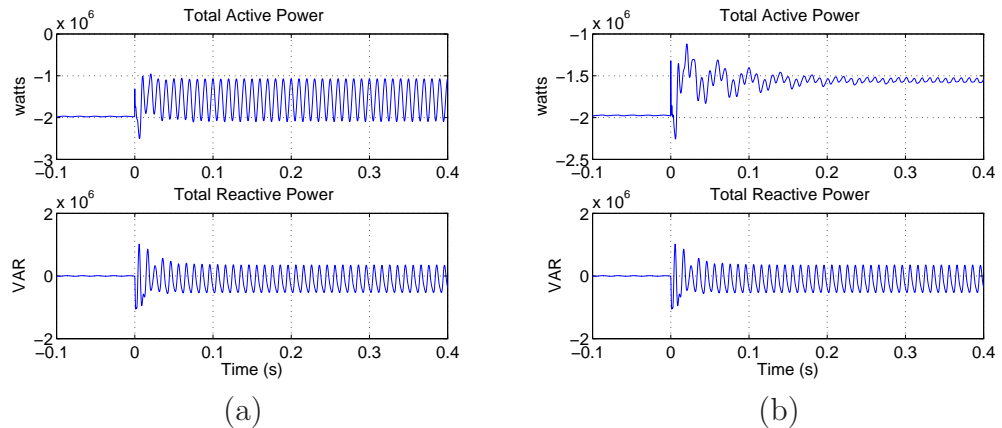


Figure 6.16: Simulation results of the total active and reactive powers (50% phase-neutral voltage sag,  $\theta_0 = 90^\circ$  and 1950 RPM):  
 (a) - With the DPIC-Target IV strategy;  
 (b) - With the DPIC-Target IV + GSC control strategy.

The simulation results depicted in Figures 6.11 to 6.16 and Table 6.1 show the effectiveness of the DPIC strategy with the different targets. It is seen that there are just a small transients in the variables at the voltage sag beginning. These results show the machine behavior in the particular case when there is no flux natural component induced during the voltage

transient, therefore it is necessary to analyze the other cases.

In order to simplify the analysis, the case when there is the maximum natural flux ( $\theta_0 = 0^\circ$ ) is analyzed using just the Target IV and the coordinated control of the GSC, in such a way that the 100Hz pulsation in the electromagnetic torque and total active power are reduced. Figure 6.17 show the simulation results using the same conditions described previously.

Figures 6.17a and 6.17b show that the mean values of the positive and negative sequences are controlled, but the currents present a 50Hz oscillation due the natural component that decays exponentially. Observing the phase A of the rotor currents (Figure 6.17c) it is seen the presence of the negative component plus the natural component. One can notice that the currents present higher peaks than in the previous case. The rotor voltages also has higher values, as depicted in Figure 6.17d.

The stator power has the presence of the oscillations with 50Hz (natural component) and 100Hz(negative sequence). As the GSC injects current to compensate the stator active power pulsation, the total power shown in Figure 6.17e presents a predominantly 50Hz oscillation, but this component is also reduced by the control.

As the objective of the *Target IV* is eliminate the 100Hz electromagnetic torque oscillation, Figure 6.17f shows that only the 50Hz natural pulsation remains in the torque.

Through the simulation results it is seen that using the DPIC strategy the negative sequence is well controlled, reducing the rotor currents and the  $2\omega_s$  pulsation in the torque and power, but the dynamic response of the control and the natural component in the beginning of the sag degrades the control performance. Therefore, it is necessary to implement strategies to improve the control performance during the voltage sag transients.

### 6.3.6 Converter limitation analysis

In order to warrant the rotor currents control, it is necessary that the converter is capable of imposing the voltage required by the control. The maximum converter voltage depends on the DC-link voltage. Assuming the



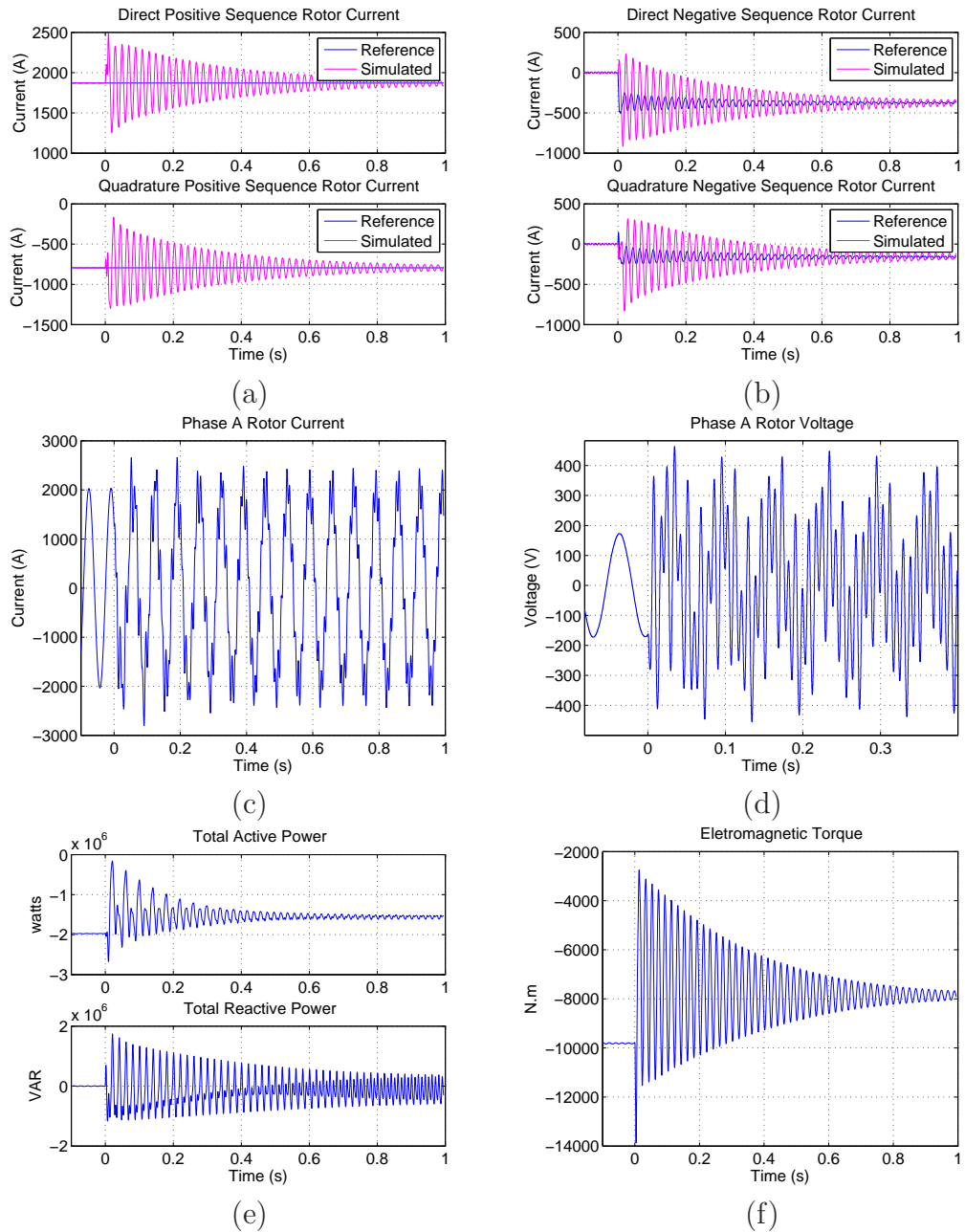


Figure 6.17: Simulation results with DPIC-Target IV (50% phase-neutral voltage sag,  $\theta_0 = 0^\circ$  and 1950 RPM):

- (a) - Positive sequence rotor current;
- (b) - Negative sequence rotor current;
- (c) - Phase A of the rotor currents;
- (d) - Phase A of the rotor voltages;
- (e) - Total active and reactive powers;
- (f) - Electromagnetic Torque.

space vector modulation (SVPWM) the maximum voltage synthesized by the converter is:

$$V_{\max} = \frac{V_{dc}}{\sqrt{3}}. \quad (6.38)$$

In turn, the maximum DC-link depends on the IGBT limits.

Equation 3.6 can be rewritten in the synchronous reference frame as:

$$\vec{v}_r^r = \left( R_r + \sigma L_r \left( \frac{d}{dt} + j\omega_r \right) \right) \vec{i}_r + \frac{L_m}{L_s} \left( \frac{d}{dt} + j\omega_r \right) \vec{\psi}_{s_d}. \quad (6.39)$$

The last term in Equation 6.39 is the parcel dependent on the stator flux, thus it is the open rotor voltage already calculated in Chapter 4. The term dependent on the derivative of the rotor current can be neglected, because generally the transient inductance ( $\sigma L_r$ ) is too small. The voltage drop in the rotor resistance is also negligible.

First the case without natural component is analyzed. Using the values of the maximum open rotor voltage positive and negative sequence (Equations 4.16 and 4.17), the Equation 6.39 can be split into:

$$V_{r_{d+}} = -\omega_{r+} \sigma L_r I_{r_{q+}} + \frac{L_m}{L_s} s_{lip} |V_{s_{d+}}|, \quad (6.40)$$

$$V_{r_{q+}} = \omega_{r+} \sigma L_r I_{r_{d+}} + \frac{L_m}{L_s} s_{lip} |V_{s_{q+}}|, \quad (6.41)$$

$$V_{r_{d-}} = -\omega_{r-} \sigma L_r I_{r_{q-}} + \frac{L_m}{L_s} (s_{lip} - 2) |V_{s_{d-}}|, \quad (6.42)$$

$$V_{r_{q-}} = \omega_{r-} \sigma L_r I_{r_{d-}} + \frac{L_m}{L_s} (s_{lip} - 2) |V_{s_{q-}}|. \quad (6.43)$$

The modulus of rotor voltage can be approximated by:

$$|V_r| \approx |V_{r+}| + |V_{r-}| \quad (6.44)$$

where  $|V_{r+}| = \sqrt{V_{rd+}^2 + V_{rq+}^2}$  and  $|V_{r-}| = \sqrt{V_{rd-}^2 + V_{rq-}^2}$ .

Assuming that the rotor current sequences are equal to the reference values, the Equations 6.40 to 6.44 can be calculated using the values given in Section 6.3.3. Thus, the results of the calculated maximum rotor voltage for different voltage sags and speeds are shown in Figure 6.18 using the 2MW WECS parameters. In this graph a unity power factor operation and the power reference following the MPPT curve was considered, using the *Target IV*. Comparing the values for 1950 RPM, which are highlighted in the figure, with the results of the Table 6.1, it is seen that the results are in good agreement.

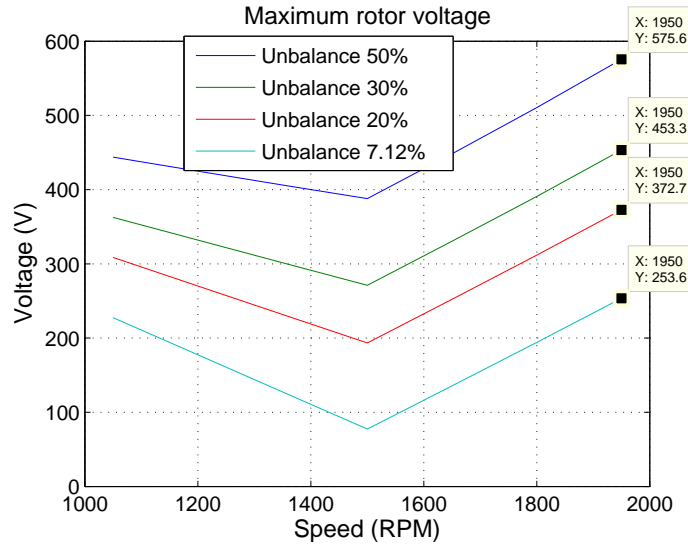


Figure 6.18: Maximum calculated rotor voltage with DPIC-*Target IV* strategy for different unbalanced voltage sags, using the 2MW WECS parameters ( $\theta_0 = 90^\circ$ ).

The values shown in Figure 6.18 is valid just for the case when there is no induced natural component. When the natural component appears the voltage requirement increases even more. Equation 4.18 gives an idea about the increasing in the rotor voltage when  $\theta_0 = 0^\circ$ , but this value cannot be added direct to the values given in 6.40 to 6.44, because the instant of the

maximums are different, as already stated. Furthermore the natural rotor current component with angular frequency  $\omega_s$  is a perturbation for both positive and negative control and vary according to the control adjustment. Therefore, extra strategies must be used, which are proposed hereafter.

If just the “steady state” during the sag is considered, through the analysis of the results shown in Figure 6.18, it is possible to calculate the necessary DC-link voltage in order to guarantee the control of both rotor current sequence components. If the converter voltage limit is not exceeded, the rotor currents references can be set in values below the converter current limits avoiding the system to trip. Following it is described the proposed method to limit the rotor currents.

As the voltage, the rotor current magnitude is given by the sum of the positive and negative sequences:

$$|I_r| \approx |I_{r+}| + |I_{r-}|, \quad (6.45)$$

where  $|I_{r+}| = \sqrt{I_{r_{d+}}^2 + I_{r_{q+}}^2}$  and  $|I_{r-}| = \sqrt{I_{r_{d-}}^2 + I_{r_{q-}}^2}$ .

As the control is implemented digitally, the limitation scheme is shown in Figure 6.19 and is divided into steps:

- First the values of the references are calculated;
- The rotor current references are compared with the converter limit. If the converter limit is not exceeded ( $|I_{r_{\max}}|$ ) the calculated references values can be applied to the control, otherwise the next step is executed;
- In the second step the direct axis component of the positive sequence rotor current is reduced until the magnitude is below the limit or the reference is zero. In each iteration the current is reduced of a factor  $\Upsilon$ . The first reference reduced is  $I_{r_{d+}}^+$  \*, because it is responsible for the active power and during a sag is more interesting to supply reactive power to the grid, helping the voltage recovering, than active power;
- If the direct axis positive sequence reference is equal to zero and the limit is still exceeded, the quadrature axis positive component reference

starts to be reduced. Observe that the reactive power reference can be set externally, even supplying reactive current to the grid;

- The last references to be reduced are the direct and quadrature negative sequences, because before controlling the active and reactive power it is necessary to reduce the power and torque oscillations. Both direct and quadrature components can be reduced simultaneously, since a priori they have the same effect on the oscillations.

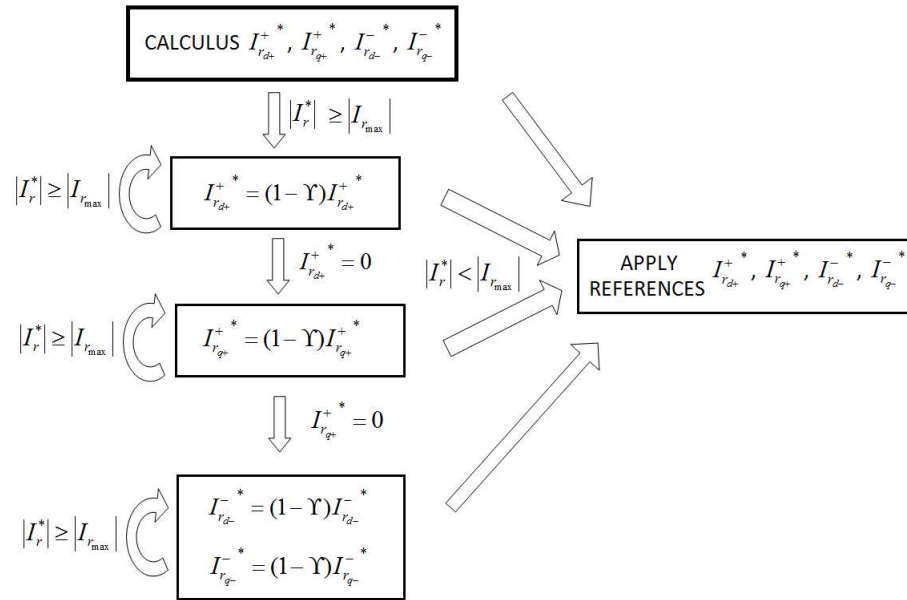


Figure 6.19: Scheme of the rotor current limitation.

The schematic of limitation is just useful if the voltage limit is not exceeded, otherwise the rotor current maximum values are not guaranteed by the control and overcurrent protections can be triggered.

### 6.3.7 Experimental results

In order to validate the DPIC strategy, the structure described was implemented in the TUD test bench and unbalanced voltage sags were tested. In all tests shown in this section the machine is operating with slip equal

to -0.15 (1750RPM) and during the sag the rotor current reference is held constant, as in the simulation results.

First, it is analyzed the case without natural component. With the *Target I*, comparing Figures 6.20(a) and 6.20(b), it is seen that the  $2\omega_s$  oscillations in the rotor currents are almost extinguished after the transient. The decreasing in the negative sequence rotor current reduces the total rotor current, increasing the chances of the system to ride-through the sag.

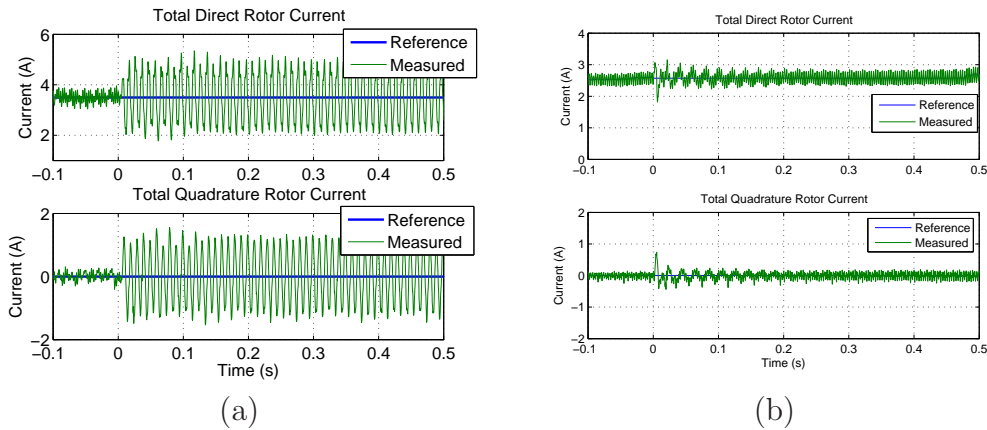


Figure 6.20: Experimental result of the total dq rotor currents - TUDb (90% phase-to-phase voltage sag,  $\theta_0 = 90^\circ$  and 1750RPM):

- (a) - Without the RTFC strategies;
- (b) - With DPIC-*Target I* strategy.

Figure 6.21 show that for controlling the negative sequence component of the currents, the rotor voltage is increased. The correct control of the currents depends on the converter voltage capability and the maximum voltage depends on the grid unbalance.

Considering now the *Target II*, comparing Figures 6.22(a) and 6.22(b) it is clearly seen the reduction in the stator current unbalance. Even when the *Target I* is used, result not shown, the stator current unbalance is reduced, because it depends on the rotor currents.

With the use of the *Target IV*, the electromagnetic pulsation is reduced, as shown in Figure 6.23. In this case the changing in the negative sequence rotor current references is not high, since the voltage sag tested is small.

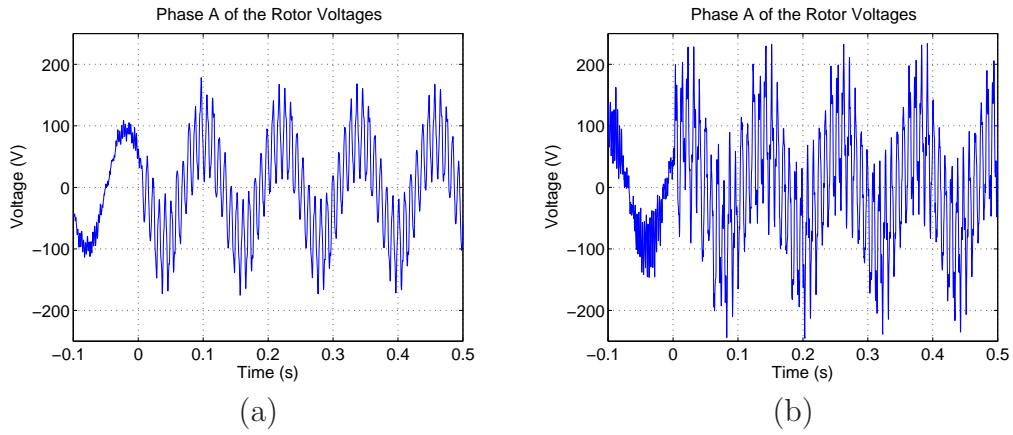


Figure 6.21: Experimental result of the phase A of the rotor voltages - TUDb (90% phase-to-phase voltage sag,  $\theta_0 = 90^\circ$  and 1750RPM):  
 (a) - Without the RTFC strategies;  
 (b) - With DPIC-Target I strategy.

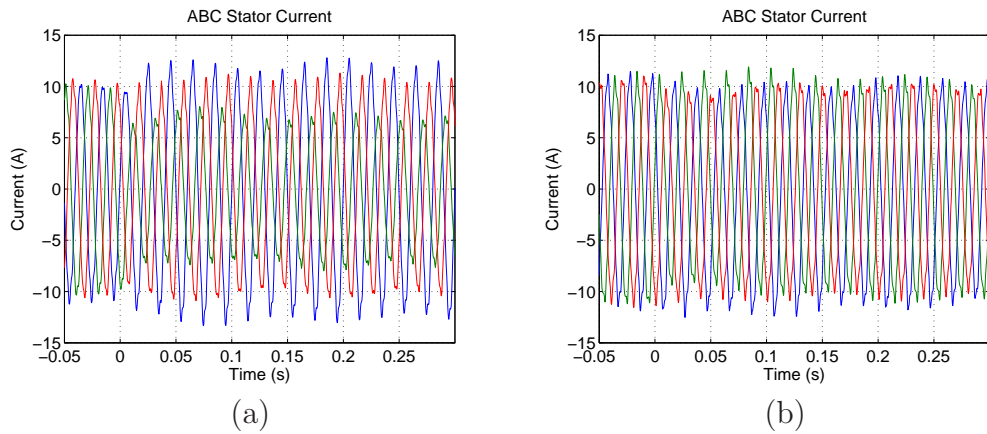


Figure 6.22: Experimental result of the ABC stator currents - TUDb (90% phase-to-phase voltage sag,  $\theta_0 = 90^\circ$  and 1750RPM):  
 (a) - Without the RTFC strategies;  
 (b) - With DPIC-Target II strategy.

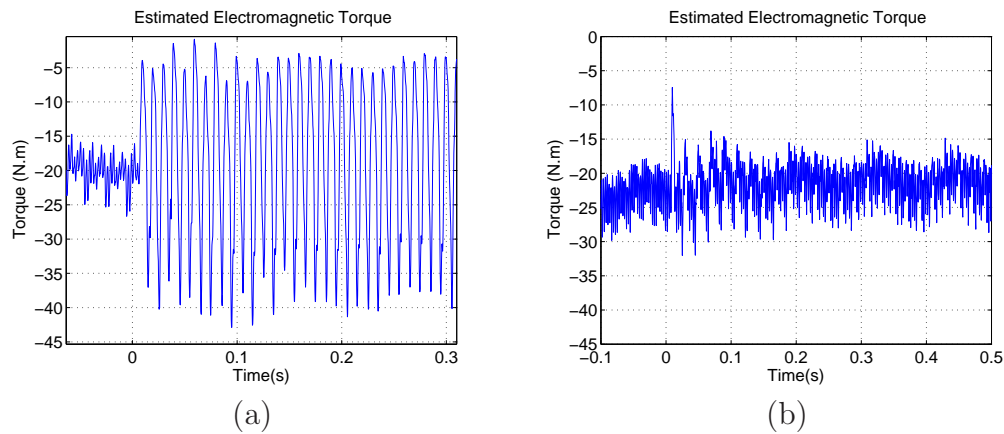


Figure 6.23: Experimental result of the estimated electromagnetic torque - TUDb (90% phase-to-phase voltage sag,  $\theta_0 = 90^\circ$  and 1750RPM):  
 (a) - Without the RTFC strategies;  
 (b) - With DPIC-*Target IV* strategy.

Using the coordinated control of the GSC with the target *Target IV*, Figure 6.24 proves experimentally the reduction in the total active power supplied to the grid.

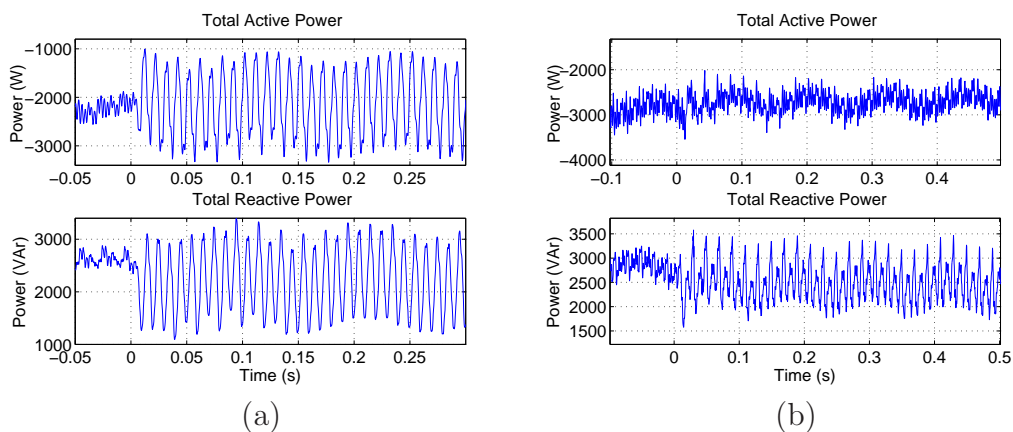


Figure 6.24: Experimental result of the total active and reactive powers - TUDb (90% phase-to-phase voltage sag,  $\theta_0 = 90^\circ$  and 1750 RPM):  
 (a) - Without the RTFC strategies;  
 (b) - With DPIC-*Target IV* + GSC control strategy.

For the case when maximum natural component is induced, just the rotor currents using *Target I* are presented. Figure 6.25 show that the 100Hz



oscillation is reduced, indicating the correct control of the negative sequence. However, the 50Hz oscillation due to the natural component is not affected and the natural oscillations continue to exist in the stator power and electromagnetic torque.

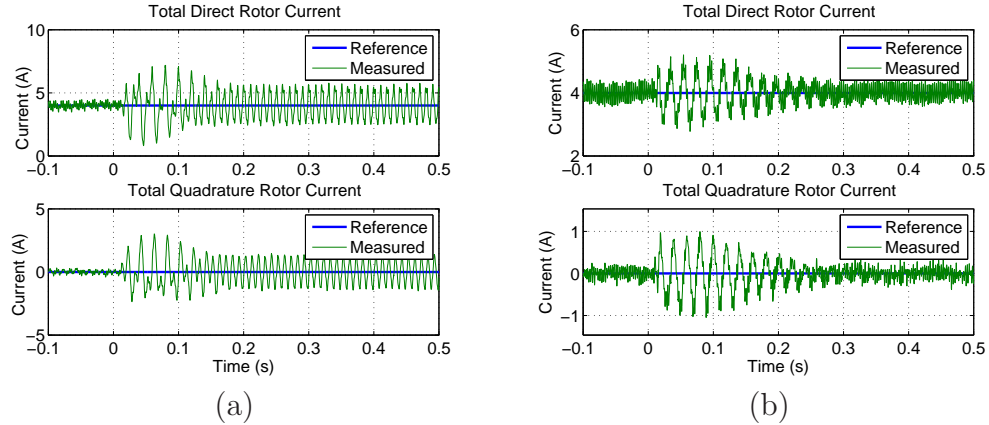


Figure 6.25: Experimental result of the total dq rotor currents - TUDb (90% phase-to-phase voltage sag,  $\theta_0 = 0^\circ$  and 1750 RPM):  
 (a) - Without the RTFC strategies;  
 (b) - With DPIC-Target I strategy.

The results for the UFMGb test bench are similar to those presented in this section, therefore they will not be shown for the DPIC strategy.

Through the experimental results, it is seen that the DPIC strategy works well also in a real system and its implementation is not so complex. Nevertheless, the natural component affects the behavior of the strategy. In the next sections, control improvements are proposed in order to deal with this issue.

### 6.3.8 Considerations about the DPIC strategy

The DPIC strategy is useful in the negative sequence control, keeping the rotor currents under acceptable values, if the converter voltage limit is not exceeded. In most papers in the literature this strategy is just used for the control of the rotor currents during a permanent unbalance without consider the transient of voltage sags. It was shown here through the simulation and

experimental results that depending on the sag instant, the natural component can affect so much the performance of the control in the sag beginning and high currents are still a problem.

Considering just the steady state, i.e., after the extinction of the natural component, one can notice that the rotor currents can be perfectly controlled, but the demanded voltage can be high depending on the unbalance. Figure 6.18 shows that the required voltage for a 50% unbalance is more than double of the voltage in a 7.12% unbalance for the rated operation. In order to meet this requirement two modifications can be done:

- Increasing the DC-link voltage. This change is not so effective because in order to increase the DC voltage above approximately 700V, it is necessary to use medium voltage IGBTs what increases so much the cost of the converter;
- Reducing the generator stator/rotor ratio. With this modification the required voltage can be reduced without changing the converter voltage limit, but it is necessary to increase the current limits.

Both propositions imply a changing in the design of the converter and in the second case also in the generator, therefore a deeper study is necessary. For now this is out of the scope of the present work.

## 6.4 PI Plus Resonant Controllers(PIRC)

Based on the same principle of controlling the negative sequence, Hu et al. (2009a), Hu and He (2009a) and Hu and He (2011) propose the use of a resonant control in the positive synchronous reference frame instead of splitting the control in positive and negative sequence controls. This method is based on the strategy used to control different harmonics in voltage source inverters, as described in Liserre et al. (2006).

The advantage of this control strategy lies in the no necessity to decompose the negative and positive sequences for the system feedback as in the DPIC strategy. As shown in the last section, this decomposition insert time

delays and reduce the system stability. Furthermore, the PIRC is implemented similarly to the classical control just adding a resonant parcel in the PI current controllers, thus its implementation is simpler than the DPIC.

In the following subsections the strategy is described with more details, a mathematical analysis is presented and the simulation and experimental results are used to validate its effectiveness.

### 6.4.1 The PIRC strategy

The control structure of the PIRC is similar to the classical control, as shown in Figure 6.26 which represents the RSC control and Figure 6.27 which depicts the GSC control. The classical PI used for the current controllers are substituted for a PI+resonant control tuned for the double grid frequency with the following transfer function:

$$G(s) = K_p + \frac{K_i}{s} + \frac{K_r s}{s^2 + (2\omega_s)^2}, \tag{6.46}$$

where  $K_r$  is the gain of the resonant part and its adjustment is discussed in the following subsection.

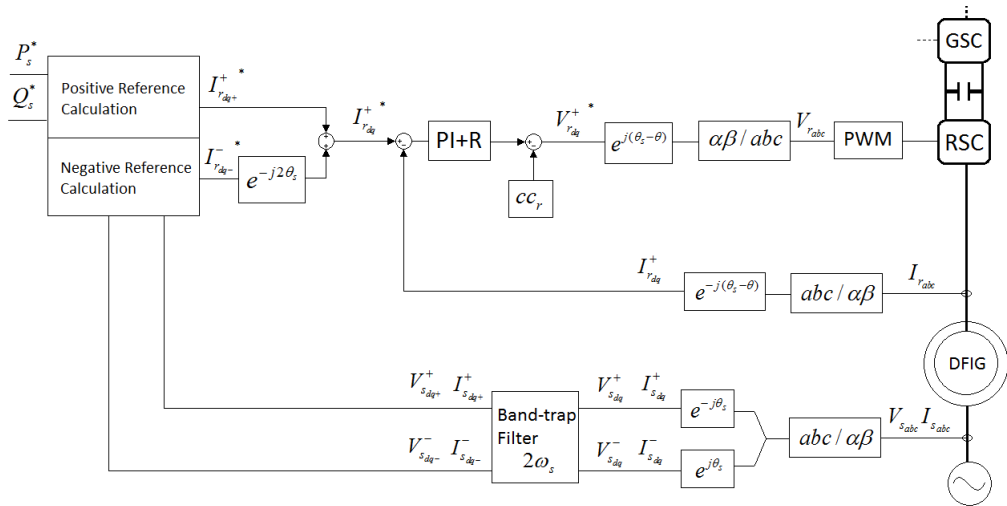


Figure 6.26: Control of the RSC using the resonant control.

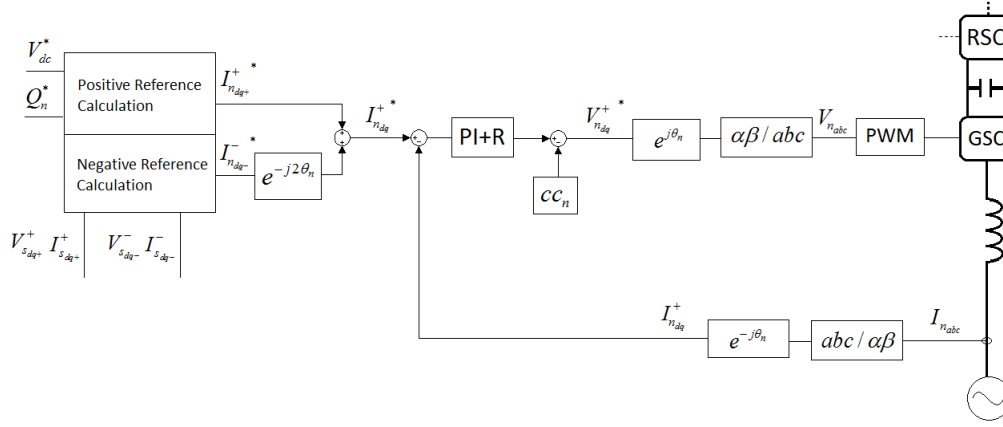


Figure 6.27: Control of the GSC using the resonant control .

The current references are calculated exactly in the same manner as described for the DPIC (section 6.3.3) for the different targets, but as here the control is just implemented in the positive synchronous reference frame, it is necessary to refer the negative sequence reference to the positive frame. Through Equation 4.23 the total current reference is given by:

$$I_{dq}^{+*} = I_{dq+}^{+*} + I_{dq-}^{-*} e^{j\omega_s t}. \quad (6.47)$$

One can notice that it is necessary to use the positive and negative sequence to calculate the current references, but this decomposition is not supposed to decrease the system stability and performance, because the decomposed values are not used for control purposes, i.e, system feedbacks or feedforwards.

## 6.4.2 Mathematical modeling during voltage sags

In Chapter 4 it was considered a PI control for the mathematical development. In this sections the development is similar, but the resonant control is used, therefore the Equations 4.39 and 4.40 can be rewritten as:

$$I_{rdq+}^+(s) = \frac{1}{\sigma L_r s + R_r} \left( K_p + \frac{K_i}{s} + \frac{K_r s}{s^2 + (2\omega_s)^2} \right) \left( I_{rdq+}^{+*}(s) - I_{rdq+}^+(s) \right) - \frac{s(L_m/L_s)}{\sigma L_r s + R_r} \psi_{sdq+}^+(s), \quad (6.48)$$

$$I_{rdq-}^+(s) = \frac{1}{\sigma L_r s + R_r} \left( K_p + \frac{K_i}{s} + \frac{K_r s}{s^2 + (2\omega_s)^2} \right) \left( I_{rdq-}^{+*}(s) - I_{rdq-}^+(s) \right) - \frac{s(L_m/L_s)}{\sigma L_r s + R_r} \psi_{sdq-}^+(s). \quad (6.49)$$

Considering the rotor current references equal to zero, as previously, the transfer functions can be rewritten as:

$$I_{rdq+}^{+t}(s) = -\frac{L_m}{L_s} \frac{s^2 (s^2 + (2\omega_s)^2)}{(\sigma L_r s + R_r) (s^2 + (2\omega_s)^2) s + F_c(s)} \psi_{sdq+}^{+t}(s), \quad (6.50)$$

$$I_{rdq-}^{-t}(s) = -\frac{L_m}{L_s} \frac{s^2 (s^2 + (2\omega_s)^2)}{(\sigma L_r s + R_r) (s^2 + (2\omega_s)^2) s + F_c(s)} \psi_{sdq-}^{-t}(s), \quad (6.51)$$

where  $F_c(s) = K_p (s^2 + (2\omega_s)^2) s + K_i (s^2 + (2\omega_s)^2) + K_r s^2$  represents the parcel of the response depended on the controller parameters.

Substituting Equations 6.50 and 6.51 in 4.43 and 4.44, yields:

$$\begin{aligned} \psi_{sd}^{+t}(s) &= \psi_{sd+}^{+t}(s) + \psi_{sd-}^{+t}(s) = \\ &= \frac{[(\sigma L_r s + R_r)(s^2 + (2\omega_s)^2) + F_c(s)] \left[ (s + 1/\tau_s)(V_{sd+}^+(s) + V_{sd-}^+(s)) + \omega_s V_{sq-}^+(s) \right]}{(s^2 + 2\frac{1}{\tau_s} s + \omega_s^2) [(\sigma L_r s + R_r)(s^2 + (2\omega_s)^2) + F_c(s)] + \frac{1}{\tau_s} \frac{L_m^2}{L_s} s^2 (s^2 + (2\omega_s)^2) (s + \frac{1}{\tau_s})}, \end{aligned} \quad (6.52)$$

$$\begin{aligned}
\psi_{s_q}^{+t}(s) &= \psi_{s_{q+}}^{+t}(s) + \psi_{s_{q-}}^{+t}(s) = \\
&= \frac{[(\sigma L_r s + R_r)(s^2 + (2\omega_s)^2) + F_c(s)] \left[ -\omega_s (V_{s_{d+}}^+(s) + V_{s_{d-}}^+(s)) + (s + 1/\tau_s) V_{s_{q-}}^+(s) \right]}{(s^2 + 2\frac{1}{\tau_s} s + \omega_s^2) [(\sigma L_r s + R_r)(s^2 + (2\omega_s)^2) + F_c(s)] + \frac{1}{\tau_s} \frac{L_m^2}{L_s} s^2 (s^2 + (2\omega_s)^2) (s + \frac{1}{\tau_s})} .
\end{aligned} \tag{6.53}$$

These equations seems to be a bit complicated, but if just the  $2\omega_s$  is analyzed, i.e.,  $s = j2\omega_s$ , the transfer functions are simplified to:

$$\begin{aligned}
\psi_{s_d}^{+t}(j2\omega_s) &= \frac{(s+1/\tau_s)}{(s^2 + 2\frac{1}{\tau_s} s + \omega_s^2)} (V_{s_{d+}}^+(j2\omega_s) + V_{s_{d-}}^+(j2\omega_s)) \\
&\quad + \frac{\omega_s}{(s^2 + 2\frac{1}{\tau_s} s + \omega_s^2)} V_{s_{q-}}^+(j2\omega_s) ,
\end{aligned} \tag{6.54}$$

$$\begin{aligned}
\psi_{s_q}^{+t}(j2\omega_s) &= \frac{-\omega_s}{(s^2 + 2\frac{1}{\tau_s} s + \omega_s^2)} (V_{s_{d+}}^+(j2\omega_s) + V_{s_{d-}}^+(j2\omega_s)) \\
&\quad + \frac{(s+1/\tau_s)}{(s^2 + 2\frac{1}{\tau_s} s + \omega_s^2)} V_{s_{q-}}^+(j2\omega_s) .
\end{aligned} \tag{6.55}$$

Transfer Functions 6.54 and 6.55 indicate that the control adjustment does not affect the stator flux linkage behavior in the  $2\omega_s$  frequency caused by the negative sequence. Despite the flux is not affected, the behavior of the current is modified. Using Equations 6.54 and 6.55 in 6.50 and 6.51, the rotor current transient responses are given by:

$$I_{r_d}^{+t}(s) = \frac{-s^2 (L_m/L_s) (s^2 + (2\omega_s)^2) \left[ (s+1/\tau_s) (V_{s_{d+}}^+(s) + V_{s_{d-}}^+(s)) + \omega_s V_{s_{q-}}^+(s) \right]}{(s^2 + \frac{2}{\tau_s} s + \omega_s^2) [(\sigma L_r s + R_r)(s^2 + (2\omega_s)^2) + F_c(s)] + \frac{L_m^2}{\tau_s L_s} s^2 (s^2 + (2\omega_s)^2) (s + \frac{1}{\tau_s})} , \tag{6.56}$$

$$I_{r_q}^{+t}(s) = \frac{s^2(L_m/L_s)(s^2+(2\omega_s)^2) \left[ \omega_s(V_{sd+}^+ + V_{sd-}^+)(s) - (s+1/\tau_s)V_{sq-}^+(s) \right]}{\left( s^2 + \frac{2}{\tau_s}s + \omega_s^2 \right) \left[ (\sigma L_r s + R_r)(s^2 + (2\omega_s)^2) + F_c(s) \right] + \frac{L_m^2}{\tau_s L_s} s^2 (s^2 + (2\omega_s)^2) \left( s + \frac{1}{\tau_s} \right)} .$$

(6.57)

If the  $2\omega_s$  frequency is evaluated in the Equations 6.56 and 6.57, one can notice that the rotor current transient response is null, i.e., the double frequency is eliminated. These transfer functions indicate that in the  $2\omega_s$  frequency the system response is independent on the system parameters and controller gains. Of course this affirmation is true just if the resonant response is adequate, therefore it depends on the gain.

In order to define the resonant gain ( $K_r$ ) it is necessary to analyze the controller frequency response. Figure 6.28 shows the bode diagram of the controller transfer function, shown in Equation 6.46, with different resonant gains. One can see that increasing the gain, the controller response in the  $2\omega_s$  frequency increases, but frequencies in the vicinity are also affected. For choosing an adequate gain it is necessary to guarantee that the gain in  $2\omega_s$  is high, but that the resonant peak is not too wide. The selectivity of the control can also be adjusted adding a quality factor  $Q$  to the resonant parcel, similar to the resonant filter presented in Equation 6.4. However, this factor also affects the resonant peak and for simplicity it is not considered in the controller.

Another important point to be considered when designing the resonant control for digital implementation is the discretization method. Depending on the method the resonant peak can be attenuated and the frequency can be shifted. In this work the Tustin method of discretization was employed.

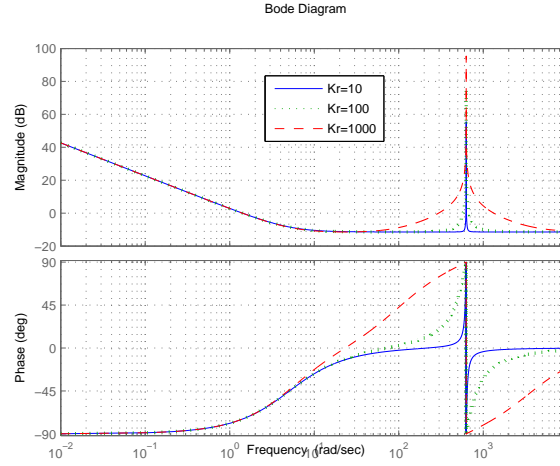


Figure 6.28: Bode diagram of the PI+resonant controller (Equation 6.46) for different gains using the 2MW system parameters.

### 6.4.3 Simulation results

For the validation of the PIRC strategy the same conditions simulated previously were considered. As the first objective of the strategy is keep the rotor currents in acceptable limits, the Target I is simulated for the case without natural component.

Figures 6.29(a) and 6.29(b) show that the positive and negative sequences are correctly controlled. One can notice that rotor current transient is smaller than the use of the DPIC strategy, but a small transient still exist due to the control dynamics. Figure 6.29(c) evidences that the transient is small and fast in the rotor currents in the stationary reference frame. This improvement in the response is due to the fact that in the PIRC strategy is not necessary to decompose the component sequences. Figure 6.29(d) shows that in order to reduce the negative sequence component of the rotor currents it is necessary to impose rotor voltages with negative sequence component. This component increases the voltage values.

Using the *Target I* the negative sequence reference is kept null, therefore in order to see the control behavior when the reference is changed, Figures 6.30 shows the result of using the *Target IV*.



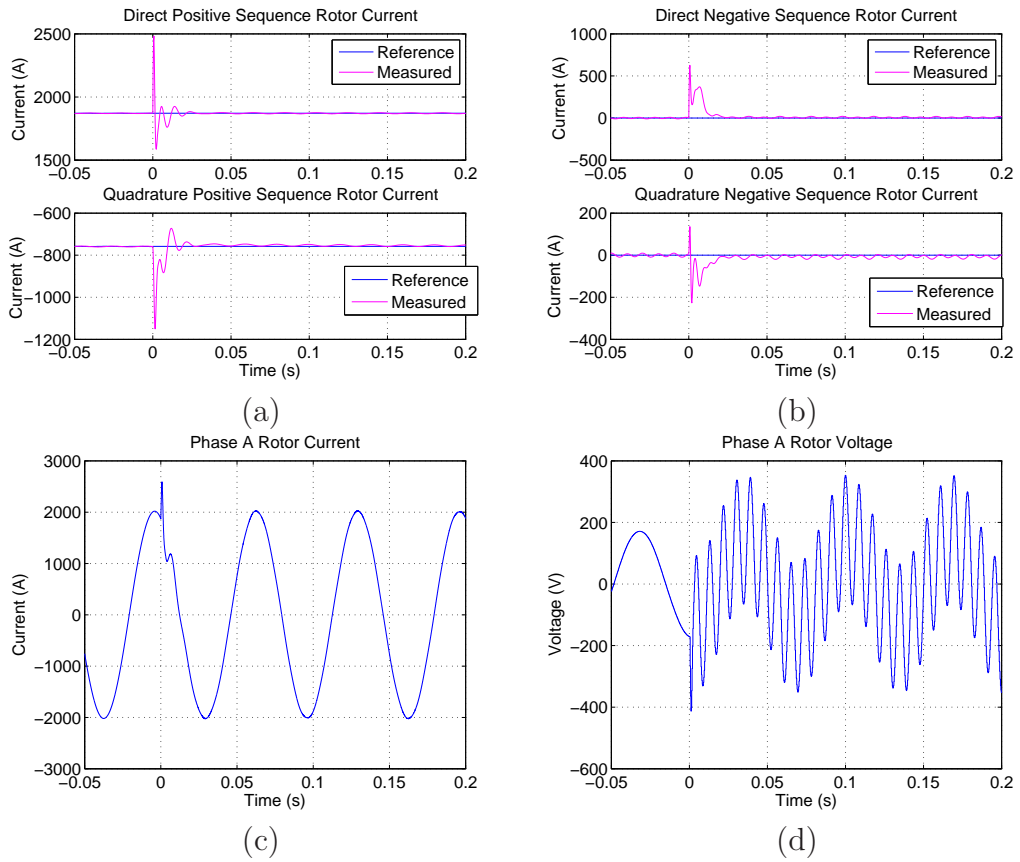


Figure 6.29: Simulation results using PIRC-*Target I* strategy (50% phase-neutral voltage sag,  $\theta_0 = 90^\circ$  and 1950 RPM):  
 (a) - Positive sequence rotor current;  
 (b) - Negative sequence rotor current;  
 (c) - Phase A of the rotor currents;  
 (d) - Phase A of the rotor voltages.

Figure 6.30(a) shows the controlled rotor current. One can notice that the reference of the negative sequence appears as a 100Hz sinusoidal signal in the synchronous reference frame and this component is totally controlled after a short transient. Comparing this result with the DPIC, one can see again that the transient is reduced, mainly in the electromagnetic torque shown in Figure 6.30(b).

Using the same principle to control the GSC converter, Figure 6.30(c) shows the behavior of the GSC currents which are used to reduce the total active power, depicted in Figure 6.30(d).

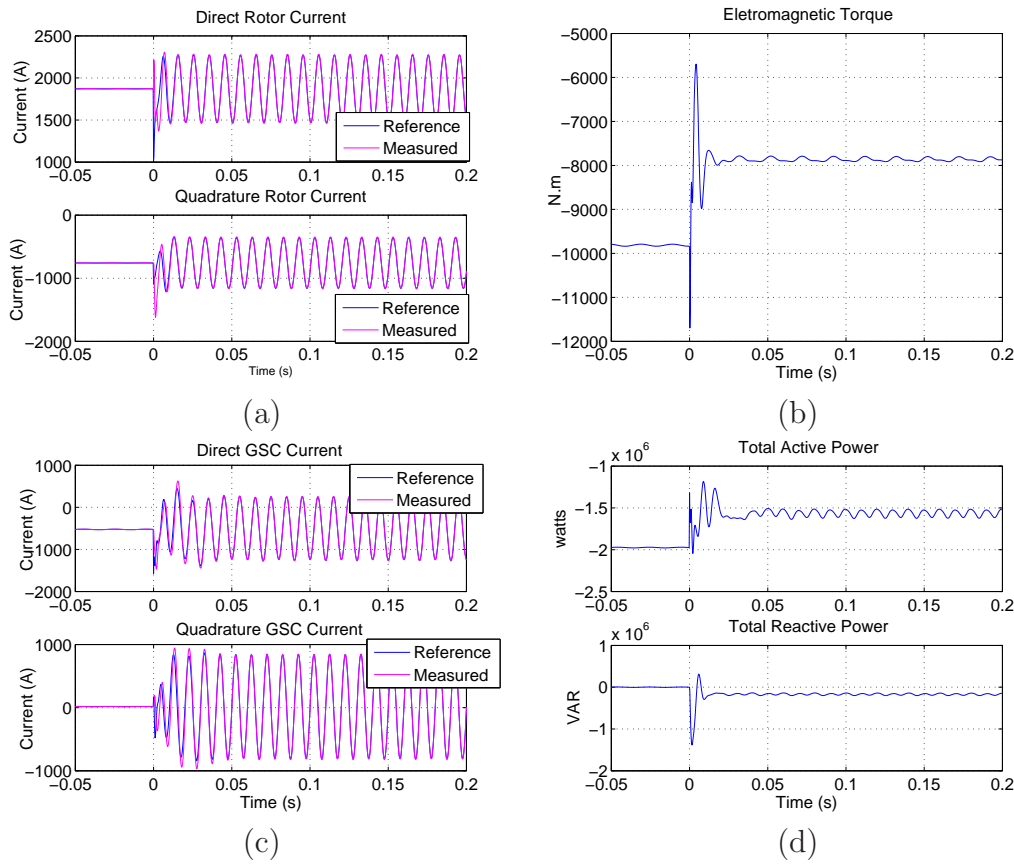


Figure 6.30: Simulation results using PIRC-*Target IV* + GSC control strategy (50% phase-neutral voltage sag,  $\theta_0 = 90^\circ$  and 1950 RPM):

- (a) - Total dq rotor currents;
- (b) - Electromagnetic Torque;
- (c) - Total dq GSC currents;
- (d) - Total active and reactive powers;

Simulating again the PIRC strategy with the Target IV and considering now that the sag entry instant causes the maximum natural flux linkage, Figure 6.31 depicts the rotor currents and the electromagnetic torque. It is seen that the natural component is not affected by the resonant control, therefore the natural component with frequency around  $\omega_s$  still exists in the currents, thus, in the torque and power. In the following section an extension of the resonant is proposed in order to deal with the natural component.

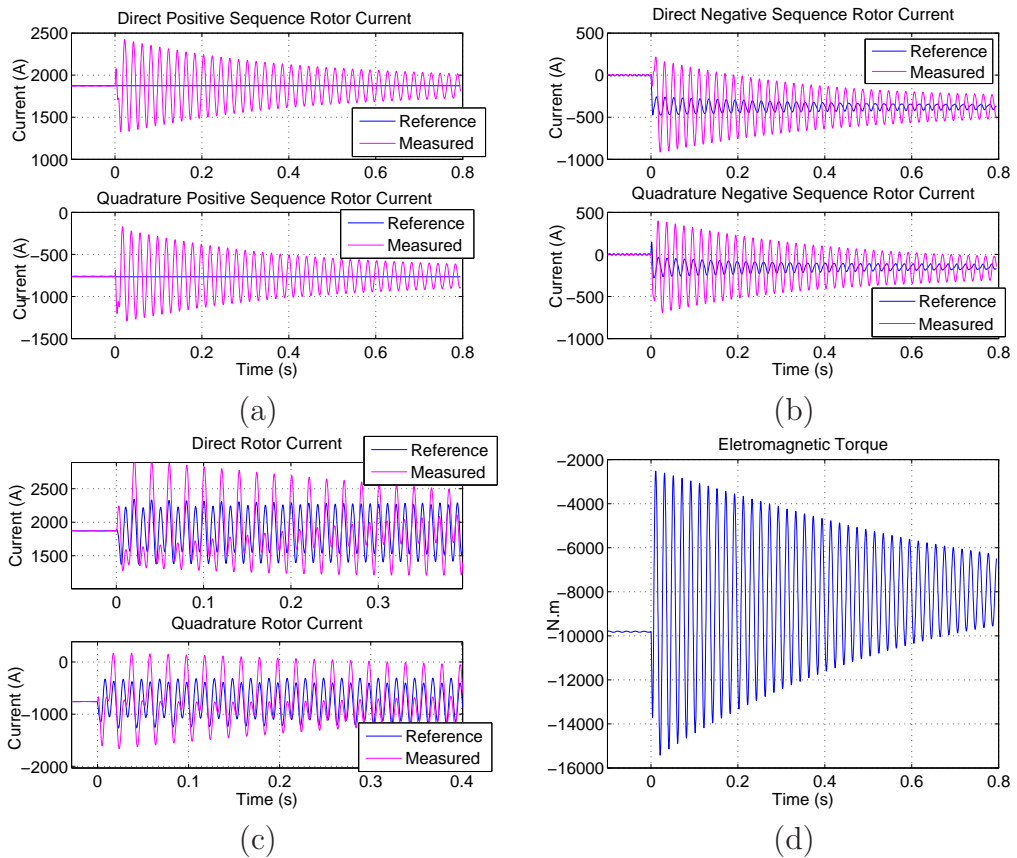


Figure 6.31: Simulation results using PIRC-Target IV strategy (50% phase-neutral

voltage sag,  $\theta_0 = 0^\circ$  and 1950 RPM):

(a) - Positive sequence rotor current;

(b) - Negative sequence rotor current;

(c) - Total dq rotor currents;

(d) - Electromagnetic Torque.

#### 6.4.4 Considerations about the PIRC

Analyzing the input (currents) and outputs (voltages) of the control system, one can notice that the behavior of both strategies are similar with differences just during the transients. Therefore, the analysis of the converter limits carried out for the DPIC strategy is still valid in the PIRC and the limitation scheme can also be employed.

Since the results for the DPIC and PIRC are similar, just with the latter presenting an improving in the sag beginning transient, the experimental results for the PIRC are not shown. The experimental results will be analyzed in the next section when a modification in the PIRC strategy is proposed.

### 6.5 Enhanced PIR Control (EPIRC)

#### 6.5.1 The EPIRC strategy

Most of the papers in the literature analyze just the permanent unbalance, therefore they propose the use of a resonant control to deal only with the negative sequence component, as described in last section. In order to control the natural component, in this work is proposed the extension of the resonant control for this component. The controller transfer function is given as:

$$G(s) = K_p + \frac{K_i}{s} + \frac{K_{r1}s}{s^2 + (2\omega_s)^2} + \frac{K_{r2}s}{s^2 + (\omega_s)^2}, \quad (6.58)$$

where one can notice the addition of a resonant parcel tuned to the grid frequency.

The control structure and the mathematical development are similar to the case already presented for the PIRC strategy, therefore following subsections are dedicated to show the simulation and experimental results.

Since the natural component appears just in the RSC, the current control of the GSC can be kept only with the resonant part of the negative sequence.

### 6.5.2 Simulation results

Considering the same conditions used in the previous simulation tests and using the *Target IV*, Figure 6.32 show the comparison between the PIRC and the EPIRC strategy.

Through Figures 6.32(a) and 6.32(b) one can see that the positive and negative sequences are controlled after a short transient and 50Hz oscillations due to the natural component disappears when the EPIRC strategy is used. Figure 6.32(c) shows the reduction in the total rotor current, but in other hand the electromagnetic torque (Figures 6.32(d)) continues to oscillate, because the stator flux is not modified.

This strategy shows to be useful reducing the rotor currents, especially if the *Target I* is used, but in the other hand the damping of the natural flux is reduced. In order to deal with this disadvantage it is possible to combine the EPIRC with the magnetizing current control (MCC), as discussed in the next section.

### 6.5.3 Experimental results

For the analysis of the experimental results with the EPIRC strategy the focus is the decreasing in the rotor currents, therefore just the results for the *Target I* is analyzed. Just the results for the UFMGb are shown and in all the tests the case with maximum induced natural component is considered.

The Figures 6.33(a) and (b) show the dq and ABC rotor currents, respectively, for the test of a 50% phase-to-phase with the machine operating at rated power (2340RPM, slip=-0.3). It is seen that natural component and the negative sequence of these currents is reduced almost to zero after a short transient. This transient comes from the control response and also the PLL response and it cannot be avoided. Nevertheless, the high rotor currents is transitory and they may be supported by the converter.

Observing the electromagnetic torque in Figure 6.33(c), it is noted that the oscillations due to the natural and negative still exist, but with smaller amplitude than the result without RTFC strategies. As already shown, the use of the *Target IV* can reduce the negative sequence, but it is necessary

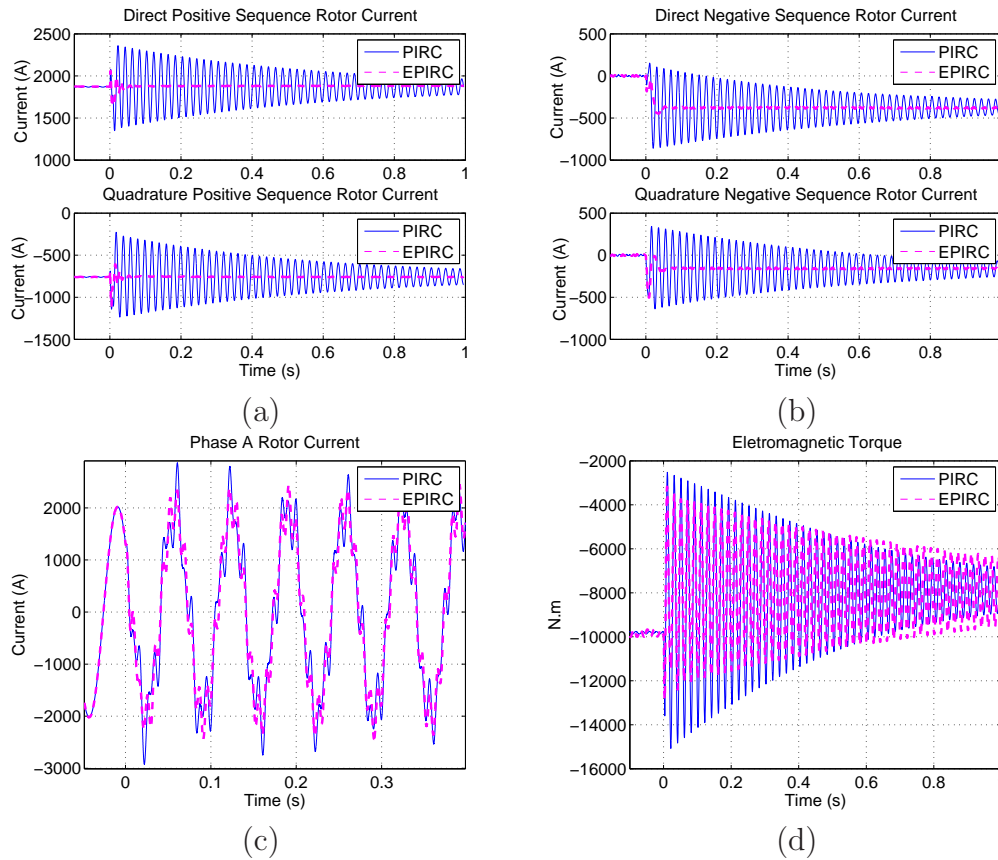


Figure 6.32: Simulation results using EPIRC-Target IV strategy (50% phase-neutral voltage sag,  $\theta_0 = 0^\circ$  and 1950 RPM):

- (a) - Positive sequence rotor current;
- (b) - Negative sequence rotor current;
- (c) - Phase A of the rotor currents;
- (d) - Electromagnetic torque.

an undesirable rotor currents increasing and the natural component is still a problem.

Through Figure 6.33(d) one can notice that the rotor voltages reached almost the RSC voltage limits, since the DC-Link voltage was set to 450V. As already stated, the main issue for the correct operation of this strategy is the converter voltage limit which is related to the DC-link voltage, therefore with the IGBTs voltage capability. Due to limitations of the UFMG test bench this voltage cannot be increased above 500V.

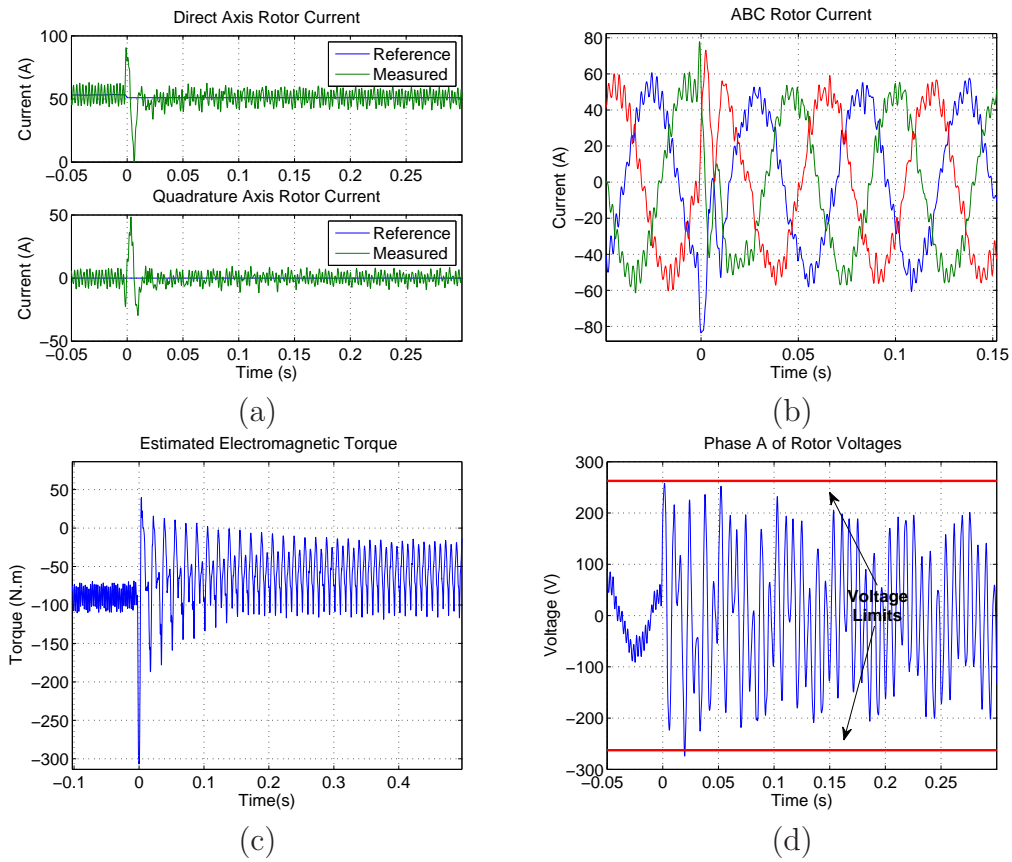


Figure 6.33: Experimental results using EPIRC-*Target I* strategy for a 50% phase-to-phase voltage sag,  $\theta_0 = 0^0$  and 2340RPM - UFMGb:

- (a) - Total dq rotor currents;
- (b) - ABC rotor currents;
- (c) - Electromagnetic Torque;
- (d) - Phase A of the rotor voltages. Straight line - voltage limits.

In order to evaluate the maximum rotor voltage necessary for the correct operation of the EPIRC, similar tests to the previous one were carried out in the UFMG test bench for different voltage sags and speeds. The worst case, i.e., maximum natural component, was considered for the tests using the EPIRC.

Figure 6.34(a) shows the maximum rotor voltages. Comparing the voltage values of these curves with the values obtained in the open rotor case, which were shown in Figure 4.7, one can see that they are close for the same speed and voltage depth. This fact occurs because the currents are under

control, therefore the difference is just the voltage drop in the rotor impedance that is small. Thereby, the open rotor analysis can be used for the obtainment of the demanded rotor voltage.

The points not plotted in Figure 6.34(a), for phase-to-phase voltage sags below 40%, are the points where the control saturate, therefore the rotor currents are not completely controled, then the converter current protection is triggered. During the tests the current protection was triggered in two situations: when the control saturate or when the rotor currents in the sag beginning are too high. Figure 6.34(b) shows the maximum rotor currents for the previous tests.

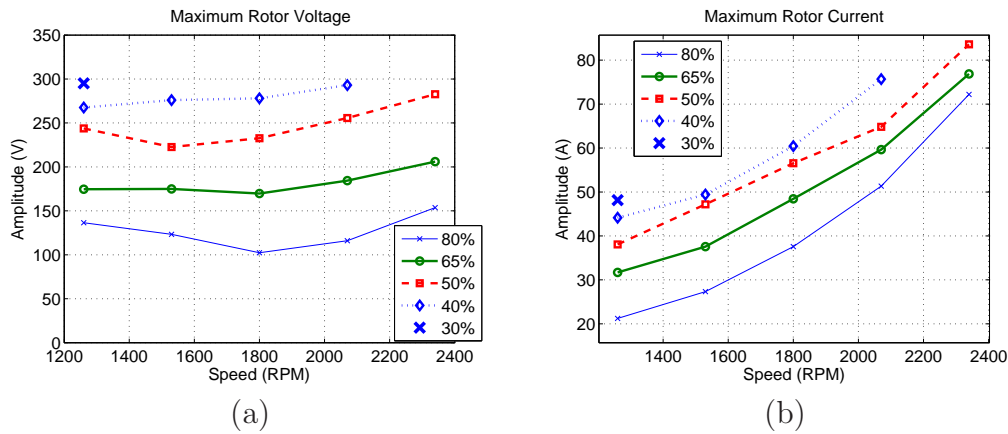


Figure 6.34: Experimental results for different voltage phase-to-phase voltage sags with maximum natural component ( $\theta_0 = 0^0$ ) and varying the speed - UFMGb:

- (a) - Maximum rotor voltages;
- (b) - Maximum rotor currents.

The overcurrents due to the control saturation are limited by the maximum voltage that the RSC can impose, therefore the limitation is the maximum DC-link voltage possible for the converter. The peak current in the sag beginning cannot be avoided, as stated before, therefore it is necessary to warrant that the converter can support the transient overcurrent or use extra protections such as the crowbar.

In the UFMG test bench the instantaneous overcurrent supported by the IGBT is limited (130% of the rated current). The conditions when the system can ride-through the unbalanced voltage sags are shown in Figure



6.34. Despite the EPIRC increase the RTFC, if this test rig was a real WECS it cannot comply with the grid codes, because of the overcurrent in the sag beginning. Other solutions may be uses in conjunction with the EPIRC strategy.

## 6.6 Resonant Control Plus Magnetizing Current Control (RMCC)

### 6.6.1 The RMCC strategy

The previous control strategies presented show that it is possible to control the positive and negative sequences of the rotor current during an unbalanced voltage if the RSC voltage limit is not exceeded. With these strategies the  $2\omega_s$  oscillation in the desired variable (torque or power or current) can be eliminated, but if during the voltage sag transient natural flux is induced, the strategies are not capable of eliminated the  $\omega_s$  oscillation. In order to eliminate the two undesired oscillations, here is proposed the use of the magnetizing current control in conjunction with the resonant control (RMCC).

Figure 6.35 shows the block diagram of the RMCC strategy which is similar to the scheme used for the MCC in the classical control. The stator reactive power control generates a current reference that is added to the magnetizing current reference that it is controlled using a proportional gain, as already explained in Chapter 5.

It is important to highlight that just the positive sequence of the magnetizing current is used in the control since the MCC loop generate only the reference of the rotor current positive sequence which is added to the negative sequence reference. The positive magnetizing current is given by:

$$I_{m+}^+ = - \left( I_{r_{q+}}^+ + I_{s_{q+}}^+ \right). \quad (6.59)$$

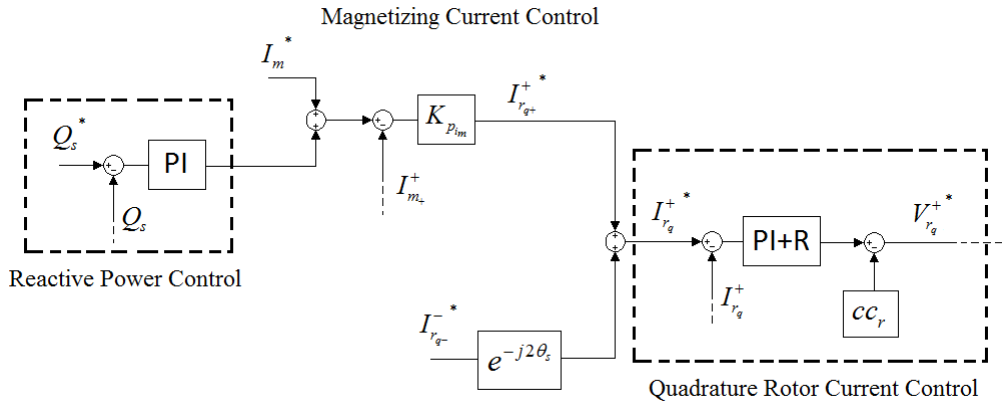


Figure 6.35: Resonant control + Magnetizing current control (RMCC).

## 6.6.2 Simulation results

Considering the same conditions already used in the previous simulations, Figure 6.36 shows the results for the RMCC strategy when the *Target IV* is set and the maximum natural flux is induced. The result using only the EPIRC is also presented for comparison.

Figure 6.36(a) shows that the behavior of the direct axis components of the rotor currents are similar in both cases and the quadrature axis component increases due to the MCC strategy. The Figure 6.36(a) demonstrate that there is an increasing in the ABC rotor currents in the sag beginning. The rotor voltages in the RMCC are reduced, as depicted in Figure 6.36(c).

The objective of the RMCC is increase the damping of the natural component, what can be seen through the electromagnetic torque depicted in Figure 6.36(d). With the *Target IV*, the resonant control actuates eliminating the negative sequence oscillation while the MCC reduces the natural component oscillations.

Although here just the results for the transient of the sag beginning are shown, the use of the RMCC improves the system response in the sag recovering. In this situation the effectiveness of the strategy may be improved, since the negative sequence disappears.

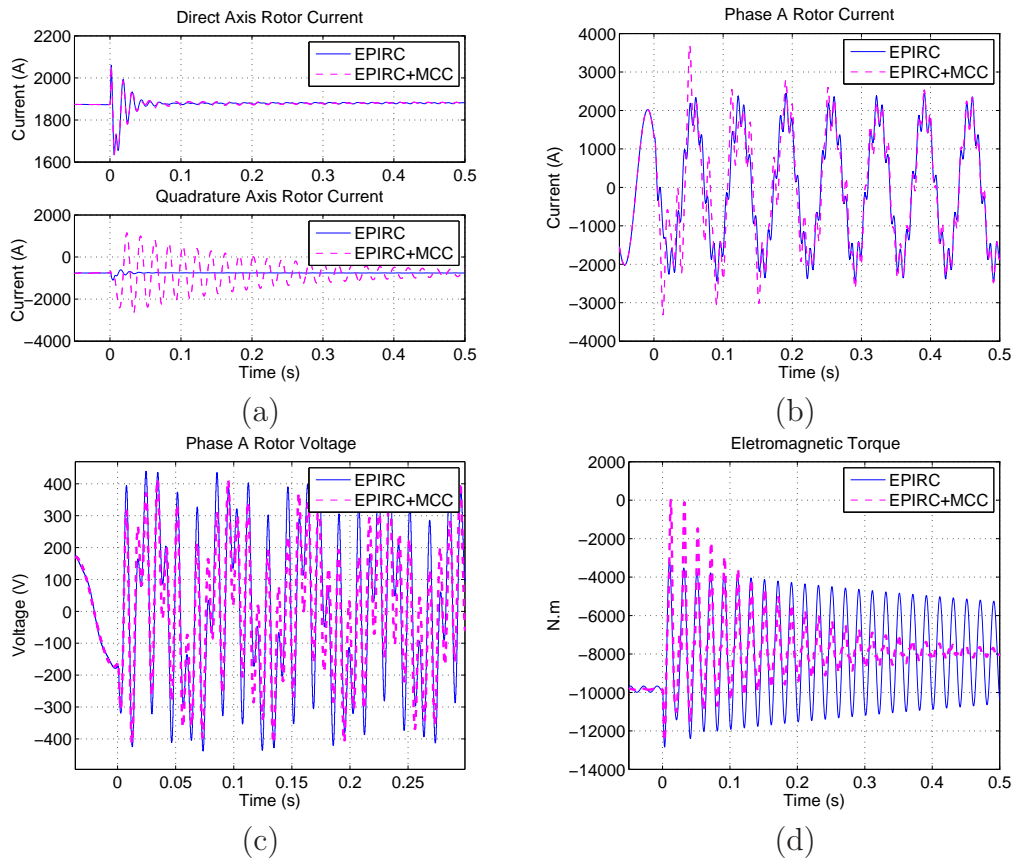


Figure 6.36: Simulation results using EPIRC and the RMCC - *Target IV* strategy (50% phase-neutral voltage sag,  $\theta_0 = 0^0$  and 1950 RPM):

- (a) - dq rotor currents;
- (b) - Phase A of the rotor currents;
- (c) - Phase A of the rotor voltages;
- (d) - Electromagnetic Torque.

### 6.6.3 Experimental results

The experimental results for the UFMG test bench are shown in Figure 6.37, using the *Target I* to reduce the rotor currents.

One can see through Figures 6.37(a) and (b), that there is an increasing in the the rotor currents in the sag beginning in order to increase the flux damping. This increase is controlled and depends on the RSC current and voltage capability.

Figure 6.37(d) depicts the electromagnetic torque where one can notice the increasing in the natural component damping. As the stator time constant of the test bench is not so high as in the simulation, the increasing in the damping is not clearly seen. The improving in the system response is clearer in the simulation results.

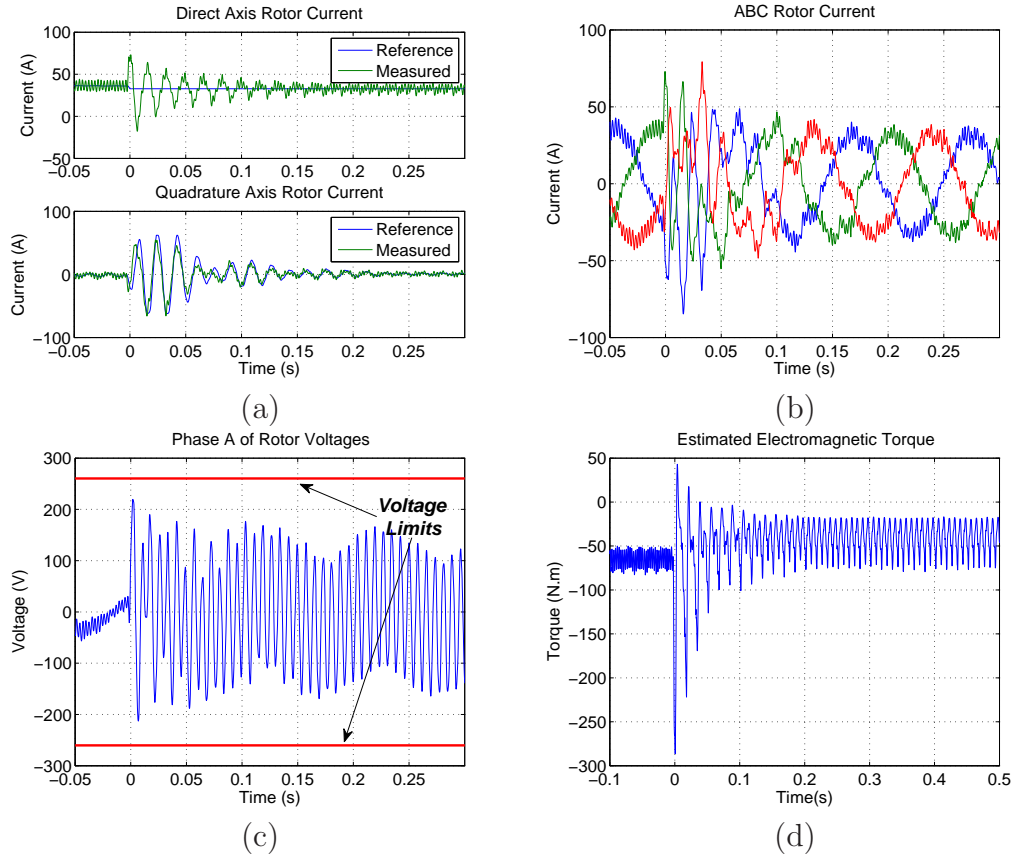


Figure 6.37: Experimental results using RMCC - *Target I* strategy for a 50% phase-to-phase voltage sag,  $\theta_0 = 0^0$  and 2070RPM - UFMGb:

- (a) - dq rotor currents;
- (b) - ABC rotor currents;
- (c) - Phase A of the rotor voltages;
- (d) - Electromagnetic torque.

The main limitation of the use of this strategy is the converter voltage and currents, as the other proposed strategies. These limits have to be analyzed more strictly. Since the RMCC increases the rotor current in the sag beginning it can be useful for small voltage sags or when the system is operating

in conditions below the rated power, permitting a greater current excursion.

## 6.7 Final Considerations

During the unbalanced voltage sags the natural component and the negative sequence cause high oscillatory currents in the rotor, causing electromagnetic torque and power oscillations. In order to improve the system ride-through capability some strategies were proposed in order to control the undesired current components. The simulation and experimental results prove that the use of these strategies are suitable and effective.

The main issue for implementation is the converter voltage and current limits, but with the property set of the references and correct dimensioning of the converter it is possible to overcome this problem. It is interesting as future works, to evaluate the economic viability of implementation of the proposed strategies when a oversizing of the converter is necessary.



---

# Conclusions and Future Work

---

## 7.1 Conclusions

The main goal of this work was the development of novel control strategies to improve the ride-through fault capability of wind conversion systems equipped with the doubly-fed induction generator technology. In order to do so, first the system behavior during balanced and unbalanced voltage sags was mathematically modeled in the time and Laplace domain, highlighting the DFIG weaknesses. Furthermore, simulation and experimental results were presented to show the time behavior of the main variables. Based on the findings, ride-through strategies were proposed and validated using again simulation and experimental results.

The studies of the DFIG behavior during voltage sags are extensively addressed in the literature, but this work goes one step further analyzing the effect of the control adjustment in the system behavior, using Laplace domain mathematical modeling. With the results obtained, the following conclusions can be enumerated:

- For the symmetrical voltage sags:
  - the main issue is caused by the natural component of the stator flux linkage which appears due to the voltage transients and decays according to the control gains;
  - the natural component induces high oscillatory rotor voltages that cause high rotor currents;

- the control adjustment influences the damping of the natural flux. The higher the rotor current control bandwidth, the higher the decrease in the stator flux linkage damping.
- the oscillation in the rotor currents causes electromagnetic torque and stator power pulsations which have the grid voltage frequency;
- For the asymmetrical voltage sags:
  - besides the natural component, it appears also negative sequence in the stator flux linkage;
  - the behavior of the natural component is similar to the balanced case;
  - the negative sequence component also induces high rotor voltages and currents, but this component is much more significant than the natural one;
  - a simple PI controller does not affect the negative sequence and it is present during all the sag;
  - besides the electromagnetic torque and stator power pulsations in the grid frequency, they also have oscillations in the double of the grid frequency due to the negative sequence component.

To deal with the natural component, it is proposed in this thesis the control of the magnetizing current to increase the stator flux linkage damping and reduce the effect of this component on the currents, torque and power. A mathematical modeling and simulation and experimental results show the efficacy of this control strategy. In the other hand, there is an increasing in the rotor currents and voltages that has to be considered.

The author concludes that the MCC strategy can be useful, but due to the converter limits, it can be used just in shallow voltage sags or when the WECS is operating with small power. As the main objective of the MCC is to reduce the torque and power oscillations, this strategy can be employed not just during voltage sags, but in all situations when natural component is induced, as in the instant of connection of the system to the grid.

For controlling the negative sequence component it is used a dual PI control scheme or PI+resonant controllers, both strategies described in the



literature. This work propose a modification in the latter strategy including a resonant parcel to deal with the natural component. The simulation and experimental results also show the improvement in the DFIG response, but an analysis of the converter limits is necessary to define the conditions where the system can ride-through the sag.

For the tests with the UFMG test bench, it was demonstrated that the system can well control the negative and natural components for phase-to-phase voltage sags above 50% in all operation conditions. The main issue for the RTFC of this test bench is the limited RSC current capability. Actually, the converter is not properly dimensioned for this transient situation. With a correct design, the author believes that the system can comply with the grid codes.

This work also demonstrate that the use of the resonant control in conjunction with the magnetizing current control can improve the system response. Although, the use of this strategy is also limited by the converter and the same conclusions stated before are valid for this strategy.

Finally, it is important to emphasize that the strategies proposed here have no intention to be unique for the solution of the ride-through problem for the DFIG. This work just gives an contribution in this theme and points out that control strategies can be used to improve the system response. The author thinks that the complete solution is just possible using control strategies in conjunction with hardware improvements in the converter and/or using devices as the crowbar. Thereby, improving the RTFC for this technology requires additional costs that have to be evaluated in final comparison point.

## 7.2 Future Works

The continuity of this work depends on the improvement of the UFMG test bench. The following modifications are necessary:

- improved dimensioning of the converter, permitting operation on the generator rated power and the use of the proposed RTFC strategies under more severe conditions;

- improvement of the protection system, allowing safer tests. This limitation does not permits now the test of more severe conditions;
- new design of the voltage sag generator using impedances, employing for example air core reactors avoiding magnet saturation;
- use of the torque transducer for real torque measurements in spite of the estimated electromagnetic torque. This transducer is already mounted, but the signals have be conditioned for the analysis;
- implementation of a crowbar device and the test of it in conjunction with the RTFC strategies proposed in this work.

As future works it is interesting to study different strategies such as the direct power control and repetitive control and evaluate them under voltage sags. The comparison between different strategies is an important step on the solution of the DFIG ride-through fault capability.

In the classical DFIG structure the GSC is connected shunt to the stator circuit. A possible modification can be the use of this converter in series with the stator, permitting the voltage control in such a way that during voltage sags the impact on the generator can be reduced.

With the experience obtained with the mounting of the test bench and the analysis carried out in this work, the next step in the research of ride-through fault capability of wind conversions systems will be studies in other technologies.

The technology using synchronous generators with full converter is a topology with high market penetration, specially in Brazil. This technology has good low voltage ride-through capability when using the chopper device, but, as in the DFIG studied in this work, control strategies are preferred to reduce the costs. Investigation on this topology is an interesting continuity proposal and future comparison with the DFIG technology, including costs evaluation, is an important point to be researched.

Furthermore, the methodologies employed in this work can be used for the analysis of low voltage ride-through capability of other generation technologies which use power electronics converters for connection to the grid as the photovoltaic systems. The present grid codes do not require RTFC of

this technology, but probably in future similar conditions of the required to WECS may be mandatory.



---

---

## References

---

- Abo-Khalil, A. G., Lee, D.-C., and Jang, J.-I. (2007). Control of Back-to-Back PWM Converters for DFIG Wind Turbine Systems under Unbalanced Grid Voltage. *IEEE International Symposium on Industrial Electronics*, pages 2637–2642.
- Anaya-Lara, O., Zifa, L., Quinonez-Varela, G., and McDonald, J. R. (2008). Optimal DFIG crowbar resistor design under different controllers during grid faults. *Electric Utility Deregulation and Restructuring and Power Technologies*, 1:2580 – 2585.
- ANEEL (2012). Matriz energética do Brasil - Eólica. Available on [www.aneel.gov.br/aplicacoes/capacidadebrasil/OperacaoGeracao-Tipo.asp?tipo=7&ger=Outros&principal=E%F3lica](http://www.aneel.gov.br/aplicacoes/capacidadebrasil/OperacaoGeracao-Tipo.asp?tipo=7&ger=Outros&principal=E%F3lica).
- Blaabjerg, F., Chen, Z., Teodorescu, R., and Iov, F. (2006). Power Electronics in Wind Turbine Systems. *Power Electronics and Motion Control Conference. IPEMC 2006*, 1:1–11.
- Bollen, M. (2000). *Understanding Power Quality Problems: Voltage Sags and Interruptions*. IEEE Press.
- Brekken, T. and Mohan, N. (2004). A novel doubly-fed induction generator control scheme for reactive power control and torque pulsation compensation under unbalanced grid voltage conditions. *Proceedings of 2004 Electronics Specialists Conference*, pages 760–764.
- Brekken, T. K. A. and Mohan, N. (2007). Control of a doubly-fed induction wind generator under unbalanced grid voltage conditions. *IEEE Transactions on Energy Conversion*, 22:129–135.

- Clements, E. (2003). Historic Turns in The Windmill City. *Fermi News*, 26.
- da Silva, J. L. (2009). Estratégia de Controle e Supervisão de um Gerador de Indução Duplamente Excitado para Turbinas Eólicas. Master's thesis, PPGEE/UFMG.
- de Araújo Lima, F. K. (2009). *Aerogerador Baseado em Máquina de Indução Duplamente Alimentada - Suportabilidade para Afundamentos de Tensão*. PhD thesis, COPPE/UFRJ.
- der Broeck, H. W. V., Skudelny, H. C., and Stanke, G. V. (1988). Analysis and Realization of a Pulsewidth Modulator Based on Voltage Space Vectors. *IEEE Transactions on Industry Applications*, 24.
- E.ON (2006). Grid Code High and Extra High Voltage. Available on <http://www.eon-netz.com>.
- Erlich, I. and Bachmann, U. (2005). Grid Code Requirements Concerning Connection and Operation of Wind Turbines in Germany. *Power Engineering Society General Meeting*, 2:1253–1257.
- Erlich, I., Wrede, H., and Feltes, C. (2007). Dynamic Behavior of DFIG-Based Wind Turbines during Grid Faults. *Power Conversion Conference Nagoya*, pages 1195–1200.
- European Wind Energy Association - EWEA (2009). Wind Energy and the Environment. Available on [http://www.enerverde.eu/cms/download/factsheet\\_environment2.pdf](http://www.enerverde.eu/cms/download/factsheet_environment2.pdf). Technical report.
- Fan, L., Yin, H., and Kavasseri, R. (2009). Negative sequence compensation techniques of DFIG-based wind energy systems under unbalanced grid conditions. *Power Electronics and Machines in Wind Applications*, pages 1–6.
- Fortescue, C. L. (1918). Method of Symmetrical Coordinates Applied to the Solution of Polyphase Networks. *Transaction of AIEE*, 37:1027–1140.
- Global Wind Energy Council (2013). Global Wind Statistics 2012. Available on <http://www.gwec.net/global-figures/graphs/>. Technical report.

- Gomis-Bellmunt, O., Junyent-Ferre, A., Sumper, A., and BergasJane, J. (2008). Ride-through control of a doubly fed induction generator under unbalanced voltage sags. *IEEE Transactions on Energy Conversion*, 23:1036–1045.
- Heier, S. (2005). *Grid Integration of wind energy conversion system*. John Wiley & Sons.
- Hopfensperger, B., Atkinson, D. J., and Lakin, R. A. (2000). Stator-flux-oriented control of a doubly-fed induction machine with and without position encoder. *Electric Power Applications, IEE Proceedings*, 174:241–250.
- Hu, J. and He, Y. (2008). Modeling and control of grid-connected voltage-sourced converters under generalized unbalanced operation conditions. *IEEE Transaction on Energy Conversion*, 23:903–913.
- Hu, J. and He, Y. (2009a). Modeling and enhanced control of DFIG under unbalanced grid voltage conditions. *Electric Power System Research*, pages 273–281.
- Hu, J. and He, Y. (2009b). Reinforced Control and Operation of DFIG-Based Wind-Power-Generation System Under Unbalanced Grid Voltage Conditions. *IEEE Transactions on Energy Conversion*, 24:905–915.
- Hu, J. and He, Y. (2011). DFIG wind generation systems operating with limited converter rating considered under unbalanced network conditions e Analysis and control design. *Renewable Energy*, 36:829–847.
- Hu, J., He, Y., Xu, L., and Williams, B. (2009a). Improved control of DFIG systems during network unbalance using PI-R current regulators. *IEEE Transactions on Industry Electronics*, pages 439–451.
- Hu, J., Wang, H., He, Y., and Xu, L. (2009b). Improved Rotor Current Control of Wind Turbine Driven Doubly Fed Induction Generators During Network Unbalance. *International Conference on Sustainable Power Generation and Supply*, pages 1–7.
- IEC (2008). IEC 61400-21: Wind turbine: Measurement and assessment of power quality characteristics of grid connected wind turbines.

- IEC (2009). Electromagnetic compatibility (EMC) - Part 4-34: Testing and measurement techniques - Voltage dips, short interruptions and voltage variations immunity tests for equipment with mains current more than 16A per phase.
- Instituto Acende Brasil (2011). Análise do 12º Leilão de Energia Nova. Available on [http://www.acendebrasil.com.br/archives/files/20110817\\_AnalisePos\\_A-3\\_Rev2.pdf](http://www.acendebrasil.com.br/archives/files/20110817_AnalisePos_A-3_Rev2.pdf).
- Instituto Acende Brasil (2012). Análise do Leilão A-5 2012. Available on [http://www.acendebrasil.com.br/archives/files\\_2012/20121214\\_AnalisePos\\_A-5.pdf](http://www.acendebrasil.com.br/archives/files_2012/20121214_AnalisePos_A-5.pdf).
- Jamil, M., Gupta, R., and Singh, M. Y. (2012). A review of power converter topology used with PMSG based wind power generation. *Power India Conference, 2012 IEEE Fifth*, pages 1–6.
- Kasem, H., El-Saadany, E. F., El-Tamaly, H. H., and Wahab, M. A. A. (2008). An improved fault ride-through strategy for doubly fed induction generator-based wind turbines. *Renewable Power Generation, IET*, 2:201–214.
- Kaura, V. and Blasko, V. (1997). Operation of Phase Locked Loop System Under Distorted Utility Conditions. *IEEE Transaction on Industry Applications*, 33:58–63.
- Kearney, J. and Conlon, M. F. (2008). Control of Double Fed Induction Generator wind turbine during network voltage unbalance conditions. *Universities Power Engineering Conference*, pages 1–5.
- Kessler, C. (1955). Über die Vorausberechnung optimal abgestimmter Regelkreise - Teil 3. Die optimale Einstellung des Reglers nach dem Betragsoptimum. *Regelungstechnik*, 3:40–49.
- Kessler, C. (1958). Das symmetrische Optimum. *Regelungstechnik*, 6:359–400.
- Kovács, P. K. (1984). *Transient Phenomena in Electrical Machines*. Elsevier Science Publishing Co.



- Liang, J., Qiao, W., and Harley, R. G. (2010). Feed-Forward Transient Current Control for Low-Voltage Ride-Through Enhancement of DFIG Wind Turbines. *IEEE Transactions on Energy Conversion*, 25:836–843.
- Lima, F. K. A., Luna, A., Rodriguez, P., Watanabe, E. H., and Blaabjerg, F. (2010). Rotor Voltage Dynamics in the Doubly Fed Induction Generator During Grid Faults. *IEEE Transactions on Power Electronics*, 25:118–130.
- Ling, P., Francois, B., and Yongdong, L. (2009). Improved Crowbar Control Strategy of DFIG Based Wind Turbines for Grid Fault Ride-Through. *Applied Power Electronics Conference and Exposition, APEC 2009, Twenty-Fourth Annual IEEE*, pages 1932–1938.
- Liserre, M., Blaabjerg, F., and Hansen, S. (2005). Design and Control of an LCL-Filter-Based Three-Phase Active Rectifier. *IEEE Transactions on Industry Applications*, 41:1281–1291.
- Liserre, M., Teodorescu, R., and Blaabjerg, F. (2006). Multiple harmonics control for three-phase grid converter systems with the use of PI-RES current controller in a rotating frame. *IEEE Transactions on Power Electronics*, 21:836–841.
- Liu, S. Y. (2011). Controle Direto de Potência em Gerador de Indução Duplamente Alimentado. Master’s thesis, PPGEE/UFMG.
- Lohde, R., Jensen, S., Knop, A., and Fuchs, F. W. (2007). Analysis of Three Phase Grid Failure and Doubly Fed Induction Generator Ride-through using Crowbar. *Power Electronics and Applications, European Conference on*, pages 1–8.
- López, J., Gúbia, E., Sanchis, P., Roboam, X., and Marroyo, L. (2008a). Wind Turbines Based on Doubly Fed Induction Generator Under Asymmetrical Voltage Dips. *IEEE Transactions on Energy Conversion*, 23:321–330.
- López, J., Sanchis, P., Gúbia, E., Ursúa, A., Marroyo, L., and Roboam, X. (2008b). Control of Doubly Fed Induction Generator under Symmetrical Voltage Dips. *ISIE 2008. IEEE International Symposium on*, pages 2456–2462.

- López, J., Sanchis, P., Roboam, X., and Marroyo, L. (2007). Dynamic Behavior of the Doubly Fed Induction Generator During Three-Phase Voltage Dips. *IEEE Transactions on Energy Conversion*, 22:709–717.
- Luna, A., Lima, K., Corcoles, F., Watanabe, E., Rodriguez, P., and Teodorescu, R. (2009). Control of DFIG-WT under unbalanced grid voltage conditions. *Energy Conversion Congress and Exposition*, pages 370–377.
- Meegahapola, L. G., Littler, T., and Flynn, D. (2010). Decoupled-DFIG Fault Ride-Through Strategy for Enhanced Stability Performance During Grid Faults. *IEEE Transactions on Sustainable Energy*, 1:132–152.
- Mendes, V. F. (2009). Avaliação do Comportamento de um Sistema de Conversão de Energia Eólica Utilizando Gerador de Indução Duplamente Excitado Durante Afundamentos de Tensão. Master’s thesis, Universidade Federal de Minas Gerais.
- Morren, J. and de Haan, S. W. H. (2005). Ridethrough of Wind Turbines with Doubly-Fed Induction Generator During a Voltage Dip. *IEEE Transactions on Energy Conversion*, 20:435–441.
- Navarro, D. and Richter, M. (2007). Control of doubly-fed induction generators under asymmetrical grid conditions. *European Conference on Power Electronics and Applications*, pages 1–6.
- Oliveira, R. G. (2009). *Contribuição ao Controle de um Sistema de Geração a Velocidade Variável Utilizando Gerador de Indução Duplamente Excitado*. PhD thesis, PPGEE/UFMG.
- ONS (2009a). Procedimentos de Rede - Submódulo 3.6: Requisitos técnicos mínimos para a conexão à rede básica.
- ONS (2009b). Submódulo 2.8 - Gerenciamento dos indicadores de desempenho da rede básica e de seus componentes.
- Park, H.-G., Abo-Khalil, A. G., Lee, D.-C., and Son, K.-M. (2007). Torque Ripple Elimination for Doubly-Fed Induction Motors under Unbalanced Source Voltage. *7th International Conference on Power Electronics and Drive Systems*, pages 1301–1306.

- Pena, R., Cardenas, R., Clare, J., and Wheeler, P. (2007). Control system for unbalanced operation of stand-alone doubly fed induction generators. *IEEE Transactions on Energy Conversion*, 22:544–545.
- Pena, R., Clare, J. C., and Asher, G. M. (1996). Doubly fed induction generator using back-to-back PWM converters and its application to variable speed wind-energy generation. *IEE Proceedings - Electric Power Applications*, 143:231–241.
- Peng, L., Li, Y., and Francois, B. (2009). Dynamic behavior of doubly fed induction generator wind turbines under three-phase voltage dips. *Power Electronics and Motion Control Conference*, pages 620–626.
- Petersson, A., Harnefors, L., and Thiringer, T. (2004). Comparison Between Stator-Flux and Grid-Flux-Oriented Rotor Current Control of Doubly-Fed Induction Generators. *Power Electronics Specialists Conference, PESC 2004, IEEE 35th Annual*, 1:482–486.
- Qiao, W. and Harley, R. G. (2008). Improved Control of DFIG Wind Turbines for Operation with Unbalanced Network Voltages. *Industry Applications Society Annual Meeting*, pages 1–7.
- Rabelo, B. (2009). *Optimal Reactive Power Sharing with the Doubly-Fed Induction Generators in Wind Turbines*. PhD thesis, Technische Universitat Chemnitz.
- Rahimi, M. and Parniani, M. (2010). Efficient control scheme of wind turbines with doubly induction generators for low-voltage ride-through capability enhancement. *IET-Renewable Power Generation*, 4:242–252.
- Ramos, M. C. L. (2009). Análise do comportamento de aerogeradores frente a afundamentos momentâneos de tensão. Master’s thesis, PPGEE/UFMG.
- Rasmussen, M. and Jørgensen, H. K. (2005). Current Technology for Integrating Wind Farms. *Transmission and Distribution Conference and Exhibition: Asia and Pacific*, pages 1–4.
- Rodriguez, P., Teodorescu, R., Candela, I., Timbus, A. V., and Blaabjerg, F. (2006). New positive-sequence voltage detector for grid synchronization of power converters under faulty grid conditions. *37th IEEE Power Electronics Specialists Conference*, pages 1–7.

- Seman, S., Niiranen, J., Karneva, S., Arkkio, A., and Saitz, J. (2006). Performance Study of a Doubly Fed Wind Power Induction Generator Under Network Disturbances. *IEEE Transactions on Energy Conversion*, 21:883–890.
- Song, H.-S. and Nam, K. (1999). Dual Current Control Scheme for PWM Converter Under Unbalanced Input Voltage Conditions. *IEEE Transactions On Industrial Electronics*, 46:953–959.
- Suul, J. A., Molinas, M., Norum, L., and Undeland, T. (2008). Tuning of Control Loops for Grid Connected Voltage Source Converters. *2nd IEEE International Conference on Power and Energy (PECon)*, 1:797–802.
- Tang, Y. and Xu, L. (1992). Stator field oriented control of doubly-excited induction machine in wind power generating system. *Proceedings of 35th Midwest Symposium Circuits and Systems*, 2:1446–1449.
- Vítecková, M. and Vítecek, A. (2003). Modulus optimum for digital controllers. *Acta Montanistica Slovaca*, 8.
- Wagner, C. F. and Evans, R. D. (1933). *Symmetrical Components as Applied to the Analysis of Unbalanced Electrical Circuits*. McGraw-Hill.
- Wang, H., Zhang, W., Hu, J., and He, Y. (2009). Improved dual-PI rotor current control scheme for a wind-driven DFIG during asymmetrical grid voltage dips. *Electric Machines and Drives Conference*, pages 171–176.
- Wang, Y. and Xu, L. (2010). Coordinated Control of DFIG and FSIG-Based Wind Farms Under Unbalanced Grid Conditions. *IEEE Transactions on Power Delivery*, 25:367–377.
- Wang, Y., Xu, L., and Williams, B. W. (2008). Improved Operation of DFIG and FSIG-based Wind Farms during Network Unbalance. *Power and Energy Society General Meeting - Conversion and Delivery of Electrical Energy in the 21st Century*, pages 1–7.
- Xiang, D., Ran, L., Tavner, P. J., and Yang, S. (2006). Control of Doubly Fed Induction generator in a Wind Turbine During Grid Fault Ride-Through. *IEEE Transactions on Energy Conversion*, 21:652–662.

- Xu, L. (2008). Coordinated control of DFIG's rotor and grid side converters during network unbalance. *IEEE Transactions on Power Electronics*, 23:1041–1049.
- Xu, L., Andersen, B. R., and Cartwright, P. (2005). VSC transmission operating under unbalanced ac conditions - Analysis and control design. *IEEE Transaction on Power Delivery*, 20:427–434.
- Xu, L. and Wang, Y. (2007). Dynamic modeling and control of DFIG-based wind turbines under unbalanced network conditions. *IEEE Transactions on Power System*, 22:314–323.
- Yang, J., Fletcher, J. E., and O'Reilly, J. (2009). A series dynamic resistor based converter protection scheme for doubly-fed induction generator during various fault conditions. *IEEE Power & Energy Society General Meeting*, pages 1–8.
- Yin, B., Oruganti, R., Panda, S. K., and Bhat, A. K. S. (2008). An Output-Power-Control Strategy for a Three-Phase PWM Rectifier Under Unbalanced Supply Conditions. *IEEE Transactions On Industrial Electronics*, 55:2140–2151.
- Zhang, L. H., Cai, X., and Guo, J. H. (2009). Dynamic Responses of DFIG Fault Currents Under Constant AC Excitation Condition. *Power and Energy Engineering Conference*, pages 1–4.
- Zhang, X., Li, Q., Yang, S., Xie, Z., and Cao, R. (2010). Response and Protection of DFIG System under Grid Fault. *Power and Energy Engineering Conference (APPEEC)*, pages 1–5.
- Zhou, Y., Bauer, P., Ferreira, J. A., and Pierik, J. (2007). Control of DFIG under Unsymmetrical Voltage Dip. *IEEE Power Electronics Specialists Conference*, pages 933–938.
- Zhou, Y., Bauer, P., Ferreira, J. A., and Pierik, J. (2009). Operation of Grid-Connected DFIG Under Unbalanced Grid Voltage Condition. *IEEE Transactions On Energy Conversion*, 24:240 – 246.



# Controllers Tuning and Orientation

---

This appendix intends to explain some details about the classical control strategy. First in the Section A.1 the Clark and Park Transforms used for the coordinates transformation for the control are presented. In the Section A.2 the methods used for the controllers tuning are described and in Section A.3 the mathematical modeling of the controls are presented, including briefly explanation about the orientation and the controllers tuning process. Finally, the section A.4 present the method of discretization used for the discrete implementation of the controls in the test benches.

## A.1 Clark and Park Transforms

The Clark Transform converts a three-phase coordinates system (ABC) to a bi-phase one ( $\alpha\beta$ ) both being stationary in relation to a fixed point. Whereas the A, B and C axis are  $120^\circ$  spatially separated each other the  $\alpha$  and  $\beta$  axis are  $90^\circ$  separated. Equations (A.1) and (A.2) show the direct and inverse Clark Transforms, respectively, where the variable “x” can be voltages, currents, fluxes, etc.

$$\begin{bmatrix} x_\alpha \\ x_\beta \end{bmatrix} = \frac{2}{3} \begin{bmatrix} 1 & -\frac{1}{2} & -\frac{1}{2} \\ 0 & \frac{\sqrt{3}}{2} & -\frac{\sqrt{3}}{2} \end{bmatrix} \begin{bmatrix} x_A \\ x_B \\ x_C \end{bmatrix}, \quad (\text{A.1})$$

$$\begin{bmatrix} x_A \\ x_B \\ x_C \end{bmatrix} = \begin{bmatrix} 1 & 0 \\ -\frac{1}{2} & \frac{\sqrt{3}}{2} \\ -\frac{1}{2} & -\frac{\sqrt{3}}{2} \end{bmatrix} \begin{bmatrix} x_\alpha \\ x_\beta \end{bmatrix}, \quad (\text{A.2})$$

The Park Transform refers the variables of the stationary reference frame ( $\alpha\beta$ ) to a rotating frame (dq). The direct and inverse Park Transforms are shown in Equations A.3 and A.4, where  $\theta$  is the angle between the stationary and rotating reference frames.

$$\begin{bmatrix} x_d \\ x_q \end{bmatrix} = \begin{bmatrix} \cos(\theta) & \text{sen}(\theta) \\ -\text{sen}(\theta) & \cos(\theta) \end{bmatrix} \begin{bmatrix} x_\alpha \\ x_\beta \end{bmatrix}, \quad (\text{A.3})$$

$$\begin{bmatrix} x_\alpha \\ x_\beta \end{bmatrix} = \begin{bmatrix} \cos(\theta) & -\text{sen}(\theta) \\ \text{sen}(\theta) & \cos(\theta) \end{bmatrix} \begin{bmatrix} x_d \\ x_q \end{bmatrix}. \quad (\text{A.4})$$

Figure A.1 depicts the graphical representation of Clark and Park Transforms.

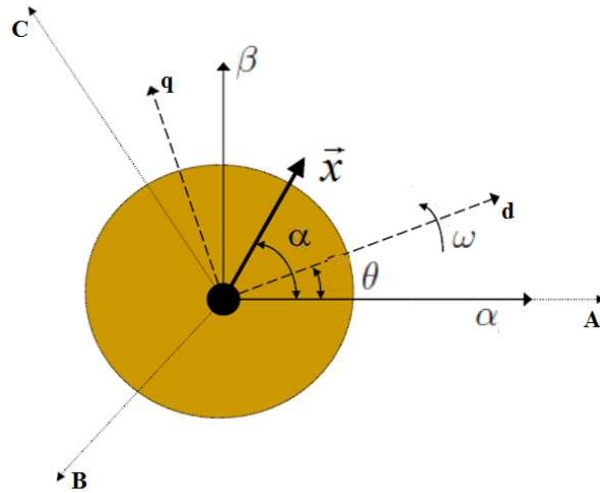


Figure A.1: Graphical representation of Clark and Park Transforms.

Through Equations A.1 to A.4 it is possible to write the direct and inverse transformation of the stationary coordinates system ABC to the rotating



coordinates system dq:

$$\begin{bmatrix} x_d \\ x_q \end{bmatrix} = \frac{2}{3} \begin{bmatrix} \cos(\theta) & \cos(\theta - 120^\circ) & \cos(\theta + 120^\circ) \\ -\text{sen}(\theta) & -\text{sen}(\theta - 120^\circ) & -\text{sen}(\theta + 120^\circ) \end{bmatrix} \begin{bmatrix} x_A \\ x_B \\ x_C \end{bmatrix}, \quad (\text{A.5})$$

$$\begin{bmatrix} x_A \\ x_B \\ x_C \end{bmatrix} = \begin{bmatrix} \cos(\theta) & -\text{sen}(\theta) \\ \cos(\theta - 120^\circ) & -\text{sen}(\theta - 120^\circ) \\ \cos(\theta + 120^\circ) & -\text{sen}(\theta + 120^\circ) \end{bmatrix} \begin{bmatrix} x_d \\ x_q \end{bmatrix}. \quad (\text{A.6})$$

In control of power converters and electric machines the use of Park Transform is very useful, because choosing  $\theta$  accordingly, that is, choosing an adequate rotating reference frame orientation it is possible to transform three-phase sinusoidal variables to bi-phase DC variables.

## A.2 Modulus Optimum and Symmetrical Optimum

Most of the dynamics involved in the process of electric machine control can be approximated by second order transfers functions with two different time constants:

- a large or slow time constant ( $\tau_{lr}$ ), which represents the machine electrical dynamics;
- a small or fast time constant ( $\tau_{sm}$ ), which represents the converter and measurement system dynamics.

It is a common practice in German literature to use two methods to adjust PI controllers for this kind of system: the Modulus Optimum (MO) (Kessler, 1955) and the Symmetrical Optimum (SO) (Kessler, 1958). More details about these methods can be found in Vítecková and Vítecek (2003) and Suul et al. (2008).

The PI controller transfer function can be written as:

$$G_c(s) = K_p \left( 1 + \frac{1}{T_i s} \right), \quad (\text{A.7})$$

where  $K_p$  is the proportional gain and  $T_i$  is the integrative time.

In the MO method the closed loop gain is kept equal to 1 for a bandwidth as large as possible. The zero of the PI controller is used to cancel the dynamics of the dominant pole (large time constant) and the proportional gain is adjusted in order to set the closed loop damping equal to  $\frac{1}{\sqrt{2}}$ . Therefore the control response for a step changing in the reference presents a small overshoot (4,3%) and a rising time of  $4,7^* \tau_s m$ . The following equations are used to calculate the controller gains:

$$T_i = \tau_{lr}, \quad (\text{A.8})$$

$$K_p = \frac{\tau_{lr}}{2K_s \tau_{sm}}, \quad (\text{A.9})$$

where  $K_s$  is the system open loop gain.

The SO method is similar to the MO, but a closed loop gain of 0.5 is chosen and, thus a overshoot of approximately 8.1% and a rising time of  $7.6^* \tau_s m$  are obtained. This method is more suitable for systems with pure integrators (Suul et al., 2008). Even with an integrator in the system to be controlled, a control integrative parcel is used to improve the phase margin. The gains are calculated as following:

$$T_i = 4\tau_{sm}, \quad (\text{A.10})$$

$$K_p = \frac{1}{2K_s \tau_{sm}}. \quad (\text{A.11})$$

## A.3 Control Mathematical Modeling and Gains Tuning

### A.3.1 GSC control

The classical GSC control strategy uses internal loops controlling the grid (filter) currents oriented in a synchronous reference frame. For the orientation, the angle of the grid voltage is used in the Park Transformation (Section A.1). This orientation permits a decoupled control of active and reactive power.

#### A.3.1.1 GSC Current Control

Equation 2.10 can be divided in real (d) and imaginary (q) parts, then it is rewritten as:

$$v_{n_d} = -R_f i_{n_d} - L_f \frac{di_{n_d}}{dt} + v_{N_d} + \omega_N L_f i_{n_q}, \quad (\text{A.12})$$

$$v_{n_q} = -R_f i_{n_q} - L_f \frac{di_{n_q}}{dt} + v_{N_q} - \omega_N L_f i_{n_d}. \quad (\text{A.13})$$

Using the grid voltage orientation  $v_{N_q} = 0$ , thus these equations can be again rewritten as:

$$v_{n_d} = -R_f i_{n_d} - L_f \frac{di_{n_d}}{dt} + v_{N_d \text{comp}}, \quad (\text{A.14})$$

$$v_{n_q} = -R_f i_{n_q} - L_f \frac{di_{n_q}}{dt} + v_{N_q \text{comp}}, \quad (\text{A.15})$$

where  $v_{N_d \text{comp}} = v_{N_d} + \omega_N L_f i_{n_q}$  and  $v_{N_q \text{comp}} = -\omega_N L_f i_{n_d}$ . These are called cross-coupling terms and they can be compensated as depicted in Figure 2.3.

Applying the Laplace Transformation in Equations A.14 and A.15, and considering that the cross-coupling terms are totally compensated, Equation

A.16 gives the transfer function that describes the current dynamics:

$$G_{i_n}(s) = \frac{i_n(s)}{v_n(s)} = -\frac{1}{L_f s + R_f}. \quad (\text{A.16})$$

In this transfer function the subscript d and q are omitted, since both components have the same dynamics. The GSC current control loop is depicted in Figure A.2. Besides the current dynamics, there exist the converter dynamics ( $G_a$ ).

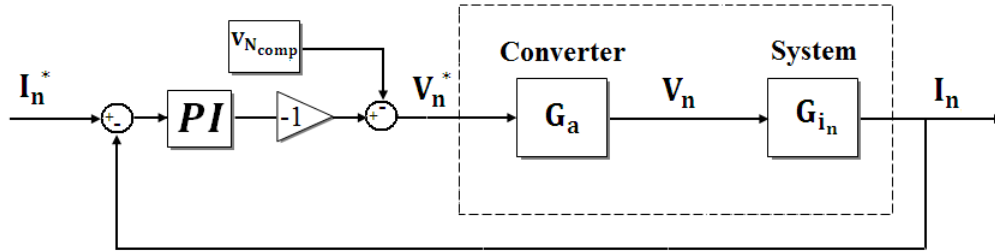


Figure A.2: Block diagram of the GSC current control.

The complete modeling of the converters requires studies that are out of the scope of the present work. Nevertheless, the converter dynamic behavior influences the control system. Therefore, a simple first order transfer function plus time delay (dead time) is used to model this dynamics:

$$G_a(s) = \frac{e^{-T_d}}{\tau_a s + 1}, \quad (\text{A.17})$$

where  $T_d$  is the dead time and  $\tau_a$  is the time constant of the approximated converter dynamic behavior. This time constant and dead-time can also include the dynamic of the measurement system that also influences the control behavior.

Through the transfer functions given in Equations A.17 and A.16 and using the method of Modulus Optimum (MO), which was described previously, the GSC current controllers gains can be calculated as following:

$$T_i = \frac{L_f}{R_f}, \quad (\text{A.18})$$

$$K_p = \frac{L_f}{2\tau_a}. \quad (\text{A.19})$$

The transfer function of the closed loop using this gains can be approximated by (Suul et al., 2008):

$$G_{mf_{in}}(s) = \frac{1}{2\tau_a s + 1}, \quad (\text{A.20})$$

equation used for the project of the external control loops.

Equations A.18 and A.19 are used to calculate the GSC current controller gains for the simulation model and also for the test bench.

### A.3.1.2 DC-Link Voltage Control

The DC-link voltage control is done balancing the active power flowing through the GSC and the RSC. Three situations are possible:

- In the subsynchronous generator operation, the GSC injects in the DC-link an active power equal to the active power drawn by the RSC and supplied to the rotor;
- In the synchronous operation, no power is flowing through the DC-link;
- In the supersynchronous generator operation, the power flow is inverted and, thus, the GSC draws the power supplied by the RSC to the DC-link.

The schematic diagram of the DC-link is shown in Figure A.3. Analyzing this circuit, the following equations can be written:

$$i_{dc} = C \frac{dv_{dc}}{dt}, \quad (\text{A.21})$$

$$i_{dcn} = i_{dcr} + C \frac{dv_{dc}}{dt}, \quad (\text{A.22})$$

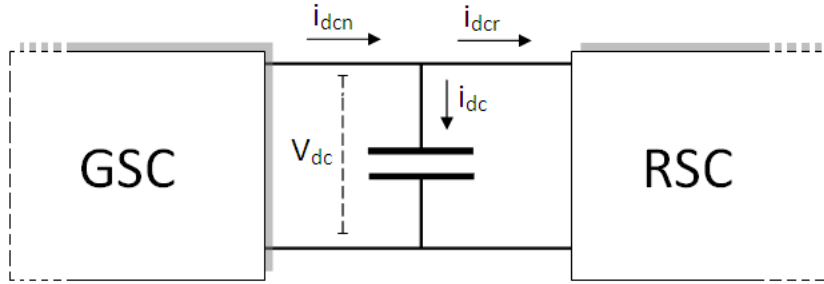


Figure A.3: Schematic diagram of the DC-link.

The regulation of the DC-link voltage is done manipulating the direct axis current flowing through the GSC. Therefore, the DC-link voltage control loop is external to the direct GSC current, as depicted in Figure 2.3.

The transfer function relating the GSC current and DC-link voltage is obtained through the Laplace transformation applied to Equation A.22 as highlighted below:

$$G_{V_{dc}}(s) = \frac{v_{dc}(s)}{i_{nd}(s)} = \frac{1}{sC}, \quad (\text{A.23})$$

where current  $i_{dcr}$  in Equation A.22 acts like a perturbation, thus, its effect can be reduced using a feedforward compensator or choosing a control with an adequate bandwidth.

Figure A.4 shows the block diagram representing the DC-link voltage control loop. Besides the DC-link dynamics, it is represented the dynamics of the internal current control loop.

The presence of a pure integrator in the system leads to the use of the Symmetrical Optimums (SO) method for the control adjustment:

$$T_i = 4\tau_{vdc}, \quad (\text{A.24})$$

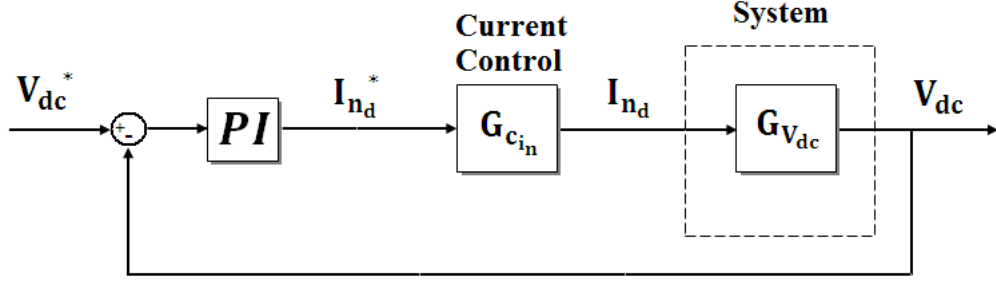


Figure A.4: Block diagram representing the DC-link voltage control loop.

$$K_p = \frac{C}{2\tau_{vdc}}, \quad (\text{A.25})$$

where  $\tau_{vdc}$  represents the delay inserted by the measurement system plus the dynamics of the current control loop, which is given in Equation A.20.

### A.3.1.3 GSC Reactive Power Control

The reactive power has several purposes such as minimizing losses, control the grid power factor, compensate harmonics, guarantee voltage support, etc.

With the grid voltage angle orientation, the reactive power control loop is implemented externally to the loop controlling the quadrature current. The reactive power is not direct measured, but calculated through the following equation:

$$Q_n = -\frac{3}{2}v_{N_d}i_{n_q}. \quad (\text{A.26})$$

Generally the calculated power is noisy, because it is used the multiplication between the measured current and voltage that are a bit noisy due to the grid harmonics. It is common the use of a filter which is considered a first order one in the present work. Therefore, the transfer function of the system to be controlled is:

$$G_{Q_n}(s) = \frac{Q_n(s)}{i_{nq}(s)} = \frac{-\frac{3}{2}v_{Nd}}{T_{f_{Q_n}}s + 1}, \quad (\text{A.27})$$

where  $T_{f_{Q_n}}$  is the filter time constant. The closed loop is represented in Figure A.5.

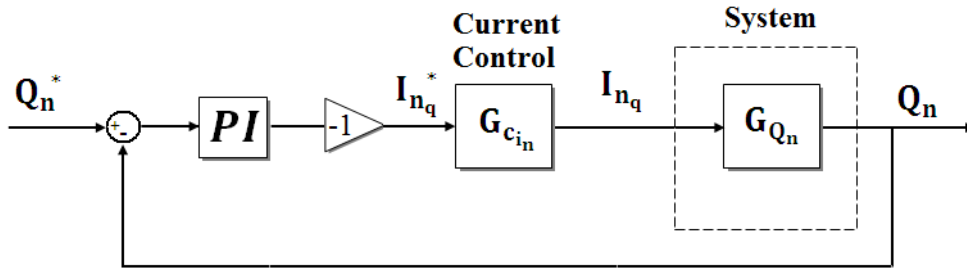


Figure A.5: Block diagram representation of the GSC reactive power control.

Through Equations A.20 and A.27, using the MO method the gains are calculated as:

$$T_i = \tau_{f_{Q_n}}, \quad (\text{A.28})$$

$$K_p = \frac{\tau_{f_{Q_n}}}{3v_{nd}\tau_a}. \quad (\text{A.29})$$

The reactive power control does not need to be so fast, that is, it is not necessary a large bandwidth to avoid power quality problems. Therefore, the filter time constant is chosen large and the bandwidth resulting from the MO method can be reduced dividing the proportional gain accordingly.

### A.3.2 RSC control

Figure 2.5 shows the block diagram representation of the control structure. Before starting the presentation of each RSC control loop, in the following subsection the orientation of the generator variables is analyzed.



### A.3.2.1 Generator Variables Orientation

Similar to the GSC control, it is desirable to use the rotor currents orientation that permits the decoupled control of active and reactive power. In electrical machines is common to use the stator, the rotor or the mutual fluxes for the control orientation (Hopfensperger et al., 2000). For the doubly-fed machine normally the so called virtual grid flux is used for the rotor currents orientation (Pettersson et al., 2004), (Hopfensperger et al., 2000).

In steady state the grid virtual flux ( $\psi_{s_v}$ ), or similarly the stator virtual flux, is calculated from Equation 2.1 neglecting the voltage drop in the stator resistance, since this resistance is generally small:

$$\vec{\psi}_{s_v} = \frac{\vec{v}_s}{j\omega_s}. \quad (\text{A.30})$$

Equation A.30 shows that the virtual flux has the same frequency of the grid ( $\omega_s = \omega_N$ ) and it is  $90^\circ$  lagging the grid voltage. Figure A.6 depicts the the vector diagrams for the orientation of the direct axis in the direction of the virtual flux and stator flux. One can notice that using the virtual flux orientation, the angle difference compared with the use of the stator flux is small if the voltage drop in the stator resistance is relatively small.

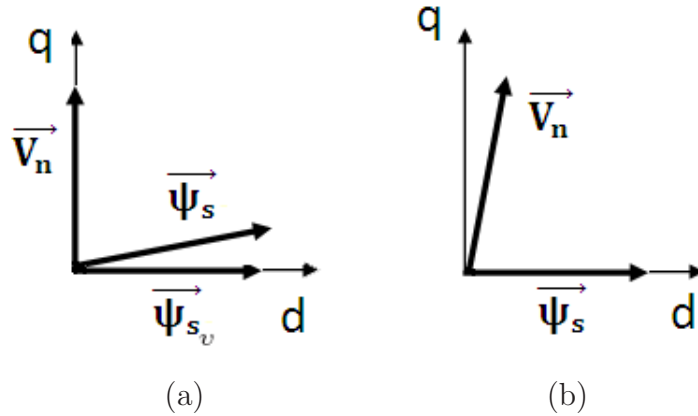


Figure A.6: Vector diagram of the grid voltage and stator flux:

- (a) - Virtual flux orientation;
- (b) - Stator flux orientation.

Instead of using the virtual flux, in this work the stator currents and voltages are orientated using angle of the stator (grid) voltage (transformation angle  $\theta_N$ ), as depicted in the vector diagram of Figure A.7. With this orientation the stator current direct current controls the active stator power whereas the quadrature stator current is responsible for the reactive power, similar to the GSC.

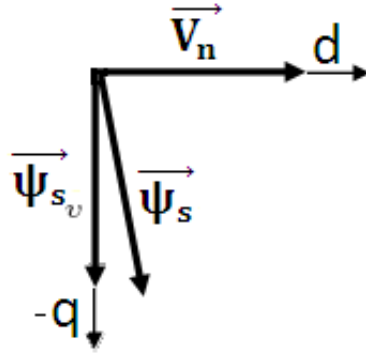


Figure A.7: Stator or grid voltage orientation.

Petersson et al. (2004) analyzes the advantages of using the stator voltage orientation. This paper shows that, using this orientation, the system stability and damping are independent of the rotor currents, thus, independent of the RSC control, different from the case that uses the stator flux orientation. It is possible to implement a decoupled control of active and reactive stator power manipulating the rotor currents, as demonstrated below.

Using Equations 2.1 to 2.6 the stator currents can be written as:

$$i_{sd} \cong -\frac{L_m}{L_s} i_{rd}, \quad (\text{A.31})$$

$$i_{sq} \cong \frac{|\vec{\psi}_s|}{L_s} - \frac{L_m}{L_s} i_{rq}. \quad (\text{A.32})$$

Through Equations A.31 and A.32 it is seen that the direct and quadrature axes rotor currents affect only its respective stator current components. Therefore, the active and reactive stator power equations can be written as:

$$P_s = \frac{3}{2}v_{s_d}i_{s_d} = -\frac{3}{2}\frac{L_m}{L_s}v_{s_d}i_{r_d}, \quad (\text{A.33})$$

$$Q_s = -\frac{3}{2}v_{s_d}i_{s_q} = \frac{3}{2}\frac{v_{s_d}^2}{\omega_s L_s} + \frac{3}{2}\frac{L_m}{L_s}v_{s_d}i_{r_q}. \quad (\text{A.34})$$

One can notice that the active stator power depends on the direct axis rotor current and the reactive power depends on the quadrature axis rotor current. Therefore, decoupled rotor currents control loops with external active and reactive power control loops are used, as depicted in Figure 2.5.

Through Equations 2.8 and A.30 the electromagnetic torque can be calculated as:

$$T_e = -\frac{3}{2}\frac{L_m}{L_s}\frac{v_{s_d}}{\omega_s}i_{r_d}, \quad (\text{A.35})$$

therefore just depending on the direct rotor current.

### A.3.2.2 RSC Current Control

Using the stator voltage orientation, Equation 2.2 is divided in direct (real) and quadrature (imaginary) components and is rewritten as:

$$v_{r_d} = R_r i_{r_d} + \sigma L_r \frac{di_{r_d}}{dt} - \omega_r \frac{L_m}{L_s} \psi_{s_q} - \omega_r \sigma L_r i_{r_q}, \quad (\text{A.36})$$

$$v_{r_q} = R_r i_{r_q} + \sigma L_r \frac{di_{r_q}}{dt} + \omega_r \sigma L_r i_{r_d}, \quad (\text{A.37})$$

where  $\sigma = 1 - \frac{L_m^2}{L_s L_r}$  is the machine leakage coefficient. The last terms in these equations are the cross-coupling between direct and quadrature axes. The term dependent on the stator flux linkage in Equation A.36 is the back electromotive force (EMF). Equations A.36 and A.37 can be written grouping these terms:

$$v_{r_d} = R_r i_{r_d} + \sigma L_r \frac{di_{r_d}}{dt} + v_{r_d comp}, \quad (\text{A.38})$$

$$v_{r_q} = R_r i_{r_q} + \sigma L_r \frac{di_{r_q}}{dt} + v_{r_q comp}, \quad (\text{A.39})$$

where  $v_{r_d comp} = -\omega_r \frac{L_m}{L_s} \psi_{s_q} - \omega_r \sigma L_r i_{r_q}$  and  $v_{r_q comp} = \omega_r \sigma L_r i_{r_d}$ . These terms act like a perturbation for the current control and, as it is possible to estimate them, compensators are used to improve the perturbation rejection.

Applying the Laplace Transform and neglecting the perturbation terms, Equations A.38 and A.39 are written in the frequency domain as:

$$G_{i_r}(s) = \frac{i_r(s)}{v_r(s)} = \frac{1}{\sigma L_r s + R_r}. \quad (\text{A.40})$$

The subscripts dq were suppressed since both axes have the same transfer function. The rotor currents are controlled imposing a voltage in the rotor circuit through the converter, as depicted in Figure A.8.

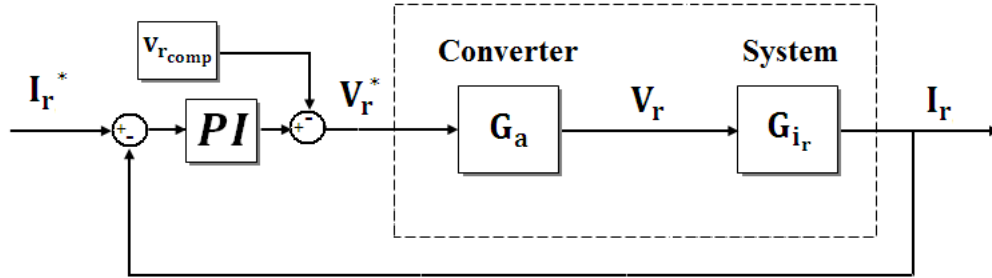


Figure A.8: Block diagram representation of the rotor currents control structure.

For the rotor current control adjustment is also used the MO method, thereby using the transfer function given in Equation A.40 the controllers gains are calculated:

$$T_i = \frac{\sigma L_r}{R_f}, \quad (\text{A.41})$$

$$K_p = \frac{\sigma L_r}{2\tau_a}. \quad (\text{A.42})$$

The closed loop response of the rotor current control can be approximated by a first order system given in Equation A.43 that is used to calculate the control parameters of the external control loops, as presented in the next subsection.

$$G_{mf_{i_r}}(s) = \frac{1}{2\tau_a s + 1}. \quad (\text{A.43})$$

### A.3.2.3 Stator Active and Reactive Power Control

Equations A.33 and A.34 show the calculation of the active and reactive stator power using the stator voltage orientation. Similar to the GSC control, active and reactive powers are filtered using a first order filter. Equation A.44 and A.45 show the transfer function representing the dynamics of the active and reactive power, respectively. Figures A.9 and A.10 depict the control loop blocks diagram.

$$G_{P_s}(s) = \frac{P_s(s)}{i_{r_d}(s)} = \frac{-\frac{3}{2} \frac{L_m}{L_s} v_{s_d}}{T_{f_{P_s}} s + 1}. \quad (\text{A.44})$$

$$G_{Q_s}(s) = \frac{Q_s(s)}{i_{r_q}(s)} = \frac{\frac{3}{2} \frac{L_m}{L_s} v_{s_d}}{T_{f_{Q_s}} s + 1}. \quad (\text{A.45})$$

The active and reactive stator power, controlled through the RSC, is similar to the GSC reactive power control, therefore the gains are calculated as:

$$T_i = T_{f_{P_s}} = T_{f_{Q_s}}, \quad (\text{A.46})$$

$$K_p = \frac{T_{f_{P_s}}}{3 \frac{L_m}{L_s} \tau_a}. \quad (\text{A.47})$$

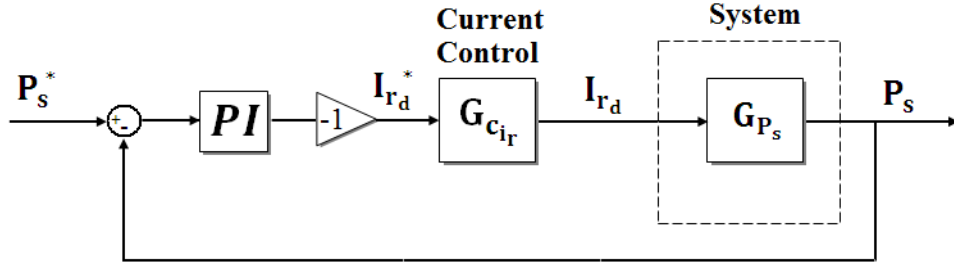


Figure A.9: Block diagram representation of the stator active power control structure.

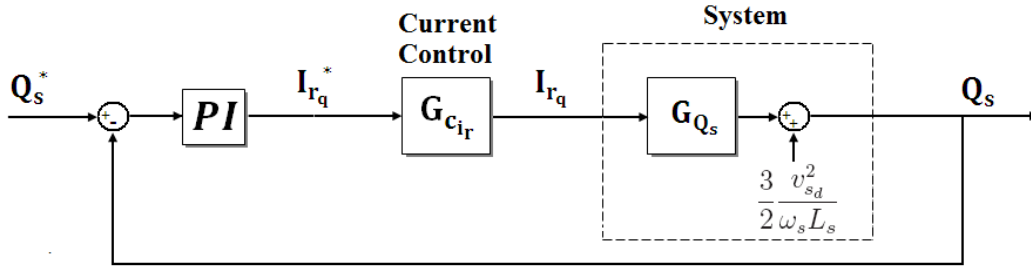


Figure A.10: Block diagram representation of the stator reactive power control structure.

## A.4 Controller Discretization

The MO and SO methods described previously are employed using the continuous transfer functions, but generally the control is implemented digitally. Therefore, it is necessary to make the discretization of the controller. In this work the Euler approximation, which is shown in Equation A.48, is used.

$$s \rightarrow \frac{1 - z^{-1}}{T_s}, \quad (\text{A.48})$$

where  $T_s$  is the sampling time and  $z^{-1}$  is the unity delay in the Z-Transform. Choosing a sampling time much smaller than the system time constants, the project using the continuous transfer functions does not differ from the

project in the discrete domain (Suul et al., 2008).

The Euler approximation in this work is used to implement the PI controllers and also the digital filters used in some situations.

# TUD Test Bench Parameters

---

Table B.1: Parameters of the generator of the TUD test bench.

<i>Variable</i>	<i>Value</i>	<i>Unity</i>
Rated Power	4	kW
Stator Voltage	400	V
Rotor Voltage	950	V
Frequency ( $f_s$ )	50	Hz
Number of Poles (P)	4	-
Magnetizing Inductance ( $L_m$ )	160.1	mH
Stator Self Inductance ( $L_s$ )	169.7	mH
Rotor Self Inductance ( $L_r$ )	169.7	mH
Stator Resistance ( $R_s$ )	1.07	$\Omega$
Rotor Resistance ( $R_r$ )	1.32	$\Omega$
Inertia (J)	0.032	$\text{Kg}\cdot\text{m}^2$
Friction (B)	0.007	N.m.s

Table B.2: Voltage sag parameters of the TUD test bench.

<i>Variable</i>	<i>Value</i>	<i>Unity</i>
$L_1$	20	mH
$L_2$	3	mH
$R_1$	0.3	$\Omega$



Table B.3: Controller gains of the TUD test bench.

<b><i>Control Loop</i></b>	<b><i>Proportional Gain (<math>K_p</math>)</i></b>	<b><i>Integral Gain (<math>K_i</math>)</i></b>
GSC Currents	8.2 [ $\Omega$ ]	3300 [ $\Omega/s$ ]
DC-link Voltage	0.5 [S]	125 [S/s]
RSC Currents	50 [ $\Omega$ ]	3000 [ $\Omega/s$ ]
Stator Power	0.0013 [1/V]	0.04 [1/(V.s)]

Table B.4: Other parameters of the TUD test bench.

<b><i>Variable</i></b>	<b><i>Value</i></b>	<b><i>Unity</i></b>
DC-link Voltage ( $V_{dc}$ )	450	V
DC-link Capacitance (C)	1	mF
Filter Inductance ( $L_f$ )	8	mH
Filter Resistance ( $R_f$ )	0.5	$\Omega$
Transformer Ratio	400/70	-

## UFMG Test Bench Parameters

---

Table C.1: Parameters of the generator of the UFMG test bench.

<i>Variable</i>	<i>Value</i>	<i>Unity</i>
Rated Power*	30	kW
Stator Voltage**	400	V
Rotor Voltage	300	V
Frequency** ( $f_s$ )	50	Hz
Number of Poles (P)	4	-
Magnetizing Inductance ( $L_m$ )	100	mH
Stator Self Inductance ( $L_s$ )	102.4	mH
Rotor Self Inductance ( $L_r$ )	102.4	mH
Stator Resistance ( $R_s$ )	0.240	$\Omega$
Rotor Resistance ( $R_r$ )	0.300	$\Omega$
Inertia (J)	0.476	Kg.m <sup>2</sup>
Friction (B)	0.010	N.m.s

\* Due to the limited current capability of the converter, the rated power of this system is considered equal to 25kW, since the rated power of the generator cannot be attained, because the restrictions on rotor currents supplying.

\*\* The generator is supplied with a stator voltage equal to 380V with 60Hz.

Table C.2: Controller gains of the UFMG test bench.

<i>Control Loop</i>	<i>Proportional Gain (<math>K_p</math>)</i>	<i>Integral Gain (<math>K_i</math>)</i>
GSC Currents	6 [ $\Omega$ ]	750 [ $\Omega/s$ ]
DC-link Voltage	1 [S]	10 [S/s]
RSC Currents	3 [ $\Omega$ ]	150 [ $\Omega/s$ ]
Stator Power	0.06 [1/V]	0.64 [1/(V.s)]

Table C.3: Other parameters of the UFMG test bench.

<i>Variable</i>	<i>Value</i>	<i>Unity</i>
DC-link Voltage ( $V_{dc}$ )	450	V
DC-link Capacitance (C)	3.06	mF
Filter Inductances ( $L_f$ )	2	mH
Filter Capacitance ( $C_f$ )	20	$\mu$ F
Filter Resistance ( $R_f$ )	3	$\Omega$
Transformer Ratio	380/220	-

# Simulation Model Parameters

---

Table D.1: Parameters of the generator used in the simulation model.

<i>Variable</i>	<i>Value</i>	<i>Unity</i>
Rated Power	2	MW
Stator Voltage	690	V
Rotor Voltage	690	V
Frequency ( $f_s$ )	50	Hz
Number of Poles (P)	4	-
Magnetizing Inductance ( $L_m$ )	2.3	mH
Stator Leakage Inductance ( $L_{\sigma s}$ )	75.8	$\mu$ H
Rotor Leakage Inductance ( $L_{\sigma r}$ )	60.4	$\mu$ H
Stator Resistance ( $R_s$ )	23.81	m $\Omega$
Rotor Resistance ( $R_r$ )	23.81	m $\Omega$
Inertia (J)	59.4	Kg.m <sup>2</sup>
Friction (B)	0.007	N.m.s

Table D.2: Controller gains of the simulation.

<i>Control Loop</i>	<i>Proportional Gain (<math>K_p</math>)</i>	<i>Integral Gain (<math>K_i</math>)</i>
GSC Currents	0.4 [ $\Omega$ ]	10 [ $\Omega/s$ ]
DC-link Voltage	66 [S]	1670 [S/s]
RSC Currents	0.26 [ $\Omega$ ]	1.36 [ $\Omega/s$ ]
Stator Power	0.0026 [1/V]	0.0789 [1/(V.s)]

Table D.3: Other parameters of the simulation model.

<i>Variable</i>	<i>Value</i>	<i>Unity</i>
DC-link Voltage ( $V_{dc}$ )	2000	V
DC-link Capacitance (C)	133.7	mF
Filter Inductance ( $L_f$ )	407	$\mu$ H
Filter Resistance ( $R_f$ )	0.01	$\Omega$
Transformer Ratio	690/690	-